



HAL
open science

Personalised Electrophysiological Models of Ventricular Tachycardia for Radio Frequency Ablation Therapy Planning

Jatin Relan

► **To cite this version:**

Jatin Relan. Personalised Electrophysiological Models of Ventricular Tachycardia for Radio Frequency Ablation Therapy Planning. Other. Ecole Nationale Supérieure des Mines de Paris, 2012. English. NNT : 2012ENMP0042 . pastel-00794165

HAL Id: pastel-00794165

<https://pastel.hal.science/pastel-00794165>

Submitted on 25 Feb 2013

HAL is a multi-disciplinary open access archive for the deposit and dissemination of scientific research documents, whether they are published or not. The documents may come from teaching and research institutions in France or abroad, or from public or private research centers.

L'archive ouverte pluridisciplinaire **HAL**, est destinée au dépôt et à la diffusion de documents scientifiques de niveau recherche, publiés ou non, émanant des établissements d'enseignement et de recherche français ou étrangers, des laboratoires publics ou privés.

École doctorale n°84:
Sciences et technologies de l'information et de la communication

Doctorat ParisTech

T H È S E

pour obtenir le grade de docteur délivré par

l'École nationale supérieure des mines de Paris

Spécialité
“Informatique temps-réel, robotique et automatique”

présentée et soutenue publiquement par

Jatin RELAN

le 15 June 2012

**Personalised Electrophysiological Models of Ventricular
Tachycardia for Radio Frequency Ablation Therapy Planning**

**Modèles électrophysiologiques personnalisés de tachycardie
ventriculaire pour la planification de la thérapie par ablation
radio-fréquence**

Directeur de thèse: **Nicholas AYACHE**
Co-encadrement de la thèse: **Maxime SERMESANT**
Co-encadrement de la thèse: **Hervé DELINGETTE**

Jury

Reza RAZAVI, St. Thomas' Hospital, King's College London

Olaf DÖSSEL, Karlsruhe Institute of Technology

Yves COUDIÈRE, University of Bordeaux

Pierre JAÏS, Haut-Lévêque Hospital, University of Bordeaux

Alexander V. PANFILOV, Department of Physics & Astronomy, Gent University

Nicholas AYACHE, Asclepios Research Team, INRIA Sophia Antipolis

Hervé DELINGETTE, Asclepios Research Team, INRIA Sophia Antipolis

Maxime SERMESANT, Asclepios Research Team, INRIA Sophia Antipolis

Président

Rapporteur

Rapporteur

Examinateur

Examinateur

Directeur

Examinateur

Examinateur

MINES ParisTech

Centre de Mathématiques Appliquées

Rue Claude Daunesse B.P. 207, 06904 Sophia Antipolis Cedex, France

**T
H
È
S
E**

Personalised Electrophysiological Models of Ventricular Tachycardia for Radio Frequency Ablation Therapy Planning

Abstract:

Computer models of cardiac Electrophysiology (EP) can be a very efficient tool to better understand the mechanisms of arrhythmias. Modelling cardiac electrophysiology for arrhythmias *in silico* has been an important research topic for the last decades. In order to translate this important progress into clinical applications, there is a requirement to make macroscopic models that can be used for the planning and performance of the clinical procedures. The objective of this thesis was to construct such macroscopic EP models specific to each patient for study and prediction, in order to improve the planning and guidance of radio frequency ablation (RFA) therapies on patients suffering from post infarction Ventricular Tachycardia (VT). In this work, we approached this goal in the following way.

The construction of patient-specific macroscopic 3D EP model required model personalisation i.e. estimation of patient-specific model parameters. Before application to the patient data, a quantitative adjustment of such models to experimental data was needed in order to test their realism and predictive power, this remains a challenging issue at the organ scale. First, we proposed a framework for the personalisation of a 3D cardiac EP model, the Mitchell-Schaeffer (MS) model, and evaluated its volumetric predictive power under various pacing scenarios. This was performed on *ex vivo* large porcine healthy hearts using Diffusion Tensor MRI (DT-MRI) and dense optical mapping data of the epicardium. The 3D model parameters were optimised using features such as 2D epicardial depolarisation and repolarisation maps. The sensitivity of our personalisation framework was evaluated to different pacing locations and results on its robustness were shown. Then volumetric model predictions for various epi- and endocardial pacing scenarios were also evaluated. This work demonstrated promising results with a low personalisation and prediction error. Next, in order to apply this personalisation technique to the patient data efficiently with computations compatible with clinical constraints, we proposed a coupled personalisation framework which combines the power of the two kinds of models (simple Eikonal (EK) model & simplified biophysical MS model) while keeping the computational complexity tractable. The EK model was used to estimate the conductivity parameters, which were then used to set the parameters of the MS model. Additional parameters related to the restitution for the tissue were further estimated for the MS model. This framework was applied to a clinical dataset derived from a hybrid XMR imaging and sparse non-contact mapping procedure on a patient with heart failure. This framework was then also applied to more sparse *in vivo* contact mapping datasets for chronic infarcted hearts. The personalised model was also tested to determine the effects of using only endocardial or epicardial mapping measurements. Such quick personalisation of EP models to sparse clinical data opened up possibilities of using models in clinical settings to understand various diseases.

In order to simulate post-infarct VT with macroscopic 3D models, the structural and functional heterogeneity of the tissue near the scars i.e. peri-infarct zones (PIZ) was included. The structural heterogeneity was estimated through high resolution late gadolinium enhanced MRI, while functional heterogeneity was achieved from the estimated patient-specific tissue heterogeneities using the proposed coupled personalisation framework. The 3D MS model was also adapted to simulate the macroscopic structural behaviour of fibrosis near the scars in PIZ. Next, the simulation of an *in silico* VT stimulation study using the personalised adapted MS model was then performed, to quantify VT risk, in terms of inducibility maps, re-entry patterns and exit point maps. A rule-based modelling approach for RF ablation lesions based on state of the art studies was proposed. This approach was carried out due to the lack of patient's imaging data on RF ablation lesions. Furthermore, the acute and chronic effects of the RFA lesions were simulated. The chronic RFA lesions were then used to assist in estimating the post ablation success of RF ablation *in silico*.

Lastly, the *in silico* VT stimulation study was applied to *in vivo* personalised data of patients, who underwent the clinical VT stimulation study. A validation of the *in silico* post-infarct VT prediction was performed against the clinical induced VT. The role of spatial heterogeneity of the patient's cardiac tissue properties estimated from the personalisation framework, in the genesis of ischemic VT was learnt, along with their characteristics for entry/exit points, the potential candidates of RF ablation.

Keywords: Cardiac electrophysiology modelling, Arrhythmia modelling, Inverse problems, Non-linear optimisation, Model personalisation, Radio Frequency Ablation planning, Electroanatomic mapping, Optical mapping, Post-infarct ventricular tachycardia

Modèles électrophysiologiques personnalisés de tachycardie ventriculaire pour la planification de la thérapie par ablation radio-fréquence

Résumé : Les modèles informatiques de l'électrophysiologie (EP) cardiaque peuvent être un outil très efficace pour mieux comprendre les mécanismes des pathologies comme l'arythmie. La modélisation de l'électrophysiologie *in silico* a été un sujet de recherche important ces dernières décennies. Afin de pouvoir utiliser ces progrès importants dans les applications cliniques, il faut mettre en place des modèles macroscopiques qui peuvent être utilisés pour la planification et l'évaluation des procédures cliniques. L'objectif de cette thèse est de construire de tels modèles macroscopiques spécifiques à chaque patient pour le diagnostic et la prévision, dans le but d'améliorer la planification et le guidage de l'ablation par radio-fréquence (ARF) des patients souffrant de tachycardie ventriculaire (TV) après infarctus. Dans ce travail, nous avons abordé cet objectif en plusieurs étapes :

La construction d'un modèle macroscopique 3D spécifique à un patient requiert la personnalisation de ses paramètres aux données du patient, c'est-à-dire trouver les paramètres qui permettant de mieux reproduire les données acquises. Avant d'utiliser sur des données cliniques, cet ajustement a été validé sur des données expérimentales afin de tester le réalisme et le pouvoir prédictif, ce qui reste une question difficile à l'échelle de l'organe. Tout d'abord, nous avons proposé un cadre pour la personnalisation d'un modèle cardiaque 3D, le modèle de Mitchell-Schaeffer (MS), et nous avons évalué sa puissance prédictive dans plusieurs configurations de stimulation. Cela a été réalisé sur des données *ex vivo* de cœurs porcins sains à l'aide d'images médicales et des données cartographiques optiques de l'épicarde. Les paramètres du modèle 3D ont été optimisés en utilisant des fonctions telles que la dépolarisation épicaudique 2D et des cartes de repolarisation. La sensibilité de notre cadre de personnalisation a été évaluée avec différentes stimulations et les résultats sur sa robustesse ont été présentés. Puis, les prédictions du modèle volumétrique sur divers scénarios de stimulation épi-et endocardiques ont également été évalués. Ensuite, afin d'appliquer cette technique de personnalisation aux données du patient de manière efficace avec des calculs compatibles avec les contraintes cliniques, nous avons proposé un cadre de personnalisation couplée qui combine deux types de modèles (eikonal (EK) et MS) tout en gardant une complexité de calcul raisonnable. Le modèle EK a été utilisé pour estimer les paramètres de conductivité, qui ont ensuite été utilisés pour définir les paramètres du modèle MS. D'autres paramètres liés à la restitution du tissu ont également été estimés pour le modèle MS. Ce cadre a été appliqué à un ensemble de données cliniques provenant d'imagerie hybride XMR et d'une procédure de cartographie sans contact sur un patient souffrant d'insuffisance cardiaque. Ce cadre a ensuite été appliqué à des données de cartographie de contact pour des affections chroniques des cœurs infarcis. Le modèle personnalisé a également été testé afin de déterminer les effets de l'utilisation de mesures de cartographie endocardique ou épicaudique.

Pour simuler une TV post-infarctus avec des modèles 3D macroscopiques, l'hétérogénéité structurelle et fonctionnelle du tissu près des cicatrices (péri-infarctus zones (PIZ)) a été incluse. L'hétérogénéité structurelle a été estimée par imagerie IRM de rehaussement tardif, tandis que l'hétérogénéité fonctionnelle a été réalisée en utilisant le cadre de personnalisation couplé proposé. Le modèle 3D MS a également été adapté pour simuler le comportement macroscopique structural de la fibrose près des cicatrices dans les PIZ. Ensuite, la simulation d'une étude *in silico* de stimulation de TV en utilisant le modèle adapté personnalisé MS a été réalisée, pour quantifier le risque de TV en termes de cartes d'inductibilité, ré-entrées des modèles et des cartes de points de sortie. Une approche de modélisation pour l'ablation par RF fondée sur l'état de l'art a été proposée. Cette approche a été effectuée en raison de l'absence de données d'imagerie du patient sur les lésions d'ablation par RF. En outre, les effets aigus et chroniques des lésions RFA ont été simulés. Les lésions chroniques de ARF ont ensuite été utilisées pour aider à estimer le succès de l'ablation par RF *in silico*. Enfin, l'étude *in silico* de stimulation de TV a été appliquée aux données *in vivo* personnalisées des patients, qui ont suivi ce protocole. Une validation de la prévision *in silico* de TV post-infarctus a été réalisée et comparée à la TV clinique induite. Le rôle de l'hétérogénéité spatiale des propriétés des tissus cardiaques estimés à partir du cadre de la personnalisation dans la genèse de TV ischémique a été évalué, ainsi que les caractéristiques des points de sortie, qui sont les candidats potentiels à l'ablation par RF.

Mots clés : Modélisation d'électrophysiologie cardiaque et arythmies, problèmes inverses, optimisation non-linéaire, personnalisation des modèles, planification de l'ablation par radiofréquence, cartographie électro-anatomique, cartographie optique, tachycardie ventriculaire post-infarctus

The best material model for a cat is another [cat], or preferably the same cat.

Arturo ROSENBLUETH - Philosophy of Science, 1945

What distinguishes a mathematical model from, say, a poem, a song, a portrait or any other kind of "model," is that the mathematical model is an image or picture of reality painted with logical symbols instead of with words, sounds or watercolors.

John CASTI - Reality Rules, 1997

Acknowledgements

This thesis arose, out of years of research that has been done in the Asclepios research team, along with close collaborations with St. Thomas' Hospital, King's College London, UK, & Sunnybrook Health Science Centre, Toronto, Canada & Centre Hospitalier Universitaire, Bordeaux, France, within the framework of an European project euHeart, coordinated by Philips Technologies GmbH, Aachen, Germany. During this thesis, I have worked with a great number of people, whose contribution in assorted ways to the research deserves a special mention. It is a pleasure to convey my gratitude to them all in my humble acknowledgement.

First of all, I would like to thank my supervisor, Prof. Nicholas Ayache for giving me an opportunity to work, learn and grow with his prestigious and internationally renowned team. I express my gratitude towards his supervision, advice, and guidance from the very early stage of this research as well as his support by encouraging my work. I am grateful to my co-supervisor Dr. Hervé Delingette, for his supervision, guidance and ideas for advancement throughout my research. I gratefully acknowledge my co-supervisor Dr. Maxime Sermesant for his advice, supervision, and crucial contribution, which made him a backbone of this research and so to this thesis. I am highly indebted to him to help my research work grow internationally with collaborative experiences with various renowned research and clinical partners. Max, I am grateful to you in every possible way and making me feel more like a friend throughout my journey at Asclepios.

I am extremely grateful to the reviewers, Prof. Olaf Dössel and Dr. Yves Coudière for having spent their precious time to read my manuscript, and for being a part of my jury. I warmly thank them for their sharp and constructive comments about my work and for their encouraging compliments. I would like to thank Prof. Alexander Panfilov to encourage my work by being a member of my jury. I am also thankful to Prof. Dr. Pierre Jaïs and Prof. Dr. Reza Razavi, to highly appreciate my work and to be my jury members, and come at my defense despite their clinical commitments. Dear committee, thank you, it has been a great honour for me to have you in my jury.

I owe a great amount of gratitude to all the people I had a chance to closely work with: Dr. Zhong Chen, for his hard work in recruiting patients for this research work and I am indebted to him for helping me out with the difficult clinical data acquisition; Dr. Mihaela Pop, for providing me the most precious experimental *ex vivo* data, to start of my research work; Dr. Phani Chinchapatnam, for giving me insights on electrophysiology data processing and introducing me to the power of models in clinics; Dr. Hubert Cochet, for acknowledging and encouraging my efforts in tailoring Cardioviz3D software to meet clinical needs in cardiac electrophysiology domain; Prof. Dr. Michel Haïssaguerre, Prof. Dr. Pierre Jaïs, Prof. Dr. Reza Razavi, Dr. Aldo Rinaldi, Dr. Matt Ginks, and Dr. Kawal Rhode, for supporting and encouraging my work and helping me gather clinical data; I would also like to

thank my colleagues: Dr. Amir Jadidi, Dr. Katja Odening, Dr. Mèlèze Hocini, Dr. Nick Linton, Dr. Ryan Boucher, Dr. Julian Bostock, Dr. Nicolas Toussaint, Dr. Bjoern Menze, Dr. Rashed Karim, Dr. Radomir Chabiniok and Dr. Oscar Camara Rey

I should not forget to thank all the members of the euHeart project. In particular, Dr. Jürgen Weese from Philips Research, Aachen, Germany. I would also like to thank Martin Krüger and Walther Schulze from Institute of Biomedical Engineering, Karlsruhe, Germany, for working together on clinical data and helping me expand my knowledge about the atria and body surface potentials.

I am also very thankful to all the people who went along with me during these years. In particular, I would like to thank Dr. Stanley Durrleman, Dr. Barbara André, Dr. Florence Billet, Dr. Liliane Ramus, Dr. Ken Wong, Dr. Ender Konukoglu, Dr. Tommaso Mansi, Dr. Jean-Marc Peyrat, Dr. Romain Fernandez, Dr. Francois Chung, Dr. Pierre Fillard, Erin Stretton, Islem Rekik, Viateur Tuyisenge, Mathilde Merle, Rocio Cabrera Lozoya, Kristin Mcleod, Marine Breuilly, Adityo Prakosa, Hervé Lombaert, Hugo Talbot, Ezequiel Geremia, Stephanié Marchesseau, Jan Margeta, Marco Lorenzi, Federico Spadoni, Christof Seiler, Vikash Gupta, Loic Le Folgoc, Nicolas Cordier, Thomas Benseghir, Arnaud Le Carvenec, Chloe Audigier, Alan Garny, Sonia Durand, Bishesh Khanal, Erik Pernod, Benoît Bleuzé, Vincent Garcia, Florian Vichot, John Stark, Brina Goyette, Michael Knopke, Florence Dru, Aurélie Canale, Daniel Barbeau, Dr. Olivier Clatz, Dr. Grégoire Malandain, Dr. Xavier Pennec and all the Asclepios team for the warm welcome and the good time we spent together. I am also extremely grateful to Isabelle Strobant, for being always there when needed.

Last but not least, I would have never got this far without the support and love of my close friends, my mother and my family. Finally I would like to thank God for helping me and being with me all my way through this thesis work and my life. Let this be a gratification to you.

Table of Contents

I	INTRODUCTION	1
1	Introduction	3
1	Clinical Context	3
2	Manuscript Organisation	5
2	Cardiac Electrophysiology	8
1	Anatomy	8
2	Cardiac Electrical System & Arrhythmias	9
3	Mapping Cardiac Electrophysiology	12
4	Modelling Cardiac Electrophysiology	17
5	Modelling Cardiac Arrhythmias	25
6	Conclusion	27
II	PERSONALISATION OF CARDIAC ELECTROPHYSIOLOGY MODELS	29
3	Building Personalised EP Models using <i>ex vivo</i> Experimental Data (Optical Mapping)	31
1	Introduction	32
2	Data Acquisition and Processing	34
3	Model Simulation: Direct Problem	37
4	Model Personalisation: Inverse Problem	38
4.1	Case 1: Personalisation Using a Single PF	39
4.2	Personalisation of DT Isochrones	39
4.3	Personalisation of Action Potential Duration	42
4.4	Case 2: Personalisation Using Multiple PF	42
4.5	Personalisation of Restitution curves	42
4.6	Personalisation of DT Isochrones	43
5	Results	43
5.1	DT & APD error maps	44
5.2	Fitting of restitution curves	44
5.3	Robustness to Pacing Location	46
5.4	Evaluation of Volumetric Predictions	46
6	Discussion	47
7	Conclusion	50

4	Building Personalised EP Models using <i>in vivo</i> Clinical Data (Non-Contact Mapping)	51
1	Introduction	52
2	Clinical Context	54
	2.1 Depolarisation and Repolarisation times extraction	55
3	Cardiac Electrophysiology Models	56
	3.1 Eikonal Model (EK Model)	56
	3.2 Simplified Biophysical Model (MS Model)	57
4	Coupled Personalisation Method	58
	4.1 Apparent Conductivity Parameter Estimation	58
	4.2 Coupling of EK and MS Model Parameters	59
	4.3 Parameter Estimation for APD Restitution	60
5	Results	62
	5.1 Parameter Estimation	62
	5.2 Assessment of Heterogeneity Maps	64
6	Discussion	64
	6.1 Data Limitations	64
	6.2 Model Simplifications	65
	6.3 Conclusion	66
5	Building Personalised EP Models using <i>in-vivo</i> Experimental Data (Contact Mapping)	67
1	Introduction	68
2	3D Electrophysiology Model with Chronic Infarction	68
3	Contact Mapping and MR Dataset Processing	69
4	Building personalised electrophysiological model	71
	4.1 Coupled personalisation approach (EK-MS)	71
	4.2 Application	71
5	Conclusion	73
III MODELLING VENTRICULAR TACHYCARDIA & RF ABLATION		75
6	Personalised Ventricular Tachycardia Modelling	77
1	Introduction	78
2	Modelling Post-infarction Ventricular Tachycardia	80
	2.1 Structural Heterogeneity	80
	2.2 Functional Heterogeneity	87
3	Modelling of Clinical VT-Stimulation Protocol	90
	3.1 VT Induction	90
	3.2 VT-Stim Modelling	91
4	VT Risk Stratification	92
5	Conclusion	94

7	Modelling Radio-Frequency Ablation	95
1	Radio-frequency Ablation: Concepts & Modelling	96
1.1	Types of Ablation	97
1.2	RF Ablation of VT	98
1.3	Lesion Formation	99
1.4	Lesion Size	104
1.5	Lesion Characteristics & Modelling	105
2	Radiofrequency Ablation on VT patients	106
2.1	Simulation of Radiofrequency Ablation	106
2.2	Short Term Effect of RF Ablation	106
2.3	Long Term Effect of RF Ablation	108
3	Conclusion	109
IV	CLINICAL APPLICATION & VALIDATION	111
8	Planning of Radio Frequency Ablation using <i>in-vivo</i> Clinical Data	113
1	Introduction	114
2	Methods	115
2.1	Clinical Study: Patient Recruitment and Pacing Protocol	115
2.2	Data Analysis	116
2.3	VT Modelling Study: Personalisation and Pacing Protocol	117
3	Results	122
3.1	Estimation of the patient-specific spatial heterogeneities	122
3.2	Correlation of the spatial heterogeneities: Inter-patients	124
3.3	Induced VT: Clinical observations vs. Model predictions	126
3.4	VT & Exit point predictions	127
4	Discussion	128
4.1	Tissue conductivity & APD restitution slope heterogeneity	128
4.2	Data Limitations & Model personalisation	130
4.3	VT Model Predictions & Simplifications	131
5	Conclusion	131
V	CONCLUSION	133
9	Conclusions & Perspectives	135
1	Contributions	135
2	Perspectives	138
2.1	Methodological perspectives	138
2.2	Short-term & Mid-term clinical perspectives	140
2.3	Long-term clinical perspectives	141

10 List of Publications	143
1 First-authored Methodological Papers (Peer-Reviewed)	143
2 Clinical Abstracts	144
3 Co-authored Publications	145
4 European project deliverables	146
VI APPENDIX	149
Appendix A Quantitative Comparison of Two Cardiac Electrophysiology Models	151
Appendix B Time Integration schemes & Spatial and Temporal resolution	153
1 Time integration	153
1.1 First Order Schemes	153
1.2 Second Order Schemes	154
1.3 Third Order Schemes	155
2 Choosing optimum spatial & temporal resolutions	155
Appendix C Model specifications and performance	157
Appendix D Figure Glossary	160
1 EP model personalisation to <i>ex-vivo</i> optical data	161
2 EP model prediction to various pacing locations	162
3 VT induction after personalisation	163
4 <i>in-silico</i> RFA planning after personalisation	165
5 Induced VT circuit from clinical data	166
6 Integration of BSPM - Ensite Mapping	167
7 Clinical VT-Stim protocol	169
Bibliography	170

Abbreviations & Nomenclature

Table 1: Abbreviations and acronyms used in this thesis.

Acronym	Description
3D-SSFP	3 Dimensional Steady-State Free Precession MR imaging
AHA	American Heart Association
AC	Apparent Conductivity
AP	Action Potential
APath	Accessory Pathway
APD(RC)	Action Potential Duration (Restitution Curve)
APD Rest	Action Potential Duration Restitution
ARI	Activation Recovery Interval
AV	Atrioventricular Node
AVNRT	AtrioVentricular Nodal Reentry Tachycardia
BSP(M)	Body Surface Potential (Mapping)
Cath Lab	Catheterisation Laboratory
CHU	Centre Hospitalier Universitaire, Bordeaux, France
CL	Cycle Length
CT	Computed Tomography
CV	Conduction Velocity
CV Rest	Conduction Velocity Restitution
CVD	CardioVascular Disease
DCM	Dilated CardioMyopathy
DI	Diastolic Interval
DT	Depolarisation Time
ECG	ElectroCardioGraphy
ECGI	ElectroCardioGraphy Imaging derived from BSPM
ED	Eikonal-Diffusion
EK	Eikonal Model
EM	Electro-Mechanical (model)
EP	ElectroPhysiology
EPS	ElectroPhysiology Study
FEM	Finite Element Method
FK	Fenton-Karma (cell model)
FMM	Fast Marching Method
FWHM	Full Width at Half Maximum
IBT	Institute of Biomedical Engineering, Karlsruhe, Germany
ICD	Implantable Cardioverter-Defibrillator
ICM	Ischemic CardioMyopathy
ICT	Information and Communication Technology
IHD	Ischemic Heart Disease

INRIA	Institut National de Recherche en Informatique et en Automatique / Centre de recherche Sophia Antipolis - Méditerranée
KCL	King's College London, UK
LA	Left Atrium
LAT	Local Activation Times
LE MRI	Late Enhancement Magnetic Resonance Imaging
LGE-CMR	Late Gadolinium Enhanced Cardiac Magnetic Resonance imaging
LIVT	Left Idiopathic Ventricular Tachycardia
LV	Left Ventricle
LVEF	Left Ventricular Ejection Fraction
MAP	Monophasic Action Potential
MCNAB	Modified Crank-Nicolson/Adams-Bashforth
MIPS	Medical Image Processing and Simulation (INRIA library)
MI	Myocardial Infarction
MM	Minimal Model (cell model)
MR(I)	Magnetic Resonance (Imaging)
MS	Mitchell-Schaeffer (cell model)
NCM	Non-Contact Mapping
PDE	Partial Differential Equation
PF	Pacing Frequency
RA	Right Atrium
RC	Restitution Curves
RF(A)	Radio-Frequency (Ablation)
RT	Repolarisation Time
RV(A)	Right Ventricle (Apex)
RVOT	Right Ventricular Outflow Tract
SA	Sinoatrial Node
SCD	Sudden Cardiac Death
TNNP	Ten Tusscher-Noble-Noble-Panfilov (cell model)
VF	Ventricular Fibrillation
VT	Ventricular Tachycardia
VT-Stim	Ventricular Tachycardia Stimulation
XMR	Hybrid X-Ray/MR system

Table 2: Nomenclature used.

Nomenclature	Description
Na^+	Sodium ions
Ca^{2+}	Calcium ions
K^+	Potassium ions
Cl^-	Chlorine ions
C_m	membrane capacitance
I_{ion}	total ionic current
I_m	membrane current
J_{stim}	stimulus current
I_x	membrane current for ion x
J_{in}	total inward ionic currents
J_{out}	total outward ionic currents
σ	stress tensor
T_d	depolarisation time
T_r	repolarisation time
V_m	membrane voltage
D	Diffusion tensor
d	pseudo-conductivity in the fiber direction (apparent conductivity)
d_{MS}	pseudo-conductivity in the fiber direction for MS model (s^{-1})
d_{EK}	pseudo-conductivity in the fiber direction for EK model (m^2)
r	conductivity anisotropy ratio in transverse planes (no unit)
τ_{open}	opening time-constant of the gate (s)
τ_{close}	closing time-constant of the gate (s)
τ_{in}	time-constant for inward currents (s)
τ_{out}	time-constant for outward currents (s)

Part I

INTRODUCTION

Introduction

Contents

1	Clinical Context	3
2	Manuscript Organisation	5

1 Clinical Context

The pathophysiology of the heart represents a highly relevant and epidemiologically significant contributor to mortality and loss of quality of life within Europe, where each year cardiovascular diseases (CVD) cause over 4.35 million deaths including nearly half of all non-accidental deaths [PPR⁺05]. This, currently western, epidemic is now also spreading to developing nations with CVD predicted to become the most common cause of death in these countries by 2030 [Org09, Org04, Org03]. CVD is most commonly a consequence of atherosclerosis, manifesting itself in diseases such as coronary artery disease, congestive heart failure, cardiac arrhythmias and sudden cardiac death (SCD). The loss of quality and quantity of life producing a significant financial burden is spread across community sectors with approximately 62% of costs due to direct health care costs, 21% due to productivity losses and 17% due to the informal care of people with CVD. Thus the early detection and prediction of the progression of CVD are key requirements towards improved treatment, a reduction in mortality and morbidity, and of course to reduce healthcare costs within the European economy.

In the majority of cases, SCD is triggered by the onset of ventricular tachycardia (VT), an abnormally rapid heart rate originating in the ventricle [HCM01]. If undetected and untreated, VT can rapidly degenerate in ventricular fibrillation (VF) which is a chaotic propagation of the electrical impulse in the heart, causing an abnormal contraction and inefficient blood pumping. This cascade of events leads within minutes to cardiac arrest and asystole (no pulse) and eventually to death unless the heart's electrical activity is immediately restored using defibrillation shocks [RZ⁺05]. Termination of sustained VT can be achieved by cardioversion in order to reset the overall electrical activity of the heart. Cardioversion by shock therapy can be achieved by external electrical defibrillation or internally via an implantable cardioverter-defibrillator (ICD) that continuously monitors for and can detect episodes of VT. In the case of monomorphic VT, termination can also be

achieved by anti-tachycardia pacing, which is accomplished by the ICD rapidly pacing the heart. The use of ICDs for secondary prevention has been increasing because ICD therapy has been proven to reduce mortality by up to 39% in patients who survived near fatal VF or who have sustained VT [LGL⁺03]. The percentage of VT patients with appropriate ICD firing was 68% at one year and 81% at two years after implantation. However, ICD therapy is a non-curative approach to patients with VT. It does not prevent the VT from re-occurring, and up to 80% of ICD recipients still require pharmacological anti-arrhythmic therapy [FGDSG07]. Patients with frequent ICD firing due to monomorphic VT also experience significantly decreased quality of life associated with VT symptoms and distress anticipating ICD activation, and hence require additional therapy.

Radio-frequency (RF) ablation offers a potential curative therapy for monomorphic VT, which aims to interrupt the re-entry circuit by placing RF thermal lesions on the isthmus. However, the major challenge is identification of the location of the VT substrate (i.e., the isthmus in the re-entry circuit). Currently, this can be achieved with electrophysiological (EP) substrate mapping, a technique that constructs voltage, propagation and impedance maps of the endocardium and/or epicardium, most commonly via intra-cardiac catheter-based procedures. However, there is a clear need to improve the methods to characterise the substrate of VT, and to explore other modalities that can supplement diagnostic information and can help in selecting better treatment strategies. Those patients with monomorphic sustained VT associated with chronic infarct, particularly those being considered for RF ablation (RFA), are an important initial target population. Advances leading to improved treatment planning and outcomes assessment would have immediate impact on the quality of life in this substantial patient population. Thus, research efforts are focused towards construction of accurate patient-specific treatment platforms.

A large part of this thesis was performed within the euHeart¹ project, a four-year European project partially funded by the European Community (7th Framework Program) (Fig. 1.1). The project is coordinated by Philips Technologies GmbH Aachen (DE), and involved 15 technical partners (including INRIA, France) and three clinical partners, namely King's College London (London, UK), University Hospital Pontchaillou (Rennes, France) and Hospital Clínico San Carlos de Madrid Insalud (Madrid, Spain). The aim of the euHeart project is to incorporate Information and Communication Technology (ICT) tools and integrative multi-scale computational models of the heart within clinical environments to improve diagnosis, treatment planning and interventions for CVD and thus to reduce the allied healthcare costs. These computational models also provide an excellent basis to optimise the design of implantable devices for improved therapy. The opportunity of multi-scale modelling spanning multiple anatomical levels (sub-cellular level up to whole heart) is to provide a consistent, biophysically-based framework for the integration of the huge amount of fragmented and inhomogeneous data currently

¹<http://www.euheart.eu>

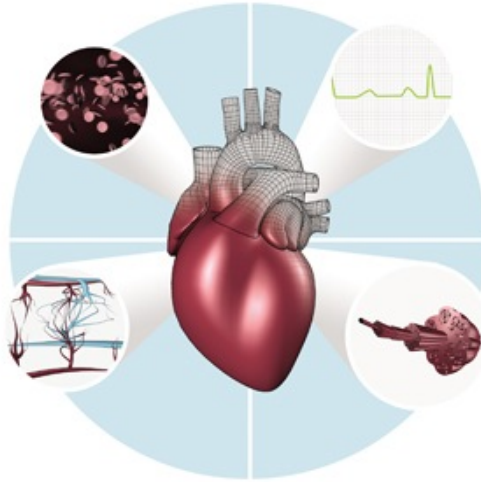


Figure 1.1: Diagram of the euHeart, a European research initiative targeting the personalised diagnosis and treatment of cardiovascular disease: the leading cause of morbidity in the western world. Image taken from <http://www.euheart.eu/>

available. However, the application of this research was not been translated into clinical environments mainly due to the difficulty of efficiently personalising the biophysical models and to the lack of multidisciplinary research.

The objective of this work was to use personalised biophysical models of the cardiac electrophysiology in order to improve the planning and guidance of radio-frequency ablation therapies on patients suffering from Ventricular Tachycardia (VT). Indeed, there is no clinical consensus about the optimum RF ablation patterns for these diseases yielding to a great deal of trial and error during the procedure which highly depends on the cardiologist's experience. This work on using personalised models to guide RF ablation therapies can provide a consensus on optimum RF ablation patterns for these diseases.

In order to plan and guide RF ablation therapy for VT the questions mainly tackled in this thesis were:

- *How do we personalise biophysical models to the sparse in vivo clinical data?*
- *How do we simulate ischemic ventricular tachycardia and RF ablation patterns, as observed as in clinics and provide guidance and planning?*
- *Are we really simulating patient-specific ischemic VT?*

2 Manuscript Organisation

The thesis is organised along our published and submitted studies, on which it is largely based. The resulting manuscript progresses from the development of personalisation tools for cardiac EP models, to the modelling & prediction of cardiac

arrhythmias for planning of RF ablation therapy. The definition of personalisation used in this thesis is: parameter estimation of 3D cardiac EP models derived from patient’s imaging and electrophysiological mapping data.

This thesis is organised in three parts demonstrating the three main contributions: 1) Development of personalisation frameworks for 3D cardiac EP models, using various cardiac EP mapping data. 2) Modelling ventricular tachycardia and RF ablation lesions, for planning of RF ablation therapy. 3) Prediction & validation of ventricular tachycardia using clinical data.

Chapter 2 gives a background on cardiac anatomy, myocardial infarction, electrophysiology and ventricular arrhythmias. It also describes the state of the art technologies used in clinics, for mapping cardiac electrophysiology. Along with the basics and state of the art research being carried out in modelling cardiac electrophysiology *in silico*.

In **Chapter 3**, based on [RPD⁺11], we propose a framework for the personalisation of a 3D simplified biophysical cardiac EP model, the Mitchell-Schaeffer (MS) model to 2D epicardial *ex vivo* optical and MR data. We also evaluate its volumetric predictive power under various pacing scenarios. The sensitivity of the personalisation framework to different pacing locations is also performed.

In **Chapter 4**, based on [RCS⁺11], we propose a coupled personalisation framework, which combines the benefits of a simplified eikonal model (EK) with a simplified biophysical MS model. We also demonstrate its applicability to *in vivo* clinical data using non-contact EP mapping data.

In **Chapter 5**, based on [RSDA11], we extend the framework’s applicability to *in vivo* contact EP mapping data. And we also evaluate the influence of using only endocardial mapping or epicardial mapping measurements, on the personalisation framework.

In **Chapter 6**, based on [RCS⁺11, RDS⁺11], we illustrate the main macroscopic characteristics of post-infarction Ventricular Tachycardia (VT) (chronic ischemic VT), and adapt the simplified biophysical MS model to incorporate those features. The personalised MS model derived from the *in vivo* clinical data is then used to perform an *in silico* simulation of a VT stimulation study to predict the induction of VT. This simulation study is used to assess the risk of VT for the patient and also to plan a potential subsequent radio-frequency (RF) ablation strategy to treat VT.

Implantation of ICD post ablation, causes the unavailability of imaging data on RF ablation lesions for VT patients. In **Chapter 7**, based on [RDS⁺11], we propose a rule based modelling approach of RF ablation lesions post ablation therapy, based on the state of the art studies. The RF ablation lesions are also modelled to simulate the acute and chronic effects of RFA therapy. The acute RF ablation lesions are then be modelled in the simulated VT stimulation study to assist in robust location of potential RF ablation lines *in silico*, while chronic RF ablation lesions could then be modelled in accessing the long-term success rate of RFA therapy.

In **Chapter 8**, based on [RCD⁺12] we apply the *in silico* VT stimulation study to *in vivo* personalised data of patients, who underwent the clinical VT stimulation

study. A validation of the *in silico* VT prediction is performed against the clinical induced VT. We also study the role of spatial heterogeneity of the cardiac tissue properties estimated from the personalisation framework, in the genesis of ischemic VT, and learn their characteristics for entry/exit points.

Lastly, **Chapter 9** concludes this thesis with the list of contributions and directs us towards the feasible perspectives to this work. **Chapter 10** provides the list of publications written during this work, along with some co-authored publications and European project deliverables.

Cardiac Electrophysiology

Contents

1	Anatomy	8
2	Cardiac Electrical System & Arrhythmias	9
3	Mapping Cardiac Electrophysiology	12
4	Modelling Cardiac Electrophysiology	17
5	Modelling Cardiac Arrhythmias	25
6	Conclusion	27

1 Anatomy

The heart is a powerful muscular organ whose shape and function optimise the pump function while minimising the muscular work. It is located anterior to the vertebral column and posterior to the sternum. It is enclosed in a double-walled sac called the *pericardium*. The superficial part of this sac is called the fibrous pericardium. This sac protects the heart, anchors its surrounding structures, and prevents overfilling of the heart with blood. The outer wall of the heart is composed of three layers. The outer layer is called the *epicardium*. The middle layer is called the *myocardium* and is composed of cardiac muscle which contracts. The inner layer is called the *endocardium* and is in contact with the blood that the heart pumps.

The human heart has four chambers, two superior atria and two inferior ventricles (Fig. 2.1). The atria are the receiving chambers and the ventricles are the discharging chambers. The pathway of blood through the heart consists of a pulmonary circuit and a systemic circuit. De-oxygenated blood flows through the heart in one direction, entering through the superior vena cava into the right atrium (RA) and is pumped through the tricuspid valve into the right ventricle (RV) before being pumped out through the pulmonary valve to the pulmonary arteries into the lungs. It returns from the lungs through the pulmonary veins to the left atrium (LA) where it is pumped through the mitral valve into the left ventricle (LV) before leaving through the aortic valve to the aorta.

Myocardial Infarction Myocardial infarction (MI) results from the interruption of blood supply to a part of the heart, causing heart cells to die. This is most commonly due to occlusion of a coronary artery following the rupture of a

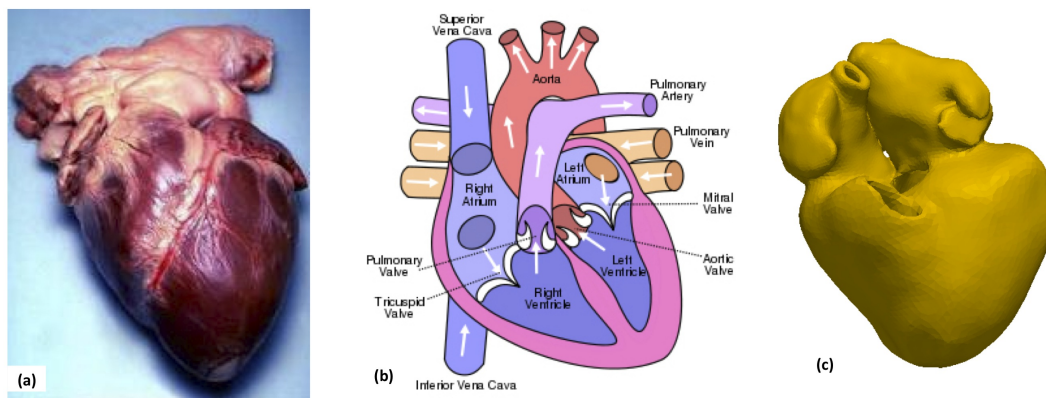


Figure 2.1: (a) Human heart, (b) Heart function (*Images from Wikipedia*) (c) Segmented whole heart model from SSFP MR images

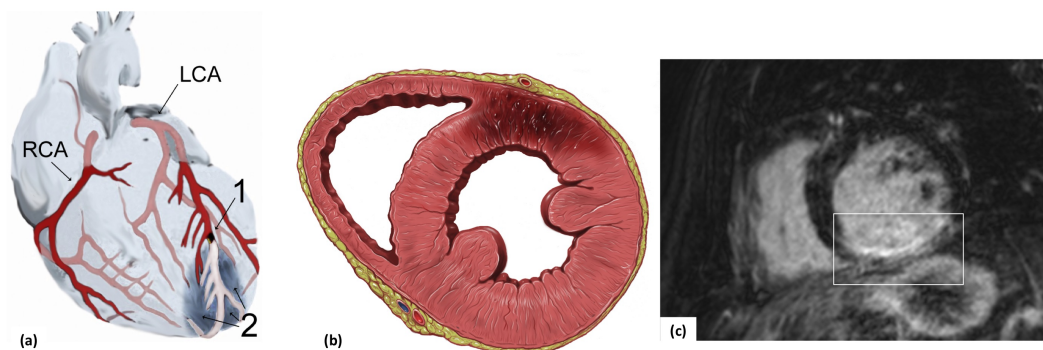


Figure 2.2: (a & b) Myocardial infarction of the tip of the anterior wall of the heart, (*Images from Wikipedia*) (c) LE-CMR images showing infarction on the posterior wall (highlighted in box)

vulnerable atherosclerotic plaque (Fig. 2.2). The resulting ischemia (restriction in blood supply) and ensuing oxygen shortage, if left untreated for a sufficient period of time, can cause irreversible damage or death (infarction) of heart muscle tissue (myocardium). Ischemic heart disease (IHD), or chronic myocardial ischemia, is a disease characterised by ischemia of the heart muscle, usually due to coronary artery disease (atherosclerosis of the coronary arteries). Infarcted tissue can cause a cardiac arrest, which is the stopping of the heartbeat, and cardiac arrhythmia, an abnormal heartbeat.

2 Cardiac Electrical System & Arrhythmias

The normal intrinsic electrical conduction of the heart allows electrical propagation to be transmitted from the Sinoatrial (SA) Node through both atria and forward

to the Atrioventricular (AV) Node, then to the ventricle or Purkinje network and respective bundle branches (Fig. 2.3). Time ordered stimulation of the myocardium allows efficient contraction of all four chambers of the heart, thereby allowing systemic blood circulation.

Cardiac action potentials arising in the SA node (and propagating to the left atrium via Bachmann's bundle) cause the atria to contract with a speed (Conduction Velocity (CV)) of ≈ 0.5 m/s. In parallel, action potentials travel to the AV node via internodal pathways. After a delay (≈ 0.07 s), the stimulus is conducted through the bundle of His (≈ 2 m/s) to the bundle branches (≈ 2 m/s) and then to the Purkinje network (≈ 4 m/s) at the endocardium (mostly apical) of the heart, then finally to the ventricular myocardium (≈ 0.5 m/s) [MKY+02].

The pathway can be summarised as: SA node \rightarrow internodal pathway \rightarrow transitional fibres \rightarrow AV node \rightarrow penetrating fibres \rightarrow distal fibres \rightarrow Bundle of his/AV bundle \rightarrow right and left bundle branches \rightarrow Purkinje network (Fig. 2.3)(a). The total time taken by the nerve impulse to travel from the SA node to the ventricular myocardium is ≈ 0.19 seconds [MKY+02].

Action potentials (Fig. 2.3(c,d)) are generated by the movement of ions through the transmembrane ion channels in the cardiac cells (Fig. 2.3)(b):

- **Phase 0 - Depolarisation** Rapid Na^+ channels are stimulated to open, flooding the cell with positive sodium ions. This causes a positively directed change in the transmembrane potential. Depolarisation of one cell triggers the Na^+ channels in surrounding cells to open as well, causing the depolarisation wave front to propagate cell by cell throughout the heart. The speed of depolarisation of a given cell (the slope of phase 0), determines how soon the next cell will depolarise, thus the CV.
- **Phase 1 - Early Repolarisation** is the initial stage of repolarisation with outflux of K^+ & Cl^- .
- **Phase 2 - Plateau** is the plateau stage where the rate of repolarisation is slowed by the influx of Ca^{2+} ions into the cell. The Ca ions enter the cell slower than the Na ions and help prevent the cell from repolarising too quickly, thus extending the refractory period. This mechanism helps regulate the rate at which cardiac tissue can depolarise. Phases 1 & 2 correspond to the absolute refractory period.
- **Phase 3 - Repolarisation** is the later stages of repolarisation with outflux of K^+ . Once repolarisation is complete, the cell will be able to respond to a new stimulus. Phase 3 is that critical period where a strong signal may trigger depolarisation which could lead to VT or VF.
- **Phase 4 - Resting** occurs after repolarisation is complete. During this phase, known as the quiet or quiescent phase, there is no ion exchange across the cellular membrane in most cardiac cells. Time difference between Phase 1 & 3 represents the Action Potential Duration (APD) for the cardiac cell.

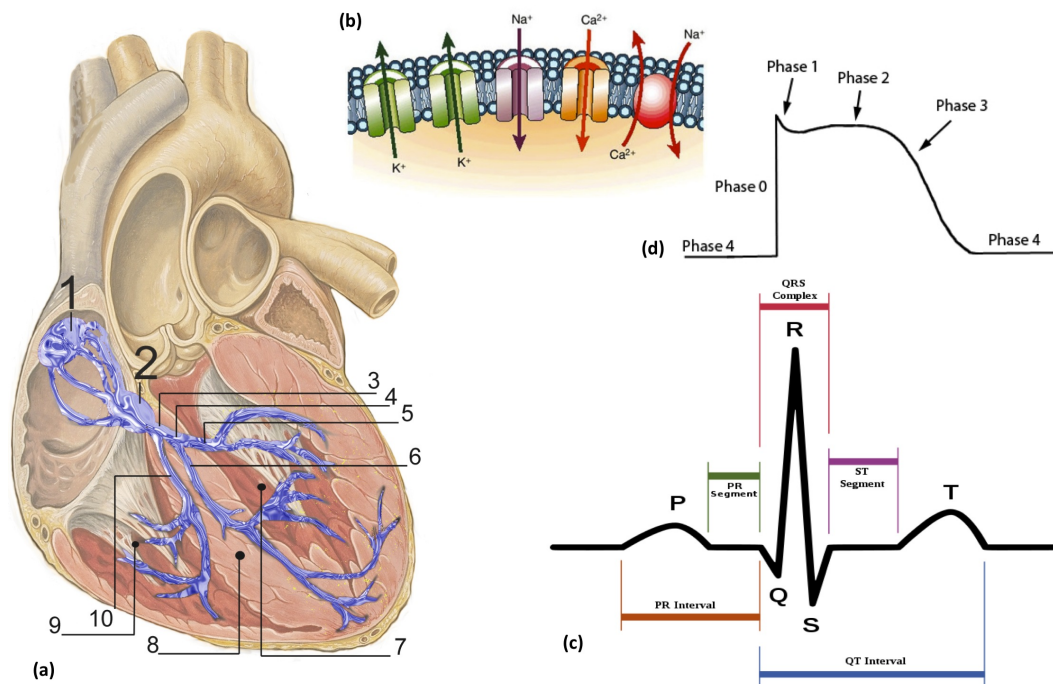


Figure 2.3: (a) Heart conduction system, the electrical activity of the heart is triggered by the sinoatrial nodes (1) and then the atrioventricular nodes (2). It is transported by the left bundle (5) and the right bundle (10) branches and finally transmitted to the myocardium (8) through the Purkinje fibres (9). (c) Simplified ECG with the main electrical waves (*Images from Wikipedia*). (b) Ion exchanges at the surface of the cell membrane that generate the cardiac action potential [Mar02]. (d) Cardiac action potential

The cells in different regions of the heart do not all have the same action potential, and thus have varying conduction velocities. Electrocardiography (ECG) is a transthoracic interpretation of the electrical activity of the heart over a period of time, as detected by electrodes attached to the torso. It is decomposed with PQRST waves. P wave for atrial depolarisation, QRS complex reflects the rapid depolarisation of ventricles, T wave represents the repolarisation of the ventricles. The atrial repolarisation is hidden in the QRS complex. QT interval represents the APD over the ventricles. Cardiac arrhythmia is any of a large and heterogeneous group of conditions in which there is abnormal electrical activity in the heart. The heartbeat may be too fast (tachycardia) or too slow (bradycardia), and may be regular or irregular.

Ventricular Tachycardia Ventricular tachycardia (VT) is a fast heart rhythm, that originates in one of the ventricles of the heart. This is a potentially life-threatening arrhythmia because it may lead to ventricular fibrillation, asystole, and

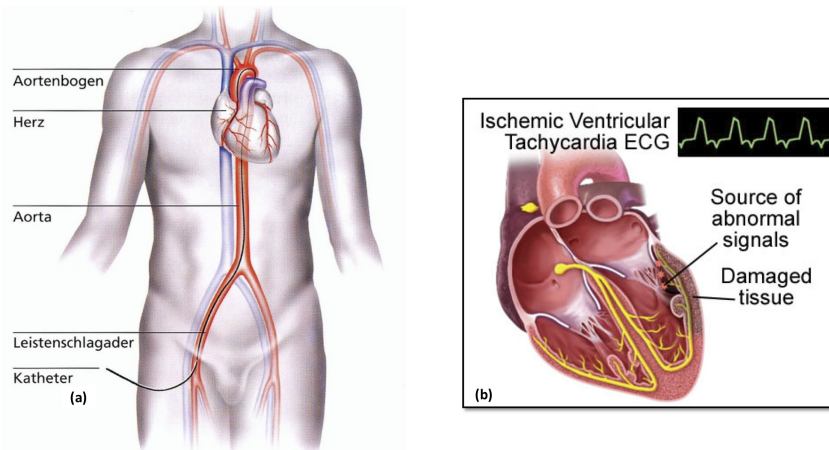


Figure 2.4: (a) Schematics of RF ablation therapy & electrophysiology study (EPS) of cardiac arrhythmias (*Images from Heart Centre Bad Krozingen*) (b) Schematics of ischemic VT on LV free wall (*www.medmovie.com*)

sudden death. VT can be classified based on its morphology: Monomorphic VT (sustained morphology) & Polymorphic VT (beat-to-beat variations in morphology). The most common setting for VT is ischemic heart disease (Fig. 2.4(b)), in which myocardial scar tissue is the substrate for electrical re-entry. Treatments include synchronised electrical cardioversion, ICD implantation, cardiac ablation & anti-arrhythmic drug therapy.

Radio-Frequency ablation of Ventricular Tachycardia Radio-frequency ablation is one of the treatment for VT. Using catheters, radio-frequency energy (low-voltage, high-frequency electricity) is targeted toward the area(s) causing the abnormal heart rhythm, permanently damaging small areas of tissue with heat. The damaged tissue is no longer capable of generating or conducting electrical impulses. If the procedure is successful, this prevents the arrhythmia from being generated, curing the patient. In some patients, insertion of a pacemaker is a planned part of the procedure. The ablation catheters are usually inserted into the vein or artery in the right and left groin (inner thigh) and are then positioned within the chambers of the heart using fluoroscopy (Fig. 2.4(a)). An electrophysiology study, as explained in the section 3, is then performed to identify regions of the heart causing arrhythmia, and then ablated.

3 Mapping Cardiac Electrophysiology

Cardiac electrophysiology can be mapped with a host of systems, depending on the state of the mapped heart (*ex-vivo* & *in-vivo*). For *in vivo* mapping, in a clinical routine, cardiac electrophysiology is usually assessed non-invasively with electrocardiograms (ECG). The ECG is obtained by placing skin electrodes on the torso,

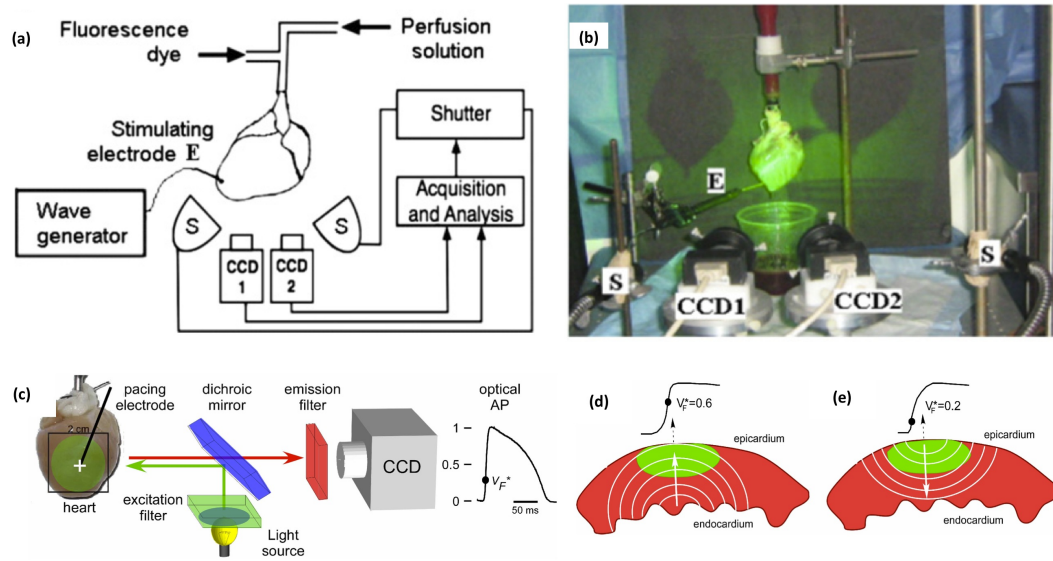


Figure 2.5: Schematic of an optical experiment using a dual-camera system to record the action potential from the heart perfused *ex vivo* via a Langendorff system (a) and a snapshot of the actual experiment (b). (a,b taken from [PSL+09]). (c) Schematics for a cardiac epi-fluorescence experiment in isolated guinea pig hearts used in [HZS+08] for 3D optical imaging. (d) Myocardial wave reconstruction based on subsurface wave front orientation (towards or away from the epicardium) and fluorescent signal (maximal time derivative) employed in [HZS+08]. (c,d taken from [HZS+08])

that measure the electrical signal produced by the heart. This routine has been widely used for centuries in clinics and the clinicians are trained to detect cardiac abnormalities based on the deflections from normal shapes of ECGs (Fig. 2.3(c)).

Optical mapping For *ex-vivo* cases, optical mapping techniques are widely used. They use imaging devices such as a photodiode array or a charge-coupled device video camera with the heart being illuminated and either continuously or spatially scanned. The basis for these techniques is the use of voltage-sensitive dyes (VSD) that bind to or interact with cell membranes. It has been the method of choice to investigate arrhythmias experimentally at the tissue or whole heart level [RJ01, ENS04]. VSDs can be introduced through coronary flow without significant tissue damage and bind to the cardiac cell membranes. They respond to changes in transmembrane potential by changes in excitation and fluorescence spectra, which allow monitoring the cells electrical activity. Although recent advances have been made towards 3D optical imaging of cardiac electrical activity [KBMP06, HBP+07, HZS+08], surface epi-fluorescence imaging remains the most widely used technique in cardiac optical imaging [RJ01, ENS04, PSL+09, PSL+12].

Recently [HBP⁺07] presented a study of the 3D propagation of electrical waves in the heart wall using Laminar Optical Tomography (LOT), and showed promising results which demonstrated that LOT can clearly resolve the direction of propagation of electrical waves within the cardiac wall in the rat ventricular tissue.

Minimally invasive electroanatomic mapping Cardiac electrophysiology can also be studied intensively for arrhythmia patients, with minimally invasive methods during an electrophysiology study (EPS). This procedure is performed in a Catheterisation laboratory (Cath lab) which is a specially equipped operating room. In order to reach the heart with a catheter, a site is prepared that will allow access to the heart via an artery or vein, usually in the groin. This site is then described as the insertion point. Once the catheter is in and all preparations are complete, the EP study begins. The X-ray machine gives a view of the heart and the position of the electrodes, and allows the doctor to guide the electrodes through the heart. The electro-physiologist begins by moving the electrodes along the conduction pathways and along the inner walls of the heart, measuring the electrical activity along the way.

A number of software tools, like the CARTO EP Contact Navigation System (Biosense Webster, Inc., CA) (Fig. 2.6) and the EnSite Velocity Non-contact Mapping system (St. Jude Medical, MN, U.S.A.) (Fig. 2.7) have been developed aiming to facilitate the mapping of measured electrical activity on the living anatomy of the heart including the relative position of the catheter. These two systems are widely available, and mainly represent the two distinct approaches, which are the contact and the non-contact technique of electroanatomical mapping. The first step of 3D electroanatomical systems is to create an accurate anatomical model. The creation of the anatomic model of a cardiac chamber is heavily operator-dependent, meaning that improper selection of points by the operators may result in an untrustworthy model. Misleading anatomy often results in diagnostic pitfalls by omitting crucial parts of the arrhythmia circuit or the arrhythmia foci. A minimum of 50 points are needed by both contact (CARTO) and non-contact (EnSite) 3D electroanatomical systems to create the anatomy of a chamber of the heart, but 100 points are usually appropriate. The accuracy of the 3D anatomical model can be compromised by uncontrolled factors such as the extreme breathing movements, tension of the mapping catheter towards the myocardial wall and movement of the reference catheter.

Comparison between contact and non-contact electroanatomical mapping

Electroanatomical mapping has been proved to be quite useful in arrhythmias of complex pathophysiological substrate and in poorly tolerated arrhythmias. Although, both contact and non-contact electroanatomical mapping can be used to facilitate ablation of VT, the non-contact mapping has the potential advantage to be applicable in cases where the arrhythmia cannot be tolerated or in cases where the clinical arrhythmia is not reproducible during the electrophysiology study. Finally, the dynamic changes of the arrhythmogenic substrate induced by radio-frequency

Table 2.1: Current applications of electroanatomical mapping systems. Table from [AKTM09]

Cardiac arrhythmia	Mapping system
AVNRT	not necessary/ NavX system
APath-related	not necessary/ NavX system
Atrial tachycardia	contact/non-contact mapping
Nonsustained	non-contact mapping
Atrial flutter	contact/non-contact mapping
Atrial fibrillation	contact mapping
Ventricular tachycardia	contact/non-contact mapping
RVOT VT/ LIVT	not necessary/only for difficult cases
IHD/DCM	contact/non-contact mapping
Nonsustained/unstable	non-contact mapping
Sustained/stable	contact/non-contact mapping

ablation can be continuously evaluated by the operator. This advantage is of clinical importance, given the unexpected changes of the complex arrhythmogenic substrate, which may occur during the ablation of ventricular tachycardias, especially in the setting of ischemic cardiomyopathy. In this setting, it is not uncommon that different forms of ventricular arrhythmias may appear after the clinical arrhythmia has been successfully ablated. Continuous monitoring of the virtual electrograms and of the propagation map, afforded by the non-contact mapping during sinus rhythm and during ventricular arrhythmias, may help the operators to effectively create a curative strategy.

Conversely, in the case of contact electroanatomical mapping, a complete remapping should be performed after the relapse of an arrhythmia because the previous electroanatomical map is no longer valid if radio-frequency ablation lesions have been applied. This is time consuming and in some cases it can be proved simply not feasible. Mapping only the area of interest can be another strategy. On the other hand, the EnSite balloon catheter is expensive and occupies a large space in the cavity of interest. In particular it consists of a 64-electrode mesh, mounted on the outside surface of a 18 x 40 mm balloon (Fig. 2.7b). After appropriate positioning in the cavity of interest, this balloon should not be moved, thereafter. The balloon itself often represents an obstacle to the manipulation of the ablation catheter.

Non-invasive body surface mapping Century-old routine of non-invasive detection and diagnosis of the cardiac electrical activity is performed with a 12-lead electrocardiogram (ECG), a widely used test that is part of routine medical care. However, this technology measures the reflection of cardiac electrical activity on the surface of the body (body surface potential), not on the heart itself. Therefore, it has limited spatial resolution for determining regional cardiac electrical activity and limited ability to locate regions of arrhythmic activity in the heart. Recently, [Rud10, WCZ⁺11, WSD⁺07] have demonstrated a similar non-invasive method that provides high spatial resolution maps of abnormal electrical

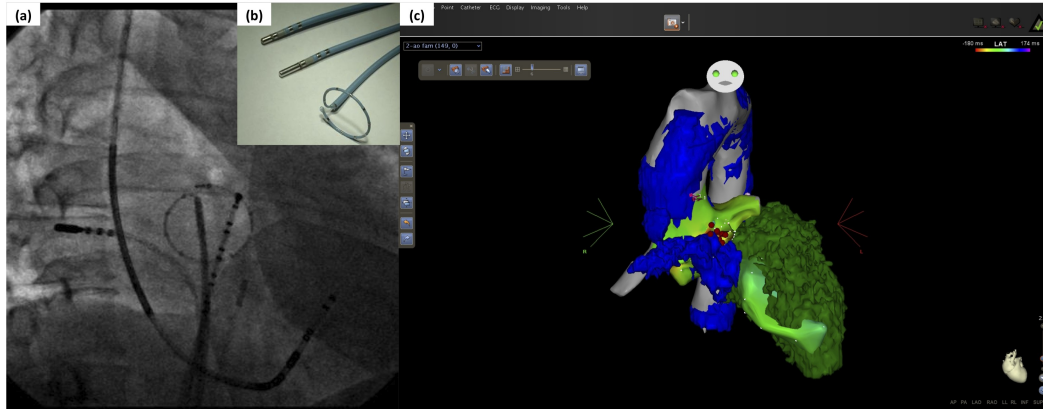


Figure 2.6: (a) Fluoroscopic images of the chest, showing CARTO contact mapping catheters in LV. (b) Close-up of the catheters. (c) Electroanatomical mapping with CARTO EP Contact Navigation System (Images from CHU, Bordeaux)

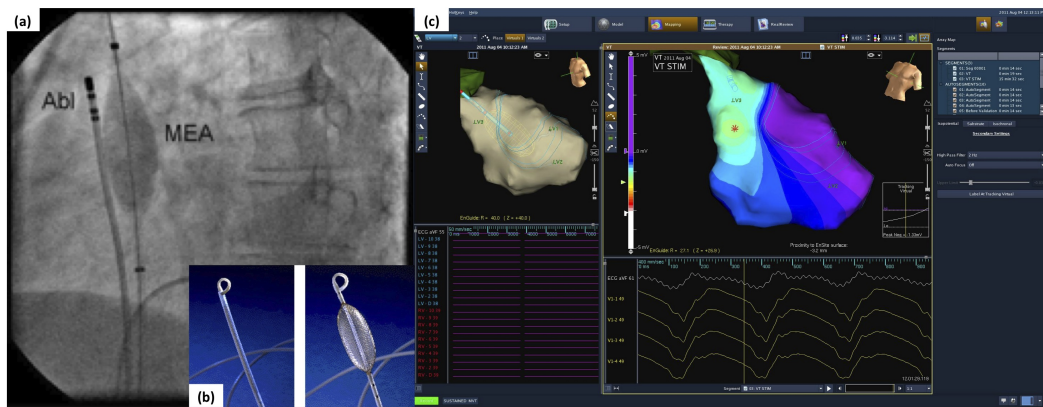


Figure 2.7: (a) Fluoroscopic images of the chest, showing EnSite balloon non-contact mapping catheters in LV. (b) Deflated and inflated EnSite balloon. (c) Electroanatomical mapping with EnSite Velocity System (Images from KCL, London)

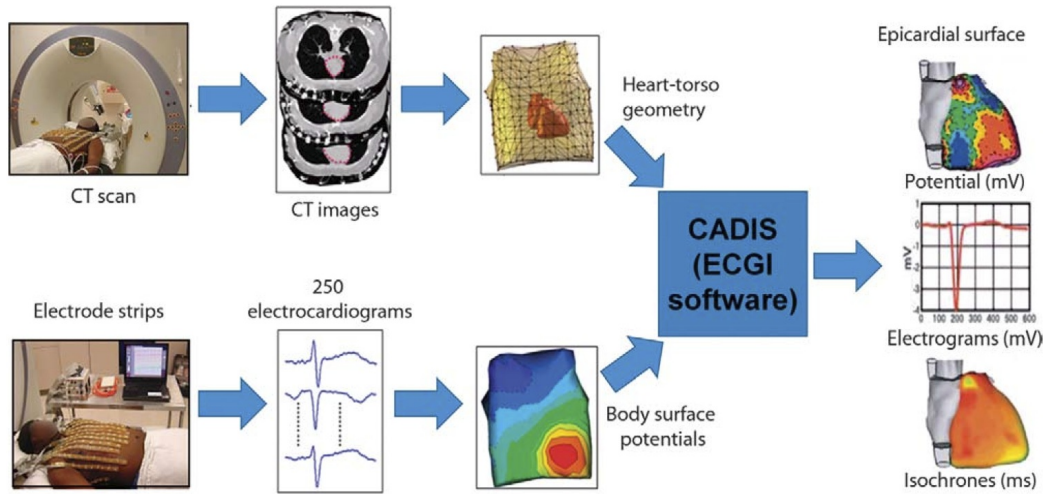


Figure 2.8: ECGI methodology to have epicardial potential and activation maps from BSPM. Figure taken from [WCZ⁺11].

activity on the heart surface (rather than on the body surface). This could contribute greatly to the understanding of the mechanisms of ventricular arrhythmias and to the diagnosis and treatment of cardiac rhythm disorders in patients. It could also help to identify patients at risk of sudden cardiac death and to develop mechanism-based therapy and guide patient-specific treatments. The technique used in [Rud10], is a non-invasive imaging method electrocardiographic imaging (ECGI) for electroanatomic mapping of cardiac electrical activation. It is obtained by solving the inverse problem of the reflected body surface potential towards the underlying cardiac activity. Such studies have also been performed in [Dös00, FD09, MGBD10, WWZ⁺11]. ECGI holds a promise to a better future with non-invasive diagnosis and early detection of CVDs, thus prevention of cardiac related deaths [RPP⁺12].

In this thesis, we work with personalising 3D biophysical ventricular models derived from imaging data to *ex vivo* optical mapping and *in vivo* electroanatomic mapping (contact & non-contact). Although as a part of this thesis, we have collaborated with IBT Germany to start personalising models with ECGI mapping derived from non-invasive BSPM mapping (Appendix D Table D.7 & D.8).

4 Modelling Cardiac Electrophysiology

Cardiac tissue contains excitable myocytes. Local depolarisation of the cardiac myocyte membrane above a threshold voltage, for example in response to current injection from a stimulating current provided by neighbouring myocytes, triggers the opening of voltage-gated Na^+ channels and a rapid membrane depolarisation, which

generates an action potential. The action potential upstroke produces local gradients in membrane voltage that cause current flow within the tissue. This current flow acts in turn to open voltage-gated Na^+ channels in neighbouring electrically connected cells, resulting in propagation of the action potential through the tissue. The speed and pattern of propagation depends on local tissue micro-structure, although at macroscopic spatial scales cardiac tissue behaves as a functional syncytium.

Hence, most models of cardiac electrophysiology assume that cardiac tissue can be treated as a continuum with diffused wave propagation in the tissue. Thus heart electrical behaviour can be governed by reaction diffusion equations. The biophysics of this process has been reviewed extensively elsewhere [KR04, PB00, CBC⁺11, FNC⁺11]. In this thesis, we simulate this action potential propagation in 3D on a ventricular model derived from patient's imaging data.

At the tissue scale cardiac tissue behaves as a functional syncytium of electrically coupled cells. A homogenisation of the discrete representation of cardiac tissue as a resistor network can be applied to derive a continuous description [NK⁺93], and its idealised electrical behaviour may be considered as an excitable medium in 3D, where excitable cells are coupled diffusively via the transmembrane voltage [KKS09].

Bi-domain & Mono-domain models Bi-domain models represent cardiac tissue as a syncytium composed of intracellular and extracellular domains. It is assumed that both domains are overlapping and continuous, but separated by the cell membrane. The bi-domain model of cardiac tissue is based on current flow, distribution of electrical potential and the conservation of charge and current [H⁺93]. It treats the intracellular and extracellular spaces separately, leading to the following coupled partial differential equations:

$$\nabla \cdot (D_i + D_e)\phi_e = -\nabla \cdot (D_i \nabla V_m) \quad (2.1)$$

$$\nabla \cdot (D_i \nabla V_m) + \nabla \cdot (D_e \nabla \phi_e) = -\beta(C_m \partial_t V_m + I_{ion}) \quad (2.2)$$

where $\nabla \cdot$ is the divergence operator, ∇ the gradient operator, ϕ_e is the extracellular potential, D_i and D_e are the intracellular and extracellular conductivity tensors [Rot92], β is the surface-to-volume ratio, and the membrane voltage is given by $V_m = \phi_i - \phi_e$, with ϕ_i as the intracellular potential.

The bi-domain model has the strong advantage to be based on a clear and physiologically relevant modelling process including an homogenisation step from a microscopic tissue scale to a macroscopic organ one. This underlying interpretation at a microscopic tissue scale makes possible the embedding of the bi-domain model with a full torso model via physiologically relevant coupling conditions at the heart/torso interface [NK⁺93], allowing the simulation of the extra-cardiac potential field and of the ECG. For these reasons the bi-domain model is very popular for the simulation of the heart and torso coupled electrical activity [LGT03]. Meanwhile, the bi-domain model is numerically highly demanding and various simplifications of this model have been widely used. For example, the eikonal model variant [CFGR90] allows

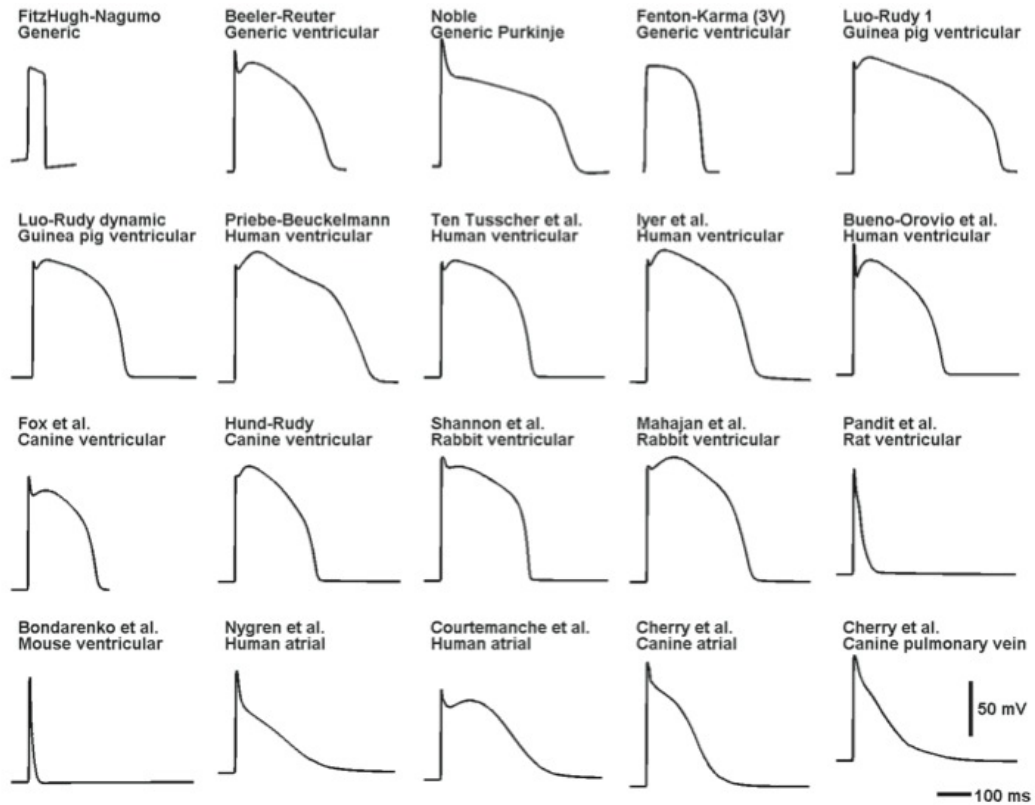


Figure 2.9: Simulated Action Potential Waveforms from a broad range of simple and complex mathematical models of cardiac cells [FC08].

to model the spread of transmembrane potential wavefront during depolarisation, and extra-cardiac potential fields can also be recovered during the depolarisation sequence using the oblique dipole layer representation [CFGV⁺82]. All these simplified version of the bi-domain model have their own limitations and this strategy does not properly capture the feedback between the extra-cellular and extra-cardiac potential fields.

In 1D, or when the intracellular and extracellular anisotropy ratios are equal in 2D or 3D, the bi-domain representation reduces to the *mono-domain*. In the mono-domain formulation, the governing differential equation is

$$\partial_t V = \nabla \cdot (D \nabla V) - I_{ion}/C_m \quad (2.3)$$

where D is the conductivity tensor, C_m is the membrane capacitance, and I_{ion} is the ionic current specified by the model formulation used in each case. If there is no injection of current into the extracellular space, descriptions of physiological action potential propagation provided by mono-domain and bi-domain models are close to each other even under the condition of unequal anisotropy ratio in the extracellular

and intracellular spaces [CFPT05]. Complex patterns of action potential dynamics in a realistic framework have been successfully simulated using the mono-domain models [CGH03].

More recently [CNLH04, PDR⁺06], a new model referred to as the *adapted mono-domain model* was proposed both to address the bi-domain model high computational cost problem and the coupling difficulty between the cardiac and extra-cardiac space for the mono-domain model. In this framework, the transmembrane potential field is governed by a single reaction diffusion equation as for the mono-domain model, the computation of which remains decoupled from the extra-cellular/-cardiac potential fields. A complete extra-cardiac/-cellular potential field is then reconstructed from the transmembrane potential which construction naturally includes the physiological coupling between extra-cardiac and extra-cellular potentials on the heart surface. The adapted mono-domain model is considered as an approximation of the bi-domain model, providing both a much lower computational cost (since the extra-cardiac/-cellular potential field can be computed when desired only) and a correct coupling on the heart surface between the extra-cardiac and extra-cellular potential fields. The bi-domain and adapted monodomain models have been compared extensively in [PRB⁺09], and the two models provided results in good agreement.

Myocardial model simulation in 3D As described earlier, models of cardiac tissue electrophysiology are based on reaction-diffusion systems where the reaction process is attributed to the cellular action potential, and the diffusion process represents current flow between cells. Most modelling approaches including mono-, bi-, or multidomain models assume that cardiac tissue behaves as a functional syncytium.

Whole heart models are commonly composed of discrete volume elements, for example tetrahedra [BEL03, VAT02] and hexahedra [FP04, SSK⁺10]. Each element type has advantages and disadvantages. For instance, a mesh assembled from uniform cubic voxels can be derived easily from imaging data, but does not reconstruct curved surfaces such as the epicardium effectively. In contrast, irregular tetrahedral meshes can improve the representation of surfaces, but mesh generation can be more difficult and the numerical methods associated with irregular meshes can result in higher computational costs. Recent work aims at providing adaptive meshes with high spatial accuracy that are appropriate for simulation of tissue electrophysiology in details in the regions of interest.

In our work, we generate an adaptive tetrahedral mesh from the patient's MR images for simulations in 3D. Whole heart segmentation from 3 dimensional steady-state free precession (3D-SSFP) MRI is done using a plug-in developed by Philips Technologies GmbH, Aachen, Germany, in the framework of euHeart project. For cases without 3D-SSFP MRI, ventricular segmentation is done from cine-MRI using CardioViz3D¹. The scar and peri-infarct zones (PIZ) segmentation is done using widely accepted full width at half maximum (FWHM) method [KFFK09], more

¹<http://www-sop.inria.fr/asclepios/software/CardioViz3D>

details are listed in Section. 2.2.1. This segmentation is done in OsiriX¹. The tetrahedral mesh generation is done by VTK² & CGAL³. Simulations are done in MIPS⁴. And visualisations are done in ParaView⁵). Adaptive meshes, with uniform large elements used to represent less important regions and grid refinement at critical points (e.g. border zones (PIZ)) are used for the simulations.

A Reaction-Diffusion system is a set of partial differential equations (PDEs). To solve these PDEs, numerical techniques implemented on computers approximate the PDEs and transform them into linear systems of equations (LSE) using discretisation techniques. In cardiac electrophysiology, the Finite Difference Method (FDM), the Finite Volume Method (FVM) and the Finite Element Method (FEM) are commonly used. In our work, we use FEM implementation of reaction-diffusion systems on the tetrahedral elements, based on the work of [Ser03],

Explicit, implicit, and semi-implicit methods can be used to solve the equations describing the time dependence of action potential propagation. The choice of numerical method influences the stability, computational cost and the accuracy of the implemented model. Explicit methods have been used extensively [BP84, HP90]. They have low computational cost for each time step, but require the time step to be small to guarantee stability for the diffusion operator. Implicit schemes can be stable with longer time steps, but require solution of a non-linear system of equations at each time step, and so are more computationally expensive. A good compromise between these two methods are the semi-implicit methods, they are studied extensively for bi-domain models in [EB08]. In this thesis, we implemented and studied those schemes extensively for mono-domain models, in order to choose the scheme which produced stable and accurate solutions. This study is described in Appendix B.

Choosing an appropriate spatial and temporal resolution for a tissue model is important and depends on the numerical method, cell electrophysiology model, diffusion coefficients and their anisotropy ratio, and geometrical properties of the tissue anatomy. Their choice affects the accuracy of the solution and results in errors w.r.t conduction velocity and action potential duration [CGH03, Cou96]. For the mono-domain models used in this work, we studied the effects of spatial and temporal resolutions on the solution, with respect to CV (as it had negligible effects on APD). The study led us to the selection of an optimum temporal and spatial resolutions with low errors on the accuracy. This study is detailed in Appendix B.

Propagation in 3D is influenced by tissue anisotropy and curvature. There is emerging evidence that 3D propagation is modulated by the fibre-sheet structure of the cardiac tissue [GSG⁺07, LSC⁺95, PSSL08, SGH⁺05]. The fibre anisotropy is modelled by the diffusion term in the model. The anisotropic 3×3 Diffusion tensor D used in the model is given by, $D = \text{diag}(1, r, r)$ in an orthonormal basis whose

¹<http://www.osirix-viewer.com>

²<http://www.vtk.org>

³<http://www.cgal.org>

⁴<http://www-sop.inria.fr/asclepios/software/MIPS/>

⁵<http://www.paraview.org>

first vector is along the local fibre orientation, and r as the conductivity anisotropy ratio in the transverse plane [Ser03].

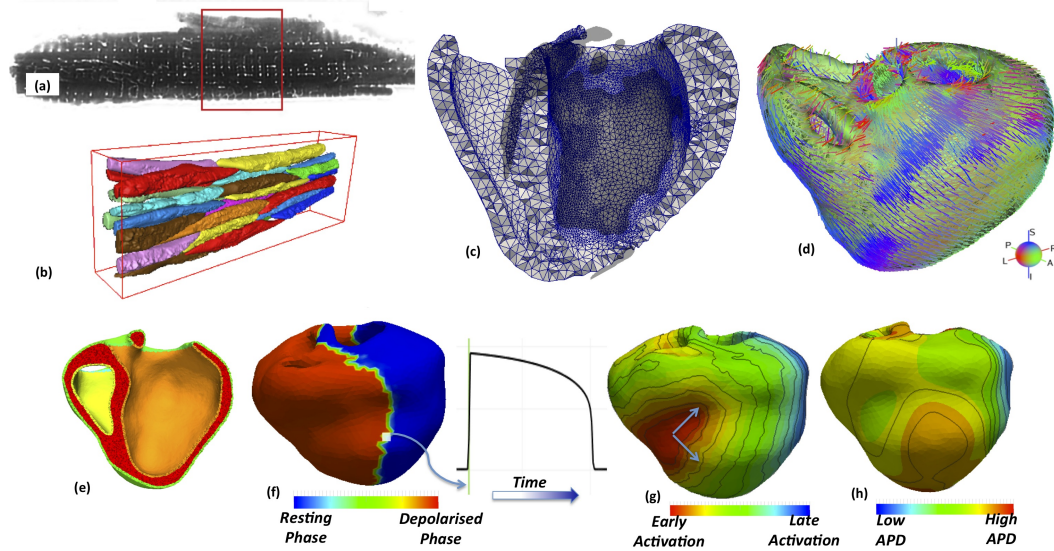


Figure 2.10: (a) Confocal microscopy of isolated living ventricular myocyte from rabbit [SGFI⁺08]. (b) 3D model of ventricular tissue with 11 complete myocytes and 11 partial myocytes [LHS09]. (c) A 3D tetrahedral ventricular model, with fine discretisation in regions around scars (black in colour) for fine modelling in PIZ. (d) fibre orientations per tetrahedra following the myocyte direction. (e) Epicardial (green), Endocardial (yellow & orange) and Myocardial (red) simulation domains on MR derived meshes. (f) 3D MS model simulation snapshot at a point in time, with action potential shown. (g) Depolarisation (Activation) isochrones from model simulation. Arrows show the tissue anisotropy in model simulation, based on fibre directions (h) APD maps from model simulation.

Classification of mono-domain cell models At the organ scale, mono-domain cell membrane models are embedded into a set of partial differential equations (PDEs) representing a continuum. Thus, we can divide the macroscopic approaches into three categories, in decreasing order of computational complexity:

- Biophysical: semi-linear Reaction-Diffusion dynamic PDEs with ionic models (over 50 variables for ions and channels) [Nob62]
- Phenomenological: semi-linear Reaction-Diffusion dynamic PDEs with mathematical simplifications of the biophysical models (2-3 variables) [Fit61]
- Eikonal: one static non-linear PDE for the depolarisation time derived from the previous models (Eikonal-Curvature, Eikonal-Diffusion, 1 variable) [KS98]

The models range from relatively simple, to more detailed models that are more specific to particular species and regions of the heart, as seen in figure 2.9. In this thesis, we use a simplified biophysical Mitchell-Schaeffer (MS) model [MS03] for pacing and arrhythmia predictions and an eikonal model [SKD⁺07] for quick parameter estimation to cope with clinical standards. We regard MS model as a *simplified* biophysical model because of the derivation of its inward and outward phenomenological currents as ionic components, similar to the derivations in Fenton-Karma models [MS03, FK98].

Parameters & Tissue properties With the introduction of propagation in tissue, the property of CV emerges. CV is related to the strength of both cell-to-cell coupling and the ionic channels, and scales as the square root of both the diffusion coefficient d (see equation 3.2) and the reaction term, as CV is also determined by the characteristics of the action potential (V_m) upstroke. Although the maximum upstroke velocity (maximum dV_m/dt) is loosely correlated with maximum CV. In this work, we estimate the parameter (termed as Apparent Conductivity (AC)) controlling CV from patients EP data, as they are good indicators of sinus rhythm blocks in diseased tissue regions [CRG⁺08].

The APD was found to progressively decrease as the wave moved away from the stimulation site, and this effect was more pronounced in directions transverse to the local fibre orientation [OKT⁺87]. Evidence of this negative linear correlation between APD and activation time has been found in several animal species including humans [HSE⁺09]. Thus the septum (muscle separating the LV and RV) is found to be depolarised first and repolarised last. However, in our work we estimate the APD distribution over the ventricles directly from the patient's EP data.

Restitution is the rate adaptation of cardiac cells and tissue. Along with APD, other quantities adapt to changes in rate. For instance, action potential amplitude often diminishes, along with APD, at rapid heart rates. The resting membrane potential can increase as well during rapid pacing. In tissue, the conduction velocity of propagating waves also depends on rate and, in most cases, slows as the rate increases.

Alternans is beat to beat alternation in action potential shape and duration, and memory is the extent to which a particular action potential depends on the sequence of preceding beats. In tissue, a number of important dynamical properties associated with restitution, alternans, and memory may be altered by the presence of electrotonic currents. The disturbance in their dynamics due to an infarction can cause the development of arrhythmias [BOPGF04, CF04, FC08, TTBHP06], as explained in the next section.

In this thesis, we use the MS model, which is able to hold the memory of one preceding cycle, and has restitution properties, thus is able to simulate arrhythmias macroscopically. We calculate the disturbance in the tissue restitution, with the slopes of the restitution curves and their heterogeneity estimated from the patient's EP data, as described in the following chapters.

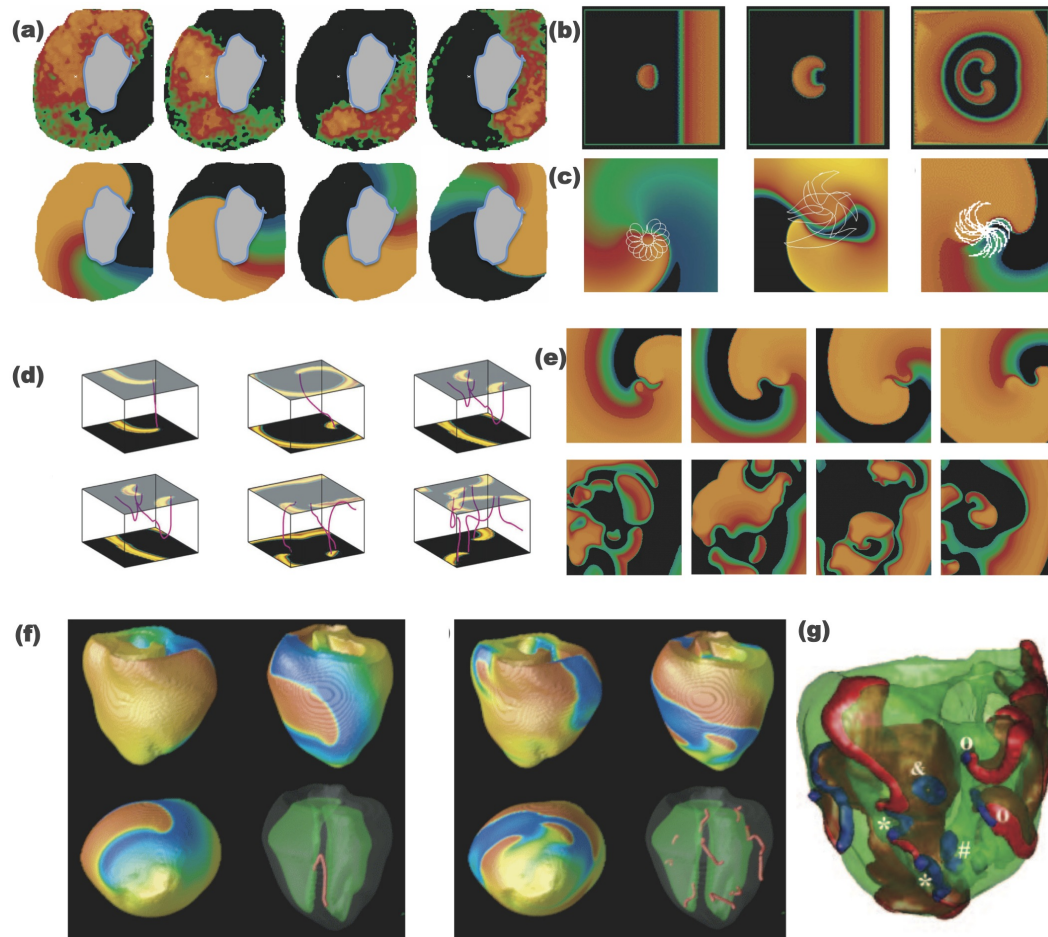


Figure 2.11: (a) Experimental (top) and simulated (bottom) anatomical re-entrant arrhythmia. (b) Initiation of a functional re-entry during the vulnerable window. (c) Different types of spiral wave tip trajectories (hypocycloidal, hypermeandering & linear). (d) Breakup of scroll waves in a simulated 3D tissue slab. (e) Spiral wave dynamics of the TNNP model [TTNNP04], stable wave and gradual breakup with pacing rate change. (f) (left) Single spiral wave in 3D on rabbit heart simulating VT, (right) multiple spiral waves in the same geometry simulating VF. (g) 3D wavefront (red) and scroll wave filaments (blue) during VF. (a-e taken from [FC08]) (g taken from [TTHP⁺07])

5 Modelling Cardiac Arrhythmias

In this section, we describe the mechanisms for ventricular tachycardia and fibrillation, and how it is modelled to understand the arrhythmogenic behaviour of the heart. Extensive details on modelling ventricular tachycardia and the state of the art is given in chapter 6 section 1 & section 2.1.1. Cardiac arrhythmias are associated with abnormal initiation of a wave of cardiac excitation, abnormal propagation of a wave of cardiac excitation, or some combination of the two. Cardiac arrhythmias can manifest themselves in many different ways, and it is still not always possible to determine the mechanism of an arrhythmia.

Arrhythmias can be classified in several ways. One useful classification is re-entrant versus non re-entrant arrhythmias. In re-entry, cardiac tissue is repetitively excited by a propagating wave circulating around an obstacle (anatomical re-entry) or circulating freely in the tissue as a scroll wave (functional re-entry). Thus, there is a strong spatial component to re-entrant arrhythmias: either a sufficiently large spatial extent is needed to support the initiation and continuation of the arrhythmia, or an appropriate geometry must be present to allow a re-entrant circuit. Non re-entrant arrhythmias usually have at particular anatomical sites, one or more pacemaker activities formed at abnormal locations (ectopic). Arrhythmias also can be classified by the heart rate. Tachyarrhythmias are rhythms in which the heart rate is faster than normal, usually taken as greater than 100 beats per minute. Tachyarrhythmias can arise from an accelerated sinus rhythm, an accelerated rhythm from an abnormal ectopic site. However, more usually tachyarrhythmias are believed to arise from re-entrant arrhythmias, in which the period of the oscillation is set by the time an excitation takes to travel in a circuitous path, rather than the period of oscillation of a pacemaker [Jos08, MKY⁺02].

In this thesis, we focus on the re-entrant type of ventricular tachycardia. Re-entrant arrhythmias can be confined to a single chamber of the heart, or can involve several chambers. In some instances, it is convenient to think of the underlying circuit for the re-entrant excitation as a one-dimensional ring (spiral (2D) & scroll waves (3D) shown in Fig. 2.11)

Anatomical re-entry Anatomical re-entry has a wave circulating around an obstacle (Fig. 2.11(a)) and can have a complex fluctuating propagation velocity that arises as a consequence of the interaction of the wavefront with its own refractory tail [QR91, CW91]. The re-entrant wave can generate through various mechanisms which include source-sink mismatch and unidirectional block [Ber00]. The instability of this wave can lead to degeneration of multiple re-entrant waves thus fibrillation (Fig. 2.11(e,g)).

The analysis of the instability of this wave, relies on employing both the APD restitution curve (APD as a function of DI) and the conduction velocity (CV) restitution curve (CV as a function of DI) for a pulse travelling in space. This instability can be analysed through discordant alternans [WFE⁺01, QGCW00]. Alternans in tissue are different spatial patterns of APD. In the simplest case, the entire tissue

experiences a long or short action potential together. The APD may vary spatially, but as long as the entire tissue still alternates long-short together, the tissue is said to exhibit spatially concordant alternans. When the tissue begins to alternate long-short in some areas but short-long in other areas, spatially discordant alternans are present. It is possible to determine whether alternans is concordant or discordant by plotting two successive APDs at all points in the tissue. Discordant alternans requires the presence of heterogeneity in APD or CV restitution to occur, otherwise alternans would always be spatially concordant. Heterogeneous steep APD restitution curve slopes due to disturbances in the electrotonic currents near scar areas, not only can give rise to discordant alternans, but also can lead to breakup of spiral waves in tissue.

A sequence of premature stimuli delivered to the heart during normal sinus rhythm can often lead to the initiation of tachycardia. In some clinical settings, analysis of the resetting, entrainment, and initiation of tachycardias offers clinicians important clues about the arrhythmia mechanism, and consequently can help the cardiologist choose an appropriate therapy [Jos08, SD00]. The ability to induce monomorphic ventricular tachycardia using a sequence of up to three premature stimuli is often taken as an indication of anatomical re-entry as a mechanism for the tachycardia. Since at least part of the re-entrant circuit is assumed to be one-dimensional, this can provide a target for ablation therapy. All the anatomically-based re-entrant arrhythmias as a first approximation can be thought of as a wave circulating on a one-dimensional ring (at least for part of the circuit). Clinically, the localisation of a re-entrant circuit is useful to the cardiologist, who can change the topology by interrupting the ring or disk using RF ablation, which destroys tissue that forms part of the anatomical circuit and thereby eliminates the anatomical basis for the arrhythmia.

Functional re-entry Single or double spiral waves or scroll waves are often generated in excitable cardiac tissue or models of cardiac tissue by a single impulse delivered in the wake of a propagating wave during the vulnerable period, as shown in Fig. 2.11(b). These re-entries do not rotate around obstacles; instead, they are called functional as they rotate around a "functional" obstacle called the core of the spiral or scroll wave. A single spiral or scroll wave with a fixed repetitious motion (which may be anchored to some anatomical feature such as a blood vessel or scar) likely would lead to a monomorphic tachycardia. If an initiated spiral wave is itself unstable, it may quickly break up into multiple waves [FK98, BWZ⁺02, BHZ94, BE93]. Clinical evidence exists for this, especially in the case of ventricular fibrillation, which is usually preceded by a short-lived ventricular tachycardia (Fig. 2.11(e)). Ventricular tachycardias occurring in patients other than those who have experienced a previous heart attack, and perhaps even in hearts with completely normal anatomy. In these individuals, it is likely that spiral and scroll waves are the underlying geometries of the excitation. A particularly dangerous arrhythmia, polymorphic ventricular tachycardia (in which there is a continually changing morphology of the

electrocardiogram complexes), is probably associated with meandering spiral and scroll waves (Fig. 2.11(d,f)) [GJP⁺95].

6 Conclusion

In this chapter, we presented a background of cardiac anatomy, myocardial infarction, electrophysiology and ventricular arrhythmias. We also described the state of the art technologies currently being used in clinics, for mapping cardiac electrophysiology. These include minimally non-invasive electroanatomic mapping with two distinct widely used techniques (contact & non-contact), recently introduced non-invasive body surface mapping with the derived epicardial ECGI, and optical mapping of *ex vivo* cases studied for research purposes. Lastly, we outlined the basics as well as the research being carried out in modelling cardiac electrophysiology and ventricular arrhythmias *in silico*.

Part II

**PERSONALISATION OF
CARDIAC
ELECTROPHYSIOLOGY
MODELS**

Building Personalised EP Models using *ex vivo* Experimental Data (Optical Mapping)

Contents

1	Introduction	32
2	Data Acquisition and Processing	34
3	Model Simulation: Direct Problem	37
4	Model Personalisation: Inverse Problem	38
4.1	Case 1: Personalisation Using a Single PF	39
4.2	Personalisation of DT Isochrones	39
4.3	Personalisation of Action Potential Duration	42
4.4	Case 2: Personalisation Using Multiple PF	42
4.5	Personalisation of Restitution curves	42
4.6	Personalisation of DT Isochrones	43
5	Results	43
5.1	DT & APD error maps	44
5.2	Fitting of restitution curves	44
5.3	Robustness to Pacing Location	46
5.4	Evaluation of Volumetric Predictions	46
6	Discussion	47
7	Conclusion	50

Based on:

[RPD⁺11] J. Relan, M. Pop, H. Delingette, G. Wright, N. Ayache, and M. Sermesant. Personalisation of a cardiac electrophysiology model using optical mapping and MRI for prediction of changes with pacing. *IEEE Transactions on Biomedical Engineering*, 58(12):3339–3349, 2011.

Additional material available in [RPD⁺10], [RSP⁺09a] and [RSP⁺09b]

Computer models of cardiac Electrophysiology (EP) can be a very efficient tool to better understand the mechanisms of arrhythmias. Quantitative adjustment of such models to experimental data (personalisation) is needed in order to test their realism and predictive power, but it remains challenging at the organ scale. In this chapter, we propose a framework for the personalisation of a 3D cardiac EP model, the Mitchell-Schaeffer (MS) model, and evaluate its volumetric predictive power under various pacing scenarios. The personalisation was performed on *ex vivo* large porcine healthy hearts using Diffusion Tensor MRI (DT-MRI) and optical mapping data. The MS Model was simulated on a 3D mesh incorporating local fibre orientations, built from DT-MRI. The 3D model parameters were optimised using features such as 2D epicardial depolarisation and repolarisation maps, extracted from the optical mapping. We also evaluated the sensitivity of our personalisation framework to different pacing locations and showed results on its robustness. Further, we evaluated volumetric model predictions for various epi- and endocardial pacing scenarios. We demonstrated promising results with a mean personalisation error around 5 ms and a mean prediction error around 10 ms (5 % of the total depolarisation time). Finally, we discussed the potential translation of such work to clinical data and pathological hearts.

1 Introduction

Modelling cardiac electrophysiology *in silico* has been an important research topic for the last decades [HH52, NVKN98, KKS09, TTNNP04], and it can be a very efficient tool to better understand the mechanisms of arrhythmias. Personalisation of such models to experimental data is needed in order to test their realism and predictive power, but remains difficult at the scale of the organ. Personalisation is defined as the estimation of model parameters which best fit simulations to data. In this chapter, we propose a robust personalisation method for a volumetric cardiac electrophysiology model using surface data and we test its predictive power. The personalisation and prediction evaluation were done using the high quality *ex vivo* electrophysiology data obtained from the fusion of optical and MR imaging.

Cardiac electrophysiology models of the myocyte Action Potential (AP) at cellular and sub-cellular scales can be broadly classified into three main categories: Ionic Models (IM), Phenomenological Models (PM) and Eikonal Models (EK). IM [HH52, BR77, LR91, NVKN98, TTNNP04] characterise ionic currents flowing through the cardiac cell membrane with varying complexity and accuracy and have many parameters and variables (it can be more than 50). Most of them are computationally expensive to simulate in volumetric domains and not well suited to solve inverse problems (parameter estimation). EK [CGPT98, KKS09, SKD⁺07] are very simple, describing only the time at which a depolarisation wave reaches a given point without precisely modelling the potential value. At the intermediate level are PM [Fit61, RV96, BWZ⁺02], which describe and capture just the shape of action potential generation and propagation along the cell membrane, without modelling

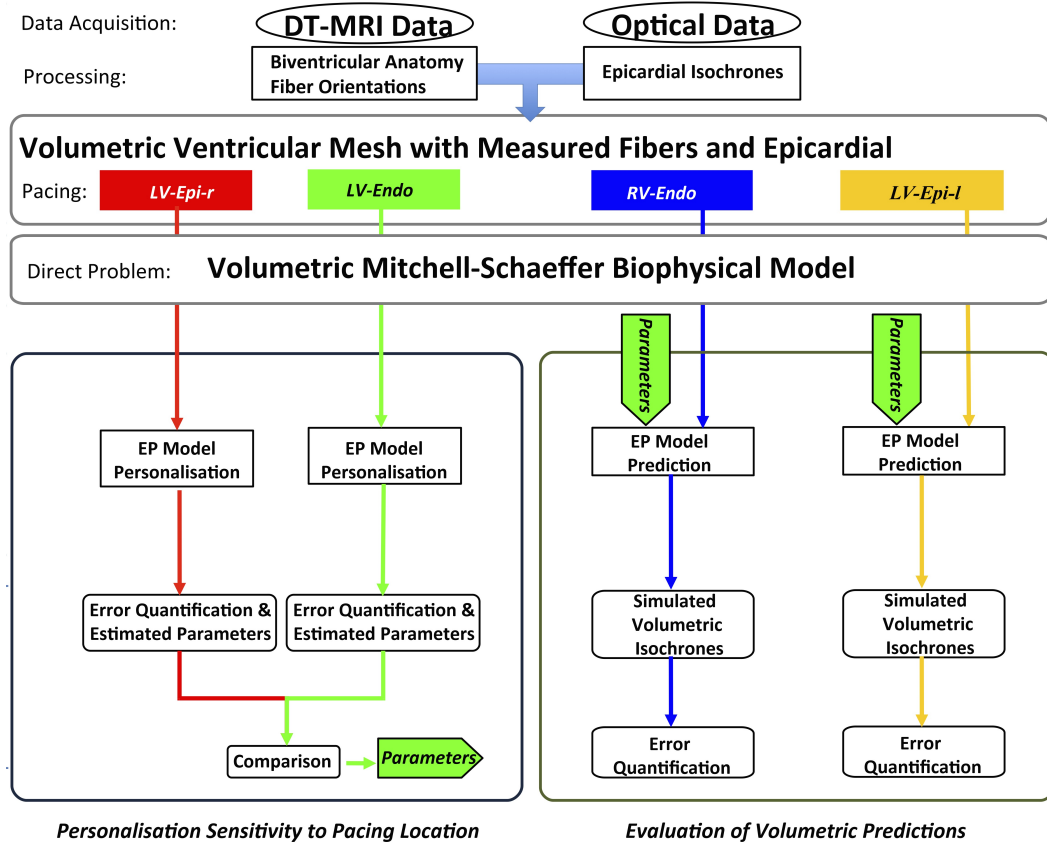


Figure 3.1: Flowchart describing the outline of this chapter.

all the ionic currents.

Here, we personalised a simplified biophysical model, the Mitchell-Schaeffer (MS) model [MS03], modelling the action potential as a combination of sodium (Na^+), calcium (Ca^{2+}) and potassium (K^+) phenomenological ionic currents. We chose this model because of the following reasons: (i) it provides a good analytical understanding of the membrane dynamics, (ii) it has a limited number of parameters (5) to estimate, (iii) each parameter has a simple physical interpretation, and (iv) it has explicit analytical formulae to express most of the measured features and restitution properties using model parameters [MS03]. Finally, it was compared to another classical PM models (the Aliev-Panfilov model [RV96]), and the MS model was providing a better fit (lower final error, especially for the APD) with a more homogeneous parameter map for conductivity [RSD⁺09].

The cardiac electrical activity was acquired *ex vivo* from controlled experiments using optical imaging of the epicardium of healthy porcine hearts [PSL⁺09]. The optical signal directly represents the tissue action potential. This data was then processed to extract features of the AP propagation such as depolarisation time (DT), repolarisation time (RT), Conduction Velocity (CV), Action Potential Dura-

tion (APD) and their restitution. These features were then fused with a volumetric mesh created from MRI of the *ex vivo* hearts, to obtain epicardial surface data.

Electrophysiology model personalisation can be basically addressed as an inverse problem of parameter estimation. This problem was first addressed using a single heart cycle for 2D phenomenological Aliev & Panfilov model in [MVDS⁺06], where the AP propagation was simulated on a simple surface mesh modelling a dog's heart epicardium. Only the model parameter for the DT feature was adjusted. It was also performed for 2D EK in [CRG⁺08] again with adjustment of the same feature but for patient data. Finally, initial step towards personalisation of the 3D Aliev & Panfilov model were taken in [LSP⁺08] with adjustment of DT and APD features from a single cycle.

Here, we propose a personalisation framework for a 3D macroscopic MS model on a volumetric bi-ventricular mesh of the myocardium using 2D epicardial surface data. The robustness of this method to different pacing locations and its predictive power were assessed.

2 Data Acquisition and Processing

The experimental data acquired consist of epicardial optical imaging that records the AP wave propagation, and Diffusion Tensor-MRI representing the anatomy and fibre orientations. The optical data have a higher spatial resolution compared to *in-vivo* mapping data and provides a direct measurement of the AP [ENS04]. Such dense and controlled data enabled the validation of the personalisation method and prediction results. The data was acquired and processed in three stages (see Fig 3.2):

Stage 1: Optical Imaging Data

The explanted heart was attached to a Langendorff perfusion system with fluorescence dye and the electro-mechanical uncoupler (to suppress heart motion) injected into the perfusion line. More details of the experimental setup can be found elsewhere [PSL⁺09] (see Fig. 2.5). The heart was paced at a given rate, with an electrode near the apex with a square wave voltage stimulus of 2-4V for 5 ms. The fluorescence signals were captured with high temporal (270 fps) and spatial ($< 1mm$) resolution, using a pair of CCD cameras. Lastly, 5-7 opaque markers were glued onto the epicardium and imaged, so as to provide a way to register the optical images with the epicardial surface of the model generated from MRI volume. Recorded 2D optical movie represents the changes in the fluorescent signal intensity, which follow the changes in the AP. The signal intensity was then analysed for each pixel of the movie to get DT and RT isochrones in the following way. First, the signal was scaled for each pixel between its baseline and maximum value, cropping under the baseline which we got from segmenting the values into two clusters, the baseline being defined as the mean value of the lowest cluster. The scaled recordings were then filtered with a 3D Gaussian convolution, spatially isotropic with a kernel width of 1.0 and temporally using a kernel width of 3.0.

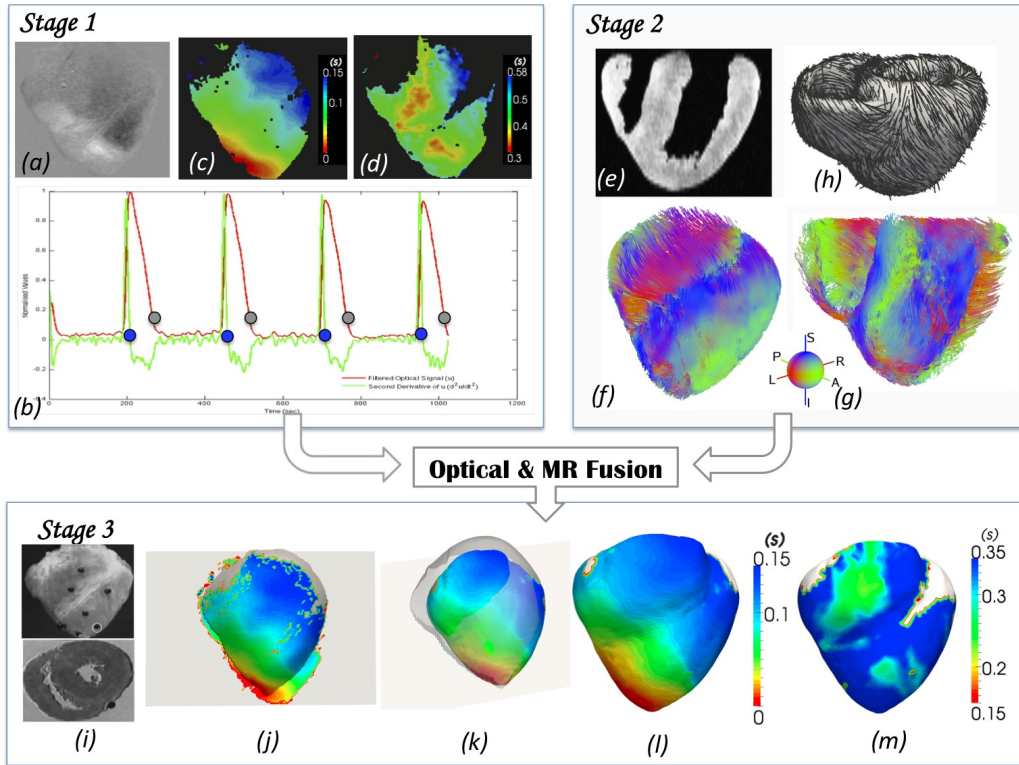


Figure 3.2: *Stage 1* (a) Raw optical data acquired (antero-lateral view). (b) Extraction of depolarisation times (blue dots) and APD_{90} (grey dots), (c) & (d) Extracted DT & APD isochronal maps. *Stage 2* (e) DT-MRI slice, (f) & (g) fibre tracking from DT-MRI, (h) Volumetric mesh with assigned fibre orientations *Stage 3* (i) top: A snapshot showing the epicardial markers using optical camera, bottom: MRI slice showing markers, (j) Stereoscopic surface generated from the two optical CCD cameras with extracted features, (k) Registration of stereoscopic surface to the volumetric mesh using markers and features projection, (l) & (m) Resulting DT and APD maps on the mesh for epicardial surface only.

The DT were detected using the zero crossing of the second (d^2F/dt^2) derivatives of the fluorescence signal intensity F (Fig 3.2(b)). The RT were detected using APD_{90} (APD at 90% repolarisation, which is 0.9 times the difference between the action potential peak amplitude and the baseline (Fig 3.2(b))). Finally, the DT isochrones and APD maps for each cycle were reconstructed as 2D images (Fig 3.2(c) & d)).

Stage 2: Diffusion Tensor-MRI Data

The hearts were then imaged using a MR scanner. The details on MR pulse sequences and setup used is described in details in [PSL+09]. An in-plane resolution of $0.5 \times 0.5 \text{ mm}^2$ and slice thickness of 1.5 mm was used. The heart anatomy was

extracted from the MR data using classical segmentation algorithms such as thresholding, mathematical morphology, isosurface extraction, and used to generate a volumetric tetrahedral mesh using CGAL (<http://www.cgal.org>) and GHS3D (TetMesh, <http://www.distene.com>) software. For each vertex, the assigned fibre direction is the principal eigenvector of the corresponding voxel in the reconstructed tensor image, see Fig 3.2(h).

Stage 3: Optical and MR Data Fusion

The optical images recorded by the two CCD cameras were used to reconstruct the 3D surface of the heart using stereoscopy (Fig 3.2(i)) [CPSW06]. The 2D isochronal maps generated were then rectified based on the cameras calibration and stereoscopic parameters. Each pixel of the isochronal maps corresponds to a vertex on the grid mesh of the stereoscopic surface (Fig 3.2(j)). The glued opaque markers were imaged with optical as well as MR data. An affine registration of the stereoscopic surface onto the volumetric mesh was then performed using these markers [PSL⁺09] (Fig 3.2(i)).

The DT isochrones and APD maps for each cycle were projected onto the volumetric mesh with an interpolation from the triangular stereoscopic surface, resulting in epicardial DT isochrones and APD maps on the bi-ventricular mesh (Fig 3.2(k-m)).

Dataset Used for Personalisation

We used two *ex vivo* hearts, which were optically imaged for steady-state heart cycles and scanned with DT-MRI. The first heart was paced to produce 4 different optical datasets, all at a frequency of 1.1 Hz, but obtained using 4 different pacing locations (Fig 3.3(1st, 2nd, 3rd & 4th column)) which were near the apex of:

- *1A-LV-Epi-l*: left ventricle epicardium (left side).
- *1B-LV-Epi-r*: left ventricle epicardium (right side).
- *1C-LV-Endo*: left ventricle endocardium.
- *1D-RV-Endo*: right ventricle endocardium.

The second heart was paced to produce 5 different optical datasets, all paced at one location near the apex of the left ventricle epicardium, but for 5 different Pacing Frequency (PF) (Fig 3.3(5th column)): 0.5 Hz (2A), 0.7 Hz (2B), 0.9 Hz (2C), 1.1 Hz (2D), 1.2 Hz (2E).

Although these were healthy hearts, we could identify discrete areas of low conductivity (see black ellipse in Fig 3.3). This was most likely due to tissue becoming ischemic around a small branch of blood vessel, partially occluded by an air bubble accidentally trapped into the perfusion line, resulting in oxygen deprivation of the tissue and further installation of acute ischemia and cellular uncoupling. As a result, an altered morphology of action potentials accompanied by a lowering of CV was observed in these areas.

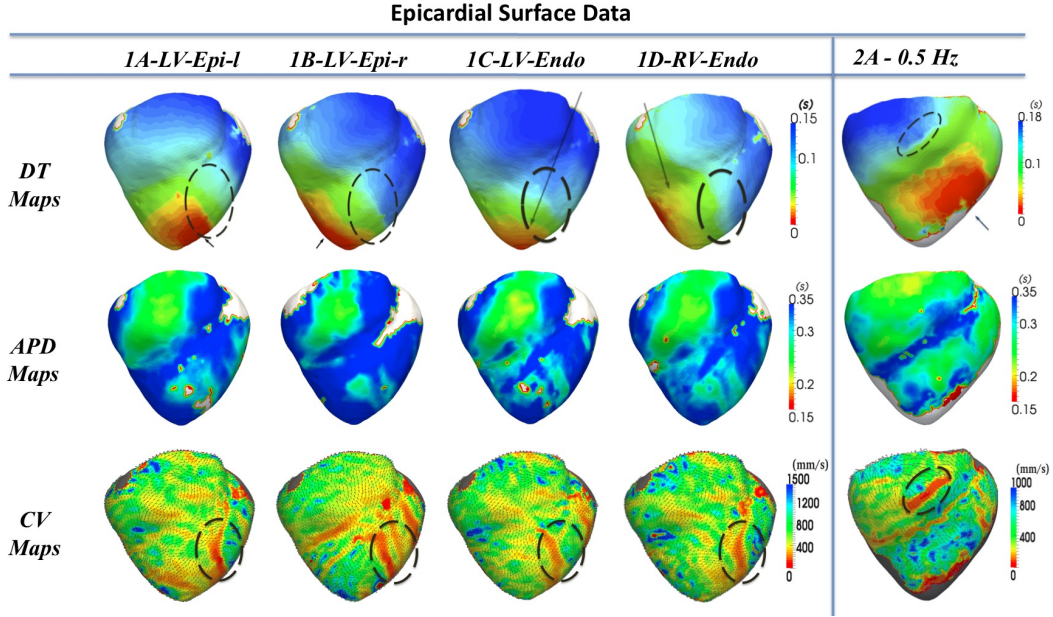


Figure 3.3: The first four columns are for dataset 1 and the last column is for dataset 2. The first row shows the measured epicardial DT isochrones for various pacing locations (depicted by arrows), the second row shows the respective APD maps and the third row shows the local CV^{msd} computed from the measured DT isochrones (small arrows on the surface show CV direction). Black ellipses highlight the regions having low conductivity.

3 Model Simulation: Direct Problem

The MS model [MS03] is a 2-current simplified biophysical model derived from the 3-current ionic Fenton Karma model [FK98]. The MS model is described by the following system of Partial Differential Equations (PDE)

$$\begin{cases} \partial_t u = \operatorname{div}(D\nabla u) + \frac{zu^2(1-u)}{\tau_{in}} - \frac{u}{\tau_{out}} + J_{stim}(t) \\ \partial_t z = \begin{cases} \frac{(1-z)}{\tau_{open}} & \text{if } u < u_{gate} \\ \frac{-z}{\tau_{close}} & \text{if } u > u_{gate} \end{cases} \end{cases} \quad (3.1)$$

where, u is the normalised action potential variable, and z is the gating variable, which makes the gate open and close, thus depicting the depolarisation and repolarisation phase. $J_{in} = (zu^2(1-u))/\tau_{in}$ represents combination of all inward phenomenological ionic currents, primarily Na^+ & Ca^{2+} , which raises the action potential voltage and $J_{out} = -u/\tau_{out}$ represents combination of all outward phenomenological currents, primarily K^+ that decreases the action potential voltage describing repolarisation. J_{stim} is the stimulation current, at the pacing location.

The parameters of the reaction terms and their standard values as reported

in [MS03] are

- τ_{open} : opening time-constant of the gate = 0.120 s
- τ_{close} : closing time-constant of the gate = 0.150 s
- τ_{in} : time-constant for inward currents = 0.003 s
- τ_{out} : time-constant for outward currents = 0.06 s

The diffusion term in the model is controlled by the anisotropic 3×3 Diffusion tensor D given by, $D = d \cdot \text{diag}(1, r, r)$ in an orthonormal basis whose first vector is along the local fibre orientation, with d representing the cardiac tissue pseudo-conductivity in the fibre direction and r as the conductivity anisotropy ratio in the transverse plane. In order to have CV three times faster in the fibre direction than in the transverse plane [KKS09], we fix a value of $r = (1/3)^2 = 0.11$ (see Eq 3.2). Thus, we have only one parameter of the diffusion term and its standard value for $CV = 50\text{cm/s}$ is given through a cardiac tissue pseudo-conductivity $d = 1.5\text{s}^{-1}$.

The model was spatially integrated on a 3D bi-ventricular tetrahedral mesh using a P1 Finite element method [SDA06]. Using an appropriate discretisation in space for the model, with a mean edge length of Δx , leads to a system of algebraic differential equations. The choice of Δx influences the numerical solution accuracy and depends on the maximum of du/dt . Thus we studied several time integration schemes (Explicit, Semi-Implicit and Implicit) for the model with respect to solution accuracy, stability and computational time expense (described in details in [EB08, RSD⁺09]). As a result of this study, for MS model, we found the following optimum choice for spatial discretisation as $\Delta x = 1.5\text{mm}$ and temporal discretisation as $\Delta t = 0.1\text{ms}$, with a semi-implicit, second order scheme known as Modified Crank-Nicolson/Adams-Bashforth (MCNAB) [EB08]. The model was simulated with initial pacing conditions as Dirichlet conditions (similar to voltage stimulus in experiments), where u and z value of 1 was imposed for certain duration to a set of vertices, which were chosen by extracting the earliest depolarising sites from the DT isochrones.

4 Model Personalisation: Inverse Problem

By model personalisation, we estimate the model parameters such that the model simulated features are similar to the extracted data features. Fortunately, MS model has this relationship defined explicitly for features like APD for a single cycle (see Eq 3.9) and APD & CV restitution (see Eq 3.11 and Eq 3.12). However CV for a single cycle is analytically defined in 1D using reaction-diffusion analysis [CTSG04] (see Eq 3.2), but in 3D, the wave front curvature also affects CV.

Using these relationships, we could determine the qualitative dependency of the extracted data features to the model parameters, see Table 3.1.

	Single PF		Multiple PF	
	DT	APD	CV Rest.	APD Rest
d	✓	–	✓	–
τ_{in}	✓	✓	✓	✓
τ_{out}	–	✓	✓	✓
τ_{open}	–	–	–	✓
τ_{close}	–	✓	–	✓

Table 3.1: Sensitivity of AP features to model parameters.

4.1 Case 1: Personalisation Using a Single PF

This case was applied to the first heart having a constant PF. In this case, we estimated the parameter d using DT isochrones and the parameter τ_{close} using the APD, while all other parameters of the model were kept to their nominal values [MS03]. These adjustments are independent as there is no coupling between them (see Table 3.1). Parameter estimation procedure is done as follows:

4.2 Personalisation of DT Isochrones

The apparent local CV (CV^{msd}) of the epicardial tissue can be estimated from the spatial gradient of the measured DT isochrones T as, $1/CV^{msd} = \|\nabla T_x\|$. To avoid the amplification of the acquisition/fusion noise by the spatial derivatives, we smoothed CV^{msd} by averaging it over a neighbouring area, see Fig 3.3(3rd row). The analysis of the MS model for CV along the simulated wavefront has been studied in 1D [CTSG04] using travelling wave train solutions and is found to be

$$CV^{sim} \propto \sqrt{\frac{d}{\tau_{\text{in}}}} \quad (3.2)$$

This relationship does not stand true in 3D propagation as the curvature of the wavefront affects CV^{sim} . Eq 3.2 shows one measured feature depending on two model parameters. We chose to estimate parameter d rather than τ_{in} , which could be either estimated from restitution curves in case 2, or kept globally constant with a standard value in case 1. The estimation of parameter d was done in the following two steps:

Calibration Here we initialise the model parameter d using the analytical relationship (see Eq 3.2). The calibration function used here was given by $CV^{sim}(d) = \alpha\sqrt{d} + \beta$, where the constants α and β were to be determined for 3D model simulation. α determines the scaling of Eq 3.2 in 3D with numerical diffusion and β was added to better fit the numerical simulations to Eq 3.2 and represents discretisation errors in 3D. The constants were determined by performing several model simulations for a range of d ($d \in [0.1; 5.0]$) over the interval of stability of $CV^{sim}(d) \approx 10\text{cm/s} - 2\text{m/s}$. For each model simulation, a median of $CV^{sim}(d)$

was computed. This gives rise to an overdetermined linear system given as

$$\begin{pmatrix} \vdots \\ medianCV_k^{sim}(d) \\ \vdots \end{pmatrix} = \begin{pmatrix} \vdots & \vdots \\ \sqrt{d_k} & 1 \\ \vdots & \vdots \end{pmatrix} \cdot \begin{pmatrix} \alpha \\ \beta \end{pmatrix} \quad (3.3)$$

where each line k is the result of a model simulation. The system (Eq 3.3) can also be written in matrix notation as,

$$medianCV^{sim} = \mathbb{D} \cdot \mathbb{P} \quad (3.4)$$

We solve Eq 3.4 in non-linear least squares sense by simply computing the pseudo-inverse : $\mathbb{P} = (\mathbb{D} \cdot \mathbb{D}^T)^{-1} \cdot \mathbb{D}^T \cdot medianCV^{sim}$ Once the relationship is estimated, d^{global} was determined from the median of CV^{msd} using

$$d^{global} = \left(\frac{medianCV^{msd} - \beta}{\alpha} \right)^2 \quad (3.5)$$

where $medianCV^{msd} = median_{i \in S} (CV_i^{msd})$ with i the vertex index and S the set of the mesh vertices having measurements.

Iterative adjustment This step was used to optimise the parameter d locally using a multi-resolution approach and the calibration result as initialisation. In order to start domain decomposition, we first divide the LV into 17 zones as defined by the American Heart Association (AHA), and similarly the RV into 9 zones. Then the zones with high cost function $J(d_{zone})$ after optimisation were subdivided further into 4 zones for level I and so on (Fig 3.4).

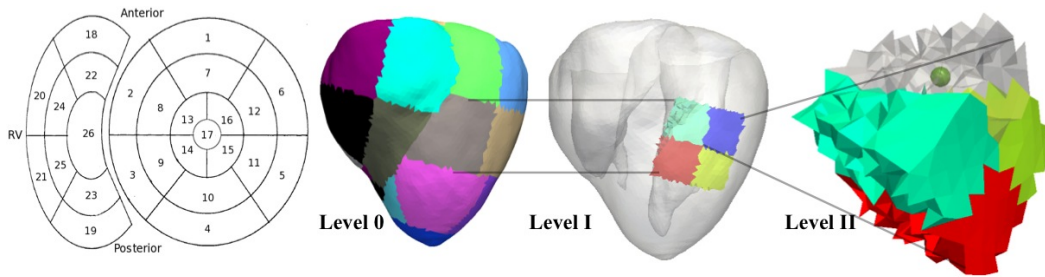


Figure 3.4: Level 0 stands for the AHA segmentation of the bi-ventricular mesh into 26 zones. Level I is the subdivision of a zone into 4, Level II is a further subdivision. The green sphere is the zone barycentre.

The cost function for each zone was given as

$$J(d_{zone}) = \sum_{\forall i \in S \cap zone} \left(DT_i^{msd} - DT_i^{sim}(d_{zone}) \right)^2 \quad (3.6)$$

with vertex i in zone, belonging to the surface S having measured data. The cost function C_d for the myocardium was

$$C_d = \sqrt{\frac{1}{n} \sum_{\forall zone \in mesh \cap S} J(d_{zone})^2} \quad (3.7)$$

where n is the number of zones having measured data. We minimise this cost function using trust region optimisation [CGT00], which finds the minima of a subproblem such as a quadratic model created using the gradient and approximate Hessian matrix at the current search point implemented using Trilinos solver (<http://trilinos.sandia.gov>). The gradient is computed using a simple finite difference scheme given by

$$\frac{\partial J(d_{zone})}{\partial d} \approx \frac{J(d_{zone} + \Delta d) - J(d_{zone} - \Delta d)}{2\Delta d} \quad (3.8)$$

This optimisation was chosen to have a few number of gradient computations as they are computationally expensive and require two simulation steps.

When using domain decomposition, we obtain piecewise constant parameter maps. In order to have smooth parameter maps over the myocardium (and regularise the optimisation), we solved at each iteration $\Delta P = 0$, where $P = d_{zone}$ and has its estimated value fixed for the barycentre of each zone (similarly as what is done in [KTTN+08]).

The regularisation parameter λ (the diffusion coefficient used in Δ) is estimated using the L-curve method, to find a good compromise between the data error and the rounding error [Han99]. The DT error norm (residual) vs. parameter d norm (solution) is computed for a range of λ and plotted as a loglog plot, shown in Fig. 3.5. The optimal λ is estimated to be 1.0

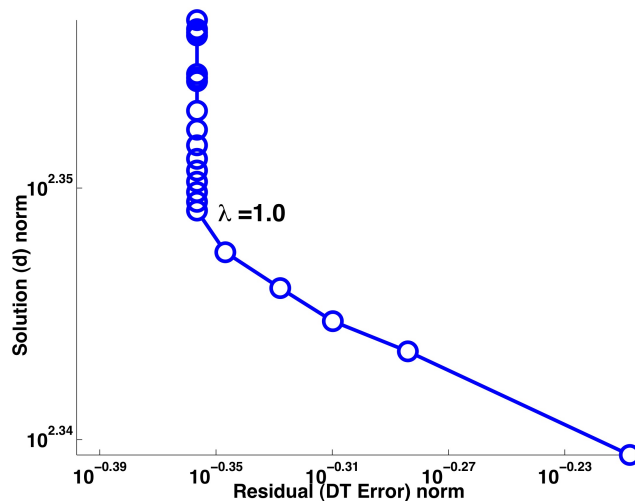


Figure 3.5: L-curve estimated from the model simulations, for a range of regularisation parameters, marked as circles

4.3 Personalisation of Action Potential Duration

APD for a single heart cycle is defined by the model as

$$APD_{max} = \tau_{close} \ln \left(\frac{1}{h_{min}} \right) \text{ where } h_{min} = 4 \left(\frac{\tau_{in}}{\tau_{out}} \right) \quad (3.9)$$

Here we again have one feature dependent on three parameters. We chose to estimate τ_{close} , while keeping the others to their standard values because the Table 3.1 shows that τ_{close} has no sensitivity to DT, whereas τ_{in} and τ_{out} do have. Thus estimation of τ_{close} does not affect the adjustment of CV done before. The defined relationship (Eq 3.9) remains valid also in 3D thus allowing us to directly estimate τ_{close} locally at each vertex without model simulations. The relationship is given as

$$\forall i \in S : \tau_{close}^i = APD_i^{msd} \{ \ln (\tau_{out}/4\tau_{in}) \}^{-1} \quad (3.10)$$

where APD_i^{msd} is the measured APD for the vertex i belonging to the surface S having data.

To propagate the estimated parameter values from the epicardium to the whole myocardium, we diffused them spatially, as explained in the previous section [KTTN+08].

4.4 Case 2: Personalisation Using Multiple PF

This case was applied to the second heart having multiple Basic Cycle Lengths (BCL). In this case, we estimated all parameters of the model in the following two steps: first we estimated the parameter set $\theta = [\tau_{in} \tau_{out} \tau_{open} \tau_{close} d]$ using APD & CV restitution features jointly. Then we refined the adjustment of d using the isochrones for the largest BCL.

4.5 Personalisation of Restitution curves

Restitution defines the dependency of the next cycle APD (resp. CV) on the previous cycle Diastolic Interval (DI). For a constant PF f , the steady-state BCL remains constant : $BCL = 1/f = APD + DI$ and thus $APD - DI$ relationship remains constant. In order to observe and extract the macroscopic restitution, we need to have the heart optically imaged for multiple pacing frequencies, thus resulting in multiple BCL and multiple $APD - DI$ pairs for a spatial point (here directly on optical data pixels, not mesh vertices). A dynamic pacing protocol [CTSG04] was used: the heart was paced with a given PF until it reaches a steady-state APD, and then the $APD - DI$ pairs were measured. APD restitution curve for MS model is analytically derived [MS03] as

$$f(DI) = APD = \tau_{close} \ln \left(\frac{h(DI)}{h_{min}} \right) \quad (3.11)$$

where $h(DI) = 1 - (1 - h_{\min}) e^{-DI/\tau_{\text{open}}}$. Similarly also CV restitution curve is derived [CTSG04] as:

$$g(DI) = \left(\frac{1}{4}(1 + \sqrt{1 - h_{\min}/h(DI)}) - \frac{1}{2}(1 - \sqrt{1 - h_{\min}/h(DI)}) \sqrt{\frac{2dh(DI)}{\tau_{\text{in}}}} \right) \quad (3.12)$$

with $g(DI) = CV$ as the next cycle CV. Parameter d in Eq 3.12 has units as cm^2/ms [Cai08], which was then converted to s^{-1} with division by $0.1l^2$, where l is the maximum length of the heart domain in m . From Eq 3.11 & Eq 3.12, we can observe parameter ratio (h_{\min}) controlling both APD & CV restitution. This shows a coupling between both restitutions. Thus we chose to estimate the parameters for CV restitution (h_{\min} , τ_{in} , d) and APD restitution (h_{\min} , τ_{open} , τ_{close}) in a joint manner, by having a cost function C_r which minimises the error on both restitution curves and is given as, $\forall i \in D$:

$$\min_{\theta} \sum_{j=1}^N ((f(DI^{i,j}, \theta^i) - APD^{i,j})^2 + (g(DI^{i,j}, \theta^i) - CV^{i,j})^2) \quad (3.13)$$

with pixel i in the optical data D having measures, N as total number of frequency datasets, $f(DI^{i,j}, \theta)$ corresponds to Eq 3.11, $g(DI^{i,j}, \theta)$ corresponds to Eq 3.12 and $\theta^i = [\tau_{\text{close}}, h_{\min}, \tau_{\text{open}}, \tau_{\text{in}}, d]$ as the estimated parameter vector. θ^i was estimated locally for each pixel i having measures for at least three different frequencies. Then a mean value for each AHA zone was computed and set to its barycentre and diffused to have smooth parameter maps. The parameter optimisation method used here is a bound-constrained active set algorithm, which uses a sequential quadratic programming method [FP63]. The bound set for parameters h_{\min} , τ_{open} , τ_{in} and τ_{close} was $[0,1]$ (s), and for d was $[0.1,5]$ (s^{-1}). Parameter τ_{out} could be estimated from estimated h_{\min} & τ_{in} using Eq 3.9.

4.6 Personalisation of DT Isochrones

In this step 2, we refined the estimation of parameter d for a single cycle at the lowest PF, since it represents the asymptotic value of CV restitution curve. This was done in order to have d take into account changes in CV due to the wavefront curvature on the volumetric mesh. Step 2 of this case was achieved similarly to step 1 in case 1, see Section 4.2.

5 Results

The two datasets used here were healthy *ex vivo* hearts. Before personalisation of the model, the simulations were computed with parameters at their standard values. Detailed quantitative results are presented in Table 3.2, we only describe here one case of each personalisation.

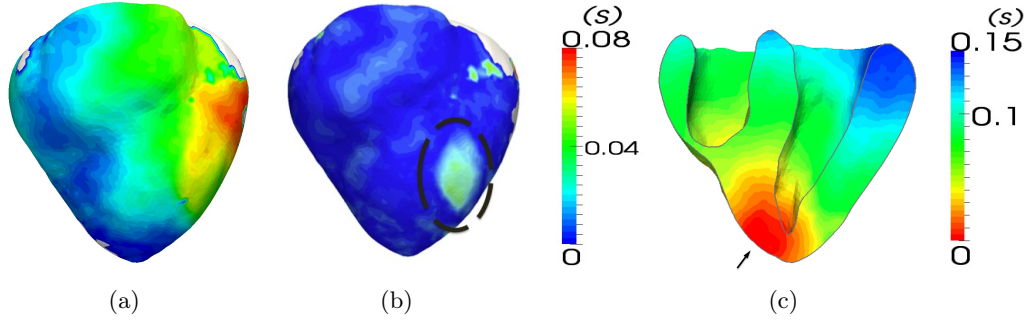


Figure 3.6: DT error maps after calibration (left) and after iterative adjustment (middle) steps of personalisation in case 1 for LV-Epi-r pacing (black arrow). Black ellipse highlights the error in the low conductivity region. (Right) simulated personalised volumetric DT isochrones[†].

5.1 DT & APD error maps

For the dataset 1B-LV-Epi-r, before personalisation, the mean absolute error on the DT was 100 ms ($\approx 58\%$ of depolarisation duration $\approx 170\text{ ms}$), see Fig 3.6. It had first reduced to 59 ms ($\approx 30\%$) using the calibration step for the d^{global} estimation (Fig. 3.6a), and then to 5 ms ($\approx 2\%$) with iterative adjustment (Fig. 3.6b). Around 25 direct model simulations were performed for the iterative adjustment step.

The resulting parameter map (Fig 3.9.a) shows the capture of the low conductivity region (black ellipse) observed in the dataset (Fig 3.3). With the personalisation of parameter τ_{close} , APD errors were reduced from 77 ms ($\approx 25\%$ of APD $\approx 300\text{ms}$) before personalisation to 9 ms ($\approx 3\%$), for Dataset 1C-LV-Endo. Fig 3.6c also shows the simulated volumetric DT isochrones after personalisation.

5.2 Fitting of restitution curves

Personalisation case 2 was applied to dataset 2. The estimated parameters were τ_{open} , τ_{close} , τ_{in} , τ_{out} and d using multiple pacing frequencies (Fig 3.7).

The absolute mean square error C_r (Eq 3.13) was 20.35 before personalisation, and reduced to 0.54 after personalisation, which implies a good fit of the both APD and CV restitution curves to the data (Fig 3.8). Nonetheless as the parameters were optimised by minimising the joint error on APD and CV restitution, we can still observe some CV restitution misfits for few pixels at low frequency.

The zonal parameters estimated showed clear differences in values of τ_{in} & τ_{out} for LV and RV. τ_{close} shows lower values at the pacing location and RV zones, thus showing APD heterogeneity between the LV and RV. τ_{open} , a parameter controlling the APD restitution slope, shows lower values (flat slope) near the pacing and basal

[†] A video on model simulation without/with personalisation for 1B-LV-Epi-r pacing is available as supplementary material at <http://ieeexplore.ieee.org>, snapshots are shown in Appendix Table D.1

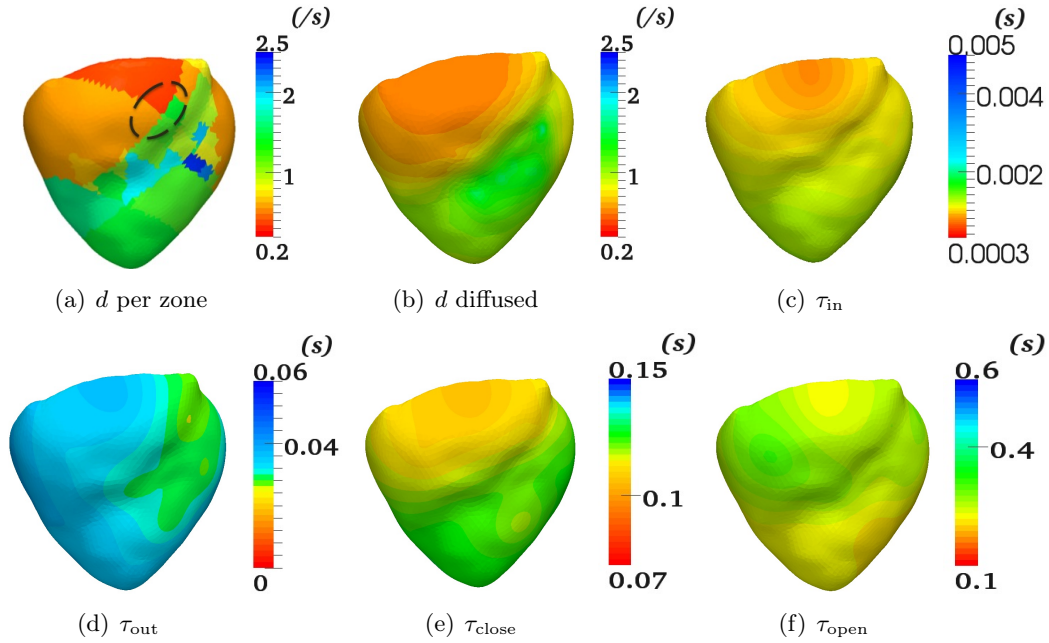


Figure 3.7: Estimated parameter values on the bi-ventricular mesh using personalisation case 2. Black ellipse represent capture of low conductivity regions (Fig 3.3(2A-0.5Hz CV maps)).

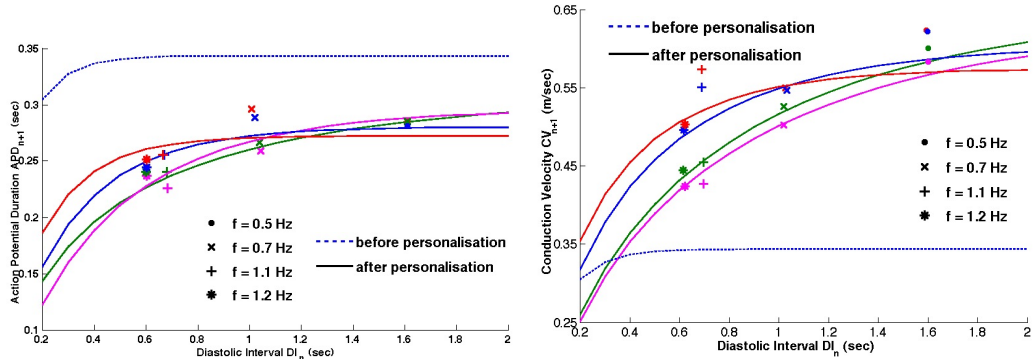


Figure 3.8: Fitting of model APD (top) and CV (bottom) restitution curves to the data points extracted from dataset 2 optical data. Red, Blue, Green and Magenta colours each represent a data point.

regions compared to the remaining epicardium. The parameters depicting the tissue conductivity from the diffusion term (d) and reaction term (τ_{in}), were also able to locate the low conductivity area observed in the dataset 2 (see black ellipse in Fig 3.3).

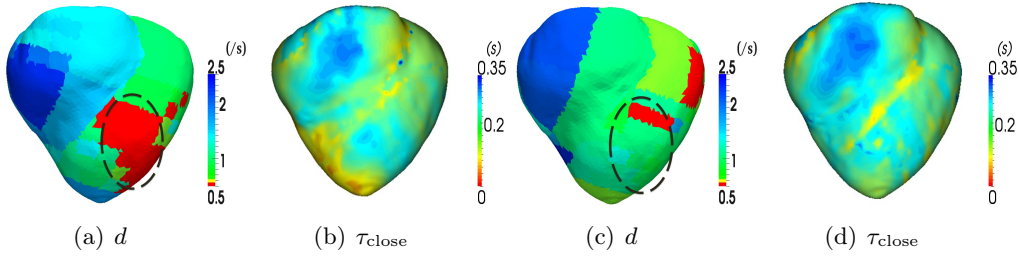


Figure 3.9: Parameter maps for LV-Endo (first two columns) and LV-Epi-r (following two columns) pacing locations. Estimated d values per zone after personalisation case 1 (first column) both capture the low conductivity region (black ellipse). The second column is the estimated τ_{close} in both cases.

5.3 Robustness to Pacing Location

We personalised the model with two different pacing scenarios for the same heart: LV epicardium (right side) and LV endocardium. As the personalisation is performed on the same heart at the same pacing frequency, we expect similar intrinsic parameters. Fig 3.9 and Table 3.2 show qualitative and quantitative comparison of the estimated parameter d and τ_{close} for both pacing locations. We can observe that the parameter values were mostly similar for both pacing locations, with the same spatial distribution and RV / LV differentiation. The low conductivity area was more basal for endocardial pacing as probably the fast conduction system is recruited. The locally estimated parameter τ_{close} was very similar for both pacing locations. This analysis does confirm the low sensitivity of the estimated parameter values to different pacing locations. Using Epi- & Endocardial pacing locations for such analysis also tests the capture of transmural wave propagation, when the dataset used to personalise is only epicardial surface data.

5.4 Evaluation of Volumetric Predictions

We evaluated volumetric predictions of the MS model for different pacing scenarios, using the parameters estimated from the personalisation using endocardial pacing (LV-Endo). The validation of the prediction was done in terms of the DT and APD error qualitatively (see Fig 3.10) and quantitatively (see Table 3.2).

Even if the predicted isochrones produce higher errors than those produced for LV-Endo, it was still small compared to the errors obtained with standard parameters (less than 10%).

These predictions also allow to evaluate the capture of the transmural wave propagation by comparing the predicted epicardial isochrones with the measured ones. The behaviour of the model reproduces quite well the observations.

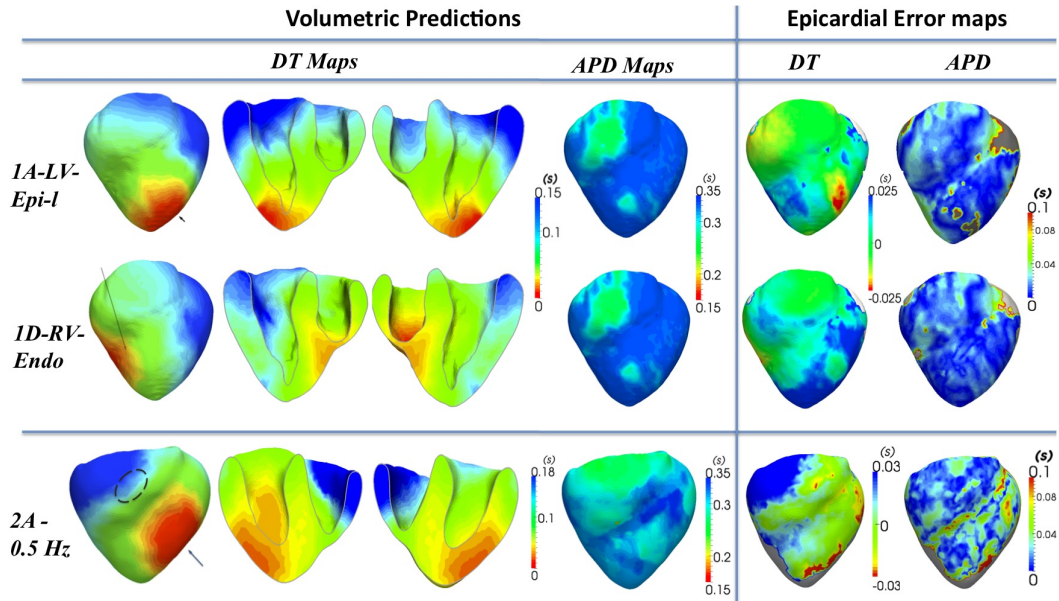


Figure 3.10: Volumetric predictions using the model personalised with LV-Endo pacing for dataset 1 and with multiple PF and LV-Epi pacing for dataset 2. First row: pacing location 1A-LV-Epi-l. Second row: 1D-RV-Endo (arrows). Third row: LV-Epi, PF: 0.5Hz. First three columns: predicted volumetric DT maps, second: predicted APD maps. Please refer to Fig 3.3 for experimental epicardial values. Third column: DT Error maps of prediction against experimental epicardial data, fourth: APD error maps[‡].

6 Discussion

Robustness to Pacing Location

Personalisation case 1 was able to recover approximately the same model parameters irrespective of the pacing scenarios. The results look qualitatively and quantitatively similar (Fig 3.6, Fig 3.9 & Table 3.2), implying low sensitivity of the personalisation framework to pacing locations. The personalisation framework was probably able to sufficiently capture the global minima of the cost function, as local minima are highly unlikely to be the same for different pacing scenarios. This also shows that the model parameters actually do not vary with different pacing locations for a single pacing frequency. However the pacing locations considered here were all near the apical regions of the endo- and epicardium. In order to have more evaluation on its robustness, we need to perform personalisations with pacing locations in the mid and basal regions, as well as with data having normal sinus rhythm conduction pathway. The fast conduction pathways can make the adjustment from epicardial data difficult because the depolarisation wave can reach the epicardial surface quite simultaneously.

Pacing Location	Parameter $d \pm \sigma$ (s^{-1})		DT Error $\Delta \pm \sigma$ (ms)	Parameter $\tau_{close} \pm \sigma \times 10^{-4}$ (ms)		APD Error $\Delta \pm \sigma$ (ms)
	LV	RV		LV	RV	
LV-Endo	0.95 ± 0.03	1.36 ± 0.16	4.22 ± 6.75	0.22 ± 1.25	0.20 ± 4.90	4.98 ± 8.89
LV-Epi-r	0.96 ± 0.03	1.38 ± 0.11	2.54 ± 5.12	0.22 ± 3.04	0.21 ± 6.81	4.73 ± 5.57
LV-Epi-l	-	-	12.16 ± 14.57	-	-	8.62 ± 9.21
RV-Endo	-	-	17.21 ± 18.15	-	-	7.32 ± 8.97

Table 3.2: Parameters and errors (Δ : mean, σ : standard deviation) for case 1 personalisation (1st row) and prediction (2nd row).

Estimation of Restitution Properties

Personalisation case 2 was able to estimate all model parameters including APD and CV restitutions and can predict isochrones similar to the measured data for multiple frequencies. Restitution properties of the cardiac tissue play a crucial role in the cause of arrhythmias, hence were required to be estimated. However, in the described case 2, we estimated the parameter vector θ and then used the estimated d as an initial guess in step 2, to refine the d estimation with DT isochrones. This second step can potentially modify the CV restitution adjustments done previously in step 1. Thus the future work would be to adjust the parameters using CV restitution and DT isochrones simultaneously.

Transmural Parameters & Volumetric Prediction

We estimated the model parameters for a volumetric mesh based on observations on the epicardial surface. But ideally, we should check our estimated parameters against measured transmural recordings. This could not be performed in this case on the *ex vivo* heart as it damages the heart muscle, making retrieval of the fibre orientation information using DT-MRI not possible. An other option is to acquire simultaneous endocardial and epicardial data. This could be possible with catheter based mapping systems used in the clinics.

Performance

On a 2.16 GHz, dual core, 2.0 GB Intel Centrino Duo PC, the computational time of one time step for the MS model on 3D bi-ventricular mesh (≈ 247250 tetrahedra) for semi-implicit MCNAB scheme was ≈ 1 s, with $\delta t = 0.1$ ms and mean edge length $\delta x = 1.5$ mm. Parameter estimation of d using DT isochrones involved $20 \sim 30$ iterations, using simulations until the depolarisation of whole ventricles ≈ 150 ms. This needs a computational time of $\approx 1500s \times n$, where n is the number of iterations. On the other hand, parameter estimation using other features such as APD and restitution curves does not involve model simulations, but is solved using explicit

[‡]Videos of model predictions for 1A-LV-Epi-l & 1D-RV-Endo pacings are available as supplementary material at <http://ieeexplore.ieee.org>, snapshots are shown in Appendix Table D.2

analytical formulae and requires inexpensive amount of time ($\approx 1min$). Thus the most time consuming part of both personalisation frameworks is the parameter estimation of d . This is due to the direct simulations of the biophysical MS model, which has a fast upstroke ($(du/dt)_{max}$), thus requires very fine spatial and temporal resolutions.

Study Limitations & Error sources

On the data processing part, one of the limitations of this study was the lack of correction of the optical signals, which are quite complex and contain information from the sub-epicardial layer [HMV+05, BRE+06]. Such corrections would give more reliable data and could improve the correspondence between the simulations and experiment, as the simulations are volumetric. However, we don't use the optical signal value as such, but we only extract depolarisation and repolarisation time-points from the data. This was extracted after filtering the data at each pixel, to constitute the DT and APD maps. We most probably get some smoothing of these maps due to the sub-epicardial layers, but we don't expect these to create major changes in the presented results as the induced error is probably small with respect to all the different error sources listed below and the resolution used.

The error sources in personalisation and prediction include: (i) Less accurate predictive power of the model due to its low complexity, (ii) Lack of successful reproducibility of transmural parameter variation due to the usage of only epicardial data. We hypothesise that these juvenile pigs do not have transmural variations, (iii) Insufficiency in modelling the actual Purkinje system, and its potential retrograde activation. However, there was no evidence from the presented data, (iv) Insufficiency of domain decomposition to reproduce accurately the spatial variation of the parameters.

Application to Pathological Cases & Clinical Data

This work can be applied to clinical data by replacing the surface optical data with surface epi- or endocardial electro-anatomical mapping of the patient. Most of the challenge lies in the reliable extraction of features such as DT and RT from sparse and noisy patient data consisting of extracellular potentials. Also the *in-vivo* acquisition of fibre orientations is challenging due to the heart motion. Nevertheless the personalisation framework can be performed using the rule-based fibre orientation, and still provides promising results [RCS+10]. Personalisation case 1 would prove to be more efficient for predictions at a constant pacing frequency as it is the case in Cardiac Resynchronisation Therapy (CRT). On the contrary, case 2 would be more preferred for arrhythmias as it can reveal more features such as APD and CV restitution properties for healthy, scars and grey zones. Also, an evaluation on the level of complexity required for simulating arrhythmias in pathological cases is needed. However, additional complexity has a strong impact on the tractability [GNK05] and on the parameters identifiability [FN09].

7 Conclusion

We presented a novel method for estimating *volumetric* model parameters from *surface* data with single and multiple pacing frequencies. We extracted features such as CV, APD, CV and APD restitution macroscopically from the measured cardiac data and used them to personalise the model. We estimated all the model parameters making the model heart-specific. We evaluated the sensitivity of the personalisation to different epi- and endocardial pacing scenarios and the results show a robust behaviour of the framework to pacing location. Then we also tested the volumetric prediction ability of the model for different pacing scenarios and showed promising results.

Building Personalised EP Models using *in vivo* Clinical Data (Non-Contact Mapping)

Contents

1	Introduction	52
2	Clinical Context	54
2.1	Depolarisation and Repolarisation times extraction	55
3	Cardiac Electrophysiology Models	56
3.1	Eikonal Model (EK Model)	56
3.2	Simplified Biophysical Model (MS Model)	57
4	Coupled Personalisation Method	58
4.1	Apparent Conductivity Parameter Estimation	58
4.2	Coupling of EK and MS Model Parameters	59
4.3	Parameter Estimation for APD Restitution	60
5	Results	62
5.1	Parameter Estimation	62
5.2	Assessment of Heterogeneity Maps	64
6	Discussion	64
6.1	Data Limitations	64
6.2	Model Simplifications	65
6.3	Conclusion	66

Based on:

[RCS⁺11] J. Relan, P. Chinchapatnam, M. Sermesant, K. Rhode, M. Ginks, H. Delingette, C. A. Rinaldi, R. Razavi, and N. Ayache. Coupled personalization of cardiac electrophysiology models for prediction of ischaemic ventricular tachycardia. *Journal of the Royal Society Interface Focus*, 1(3):396–407, 2011.

Additional material available in [RCS⁺10]

*In order to translate the important progress in cardiac electrophysiology modelling of the last decades into clinical applications, there is a requirement to make macroscopic models that can be used for the planning and performance of the clinical procedures. This requires model personalisation i.e. estimation of patient-specific model parameters and computations compatible with clinical constraints. Simplified macroscopic models can allow a rapid estimation of the tissue conductivity, but are often unreliable to predict arrhythmias. Conversely, complex biophysical models are more complete and have mechanisms of arrhythmogenesis and arrhythmia-sustainability, but are computationally expensive and their predictions at the organ scale still have to be validated. We present a coupled personalisation framework which combines the power of the two kinds of models while keeping the computational complexity tractable. A simple Eikonal (EK) model is used to estimate the conductivity parameters, which are then used to set the parameters of a biophysical model, the Mitchell-Schaeffer (MS) model. Additional parameters related to Action Potential Duration (APD) restitution curves for the tissue are further estimated for the MS model. This framework is applied to a clinical dataset derived from a hybrid XMR imaging and non-contact mapping procedure on a patient with heart failure. This personalised MS Model will then be used to perform an *in silico* simulation of a Ventricular Tachycardia (VT) stimulation protocol to predict the induction of VT, as detailed in Chapter 6. This proof of concept opens up possibilities of using VT induction modelling in order to both assess the risk of VT for a given patient and also to plan a potential subsequent radio-frequency ablation strategy to treat VT.*

1 Introduction

Cardiac arrhythmias including ventricular tachycardia are increasingly being treated by Radio-Frequency (RF) ablation. These procedures can be very effective but still have unsatisfactory success rates widely ranging from 50–90%, with a 20–40% late recurrence rate, due to a lack of clinical consensus on the optimum RF ablation strategy [ASAG09]. There is a need for substantial guidance in locating the optimum ablation strategy [SKS+93].

This guidance could be provided by personalised *in silico* cardiac electrophysiology models, as such models may allow different ablation strategies to be tested. A personalised model incorporates estimation of patient-specific parameters which best fit the clinical data. Such a step is necessary to reveal hidden properties of the tissue that are used to predict the behaviour under different pacing conditions.

There is a large variety of cardiac electrophysiology models for myocyte action potential developed at cellular and sub-cellular scales [FC08, LR91, NVKN98, TTNNP04, FNC+11]. Cardiac tissue and whole-heart electrophysiological computations of these models are based on the principles of reaction-diffusion systems [Sac04, CBC+11]. According to the reaction term computation, these models can be broadly categorised as Biophysical Models (BM), Phenomenological Models (PM) and Generic Models (GM). BM [NVKN98, TTNNP04] model ionic currents

and are the most complete and complex but are less suitable for parameter estimation from clinical data due to a high computational cost and to the lack of observability of their parameters. PM [BWZ⁺02, BOCF08] are based on PDEs and are of intermediate complexity level and less computationally expensive. GM [Fit61, RV96] represent simplified action potentials and are the least complex. Simple Eikonal Models (EM) [KKS09, CFGR90, SKD⁺07] model the action potential propagation in the cardiac tissue without modelling the action potential itself. They can be very fast to compute [CRG⁺08], but less reliable in arrhythmia predictions due to the complexity of both the refractoriness and the curvature of the wavefront.

Computational modelling of cardiac arrhythmogenesis and arrhythmia maintenance using such models has made a significant contribution to the understanding of the underlying mechanisms [CW91, WFE⁺01, PK95, JG96, CF04, CR95]. These studies have shown a host of factors involved in the onset of arrhythmia with wave fragmentation and spiral wave breakups, which include realistic ventricular geometry [TT09], heterogeneity in repolarisation [KSGH08] and APD restitution [YFRM05, ART07] and CV restitution [BG02]. A combined clinical study and synthetic modelling of APD restitution was shown in [NBS⁺06]. In this chapter, we study these properties for a clinical dataset and evaluate its role in ischemic Ventricular Tachycardia (VT) induction.

To introduce models directly into clinical practice, the ideal requirements are low computational complexity, fast estimation of parameters (quick personalisation) and reliable predictions. These attributes cannot be found in one single model, thus here we present a novel approach, wherein we combine two models to obtain these attributes and apply them to a clinical dataset. We use a coupled personalisation framework, which is fast and combines the benefits of an Eikonal (EK) model [SCMV⁺05] with those of a simplified biophysical model, the Mitchell-Schaeffer (MS) model [MS03]. The fast 3D EK model is used to estimate the tissue conductivity parameter over the ventricles derived from non-contact mapping of the endocardial surface potential, using an adaptive iterative algorithm. This is then used to set the conductivity parameter of the 3D MS model. Additional parameters related to APD restitution properties of the tissue are then estimated locally using directly the 3D MS model and the measured endocardial surface potential.

This framework is applied to a clinical dataset from a patient with heart failure and myocardial scar on MRI scanning using electrophysiological data from a non-contact mapping study performed in a hybrid X-ray/magnetic resonance (XMR) suite [RSB⁺05]. The ventricles were mapped with a statistical atlas for cardiac fibres [PSP⁺07](Fig. 4.2). The resulting personalised 3D MS model is then used to simulate a clinical VT-Stimulation (VT-Stim) procedure to show a potential application of VT induction modelling. Fig. 4.1 shows the framework of the coupled personalisation method and VT induction modelling, used.

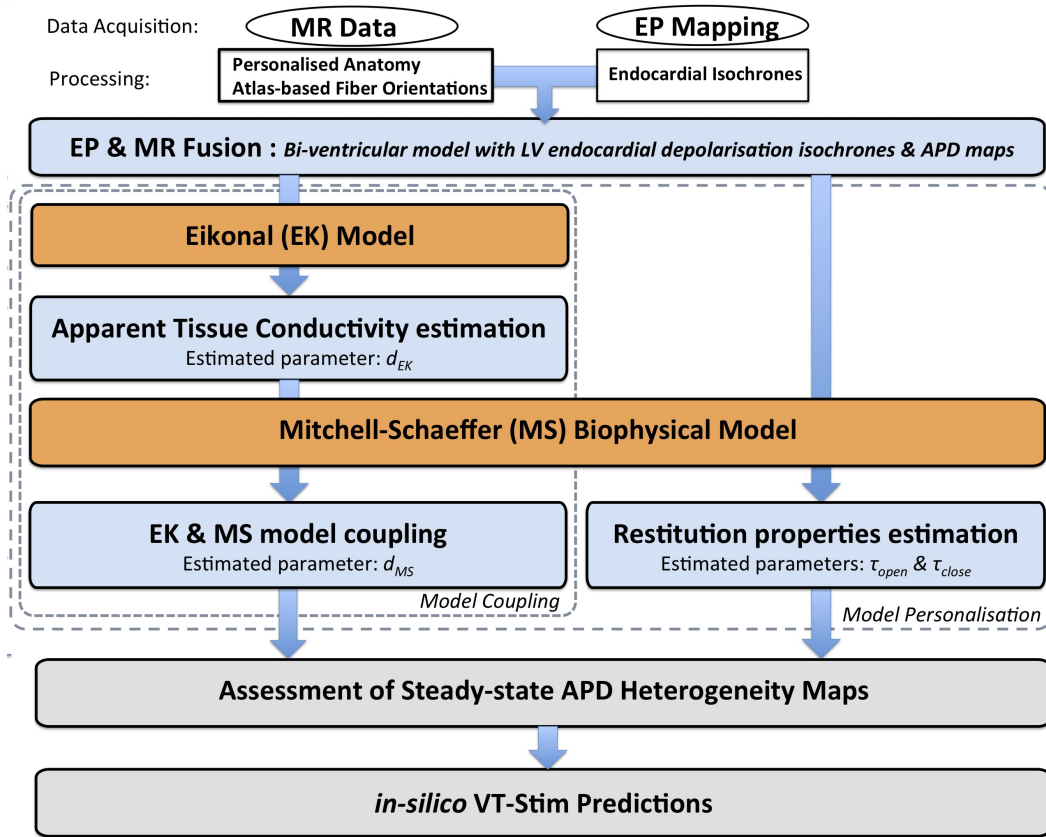


Figure 4.1: Flowchart describing the outline of this chapter.

2 Clinical Context

In order to evaluate the inducibility of VT in patients, the clinical procedure involves stimulation with an EP catheter usually in the RV apex at different cycle lengths. This type of protocol is used to test if re-entrant VT can be induced by such pacing in patients at risk of VT. Such studies may be useful in predicting the risk of VT for an individual patient but provide limited information on which to base a potential ablation strategy of re-entrant VT circuits.

Our aim is to create a personalised electrophysiological model of a given patient to which a virtual VT stimulation procedure can be applied. Moreover, a virtual RF ablation procedure can then be applied to the model in order to test potential ablation strategies.

In order to validate this approach, we have used an extensive clinical dataset, derived from mapping of the LV endocardium. Such mapping is not routinely performed for a VT-Stim procedure, however it is sometimes used to guide RF ablation. This clinical dataset was obtained from an electrophysiology study performed in a hybrid X-ray/MR environment. The electrical measurements obtained using an En-

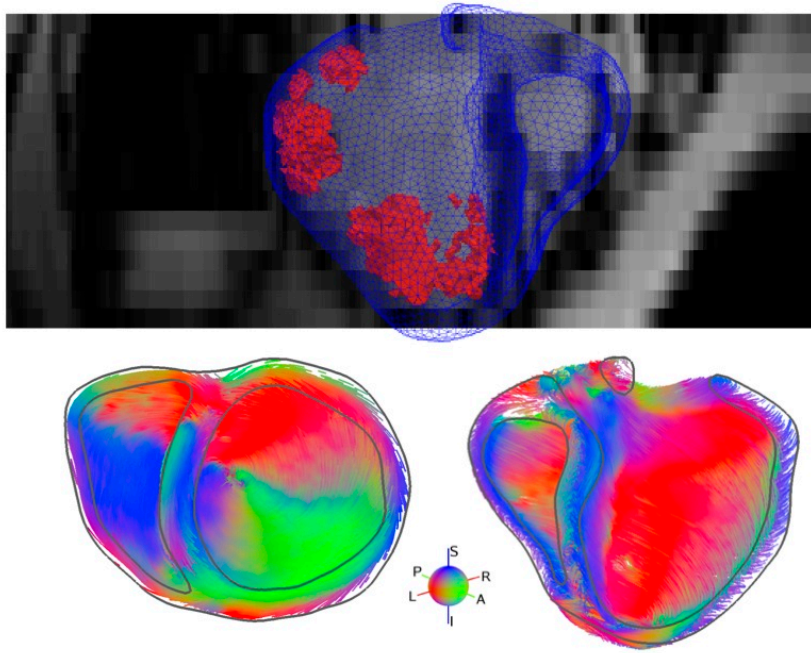


Figure 4.2: Top: MR derived segmented mesh with scars (in red). Bottom: fibre orientations based on a statistical atlas.

site system (St Jude Medical, MN, US) (see Fig. 2.7) were registered to the patient anatomy using XMR registration [RSB⁺05] (Fig. 4.4b).

2.1 Depolarisation and Repolarisation times extraction

The electrical data was collected with high pass filter settings for prominent QRS detection and with low pass filter for T-Wave detection.

The depolarisation times were detected within the QRS window set from surface ECG (Fig 4.3a) and were derived from the zero crossings of the Laplacian of the measured unipolar electrograms V (Fig. 4.3b & 4.5a). The surface Laplacian of electrograms gave reasonable results even in the case of multiple deflections and also allows detection of local activation without interference from far-field activity [CWSdG⁺00].

The repolarisation times were detected within the ST window in surface ECG (Fig 4.3a) and were derived using the "alternative method" as compared to the standard wyatt method, because (i) most of the positive T-wave electrograms had an indiscernible steep upstroke for repolarisation time detection with wyatt method, (ii) a closer correlation was obtained between ARI and MAP duration with alternative method, as discussed in [YFRM05] and (iii) difference in APD extraction from the two methods had only a minimal influence on the restitution slopes and spatial distributions [NBS⁺06]. The measured T-wave polarity maps had positive T-waves for early repolarising sites and negative for late as in agreement to [PVOC09]

(Fig. 4.4).

The alternative method has repolarisation times derived from dV/dt_{max} for the negative T-wave, at the dV/dt_{min} for the positive T-wave, and the mean time between dV/dt_{max} and dV/dt_{min} for the biphasic T-waves (Fig. 4.3c, 4.4, 4.4c & 4.5c).

The data was collected during intrinsic sinus rhythm and atrial pacing mode at 100 beats per minute (bpm), see Fig. 4.4c & 4.4d. Myocardial scar was segmented manually from the Delayed Enhancement MR image.

The patient was a sixty year old woman with heart failure and NYHA class III symptoms. The patient had a dilated cardiomyopathy with sub-critical disease on coronary angiography although cardiac MRI showed subendocardial posterolateral scar in the left ventricle. The left ventricular ejection fraction was 25% on maximal tolerated heart failure medication. The surface ECG demonstrated significant conduction disease with left bundle branch block (LBBB) and a QRS duration of 154 ms (normal QRS is less than 120 ms). Echocardiography, including Tissue Doppler, confirmed significant mechanical dyssynchrony in keeping with the ECG findings.

This patient was selected for cardiac resynchronisation therapy (CRT). When implanting a CRT device, there is a choice between a standard device, or one also integrating a defibrillator. Therefore, evaluating the risks of VT in such CRT patients is important.

3 Cardiac Electrophysiology Models

3.1 Eikonal Model (EK Model)

The EK model simulates the propagation of the depolarization wave in cardiac tissue, ignoring repolarisation phase. The EK model is governed by the eikonal-diffusion (ED) equation [THP02, CFGR90] and is solved using the Fast Marching Method (FMM). It can be written as

$$c_0 \sqrt{d_{EK}} \left(\sqrt{\nabla T(x)^t \mathbf{M} \nabla T(x)} \right) - \nabla \cdot (d_{EK} \mathbf{M} \nabla T(x)) = \tau(x) \quad (4.1)$$

where the superscript t denotes transpose, c_0 is a dimensionless constant ($= 2.5$), and $\tau(x)$ is the cell membrane time constant ($= 0.003$ s). d_{EK} is the square of the tissue space constant along the fibre and is related to the specific conductivity of the tissue in the fibre direction, and has units of m^2 . The anisotropy is incorporated in the diffusion tensor $\mathbf{M} = \text{diag}(1, \rho, \rho)$, with ρ the anisotropy ratio between longitudinal and transverse diffusion. We use $\rho = 1/2.5^2$ in order to have Conduction Velocity (CV) 2.5 times faster in the fibre direction [KKS09]. The non-linear Eq 4.1 is solved using a fixed point iterative method combined with a very fast eikonal solver as explained in details in [SCMV⁺05, CRG⁺08].

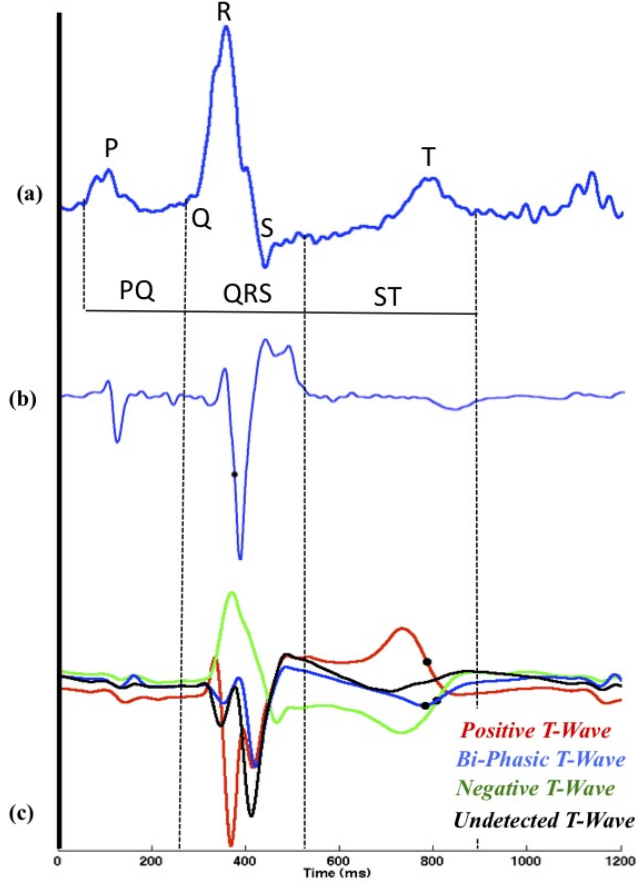


Figure 4.3: (a) Measured surface ECG I, with QRS window (for depolarisation time extraction) and ST window (for repolarisation time extraction). Ensite surface unipolar electrograms (b) with high-frequency band-pass filter for detection (black dots) of depolarisation times, and (c) with low-frequency band-pass filter for detection repolarisation times, from positive (red), negative (green) and biphasic (blue) T-waves. Few electrograms had indiscernible T-waves (black).

3.2 Simplified Biophysical Model (MS Model)

The MS model [MS03] is a 2-variable simplified biophysical model derived from the 3-variable Fenton Karma (FK) ionic model [FK98]. It models the transmembrane potential as the sum of a passive diffusive current and several active reactive currents including combination of all inward (primarily Na^+ & Ca^{2+}) and outward (primarily K^+) phenomenological ionic currents. The MS model is described by the following system of partial differential equations,

$$\begin{cases} \partial_t u = \text{div}(d_{MS} \mathbf{M} \nabla u) + \frac{z u^2 (1-u)}{\tau_{in}} - \frac{u}{\tau_{out}} + J_{stim}(t) \\ \partial_t z = \begin{cases} \frac{(1-z)}{\tau_{open}} & \text{if } u < u_{gate} \\ \frac{-z}{\tau_{close}} & \text{if } u > u_{gate} \end{cases} \end{cases} \quad (4.2)$$

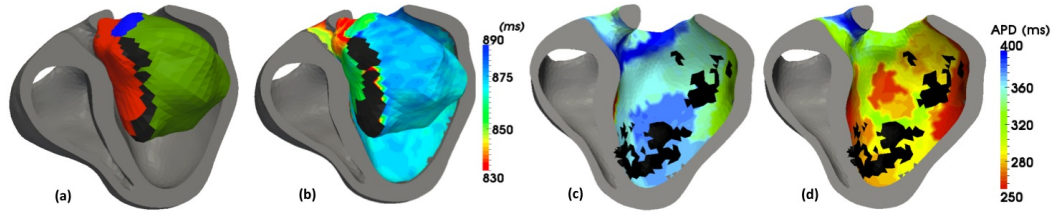


Figure 4.4: (a) T-Wave polarity map on EnSite LV surface, with positive (red), negative (green), bi-phasic (blue) and undetected (black) T-waves. (b) Repolarisation times projection from EnSite LV surface to MR LV endocardium after XMR registration. (Black: undetected repolarisation times). Steady-state APD values estimated and projected on the LV surface, for (c) baseline and (d) pacing in the atria (at 100 bpm). (Black represents scars)

where, u is a normalised transmembrane potential variable, and z is a gating variable which makes the currents gate open and close, thus depicting the depolarisation and repolarisation phase. $J_{in} = (zu^2(1-u))/\tau_{in}$ represents the the inward currents which raises the action potential voltage and $J_{out} = -u/\tau_{out}$ represents the outward currents that decreases the action potential voltage describing repolarisation. J_{stim} is the stimulation current, at the pacing location. The literature values for reaction term parameters are given in [MS03]. τ_{in} , τ_{out} , τ_{open} and τ_{close} has units of s . The diffusion term in the model is also controlled by the diffusion tensor \mathbf{M} . In the longitudinal direction of the fibre, this pseudo-conductivity is set to d_{MS} which is one of the parameters we adjust, and to $d_{MS}\cdot\rho$ in the transverse directions. d_{MS} has units of s^{-1} . The electrophysiology model is solved spatially using P1 Finite Element Method (FEM), and in time using an semi-implicit scheme as Modified Crank-Nicolson/Adams-Bashforth (MCNAB) scheme, which is evaluated in terms of accuracy, stability and computational time [RSD⁺09]. The parameter values and simulation details are given Table. C.1 & Table. C.2 in Appendix C.

Scars were modelled with zero conductivity in the ischemic zones. While the grey zones and the regions between scars (isthmus) had conductivity, APD RCs estimated from the data, as shown in Sec. 5.1

4 Coupled Personalisation Method

4.1 Apparent Conductivity Parameter Estimation

Cardiac tissue conductivity is a crucial feature for the detection of conduction pathologies. The Apparent Conductivity (AC) of the tissue can be measured by the parameter d_{EK} in the EK model.

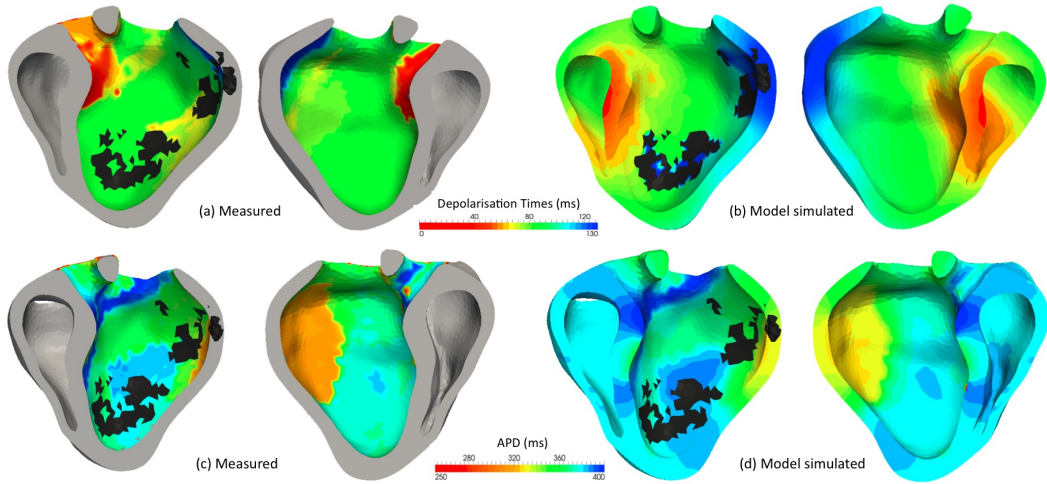


Figure 4.5: Upper row shows the comparison of the measured Depolarisation Time (DT) isochrones on the LV surface only with model simulated DT isochrones on the whole heart, lower row shows the same for measured (LV surface only) and model simulated (whole heart) APD maps. Measurements are for baseline.

LV Endocardial values AC is initially estimated on the endocardial surface as a global value using a simple bisection method which matches the average conduction velocity of the measured Depolarisation Time (DT) isochrones to the simulated ones. Using it as an initial guess, an adaptive multi-level domain decomposition algorithm is used, which minimises the mean-squared difference of the simulated and measured DT isochrones at each level using a Brent’s Optimisation Algorithm presented in [CRG⁺08]. Due to the absence of transmural electrical propagation information, we assume no variation across the left ventricle myocardium (excluding LV endocardium and scars) and hence we prescribe a single value for the myocardial tissue across the LV wall.

LV & RV Myocardial values The AC values for RV endocardium and RV myocardial mass are set at 5.0 mm^2 and 0.64 mm^2 (from literature [KKS09]). The LV myocardial AC value is estimated by one-dimensional minimisation of the following cost function (mean-squared difference of simulated and measured isochrones at endocardium + squared difference of simulated and measured QRS duration). The simulated QRS duration is calculated as the difference between the maximum and the minimum depolarisation times in the biventricular mesh and the measured QRS duration is estimated from the surface ECG.

4.2 Coupling of EK and MS Model Parameters

The AC parameter for EK model d_{EK} (Eq 4.1) is a scale for the diffusion speed of the depolarisation wavefront in the tissue. The model Conduction Velocity (CV) is

related to d_{EK} (Fig. 4.6) as,

$$c_{EK} = \frac{c_0 \sqrt{d_{EK}}}{\tau} \text{ in 1D \& } c_{EK} = \alpha_{EK} \sqrt{d_{EK}} + \beta_{EK} \text{ in 3D} \quad (4.3)$$

where the constants α_{EK} and β_{EK} are introduced to take into account the discretization errors (in particular of the curvature) in 3D.

The corresponding conductivity parameter for MS model, d_{MS} is also a scale for the wave diffusion speed in the tissue. The model CV here is related to d_{MS} (Fig. 4.6) as,

$$c_{MS} \propto \sqrt{\frac{d_{MS}}{\tau_{in}}} \text{ in 1D \& } c_{MS} = \alpha_{MS} \sqrt{d_{MS}} + \beta_{MS} \text{ in 3D} \quad (4.4)$$

where the constants α_{MS} and β_{MS} are introduced for the same reasons as of EK model, while τ_{in} is kept as a constant. The estimated AC parameter d_{EK} can then be used to estimate the parameter d_{MS} . The parameter d_{EK} gives model CV c_{EK} , which is similar to the actual measured data CV (c_{msd}) after the parameter estimation step. Thus to have MS model CV (c_{MS}) similar to the measured data, it has to be similar to EK model CV (c_{EK}). The constants α_{EK} and β_{EK} represent numerical curvature, diffusion and discretisation errors for EK model based on FMM. They are different from the constants α_{MS} and β_{MS} , which are diffusion and discretisation errors based on FEM. These constants are determined in 3D for the ventricular mesh. We performed several simulations with various d_{EK} and d_{MS} values and noted the corresponding c_{EK} and c_{MS} values. Then, we fit the analytical curves given in Eq 4.3 & 4.4 in least square sense and determine the constants. The constants estimated are $\alpha_{EK} = 802.25$, $\beta_{EK} = -268.54$, $\alpha_{MS} = 995.87$ and $\beta_{MS} = -554.38$. Thus from eq 4.3 & 4.4, we have $c_{EK} = 802.25\sqrt{d_{EK}} - 268.54$ and $c_{MS} = 995.87\sqrt{d_{MS}} - 554.38$. For a given CV, d_{MS} is slightly different from d_{EK} . This may be due to the fact that d has different units, as for EK model we model depolarisation time and for MS model we model transmembrane potential. However they both are scales for diffusion, thus such a coupling is performed. Then, the personalised d_{MS} values are computed from corresponding estimated d_{EK} values using 4.5 based on the condition, that $c_{msd} = CV = c_{EK} = c_{MS}$ after personalisation. Thus from eq 4.3 & 4.4, we have

$$d_{MS} = \left(\frac{\alpha_{EK} \sqrt{d_{EK}} + \beta_{EK} - \beta_{MS}}{\alpha_{MS}} \right)^2 \quad (4.5)$$

4.3 Parameter Estimation for APD Restitution

APD Restitution is an electrophysiological property of the cardiac tissue and defines the adaptation of APD as a function of the heart rate. It's slope has a heterogeneous spatial distribution, which can play a crucial role in arrhythmogenesis [CF04, NBS⁺06, CBC⁺11]. The APD Restitution Curve (RC) defines the

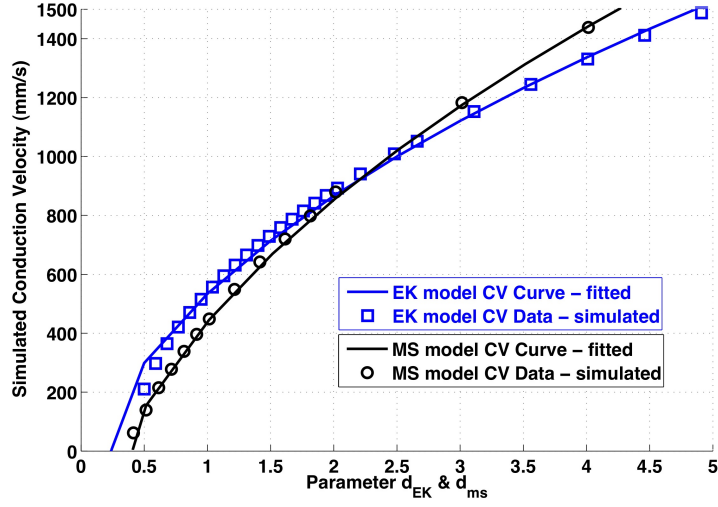


Figure 4.6: Parameter d_{EK} and d_{MS} relationship with simulated CV.

relationship between the next cycle APD and the Diastolic Interval (DI) of the previous cycle. The slope of these RCs is controlled by τ_{open} and depicts the APD heterogeneity present at multiple heart rates. APD RC for MS model is explicitly derived as [MS03],

$$APD_{n+1} = f(DI_n) = \tau_{close} \ln \left\{ \frac{1 - (1 - h_{min})e^{\frac{-DI_n}{\tau_{open}}}}{h_{min}} \right\} \quad (4.6)$$

where $h_{min} = 4(\tau_{in}/\tau_{out})$ and n is the cycle number. The maximum value of APD is also explicitly derived as,

$$g = APD_{max} = \tau_{close} \ln \left(\frac{1}{h_{min}} \right) \quad (4.7)$$

LV Endocardial values We had recordings for the paced mode with 100 bpm and a sinus rhythm rate (baseline). Therefore, for the estimation of the RC slope from APD-DI values at two rates, we assume that APD_{max} (asymptotic value of APD RC) should be approximately equal to the normal sinus rhythm APD, and the slope value is adjusted with paced mode APD. From eq 4.6 & eq 4.7, we can observe that τ_{close} and h_{min} control both APD RC and APD_{max} , hence we estimate the parameters minimising the error on them jointly. The cost function minimised is,

$$\min_{\theta} \sum_{j=1}^N ((f(DI_{msd}^{i,j}, \theta^i) - APD_{msd}^{i,j})^2 + (g(\theta^i) - APD_{SR_{msd}}^{i,j})^2) \quad (4.8)$$

with N as total number of pacing rates, i as the vertex having data (LV surface only), $\theta = [\tau_{close}, \tau_{open}]$, $APD_{SR_{msd}}$ as measured sinus rhythm APD and DI_{msd}

measured from the data as $DI_{msd} = 1/f - APD_{msd}$, where f is the heart rate (in Hz).

Only APD restitution is estimated as we only have two pacing frequencies, but additional data would allow to also estimate CV restitution, as demonstrated on experimental data in [RPD⁺11, RPD⁺10]. Parameter h_{min} is not estimated here but kept to the literature value [MS03] as it also controls the CV unlike τ_{close} & τ_{open} , thus disturbing the CV adjustments done before. The parameter optimisation method used here is a non-linear constrained Active-Set Algorithm, with constraints on τ_{close} & τ_{open} to be in the range of literature values [MS03]. Fig. 4.7c shows the fit of RC to data.

Minimum DI can also be computed explicitly from the estimated parameter values (Fig. 4.7c) as described in [MS03],

$$DI_{min} = \tau_{open} \ln \left(\frac{1 - h_{min}}{1 - h_{thr}} \right) \quad (4.9)$$

where,

$$h_{thr} = \frac{h_{min}}{4v_{stim}(1 - v_{stim})} \text{ with } v_{stim} \approx \int J_{stim}(t)dt$$

with J_{stim} as defined in eq 4.2.

LV & RV Myocardial values For RV, we fix one value measured from the QT interval given through the surface ECG. To have a smooth gradation of APD restitution from epicardium to endocardium, we diffuse the τ_{close} & τ_{open} values spatially in the LV myocardium from endocardium to epicardium as in [KTTN⁺08] (Fig. 4.7d).

Steady-state APDs for a pacing frequency f could then be estimated from the intersection of the line $DI_n = 1/f - APD_{n+1}$ with the personalised RCs (Fig. 4.8(a)). The model personalisation times are given in Table. C.2 in Appendix B.

5 Results

5.1 Parameter Estimation

The AC parameters estimated using the EK model, see Fig. 4.7a, show high conduction areas on parts of the endocardium, potentially depicting the Purkinje network extremities, and a conduction block near the scar. The coupled MS model conductivity parameters were then estimated from this AC map. The mean absolute error on simulated depolarisation times after personalisation was 7.1ms for the EK model and 18.5ms for the MS model ($\approx 10 - 14\%$ of depolarisation duration 131ms), see Fig. 4.5 & 4.8b. The mean absolute error on APD was 8.71ms ($\approx 2\%$ of APD 300ms), showing a good fit as well, see Fig. 4.5 & 4.8c.

Fig. 4.7b shows the heterogeneity of the steady-state APD in terms of the estimated parameter τ_{close} , as it is shorter on the free wall of the LV compared to the septum (white ellipse). Also there is a longer APD compared to the neighbours

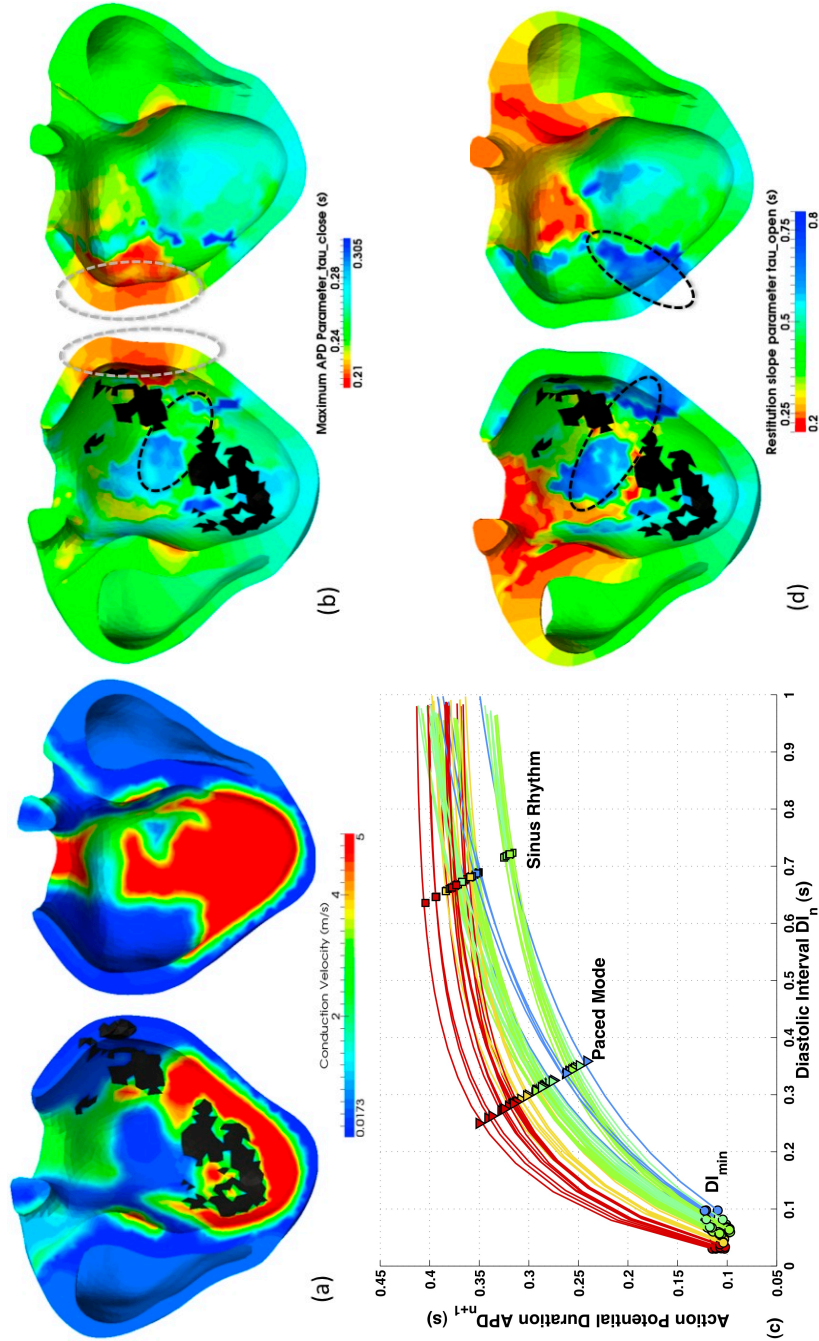


Figure 4.7: Estimated parameters: (a) conduction velocity estimated from AC maps, (b) APD parameter τ_{close} , lower τ_{close} values correspond to lower measured APD (white ellipse), (c) & (d) heterogeneous APD restitution curves and APD RC parameter τ_{open} maps respectively, low τ_{open} values (red) correspond to steep RC slopes & high values (blue) correspond to flat RC slopes. Heterogeneous Minimum DI values for the restitution curves are also shown in (c)

near the scar (grey zones) and the region between the two scars (isthmus) Fig. 4.7b (black ellipse). For APD restitution, the mean absolute error after fitting the curves was $1.13ms$, showing a good fit, see Fig. 4.7c. The region around the scars and the isthmus were more heterogeneous for RC slope parameter τ_{open} than the rest of the LV, see Fig. 4.7d black ellipses. In Fig. 4.7d, red colour (low values of τ_{open}) corresponds to steep slopes and blue colour (high values of τ_{open}) corresponds to flat slopes, as shown in Fig. 4.7c. The colour bar is also applicable to the RCs. A smooth apex-to-base gradient for APD RC can be observed in Fig. 4.7d. Isthmus and grey zones were seen to have high APD values with more heterogeneous RC slopes and conduction. All of these factors along with the scar geometry did play a crucial role in induction of ischemic VT as explained later in Chapter 6.

5.2 Assessment of Heterogeneity Maps

Such maps reveal areas with a risk of VT (black ellipse in Fig. 4.8). But this is also highly dependent on the pacing location, thus in order to really assess this risk we simulate VT-Stim procedures with various pacing locations, as explained later in Chapter 6.

In order to better interpret these parameter maps, we estimated the steady-state APD maps for different pacing frequencies, see Fig. 4.8. We can observe that this map is quite homogeneous for slow pacing frequency (60 bpm (1000 ms CL)), but its heterogeneity then increases with pacing rate (100 bpm (600 ms CL), 150 bpm (400 ms CL)). Eventually it reaches a kind of plateau where it is then quite homogeneous (200 bpm (300 ms CL)).

6 Discussion

6.1 Data Limitations

As only LV endocardial mapping data were used, the model personalisation had several limitations, few of which are: (i) Lack of estimation of local RV and transmural spatial distributions of conductivity and restitution properties. A global estimation of these properties was done using body surface ECG waveforms as explained in Sec. 4.1 & 4.3. (ii) Only two heart rates were used for fitting APD RCs. Thus only two model parameters were estimated, and an assumption was made by considering the sinus rhythm APD, as a constraint on the asymptotic value of APD RCs controlled by the parameter τ_{close} , while the paced mode APD was used to adjust the RC slope controlled by the parameter τ_{open} . However, more measurements for frequencies in the slope region (region between minimum DI and maximum value of APD on APD RC) could have depicted the RC slope more accurately. (iii) Lack of minimum DI measurement with pacing periods reaching up to the refractory period of the myocardium. As these values can play a crucial role in the initiation and sustainability of arrhythmias. However the model had its own simulated minimum DI derived from the estimated parameters as shown in Sec. 4.3 and (iv) Usage of Non-

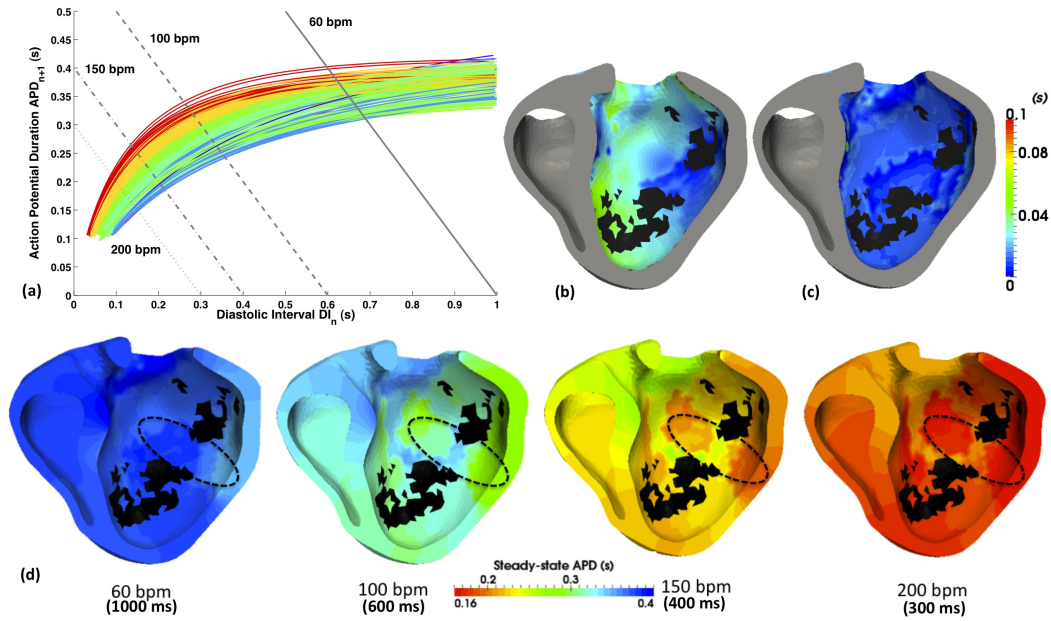


Figure 4.8: Maps of absolute depolarisation time error (b) and APD error (c) between simulated and measured isochrones. Computation of local steady-state APDs (a) for different cycle lengths from the estimated restitution curves. Red to blue colours represent steep to flat slopes. Steady state values of APD for different heart rates (cycle lengths in ms) (d). Black ellipse highlights the changes in heterogeneity near PIZ

Contact Mapping (NCM) data and EP & MR fusion errors. Although NCM data do have an advantage of measuring temporal EP data with more spatial acquisition (surface) than the contact mapping data (point), the NCM data can be challenging for local depolarisation and repolarisation time estimations. Also uncertainty on the data can be added due to the difficult registration between the EnSite LV surface and the MR-derived LV surface (Fig. 4.4).

6.2 Model Simplifications

In order to have a clinical relevant model for personalisation and VT risk assessment, the MS model used had several simplifications, few of which are, (i) No actual Purkinje network modelling. Exact locations of these Purkinje network extremities are ambiguous and inextractable from the patients data, although they could play a crucial role in arrhythmogenesis [BGR⁺06, SSW⁺04]. However, a high conductivity endocardial region was obtained, which may be inferred as depicting the underlying Purkinje network with personalisation (Sec. 4.1 & Fig 4.7a). A local estimation of endocardial restitution properties (Sec. 4.3 & Fig 4.7d) also helped potentially depict the abnormalities in the Purkinje network around scars, leading to arrhythmia generation. (ii) Use of an atlas-based cardiac fibre model. Extraction of true *in vivo*

cardiac fibre orientations is the subject of ongoing research and including them would give more accuracy to the VT-Stim predictions and inducibility maps. Finally, orthotropic anisotropy could change the model behaviour, but acquiring patient-specific data on cardiac laminar sheets seems even more challenging.

6.3 Conclusion

The proposed approach of coupled model personalisation for fast estimation of hidden parameters such as conductivity and APD restitution could enable the clinical use of cardiac electrophysiology models in the future. The parameter estimation algorithm is used on clinical interventional data and the obtained results are very encouraging. The estimated conductivity and APD restitution parameters are able to distinguish between the healthy areas and the pathological ones (scar and isthmus). Next, we need to validate the personalised model predictions with mapping data for arrhythmias and integrate the simulation of RF ablation into a first cohort of clinical cases.

Building Personalised EP Models using *in-vivo* Experimental Data (Contact Mapping)

Contents

1	Introduction	68
2	3D Electrophysiology Model with Chronic Infarction	68
3	Contact Mapping and MR Dataset Processing	69
4	Building personalised electrophysiological model	71
	4.1 Coupled personalisation approach (EK-MS)	71
	4.2 Application	71
5	Conclusion	73

Based on:

- [RSDA11] J. Relan, M. Sermesant, H. Delingette, and N. Ayache. Personalisation of a 3D ventricular electrophysiological model, using endocardial and epicardial contact mapping and MRI. In *Statistical Atlases and Computational Models of the Heart. Imaging and Modelling Challenges - Second International Workshop, STACOM 2011, Held in Conjunction with MICCAI 2011*, pages 14–22, 2011.

Personalisation, i.e. parameter estimation of a cardiac ElectroPhysiology (EP) model is needed to build patient-specific models, which could then be used to understand and predict the complex dynamics involved in patient's pathology. In this chapter, we present an EP model personalisation approach applied to an infarcted porcine heart, using contact mapping data and Diffusion Tensor MRI. The contact mapping data was gathered during normal sinus rhythm, on the ventricles in-vivo, endocardially as well as epicardially, using a CARTO mapping system. The Diffusion Tensor MRI was then obtained ex-vivo, in order to have the true cardiac fibre orientations, for the infarcted heart. Both datasets were then used to build and personalise the 3D ventricular electrophysiological model, with the proposed personalisation approach. Secondly, the effect of using only endocardial mapping or epicardial mapping measurements, on the personalised EP model was also tested.

1 Introduction

Modelling of the cardiac electrophysiology has been an important research interest for the last decades, but in order to translate this work into clinical applications, there is an important need for personalisation of such models, i.e. estimation of the model parameters which best fit the simulation to the clinical data. Cardiac model personalisation is required to develop predictive models that can be used to improve therapy planning and guidance.

In this chapter, we apply the proposed coupled personalisation framework (EK-MS) in Chapter 4, to an infarcted porcine heart. The fast 3D EK model is used to estimate the tissue conductivity parameter over the ventricles from the contact mapping of endocardial & epicardial surface potentials, using an adaptive iterative algorithm. This is then used to set the conductivity parameter of the 3D MS model, which could be then used for reliable arrhythmia predictions.

The contributions of this chapter are: 1) Application of the EK-MS personalisation approach to an infarcted porcine heart, using contact mapping data and DT-MRI, and 2) Study of the effect of using either endocardial only or epicardial only measurements, on the EP model personalisation.

2 3D Electrophysiology Model with Chronic Infarction

The models used in the EK-MS personalisation approach are simple Eikonal (EK) model and a simplified biophysical model, the Mitchell-Schaeffer (MS) model.

The EK model simulates the propagation of the depolarization wave in quiescent tissue, ignoring repolarisation phase. The EK model is governed by eikonal-diffusion (ED) equation and is based on anisotropic Fast Marching Method (FMM). More detailed analysis can be found in [CRG⁺08]. The model is simulated, as explained before in Chapter 4.

The MS model [MS03] is a 2-variable simplified biophysical model derived from the 3-variable Fenton Karma (FK) ionic model [FK98]. It models the transmem-

brane potential as the sum of a passive diffusive current and several active reactive currents including a sodium ion (influx) current and a potassium ion (outflux) current. Unlike FK model, it does not model the Calcium ion current. More detailed analysis can be found in [MS03]. The simulation details are the same as in Chapter 4 and as given in Table. C.2 in Appendix C.

In this chapter, we focus only on conductivity estimation, thus chronic scars are modelled with low conductivity in the ischemic zones. While the grey zones (the regions around scars) had conductivity estimated from the data, as shown later. However, we had shown the approach of modelling chronic scars along with APD heterogeneity before in the Chapter 4. The true fibre orientations in healthy and infarcted areas, estimated from DT-MRI, are taken into account for simulations.

3 Contact Mapping and MR Dataset Processing

The adjustments were performed on an infarcted porcine heart. The acquired data consists of contact mapping data gathered on the ventricles *in vivo* during normal sinus rhythm, endocardially as well as epicardially, using a CARTO mapping system, and a Diffusion Tensor MRI (DT-MRI) representing geometry and fibre orientation *ex-vivo*.

The 3D mapping system (CARTO) localises the extracellular potentials at points in 3D space and on a 3D ventricular geometry acquired by connecting all those points, during the interventional procedure, using invasive catheters (see Fig. 2.6). The measurement of extracellular potentials could be unipolar or bipolar (Fig 5.2(b)). The mapping system then extracts the local activation times (LAT) for the contact points in 3D space and produces a local activation map on the 3D ventricular geometry, representing the action potential wave propagation pattern, as shown in Fig 5.2(a).

The DT-MRI is used to reconstruct the cardiac fibres using the principal eigenvector of the diffusion tensor. It is also used to create the 3D ventricular model, as shown in Fig 5.1.

The 3D ventricular geometry acquired using CARTO is then registered to the 3D ventricular model. The measurement contact points of the CARTO, are then projected on to the 3D ventricular geometry using closest points projections (Fig 5.2(c & d)). Finally, the LATs measured at those points is then interpolated on the endocardial and epicardial surface, to have a rough guess on the action potential wave propagation, as shown in Fig 5.3.

The interpolated epicardial and endocardial LAT maps on the 3D ventricular model, are then used as input for EP model personalisation. In order to penalise the point projection and interpolation errors, we use the projection distance of the points and the interpolated projection distance maps (Fig 5.4) as a spatial penalising factor in the conductivity estimation procedure, as explained later.

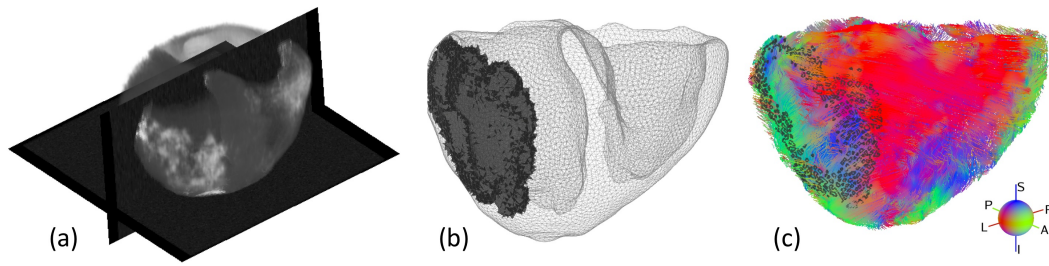


Figure 5.1: (a) Volume rendering of DT-MRI to visualise scars (bright in intensity), (b) 3D ventricular model constructed from DT-MRI, with labelled scar zones (black), (c) cardiac fibre construction from DT-MRI, showing the fibre disorientation in and around scars (black contour).

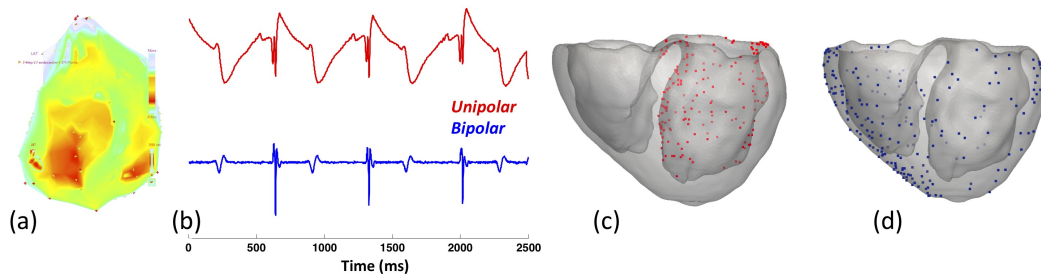


Figure 5.2: (a) LAT map constructed on a 3D ventricular geometry using CARTO mapping system, (b) Unipolar & bipolar extracellular potentials measured using invasive catheters, (c & d) measurement contact points (red - endocardial & blue - epicardial) gathered in 3D space using CARTO, registered and then projected on the endocardial (c) & epicardial (d) surface respectively, of the 3D ventricular model.

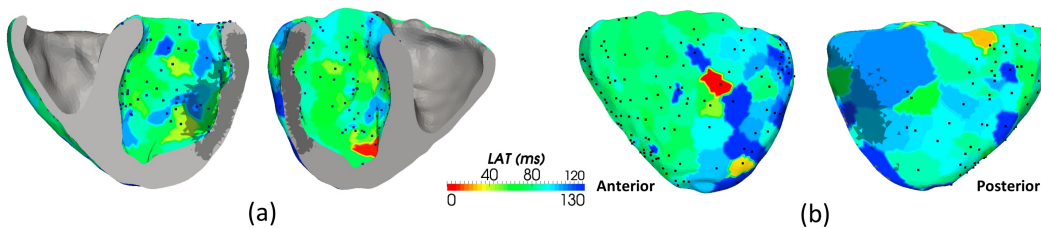


Figure 5.3: LAT maps construction from linear interpolation of the measurement contact points (black) for (a) endocardial and (b) epicardial surfaces of the 3D ventricular model.

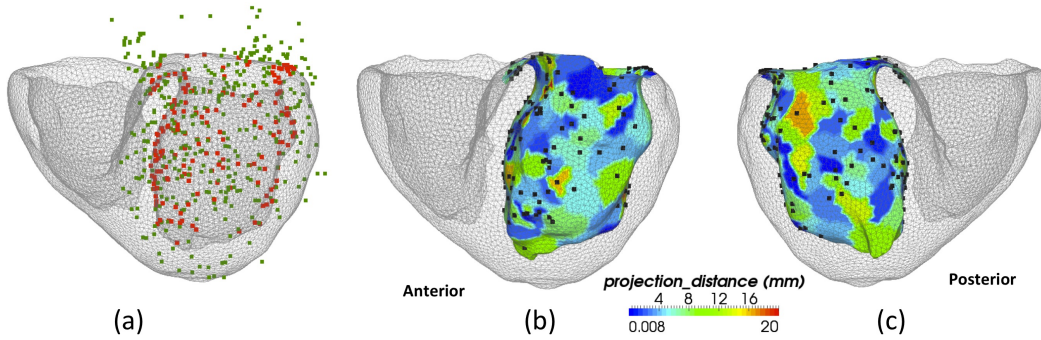


Figure 5.4: Projection distance calculated and interpolated from the contact points (black), on to the endocardial surface.

4 Building personalised electrophysiological model

4.1 Coupled personalisation approach (EK-MS)

The coupled personalisation procedure used is explained in Chapter 4 in Section 4. The input to the algorithm are the linearly interpolated LAT maps on the surface of the ventricular model (Fig 5.3). The cost function for each zone to minimise, is adapted here, and is given as

$$J(d_{zone}) = \sum_{\forall i \in S \cap zone} (PenaltyFactor_i * (LAT_i - DT_i^{sim}(d_{zone})))^2 \quad (5.1)$$

with vertex i in zone, belonging to the surface S having measured data, DT_i^{sim} are the simulated depolarisation times from the EK model, and $PenaltyFactor$ is computed from the normalisation of interpolated projection distance maps (Fig 5.4(b & c)), with 1.0 representing lowest distance and $8.14e^{-9}$ representing the farthest distance.

4.2 Application

In order to assess the influence of mapping (endocardial and epicardial) details on the model personalisation, we tested model personalisation with various configurations as follows.

4.2.1 With endocardial and epicardial mapping

In the state of the art in clinics, simultaneous endocardial and epicardial mappings are the finest amount of acquisition details possible for capturing the action potential wave propagation dynamics during normal sinus rhythm. Thus we use the apparent conductivity estimated using this mapping data, as the closest approximation of the true tissue conductivity distribution, with the proposed personalisation approach. The mean error on activation times, after model personalisation was

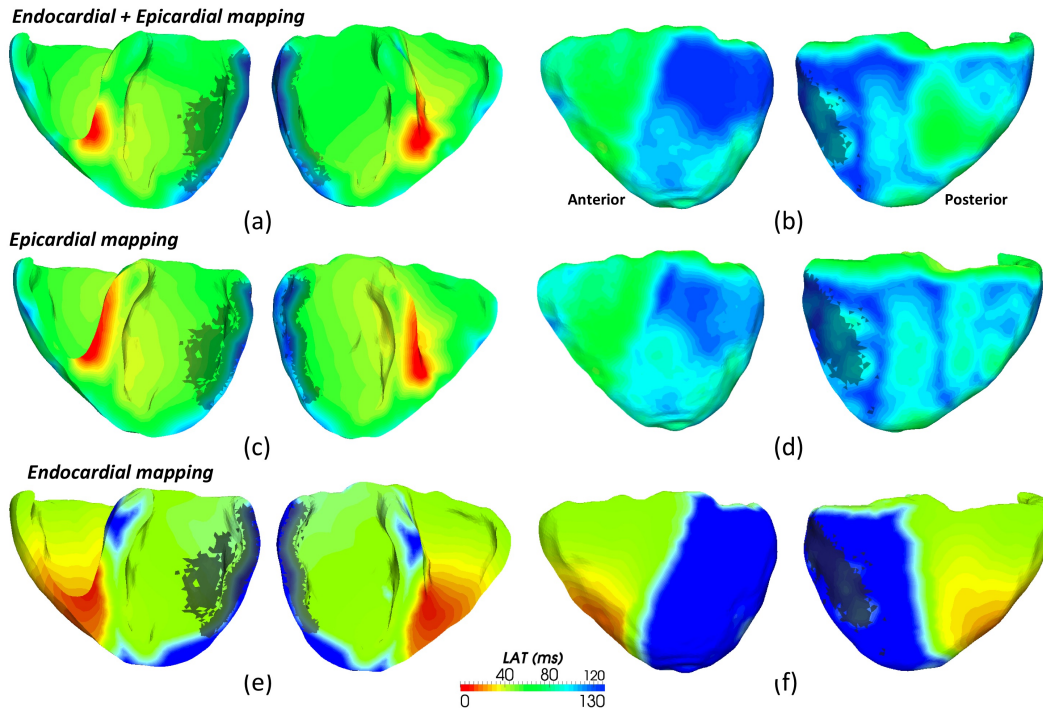


Figure 5.5: Volumetric activation times after personalisation using endocardial & epicardial mapping (top row), only epicardial mapping (middle row) and only endocardial mapping (bottom row).

15.93 ms. Fig 5.5(a & b) shows the activation isochrones after personalisation, and Fig 5.6(a & b) shows the AC distribution, along with the residual activation time error after optimisation.

4.2.2 With endocardial mapping

Now we use only the endocardial mapping, to estimate the AC distribution. The mean error on activation times, after personalisation was 15.26 ms. Fig 5.5(e) shows matching of the LV endocardial isochrones with Fig 5.5(a) and data (Fig 5.3(a)), but has a large misfit of the epicardial isochrones (Fig 5.5(f) compared against Fig 5.5(b) and Fig 5.3(b)). Thus the reproducibility of the isochrones on the epicardial side is highly prone to errors. This is confirmed by the large prediction errors on the epicardial surface, as shown in Fig 5.7(c).

4.2.3 With epicardial mapping

Here we use the epicardial mapping, to estimate the AC distribution. The mean error on activation times, after personalisation was 9.59 ms. Fig 5.5(c & d) shows good matching of the LV endocardial isochrones, as well as epicardial isochrones with Fig 5.5(a & b) and data (Fig 5.3(a & b)). Thus epicardial mapping could be

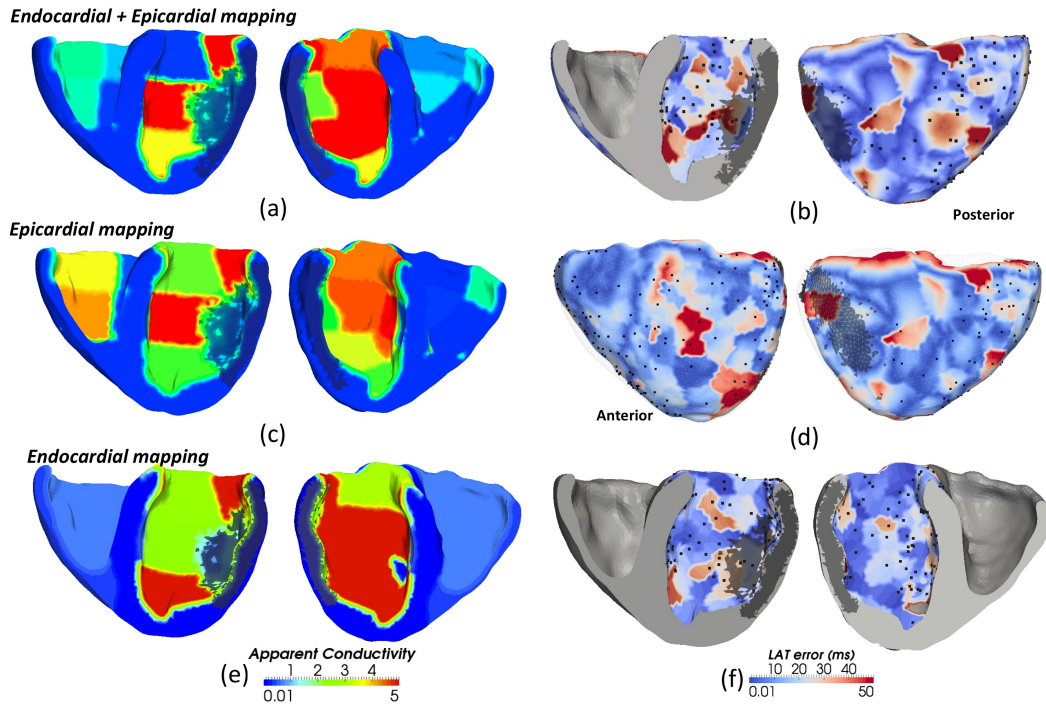


Figure 5.6: The first two columns show estimated AC distributions (d_{EK} (m^2), d_{MS} (s^{-1})) and last two columns show residual error after personalisation, for various configurations explained.

sufficient enough to reproduce the true wave propagation dynamics, as compared to endocardial mapping data. This is confirmed by the low prediction errors on the endocardial surface, as shown in Fig 5.7(b).

5 Conclusion

In this work, we have shown the application of a proposed coupled personalisation framework to the contact mapping data of an infarcted porcine heart. The cardiac fibre orientations estimated from DT-MRI were incorporated inside the model personalisation for a more accurate tissue conductivity estimation. We also tested the influence of mapping details on the model personalisation algorithm. We found that personalisation using epicardial mapping gave a conductivity estimation closest to the one obtained with personalisation using both endocardial and epicardial mapping, and also showed a low prediction error. On the other hand, the personalisation with endocardial mapping had an important deviation from the estimated distribution obtained with both endocardial & epicardial mapping. It also had an important prediction error on the epicardial surface. Thus, within this experimental setting, epicardial mapping proved to be a sufficient acquisition to reproduce a tissue conductivity distribution, closer to the one estimated using both endocardial

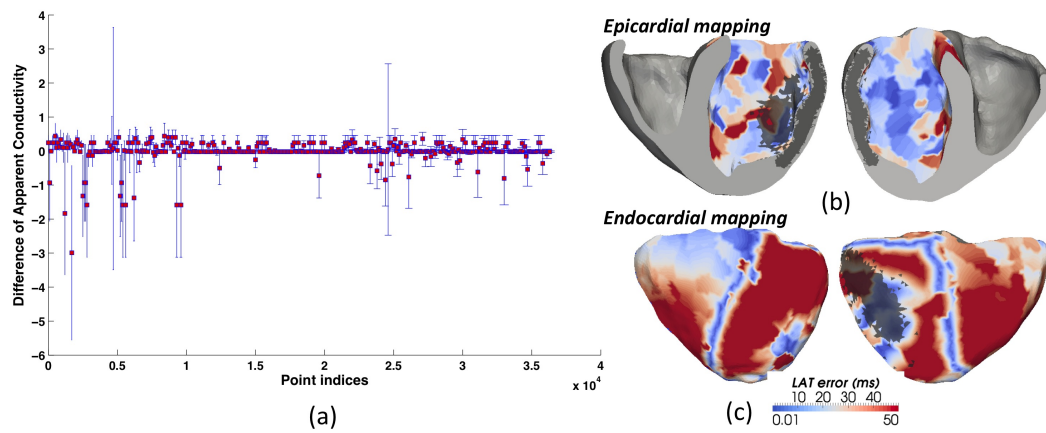


Figure 5.7: Graph: mean and standard deviation of the difference of AC values estimated for the 3 configurations. Zero mean with low standard deviation shows good agreement between the AC values for a given data point. Other figures show the prediction error on the endocardial side, for personalisation with epicardial mapping (b) and on the epicardial side, for personalisation with endocardial mapping.

and epicardial mapping. This was also the case when the personalisation was done on similar data from a clinical case [KRC⁺11]. Such finding has to be tested on other configurations, for different healthy and pathological cases.

Part III

MODELLING VENTRICULAR
TACHYCARDIA & RF
ABLATION

Personalised Ventricular Tachycardia Modelling

Contents

1	Introduction	78
2	Modelling Post-infarction Ventricular Tachycardia	80
2.1	Structural Heterogeneity	80
2.2	Functional Heterogeneity	87
3	Modelling of Clinical VT-Stimulation Protocol	90
3.1	VT Induction	90
3.2	VT-Stim Modelling	91
4	VT Risk Stratification	92
5	Conclusion	94

Based on:

- [RCS⁺11] J. Relan, P. Chinchapatnam, M. Sermesant, K. Rhode, M. Ginks, H. Delingette, C. A. Rinaldi, R. Razavi, and N. Ayache. Coupled personalization of cardiac electrophysiology models for prediction of ischaemic ventricular tachycardia. *Journal of the Royal Society Interface Focus*, 1(3):396–407, 2011.
- [RDS⁺11] J. Relan, H. Delingette, M. Sermesant, N. Ayache, M. W. Krueger, W. Schulze, G. Seemann, and O. Dössel. Planning of Radiofrequency Ablation for Patients with Ventricular Tachycardia. Deliverables D6.3.2, European project euHeart, June 2011.

In order to develop an in silico RFA planning platform for cardiac arrhythmias, there is a need to simulate arrhythmias with macroscopic 3D models. Here, we illustrated the main macroscopic characteristics of an ischemic VT. These include the structural and functional heterogeneity of the tissue near the scars i.e. peri-infarct zones (PIZ). We adapted a mono-domain 3D EP model to simulate its macroscopic structural behaviour. The macroscopic functional heterogeneity was achieved from the estimated patient-specific tissue heterogeneities (CV, APD, CV & APD restitution) using the proposed coupled personalisation framework as explained earlier in Chapter 4. Next, we showed the simulation of an in silico VT stimulation study using the personalised and adapted MS model, to quantify VT risk, in terms of inducibility maps, re-entry patterns and exit point maps.

1 Introduction

There are various forms of Ventricular Tachycardia (VT) reported in the literature. The details on different types of VT is given in table 6.1. They can be classified into two main groups as given in Fig. 6.1 [MKY⁺02]. In idiopathic VT cases, VT may arise through abnormal firing of a small group of cells in an otherwise normal heart, called as early or delayed after depolarisations, depending on their firing times. If these small critical areas can be located, (they are usually in certain well-defined anatomical regions), focal, point catheter Radio-Frequency (RF) ablation can cure the problem [WK07]. The most common form of VT reported is with scarred ventricles (e.g. after myocardial infarction or congenital heart disease surgery or in heart muscle disorders) called as infarct-related or scar-related VT [ASAG09]. VT associated with other forms of structural heart disease (e.g. hypertrophic and dilated cardiomyopathy, arrhythmogenic RV cardiomyopathy) are observed to have similar mechanisms as scar-related VT [MKY⁺02]. The RF ablation strategy of scar-related VT is very different from normal heart VT and targets the whole arrhythmogenic zone [WK07]. Despite of using complex electrical mapping systems, the long-term success rates of scar-related VT is 30 – 60% only, as reported in [ASAG09]. In this work, we focus on modelling scar-related VT.

After the occurrence of scar (myocardial infarction), structural, functional and electrical remodelling of the ventricles takes place. Which is characterised by progressive dilation, hypertrophy, distortion of the cavity shape, and deterioration in contractile function. The relation between ventricular remodelling and ventricular tachycardias after acute myocardial infarction has not been explored systematically yet. Ventricular tachycardia is mainly due to a re-entry caused by a unidirectional block and slowed conduction within the re-entrant circuit [WE00]. Post-infarction structural remodelling creates partially healed regions (called peri-infarct or border zones) around the scars as seen in Fig. 6.2. Slow impulse propagation velocities through peri-infarct zones are partially caused by fibrosis (see Fig. 6.5). In addition, peri-infarct zones are also observed to have longer effective refractory period compared to the normal tissue as a result of post-repolarisation refractoriness [WE00].

Table 6.1: Classification of Ventricular Arrhythmias. Table based on [AKTM09]

Classification by Electrocardiography	
Non-sustained VT	Three or more beats in duration terminating spontaneously in less than 30 seconds (rate > 100 bpm, CL < 600 ms)
Monomorphic	Non-sustained VT with single QRS morphology
Polymorphic	Non-sustained VT with changing QRS morphology at CL between 600 & 180 ms
Sustained VT	VT greater than 30 s in duration and/or requiring termination due to hemodynamic compromise in less than 30 seconds
Monomorphic	Sustained VT with stable single QRS morphology
Polymorphic	Sustained VT with changing or multiform QRS morphology at CL between 600 & 180 ms
Bundle branch related tachycardia	VT due to re-entry involving His-Purkinje system, usually with LBBB morphology, usually occurs in setting of cardiomyopathy
Bidirectional VT	VT with beat-to-beat alternans in the QRS axis.
Torsades de pointes	VT associated with long QT or QT _c and characterised by twisted peaks of the QRS complexes during the arrhythmia
Ventricular flutter	Regular (CL < 30 ms variability) ventricular arrhythmia ≈ 300 bpm (CL 200 ms) with a monomorphic appearance.
Ventricular fibrillation	Rapid, usually > 300 bpm (CL < 180 ms) irregular ventricular rhythm with variable QRS morphology.

Models of Ventricular Arrhythmias The majority of the ventricular models used in the study of arrhythmia mechanisms have focused on the rotational propagation of complex 3D electrical waves in the heart. These self-sustaining re-entrant waves (termed spiral waves in 2D and scroll waves in 3D) occur in a variety of non-linear excitable media. An experimental study using fluorescence mapping of electrical activation in the heart from [DPS⁺92] demonstrated the presence of such waves in cardiac tissue and their role in ventricular fibrillation (VF). The study [PK95] demonstrated a realistic, 3D model of scroll-wave activation in the heart. The authors captured the dynamics of excitable tissue by using the two-variable phenomenological FitzHugh-Nagumo model [NAY62] of membrane kinetics.

The studies [JG96, GJ⁺98] proposed that in small hearts (mouse, rabbit) a single rapidly drifting and meandering rotor could underlie VF, in large hearts including those of humans, VF could be sustained by numerous coexisting rotors. The role of the 3D ventricular geometry in wave fragmentation and spiral wave breakup was explored in [Rog02, XQY⁺04].

Additionally, the studies [CH04, Cla08] demonstrated that the behaviour of the vortex filaments was found to depend on action potential duration (APD) heterogeneity in the ventricles [ART07]. The study [TT09] examined VF in ventricles with both homogeneous and heterogeneous APD. The study determined that heterogeneity in APD produced increased turbulence in the ventricles. The studies

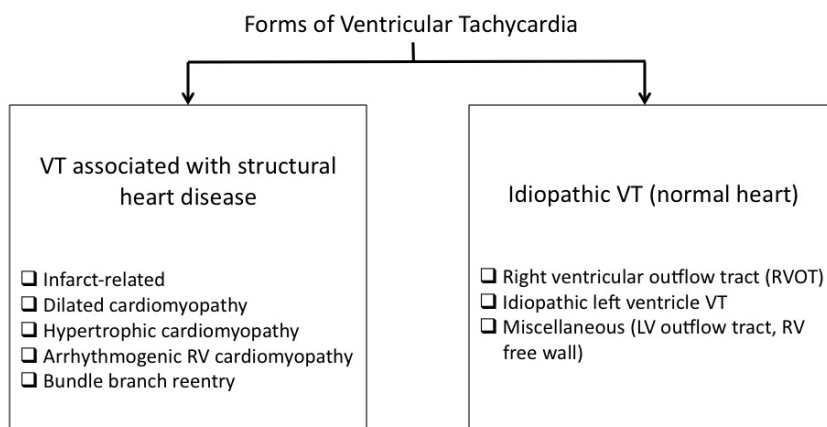


Figure 6.1: Classification of various forms of VT. Image from [MKY⁺02]

on the transition from tachycardia to fibrillation in particular, have been focused on the development of APD alternans [BRB07] and the role of alternans and APD restitution [CF04, BQH⁺07] in conduction block, dynamic stability in re-entrant activity, and transition to VF.

In recent years, significant advances have been made in the use of biophysically detailed membrane kinetics models integrated with realistic geometries to understand the mechanisms by which arrhythmias arise and are maintained in the human heart [TTHP⁺07]. However, the geometrical data for the model were obtained from an *ex-vivo* normal human heart [TTHP⁺07] and the fibre architecture of a canine heart was used. Using the TNNP model, further investigations were done on the effect of heterogeneous restitution properties in human VF by incorporating clinically measured restitution properties [KTTN⁺08]. The study found that the number of filaments and the excitation periods depended on the extent of the restitution heterogeneity. Thus, restitution heterogeneity was found to play an important role in arrhythmogenesis by providing a substrate for cardiac arrhythmias.

2 Modelling Post-infarction Ventricular Tachycardia

Post-infarction scar-related ischemic VTs are usually initiated by mechanisms of re-entry in the ventricular myocardium. Re-entry depends on the co-existence of an arrhythmogenic substrate, which is a pre-existing structural pathological condition, and a trigger, such as acute ischemia that initiates the electrical abnormality.

2.1 Structural Heterogeneity

Myocardial infarction or other pathologies (myocarditis, sarcoid etc.) results in the formation of infarcts. Infarcts show marked spatial heterogeneity, with areas of necrosis interspersed with bundles of viable myocytes, particularly at the periphery

of the infarct (called border zone or peri-infarct regions). This may lead to formation of fibrocellular, fibrosclerotic, or fibroadipose scars with irregular outlines. Schuleri et al [SCG⁺09] have reported this heterogeneity histologically and its correlation against DE-MRI and DE-MDCT techniques, for chronic myocardial infarcts (Fig. 6.2).

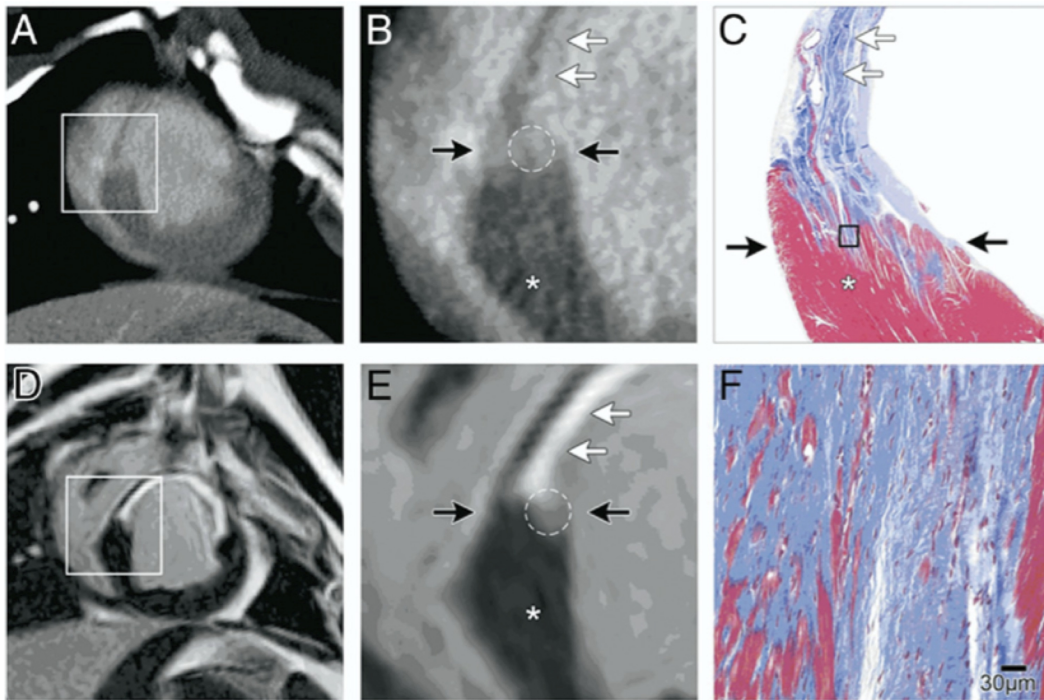


Figure 6.2: Example of matching histological data in chronic infarcts against DE-MDCT (A and B) and -MRI (D and E). The peri-infarct zone (PIZ) is visualised between 2 black arrows by intermediate signal intensity (white circle) in DE-MDCT images. In D & E, infarct scar (white arrows), and the PIZ (white circle) show different signal intensity in DE-MRI. (C and F) Masson trichrome stain depicts viable myocardium in red (*) from nonviable tissue in blue. At higher magnification (F) the islands of viable myocytes (red) within the scar tissue are visualised, showing the heterogeneity of the PIZ. Image taken from [SCG⁺09]

The peri-infarct regions mainly consists of fibrosis or fibrofatty replacement of ventricular myocardium. This replacement or scarring fibrosis corresponds to the replacement of damaged myocytes by collagen (Fig. 6.3) [MLC⁺11]. It can have a localised distribution (patchy fibrosis) or diffused distribution (diffuse fibrosis), as shown in Fig. 6.3. Patchy fibrosis is often found in ischemic cardiomyopathy and may lead to strands of conducting tissue surrounded by areas of dense unexcitable scar [DBVR06]. These strands are called "isthmus". Isthmuses typically create a substrate for potential re-entries. Fig. 6.5 shows the underlying schematics present in ischemic VT occurrence.

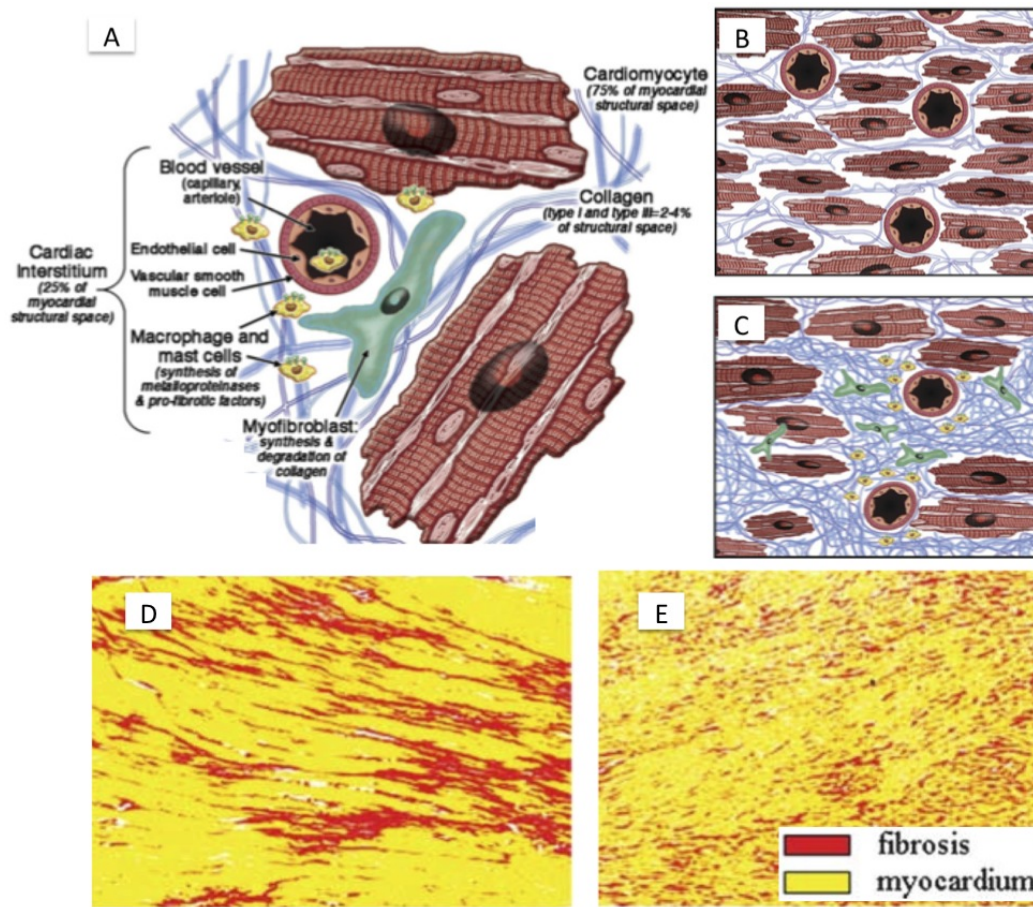


Figure 6.3: Multiple components present in a cardiac interstitium for healthy tissue (A & B) and fibrotic tissue (C) (increase of collagen matrix to replace damaged cells) [MLC⁺11]. Different textures of Fibrosis (D: Patchy and E: Diffuse) present in regions around the necrotic core [DBVR06]

Fleming et al [Fle10] have studied the fibre orientations of peri-infarct tissue against healthy and densely infarct tissue. They have reported a decrease in fibre organizations with the presence of randomised fibre orientations in peri-infarct and infarct tissue, as seen in Fig. 6.4. This has been also confirmed with the findings of Pop et al. [PSM⁺09] with DT-MRI of porcine hearts, as seen in Fig. 6.4.

2.1.1 Modelling Fibrosis

Despite the importance of fibrosis in arrhythmogenesis, most of the computer simulation research into tachyarrhythmias has so far focused on structurally normal cardiac tissue and only a few studies have dealt with modelling fibrotic tissue. The effects of large numbers of unexcitable obstacles mimicking fibrotic strands on wave propagation in a simplified model for cardiac tissue was studied in [Per97]. The study

showed that textures of fibrotic strands may induce anisotropic propagation, widening and fractionation of electrograms, and influence the rotation of scroll waves. Recently, the study [TLHHS05] showed that textures of string-like fibrotic obstacles lead to electrogram fractionation in human ventricular tissue simulated with the Priebe–Beuckelmann model. The diffuse fibrosis was simulated by removing lateral gap junctions in human atrial tissue in [SHDB07]. Increased heterogeneity in intercellular coupling was found to lead to vulnerability for partial wave block and re-entry. Most of these studies demonstrated that fibrosis could lead to increased vulnerability for re-entry.

The studies [Pan02, TTP03, TTP05] showed the possible effects of diffuse fibrosis on wave propagation, spiral wave dynamics, and spiral break-up-induced onset of fibrillatory excitation in cardiac tissue. They found that diffuse fibrosis increases the vulnerability of tissue to wave break and spiral wave formation, increases spiral wave rotation period and suppresses steep restitution-mediated spiral break-up. The same study was performed with a detailed ionic model in [TTP07] (see Fig. 6.6 top row), the results suggested that diffuse fibrosis can suppress steep restitution spiral break-up by slowing down of re-entry, causing this to be a less likely mechanism for fibrillation in fibrotic hearts. The authors expected that the effects of fibrotic tissue are more pronounced in thin than in thick cardiac tissue. In this work, we follow similar kind of approach as in [TTP07] to model fibrosis.

For modelling of peri-infarct regions structurally for ischemic VT, we incorpo-

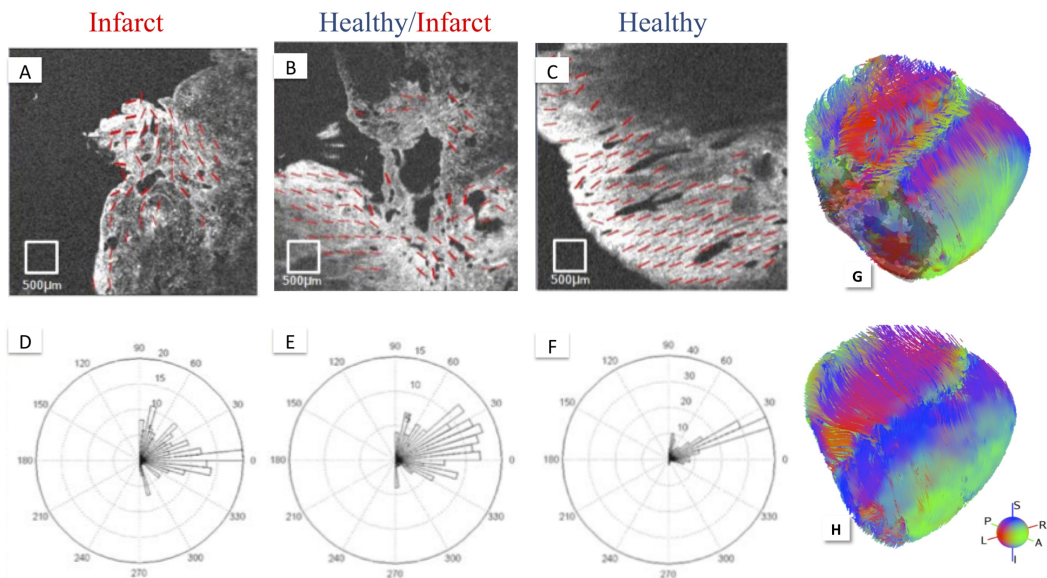


Figure 6.4: Fibre orientations within *en face* image, for infarct, PIZ and healthy tissue. Decrease in fibre organization within the infarction is reflected by the broad fibre angle histogram (A - E) [Fle10]. Influence of scar on fibre orientations generated on the ventricles using DTI (G & H) [PSM+09]

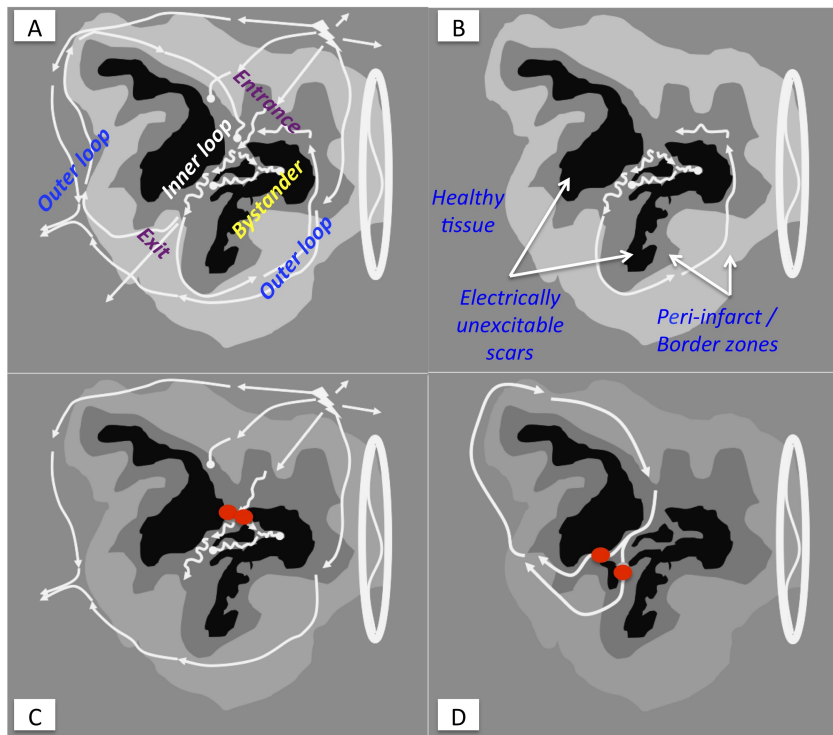


Figure 6.5: Schematics for re-entry circuits of ischemic VT, A: multiple components present in induced VT circuit with external stimulation, B: isolated self-sustained VT re-entry circuit, C & D: localization of entry and exit points.

rate patchy fibrosis, around scars in the personalised anatomical model. In practical terms, this is done by taking random tetrahedral cells in the peri-infarct regions as electrophysiologically inactive or dead, while other tetrahedra are kept as electrophysiologically healthy. The patchy fibrotic texture is enforced by making the elements cells neighbouring those already labelled as inactive in one random direction, as also inactive. The patchy nature of the myocardium can be quantified as a percentage of dead cells out of the total volume of the peri-infarct tissue. Simulations of this microscopic approach in 3D, with fibrosis in the PIZ areas is shown in Fig. 6.6.

This approach to model patchy fibrosis requires to use many small tetrahedra which is very computationally demanding. As reaction-diffusion simulation treats the cardiac tissue as a continuum with diffused wave propagation, a more macroscopic approach to model the fibrosis can be performed by considering three types of tissues in the myocardium: non-conductive tissue (necrotic core), healthy myocytes and highly resistive collagen network. The last two types could also be combined into a single class of slow conductive pathways in the peri-infarct tissue. This could be achieved by using the theory of homogenization, which is used to model the materials that often have different properties at different points [CD99]. However, we present here a first (rough) approximation which is done by a weighted sum of

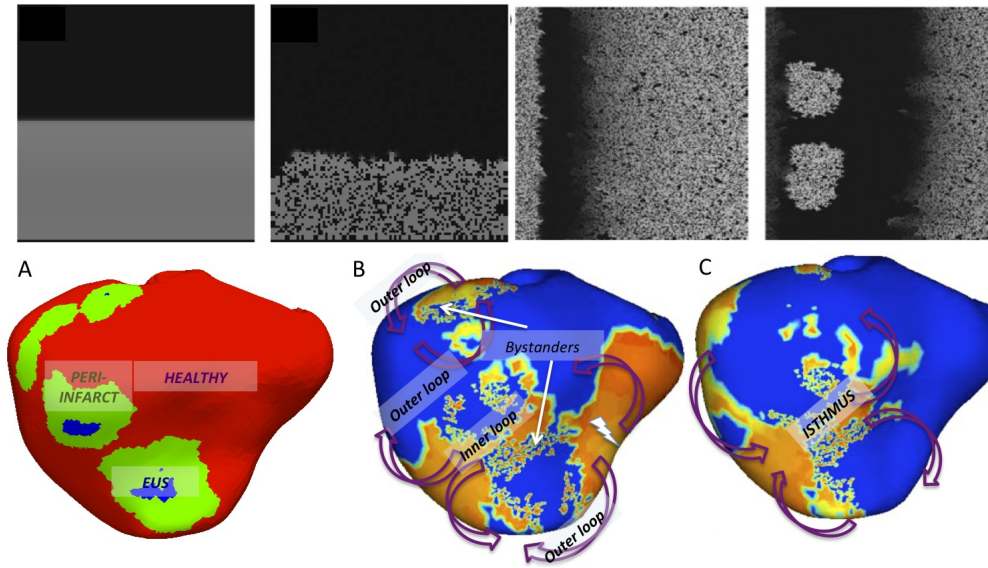


Figure 6.6: Top row: Plane wave propagation in 2D tissue without and with 30% fibrosis, figure from [TTP07]. Bottom row: Simulation of an isolated self-sustained VT re-entry circuit (C) on a personalised anatomy (A), after VT induction (B), with higher level of patchy fibrosis (60%) present in PIZ.

diffusion and reaction terms. As a first approximation, we assume that there is a linear relationship between the contributions of the two domains, on diffusion and reaction terms.

The incorporation of a decrease in fibre organisations in PIZ is done currently by using a mixture of anisotropic and isotropic propagation, the ratio of which is controlled by the percentage of patchiness in the fibrotic tissue. The loss in normal fibre orientations is also modelled synthetically by generating random fibre orientations in the necrotic core and border zones, as shown in Figure 6.7(d). Thus for modelling fibrosis, we can model its macroscopic behaviour using multi-domain models. Sub domains of which include healthy myocytes and collagen network.

Here, we present an adaptation of the simplified biophysical MS model, to represent the two domains of fibrosis. The domain of collagen network is modelled by an isotropic diffusion term with low conductivity ($d_{collagen}$), to account for the high resistivity whereas the domain of healthy myocytes is modelled with anisotropic diffusion term with normal cardiac tissue conductivity ($d_{healthy}$).

$$\begin{cases} \partial_t u &= \operatorname{div}((k d_{collagen} \mathbf{M}_{collagen} + (1-k) d_{healthy} \mathbf{M}_{healthy}) \nabla u) + (1-k) F(u, z) \\ \partial_t z &= G(u, z) \end{cases} \quad (6.1)$$

where u is the normalised transmembrane potential variable, and z is the gating variable which makes the currents gate open and close, thus depicting the depolarisation and repolarisation phase. F, G represents the reaction term of the EP model. The diffusion scaling term $d_{collagen} \ll d_{healthy}$, representing the slow conductivity in the collagen network. The anisotropy is represented by the diffusion tensor \mathbf{M} . The col-

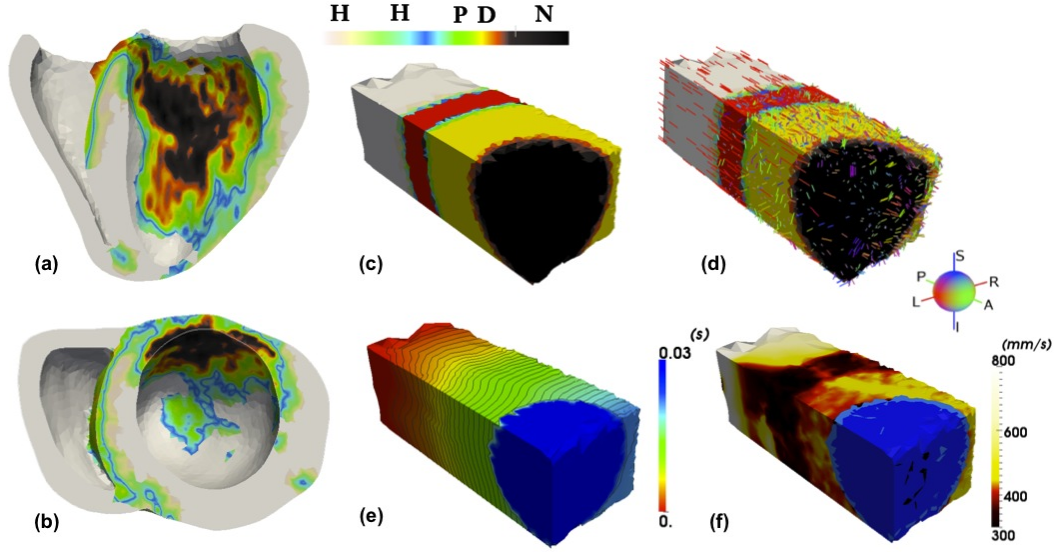


Figure 6.7: Simulation of the adapted MS model for fibrosis on a 3D tissue slab (c) with Necrotic (N) ($k = 1$, fully fibrotic), Diffuse (D) ($k = 0.8$, 80% fibrotic), Patchy (P) ($k = 0.6$, 60% fibrotic) and Healthy (H) ($k < 0.4$, 40% or less fibrotic) domains. Synthetically disorganised fibres for fibrotic regions (d). Activation times (e) and resulting CV maps (f), (f) shows the decrease in CV for fibrotic regions ($k \geq 0.6$), it also shows a patchy texture of CV for the P domain. Definition of the various fibrotic domains (scaling of k value) with LE-CMR intensity for the scar and PIZ areas (a) & (b), for *in-vivo* clinical datasets.

lagen network domain is represented as isotropic $\mathbf{M}_{\text{collagen}} = \text{diag}(1, 1, 1)$, and the healthy myocytes domain has anisotropy represented with $\mathbf{M}_{\text{healthy}} = \text{diag}(1, \rho, \rho)$, where ρ the anisotropy ratio between longitudinal and transverse diffusion.

The term k represents the ratio of collagen network and healthy myocytes present in the tissue. It gives a quantification of the fibrosis present in the tissue. $k = 1$ represents a fully fibrotic tissue, thus a necrotic core. $k = 0.9 \sim 0.7$ represents a diffuse fibrotic tissue. $k = 0.6 \sim 0.4$ represents a patchy fibrotic tissue. $k < 0.4 \sim 0$ represents a healthy tissue with low and no fibrosis respectively. A simulation of the proposed adapted monodomain MS model on a 3D tissue slab with the presence of different fibrotic domains is shown in Fig. 6.7. CV maps resulting from the simulations show the heterogeneity and the texture of fibrosis present in the macroscopic simulation (Fig. 6.7(f)). Definition of these domains for an *in-vivo* clinical dataset is done using the LE-CMR voxel intensity profiles in the scar and PIZ areas. The intensity profile is normalised, with 0 representing the healthy domain and 1 representing the necrotic core (see Fig. 6.7(c) & Fig. 6.7(d)).

2.2 Functional Heterogeneity

Heterogeneity in tissue composition and autonomic innervations in the peri-infarct regions may create areas of aberrant conduction, refractoriness heterogeneity and ectopic foci that could generate the substrate for lethal re-entrant arrhythmias [CW91].

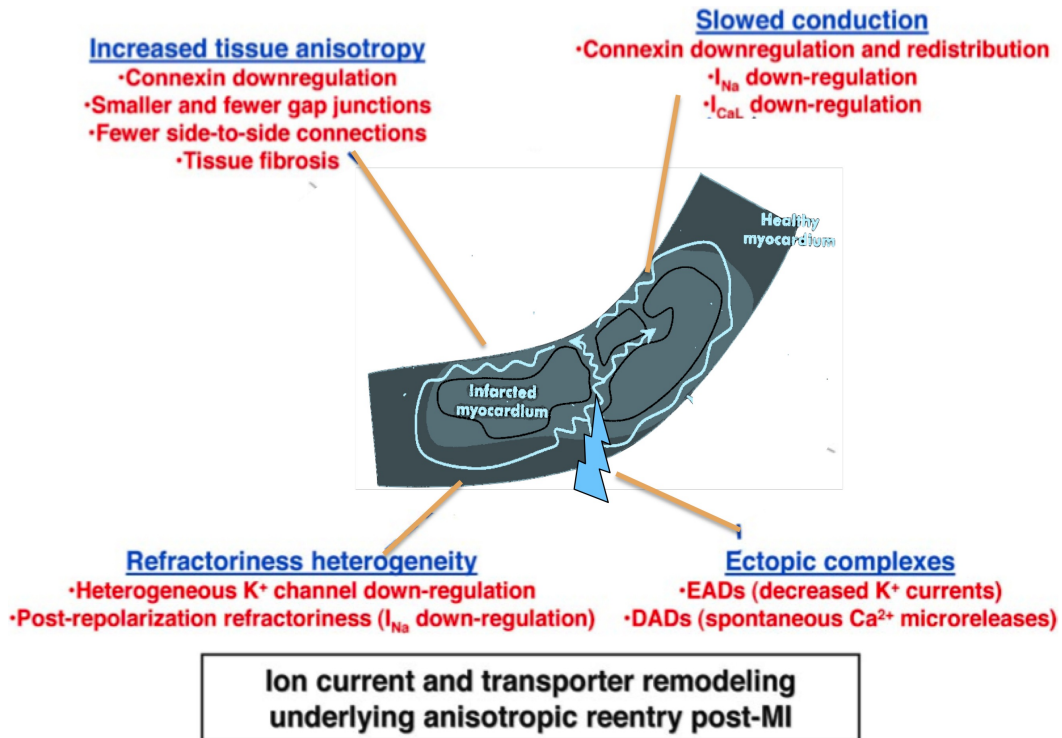


Figure 6.8: Various electrophysiological contributors to anisotropic re-entry in myocardial infarction. Image taken from [DBVR06]

Various functional heterogeneities present in the peri-infarct tissue causing ischemic VT are listed in Fig. 6.8 [CW91, WFE⁺01, PK95, JG96, CF04, CR95]. Fig. 6.9 shows the influence of the spatial heterogeneity of APD restitution in a re-entry induction with S1-S2 pacing protocol. It demonstrates the presence of steeper APD restitution slopes amidst of less steep or shallow APD restitution slopes, this can cause a re-entry formation due to the difference in APD. For modelling aspects, such patient-specific heterogeneities in the peri-infarct regions can be derived indirectly from the heterogeneous parameter maps, using electrophysiology model personalisation, as explained in Chapter 4. Heterogeneous parameter maps estimated from patient data include: Tissue conductivity maps, Maximum APD maps, APD restitution maps and Minimum diastolic interval maps. Such maps qualitatively reveal areas with a risk of VT (black ellipse representing PIZ in Fig. 6.10). But this is also highly dependent on the pacing location, thus in order to really

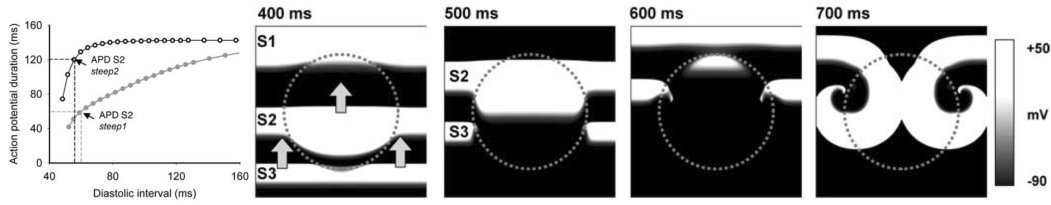


Figure 6.9: Induction of a re-entry on a 2D tissue slab to S1-S2 pacing, with APD restitution heterogeneity. Dotted grey lines enclose the region with *Steep2* restitution, elsewhere the region has *Steep1* restitution. Image taken from [NBS⁺06]

assess this risk we simulate VT-Stim procedures with various pacing locations, as explained in section 3.1. The contributions of these maps to the various functional heterogeneities present in ischemic VT are as follows:

Increased tissue anisotropy: This is mainly due to the presence of healthy long strands within a pool of collagen network. This induces a narrow stream of highly anisotropic wave propagation through the healthy long strands, which seems highly anisotropic in the PIZ, when viewed macroscopically. This feature is modelled structurally as explained in section 2.1.

Slowed conduction: A combination of healthy myocytes and highly electrophysiologically resistive collagen network, leads to slowed conduction in the PIZ. This feature is modelled using personalised tissue conductivity maps (Fig. 6.10(a)).

Refractoriness heterogeneity: Presence of unhealthy myocytes, with altered electrophysiology channels in the PIZ, could lead to such refractoriness heterogeneity [KSGH08, YFRM05, ART07, NBS⁺06]. This feature is modelled using personalised APD and CV restitution maps and minimum DI maps.

Ectopic complexes: These could be present mainly due to Early After Depolarizations (EADs) and Later After Depolarizations (LADs) developed through channel alterations [NMLBY07]. However, these are more significant during acute ischemia. For chronic ischemia modelled here, we take into account this phenomenon through maximum APD maps and minimum DI maps.

In order to better interpret these parameter maps, we also estimate the steady-state APD maps for different heart rates (Fig. 6.10) on the personalised data of a scarred patient derived from Chapter 4. We can observe that these maps are quite homogeneous for slow heart rates (< 100 bpm), but its heterogeneity particularly in PIZ, increases with heart rates (100–150 bpm). Eventually it reaches a kind of plateau where it is then quite homogeneous (> 200 bpm).

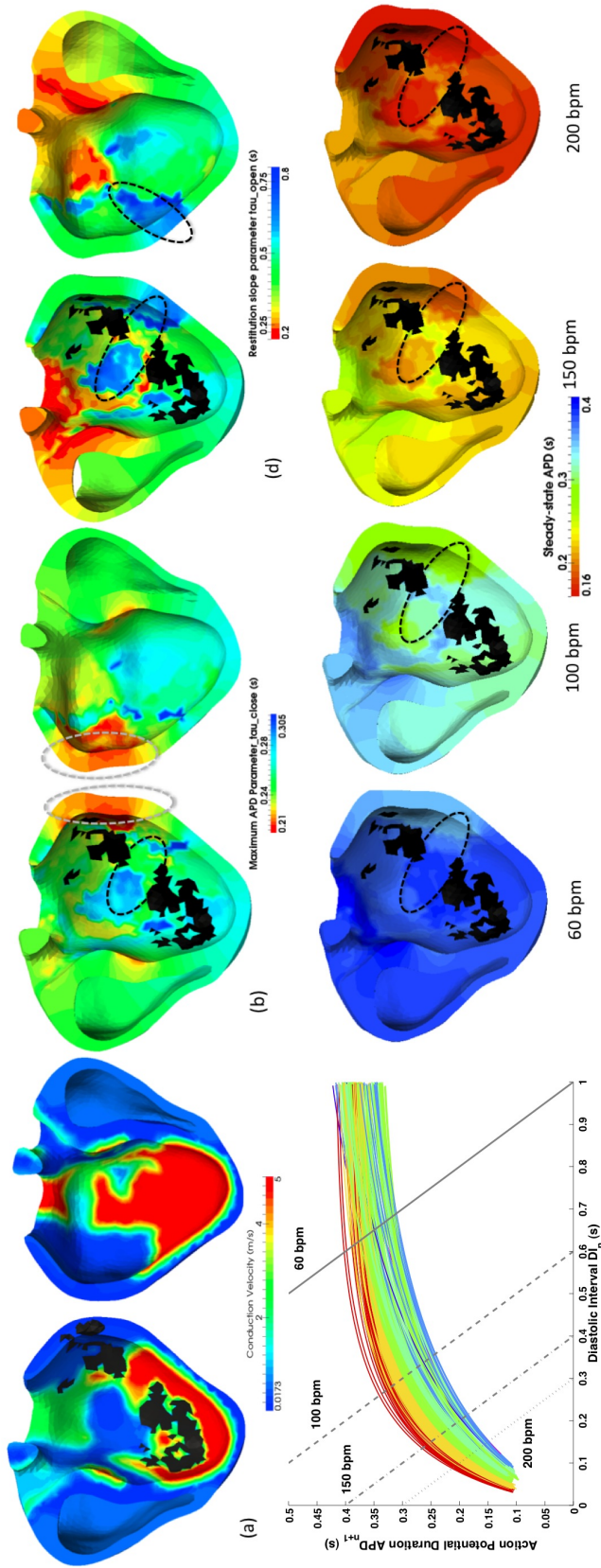


Figure 6.10: Estimated heterogeneous parameters (a) conduction velocity calculated from estimated apparent tissue conductivities, (b) maximum APD parameter maps, (c) heterogeneous APD restitution curves and (d) APD RC parameter maps respectively, low values (red) correspond to steep RC slopes & high values (blue) correspond to flat or gentle RC slopes. Heterogeneous Minimum DI values for the restitution curves are also shown in (c). Steady state values of APD for different heart rates. Black ellipse highlights the changes in heterogeneity near PIZ.

3 Modelling of Clinical VT-Stimulation Protocol

3.1 VT Induction

Programmed ventricular stimulation or *VT-Stim* is a clinical study (protocol) used to induce VT, in order to localise ablation sites (exit points) with entrainment mapping. It consists of a number of rapid stimuli usually followed by extra stimuli, and is usually introduced at two ventricular sites (RVA and RV-outflow tract (RVOT)), using various cycle lengths (CL), with varying coupling intervals [MKDB⁺91]. With entrainment mapping, electrophysiology signals are measured in the endocardium as to visualise the activation patterns. This protocol is tested directly on the patient, without any planning, to collect information about the VT and to plan the RF ablation lines.

During this protocol, the controllable inputs by electrophysiologists are (1) stimulus (strength, duration, type of current, number and rate of basic stimuli, number and interval of premature stimuli), (2) stimulation site, (3) mode of stimulation (unipolar or bipolar), and (4) inter-electrode distance [WBS85]. A snapshot of the documented VT stimulation study protocol employed at KCL, London is shown in Appendix D Fig. D.1.

The limitations of this protocol, which could eventually cause low success rate of ablation therapy are:

1. It can fail or become unfeasible, when VT is not inducible, intolerable, unstable or unmappable and recurrent. In such cases, substrate mapping consisting in detecting regions of low extracellular potentials, is used to guide the ablation therapy. This procedure sacrifices a huge amount of healthy tissue around the scars, which is unnecessary and can prove to reduce the myocardial strength, thus decreasing the LV output and LV ejection fraction [SSM⁺01].
2. It has a limited coverage around the stimulation catheter. Thus can fail to reproduce all possible VT mechanisms in the clinics, which are present in the patient's heart [SSM⁺01].
3. The ablation sites localised with such protocol and entrainment mapping is also limited to the endocardial surface, and can fail to locate exit points with wider isthmuses, and with deeper myocardial and epicardial locations of the isthmuses [NRAA⁺10]

In silico simulations of such VT-stim protocols on patient-specific model offer much more flexibility, as the model can be paced from any location and at any pacing rate, which would not be possible in practice. Personalised VT-Stim simulations can override the clinical limitations, and can help locate and plan all optimum ablation lines *in silico* before the ablation therapy.

3.2 VT-Stim Modelling

A patient-specific electrophysiological model derived from MR and electroanatomical data as described before in Chapter 4 & 5, could then be used to simulate a variety of clinically proven VT-Stim protocols *in silico*. This is done in order to test VT inducibility for various pacing locations and to locate exit points for ablation. The specifications of various clinical protocols simulated are shown in Table C.4.

Synthetic Simulations A first case of simulation of the S1-S2 protocol *in silico* was performed on the patient’s ventricular and scar geometry, but electrophysiology model parameters were synthetically set (i.e. low conductivity and more refractoriness (steep APD restitution slopes) in region between scars (isthmus)) as shown in Fig. 6.11, and detailed in [RCS⁺10].

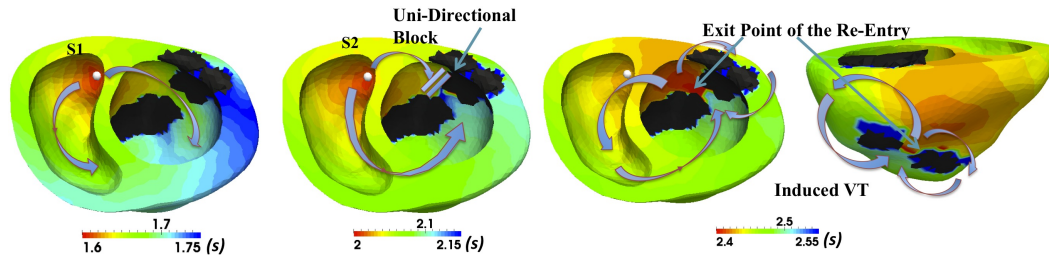


Figure 6.11: DT isochrones for simulated S1-S2 VT-Stim protocol on patients ventricle and scar geometry. Synthetic electrophysiology parameter set were used here with steep RC slopes and low CV in isthmus compared to flat RC slopes and high CV in the rest of myocardium. S_1 stimulus shows a normal propagation and S_2 shows a unidirectional block created in the isthmus due to APD heterogeneity, which leads to VT induction.

Personalised Simulations We then used the personalised 3D electrophysiological model to simulate various protocols as described in Table C.4 in Appendix C. The VT-Stim simulation using conventional RVA & RVOT on this patient did not induce any VT. This is in agreement with the clinical data on this patient who did not have any VT episode. However we could induce VT using various other pacing sites and pacing protocols. For simplicity, we demonstrate the results of an overdrive pacing protocol for a pacing location within PIZ, in Fig. 6.13 with protocol as described in Table C.3 in Appendix C. Few snapshots of the video on personalised induced VT simulation are presented in Fig. 6.12 demonstrating the re-entry wave. More snapshots on the simulation is given in Table D.3 & D.4 in Appendix D. Appendix D Table D.3 & D.4 shows the simulation results of various pacing protocols with successful VT inductions.

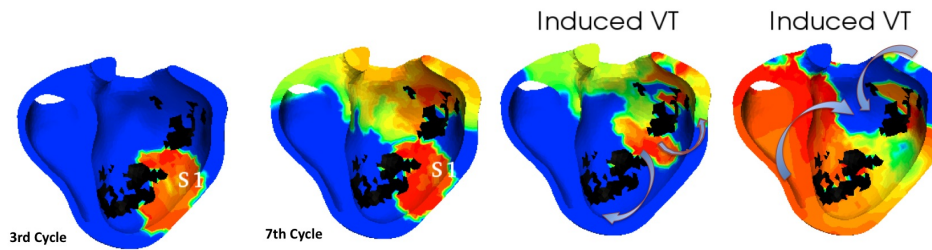


Figure 6.12: Induced VT in the personalised model. At the 7th cycle of the pacing overdrive, some areas in the isthmus have the previous S1 wave-back touching the wave-front of the next S1 wave, thus creating an uni-directional block. A monomorphic sustained VT then develops.

4 VT Risk Stratification

VT risk is defined or quantified as a vulnerability measure of the patient's heart to induce ischemic VT. Patient-specific VT risk assessment is performed by simulation of various VT-Stim protocols (Appendix C Table C.4) on personalised electrophysiology model, and deriving VT inducibility and exit point maps. The risk measure is indirectly inferred from these maps. Appendix D Table D.5 shows such maps for different pacing sites and protocols

VT inducibility maps These maps (Fig. 6.14) show the pacing locations in the heart, which were successful in inducing VT for a given protocol. In pre-ablation therapy, these maps can provide a vulnerability measure of patient's heart towards induction of VT, thus providing a patient-specific VT risk. During post-ablation

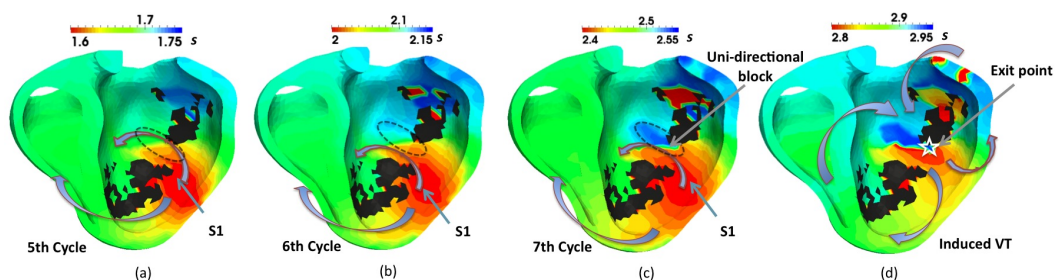


Figure 6.13: DT isochrones for simulated VT-Stim protocol for over-drive pacing using the personalised electrophysiology parameters, with pacing near the scars (shown by arrow) at 400 ms cycle length (≈ 150 bpm). (a) shows normal propagation (b) & (c) show increase in heterogeneity in conduction near the isthmus after 7 cycles due to APD and refractoriness heterogeneity (black ellipse) and (d) no pacing and induced VT of 250 ms cycle length (≈ 240 bpm) with an exit point (shown by a star).

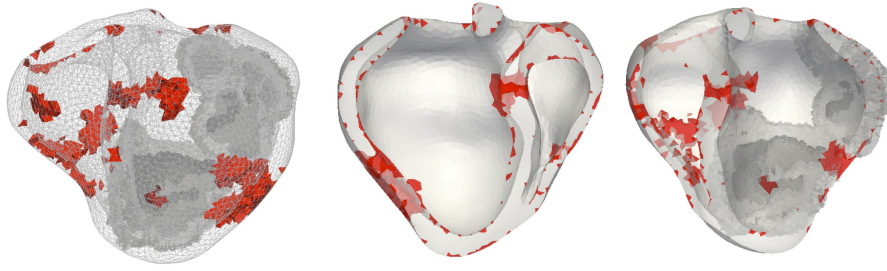


Figure 6.14: All possible locations (red) for VT inducibility for different protocols and generation of self sustained VTs. They lie mostly near the RV apex and PIZ.

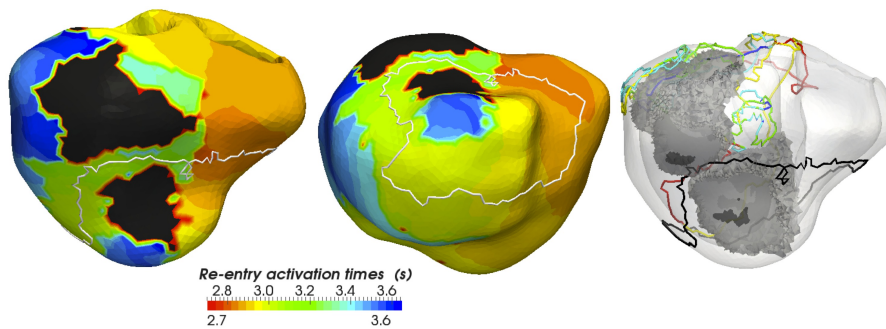


Figure 6.15: First two figures show the main re-entry pattern geodesic path of highest conduction velocity traced for a VT re-entry. The last figure on right shows all possible VT re-entry mechanisms present in the personalised model.

therapy, these maps can be of potential interest in careful placement of ICD/CRT leads to avoid inducing VT.

VT re-entry patterns These maps (Fig. 6.15) track the re-entry paths, as the geodesic path of highest conduction velocity along the re-entry isochrones. This path is related to the VT cycle length, and shows *in silico* the main re-entry pattern or path for ischemic VT, which could be of potential use in guiding the ablation lines. *In silico* VT-Stim modelling helps model different possible VT-mechanisms present in the patient, which could all be visualised using such VT re-entry patterns.

VT exit point maps These maps (Fig. 6.16) locate all the possible exit points estimated for various protocols and pacing locations. The exit points are defined as the points having earliest activation times in the re-entry isochrones. For a given protocol, various pacing locations may lead to detection of various exit points, with some of them having more probability of occurrence as shown in Appendix D Table D.5. For RF ablation procedure, only those points with higher likelihood of occurrence are used.

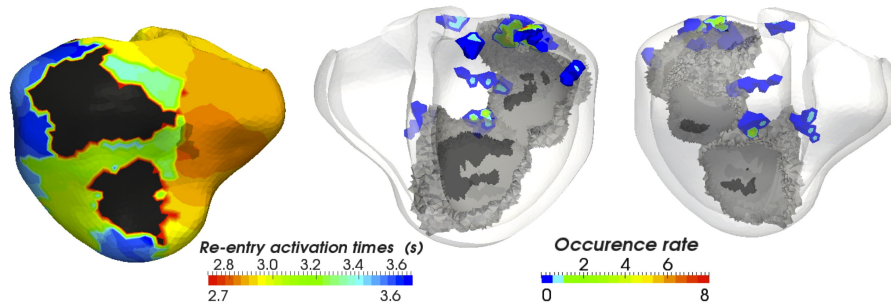


Figure 6.16: First figure shows the extraction of an exit point (red coloured region) for a particular VT re-entry. The next two figures show all the possible exit points for VT re-entries with an occurrence rate for different VT-Stim protocols.

5 Conclusion

In this work, we illustrated the main macroscopic characteristics of an ischemic VT. These include the structural and functional heterogeneity of the tissue near the scars i.e. peri-infarct zones (PIZ). PIZ are crucial in the initiation and sustainment of ischemic VT. Macroscopic structural heterogeneity was achieved with: 1) The incorporation of a decrease in fibre organisations in PIZ was performed by using a mixture of anisotropic and isotropic propagation, the ratio of which was controlled by the percentage of patchiness in the fibrotic tissue. 2) The fibrosis was modelled for its macroscopic behaviour using multi-domain models, which included healthy myocytes and collagen network. As a first approximation, the collagen network was modelled by an isotropic diffusion term with low conductivity, to account for the high resistivity whereas the domain of healthy myocytes was modelled with anisotropic diffusion term with normal cardiac tissue conductivity.

Macroscopic functional heterogeneity was achieved from the patient-specific tissue heterogeneities estimated (CV, APD, CV & APD restitution) using the proposed coupled personalisation framework. Later, we demonstrated the simulation of an *in silico* VT stimulation study using the personalised and adapted MS model, to quantify VT risk *in silico*, in terms of VT inducibility maps, VT re-entry patterns and VT exit point maps (potential RF ablation targets).

Modelling Radio-Frequency Ablation

Contents

1	Radio-frequency Ablation: Concepts & Modelling	96
1.1	Types of Ablation	97
1.2	RF Ablation of VT	98
1.3	Lesion Formation	99
1.4	Lesion Size	104
1.5	Lesion Characteristics & Modelling	105
2	Radiofrequency Ablation on VT patients	106
2.1	Simulation of Radiofrequency Ablation	106
2.2	Short Term Effect of RF Ablation	106
2.3	Long Term Effect of RF Ablation	108
3	Conclusion	109

Based on:

Section 1 is based on a joint work with IBT Germany in [KSS⁺11]

[RDS⁺11] J. Relan, H. Delingette, M. Sermesant, N. Ayache, M. W. Krueger, W. Schulze, G. Seemann, and O. Dössel. Planning of Radiofrequency Ablation for Patients with Ventricular Tachycardia. Deliverables D6.3.2, European project euHeart, June 2011.

A rule-based modelling approach for radio-frequency (RF) ablation lesions based on state of the art studies is proposed. This approach is carried out due to the lack of patient's imaging data on RF ablation lesions. Furthermore, the acute and chronic effects of the RFA lesions are simulated. The chronic RFA lesions were then used in the in silico VT stimulation study, as a post ablation protocol to assist in estimating the success of RFA lesions in silico.

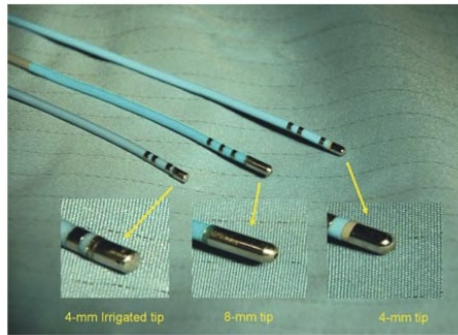
1 Radio-frequency Ablation: Concepts & Modelling

In radio-frequency (RF) ablation procedure, RF alternating current is usually administered with a continuous sinusoidal unmodulated waveform of 300 - 1000 kHz and allows the generation of well-circumscribed myocardial lesions. The most important mechanism of myocardial necrosis induction is based on the conversion of electrical energy into heat within the myocardial tissue. The extent of the tissue damage depends on the following:

- The duration of RF energy application
- The temperature in the resistive heating zone
- The RF power delivery
- The catheter contact force against the tissue

However, at a certain energy level electrode overheating may occur leading to coagulum formation and charring on the tip electrode accompanied by a rapid increase in electrical impedance that in turn leads to a loss in effective myocardial heating. To prevent overheating at the electrode-tissue interface, temperature-controlled energy application systems have been developed. A thermistor or thermocouple embedded in the tip of the ablation catheter allows temperature monitoring at the electrode-tissue interface during energy application. Maximal RF energy (usually 50 W) is delivered until the preselected target temperature has been reached and thereafter automatically titrated down to maintain the target temperature. The extent of lesion formation not only depends on RF duration and power but also on non-measurable variables like electrode-tissue contact and orientation (perpendicular vs parallel to the tissue) and external cooling by the circulating blood flow. By using cooled-tip catheters the temperature at the electrode-tissue interface can actively be cooled down and thus allowing higher currents [NE06]. A photograph of such catheter tip is shown in Fig. 7.1(b).

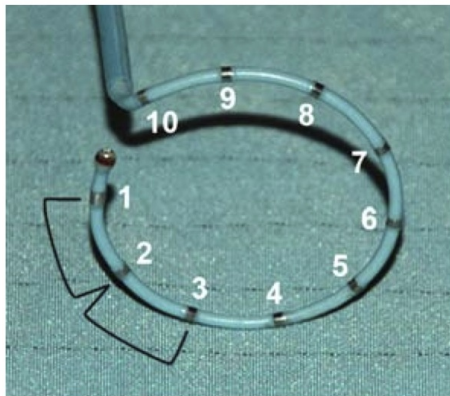
During minimally invasive RFA intervention, various catheters are introduced into the right heart via the femoral veins. Trans-septal puncture in the atria allows access to the left heart. Besides the ablation catheter (Fig. 7.1(a), 7.1(b), 7.1(d)), circular mapping catheters (Fig. 7.1(c)), multi-electrode basket catheters for contact or non-contact measurements as well as multi-electrode mapping and coronary sinus catheters may be used by the clinician.



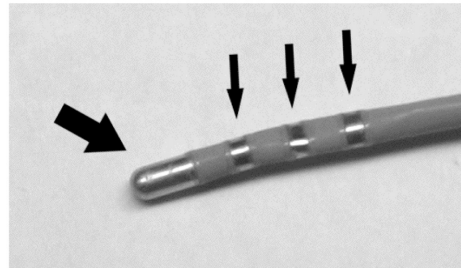
(a) Image from [NE06].



(b) Image from [NE06].



(c) Image from [DEP].



(d) Image from [Hae10].

Figure 7.1: Photographs of catheter tips used during RFA procedure.

1.1 Types of Ablation

Various possibilities to introduce lesions into the myocardium are known and used in clinical practice:

- Surgical Maze III procedure [CJSB95]
- Radio-frequency ablation
- Cryoablation [AUR+03]
- Ultrasound ablation
- Laser ablation
- Microwave ablation [vBBS+04]

In this thesis, we concentrate on RFA, as it is currently the most commonly used ablation technique in clinical practice. Instead of applying ablation lesions, some patients can and must be treated pharmacologically for their cardiac arrhythmias. Pharmacological treatment is often also accompanying the ablation therapy. For simplicity, we neglect the pharmacological influences on the patients. Further information about the complete therapy cycle can be found in a clinical review by Natale et al. [NRAA+10] and Lin & Marchlinski [LM03] for RFA of VT patients.

1.2 RF Ablation of VT

Implantable cardioverter defibrillators (ICDs) have become the mainstay of therapy for such patients; however, ICDs do not prevent the occurrence of these arrhythmias, and poorly tolerated recurrent high-voltage cardioversions or defibrillation shocks can result [MZC⁺00]. Because of the limitations of device therapy and inefficacy and poor tolerance of drug therapy, ablative therapy has become an important additional tool in the treatment of such VTs. Natale et al. [NRAA⁺10] provides an extensive international consensus on the state of the art for ablation of ventricular tachycardia and fibrillation. Lin & Marchlinski [LM03] provides a review on advances in ablation therapy for cardiac arrhythmias. The ablation strategies applied depend on the different forms of VT.

1.2.1 Ablation of stable VT

In selected patients with recurrent VT, which is inducible and hemodynamically stable and therefore mappable, radio-frequency catheter ablation has proven reasonably effective. A number of reports have documented the long-term success rate of radio-frequency ablation of VT to be greater than 70%, with serious complications in fewer than 2% of patients [SMD⁺97]. Multiple criteria have been used to guide ablation of hemodynamically stable VT and are frequently used in combination to optimise results [ESHP⁺99]. These criteria include the following:

- Presence of pre-systolic electrogram activity recorded during VT
- Evidence for concealed entrainment with pacing during VT
- A return cycle length equal to the VT cycle length
- A stimulus to QRS during pacing that is equal to the electrogram to QRS during VT.

Entrainment is the continuous resetting of the tachycardia by a drive train of stimuli and implies the presence of an excitable gap within the re-entrant circuit. Entrainment can occur during pacing at sites that are either within or outside the re-entry circuit, and entrainment alone does not indicate the location of the pacing site relative to the re-entry circuit. The phenomenon of concealed entrainment has been shown to identify a zone of slow conduction within the circuit of the VT [SFS⁺97].

The success rate with limited lesion delivery reported by various groups using the described mapping and entrainment criteria ranges from 50% to 90%, with a 20% to 40% late recurrence rate [SMD⁺97, MHK⁺93]. Limitations to entrainment mapping include the presence of a wide isthmus, a deeper anatomic location of the recorded isthmus, or dense fibrosis and calcification preventing adequate lesion size.

1.2.2 Ablation of unstable VT

In patients with hemodynamically intolerable, unstable and unmappable VT, applicability of catheter ablative therapy using standard mapping and focal ablation techniques is very limited. The reasons are the presence of multiple and changing

VT morphologies with catheter manipulation or pacing protocols, and the non-inducibility of the VT.

An ablation strategy that incorporates techniques that identify important anatomic targets is critical for widening the applicability of catheter ablative therapy for such VTs. Catheter-based mapping and surgical mapping in such VTs have confirmed the site of origin of most VT to be localised to the transition from the dense scar to the normal endocardium, the so-called border zone. A systematic approach proposed and used [SSM⁺01, LM03] to ablate unmappable VTs has the following steps:

1. Analysis of 12-lead electrocardiogram (ECG) for all induced and spontaneous VTs to regionalise an endocardial area of interest to perform more detailed pace-mapping
2. Generation of a detailed sinus rhythm voltage map to identify the location and extent of the border zone and define all aspects of the endocardial anatomy
3. Perform pace-mapping to target the border zone adjacent to the area of dense scar with the starting point of our pace-mapping attempts based on the 12-lead ECG analysis
4. Localizing the site of the closest pace maps with 12 out of 12-lead ECG match determined and tagged along the edge of the border zone and dense scar
5. Generation of linear ablation lesions created by applying a series of point lesions, with the lesions extending from the edge of normal myocardium (i.e., signal voltage amplitude $> 2\text{mV}$) or an anatomic barrier like the mitral valve across the border zone and 1 to 2 cm into the area of dense scarring (amplitude $< 0.5\text{mV}$)

In this thesis, we concentrate on RFA therapy planning for the described two forms of VTs, by providing patient-specific VT re-entry circuits and maps of exit points (optimum ablation targets), through *in silico* simulations of clinical pace-mapping protocol on patient-specific heart models. We model the acute and chronic effect of RFA lesions, to predict the acute and chronic VT inducibility risk, which could be interpreted as acute success and long-term success.

1.3 Lesion Formation

RFA lesion size in myocardium is influenced by many parameters such as delivered RF power, electrode length, electrode orientation, blood flow and tissue contact [Eic03]. We concentrate on modelling the state of RFA lesions after the ablation, it is necessary to understand the factors influencing RFA lesion formation as these build the basis for temporal post-ablation lesion behaviour. The following relationships are reported in literature:

- **Linear** relationship between **temperature** and **lesion depth** [Hai93, NDH94, Hai08]. Fig. 7.2a) shows the data from [Hai08].
- **Linear** relationship between **applied current** and **lesion depth** [Hai08]. Fig. 7.2b) shows the data from [Hai08].
- **Linear** relationship between **electrode radius** and **lesion depth** [Hai93, NE06]. Fig. 7.2c) shows the data from [Hai93].

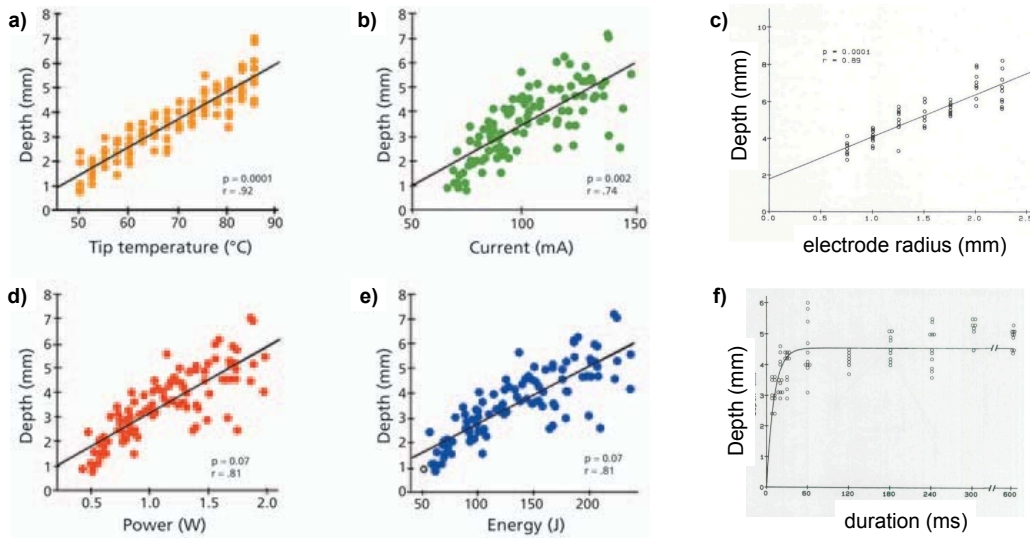


Figure 7.2: Factors influencing RFA lesion size. For details see text. Images from [Hai93, Hai08, NDH94].

- *Linear* relationship between **power** and **lesion depth** [WHRdM89, Hai93, Hai08]. Fig. 7.2d) shows the data from [Hai08].
- *Linear* relationship between **delivered energy** and **lesion depth** [Hai08]. Fig. 7.2e) shows the data from [Hai08].
- *Logarithmic* relationship between **application time** and **lesion width & depth** which reaches steady state after approximately 45-60 seconds [WHRdM89, Hai91, NDH94]. Fig. 7.2f) shows the data from [NDH94].
- *Linear* relationship between **contact force** and **lesion width** [Hai91, TDF⁺10].

As mentioned before, lesion formation in the myocardium is mostly due to a heating of myocardial tissue by radio-frequency current (hyperthermia). The myocardium needs to be heated above 50°C in order to become necrotic [NLWH93, NDH94]. Recently Wood *et al.* found this threshold to be 60°C [WGL⁺11].

If new RFA lesions are placed in areas of previous scars, an increased impedance between catheter tip and myocardium and decreased tissue temperatures can be observed [CVT⁺01]. Nevertheless, lesion formation is not affected by underlying scar as long as electrode size, tissue contact and temperature are controlled [KDP⁺06].

In the following sections we provide more detailed information about the heat transfer processes, the alterations in cardiac electrophysiology during tissue heating and the morphology of acute lesions. Although the process of lesion creation is not subject of modelling here, its understanding is essential to model post-ablation RFA lesion electrophysiology, morphology and temporal behaviour.

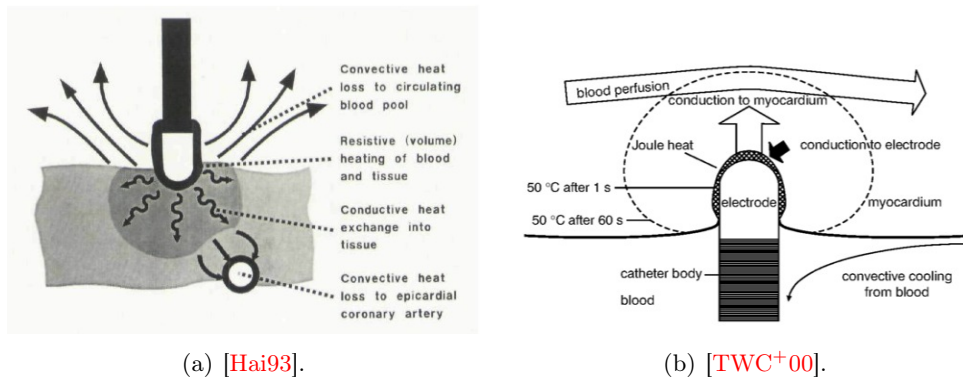


Figure 7.3: Schematics of the thermodynamic processes during RFA.

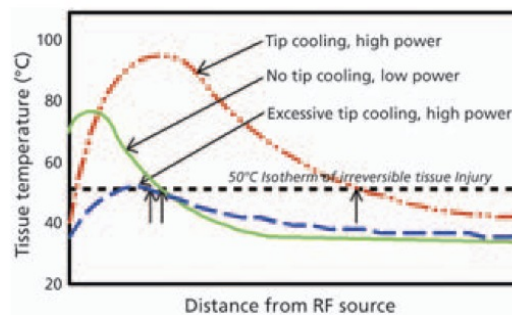


Figure 7.4: Tissue heating with regular and cooled-tip catheters. Image from [Hai08].

1.3.1 Heat Transfer Processes

During RFA, various heat transfer processes take place in the region of the catheter tip and myocardium. The desired effect is that the catheter tip exchanges heat conductively with the myocardium. Resistive heating of myocardial tissue is only effective for distances less than 2 mm from the catheter tip [NE06]. Additionally, a resistive heating of blood and tissue near the catheter tip is taking place. The catheter as well as the endocardial myocardium is cooled by convective heat loss to the circulating blood pool. Additional heat loss is observed in areas with large coronary arteries [Hai93, TWC+00]. The processes are depicted in Fig. 7.3. When tissue is overheated, charring may occur. This may build up an insulating endocardial layer, preventing a deep extent of the lesion. A greater transmural extent of the lesion can be achieved by active and controlled tip cooling using cooled-tip catheters [Hai08] (Fig. 7.4).

1.3.2 Electrophysiology during Hyperthermia

The electrophysiological properties of myocardial cells change under hyperthermia. These effects are reversible with falling temperature and are thus not subject for

model integration.

During the process of heating, tissue conductance is increased by 2% per degree Celsius [TWC⁺00]. Wood and Fuller report an increase in conduction velocity during hyperthermia, most likely caused by cell shrinkage and / or changes in cell-to-cell coupling [WF02].

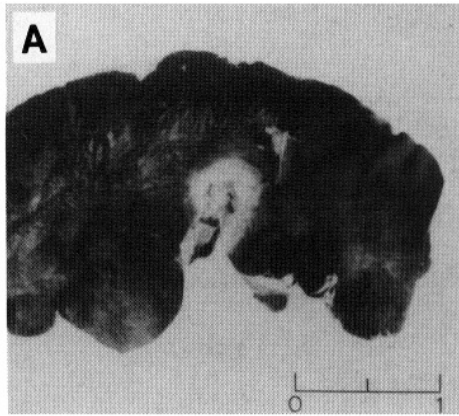
Haines reports an increased automaticity in cardiac cells which are heated around 50°C in contrast to cells at 45°C [Hai08]. Nath et al. state a sigmoidal relationship between tissue temperature and cell membrane depolarization [NLWH93, NDH94]. Nath et al. also report changes in action potential morphology and duration [NLWH93]. Additionally, they show three stages of excitability of myocardial cells during hyperthermia. The median temperature associated with normal excitability (44.0°C) is significantly lower than the median temperature associated with reversible loss of excitability (48.0°C) and irreversible loss of excitability and tissue injury (50.5°C) [NLWH93, NDH94].

1.3.3 Acute Lesion Morphology

Fig. 7.5 shows some macroscopic images of ablation lesions. Nath et al. and McRury & Haines both describe RFA lesion to have two border zones (each 3 mm radius) in the acute phase after RFA [NDH94, NWK⁺94, MH96]. Nath et al. revealed a reduced blood flow in these border zones due to micro vascular injury [NWK⁺94]. In contrast to these findings, Ndrepepa and Estner describe only two zones: A necrotic core and a haemorrhagic border zone [NE06]. The latter is caused by disruption of endothelial cells and erythrocyte passage. Their findings are based on experiments from Hindricks et al. [HHG⁺89]. They also describe spots of haemorrhage in the necrotic zone.

The shape of the lesions is caused by the thermal processes during RFA (Section 1.3.1). Circulating blood in the chamber cools the endocardial surface and thus prevents a great endocardial extent of hyperthermia. This cooling process has only very limited transmural extent and thus, the lesion extent at the endocardial surface is less than in the mid-myocardial region. Epicardially, the scar is narrower than in the centre, because the resistive heating from RFA is also decreasing with distance. Additionally, coronary vessels at the epicardial surface form another heat sink.

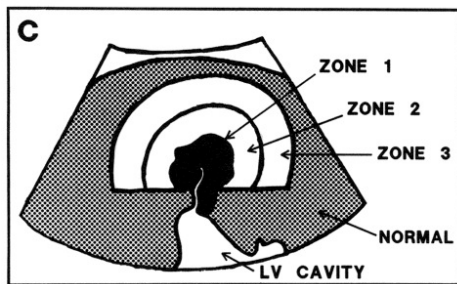
The acute lesion is covered endocardially with a fibrinous layer [NE06]. Volume loss in ablated tissue may lead to an impressed endocardial scar surface [NE06]. In excised tissue, lesions have a pale white colour, due to the local denaturation of myoglobin [NE06]. Overheating of tissue directly underneath the electrode tip may lead to small areas of vaporization of tissue. There are also hints, that if the myocardial wall is very thin, an inflammatory swelling might occur epicardially. We tried to illustrate schematically an idealised shape of acute RFA lesion in Fig. 7.6. We thereby chose to include as much known information about acute RFA lesions as possible. So the schematic drawing reflects the most complex possibility to model a RFA lesion. Depending on the purpose of a simulation, the morphology of the lesion can be simplified in the model. E. g. to model the chronic state of a lesion, border



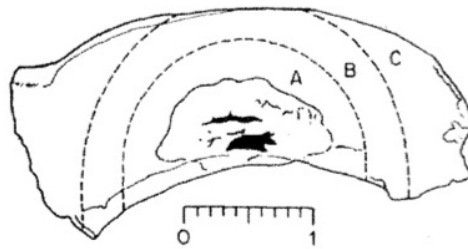
(a) [NWK⁺94].



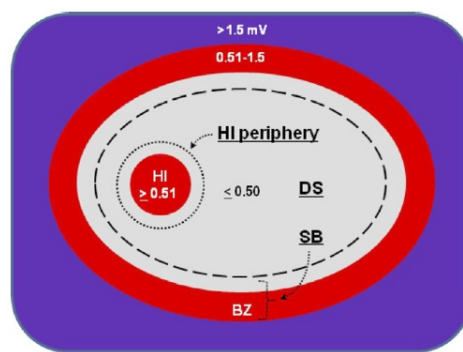
(b) [MH96].



(c) [NWK⁺94].



(d) [MH96].



(e) [NTR⁺10].

Figure 7.5: Microscopic images and schematic drawings of ablation lesions.

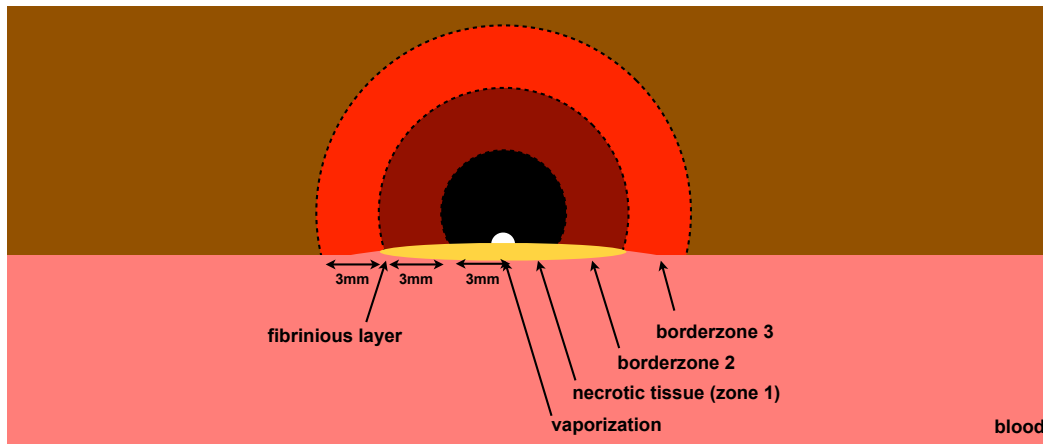


Figure 7.6: Schematic drawing of an RFA lesion.

zones, fibrinous layer and inflammatory swelling could be neglected. Additionally, for some simulation types, it is not necessary to include non-myocardial tissue into the model, as it does not influence excitation propagation under certain assumptions, e. g. rule-based excitation propagation. For VT simulations, inflammatory swelling of the myocardial wall can be neglected, as the left ventricular wall is so thick that inflammatory swelling might not play a significant role.

1.4 Lesion Size

The size of a RFA lesion is depending on its location in the heart and the time passed since the ablation process.

1.4.1 Acute effect

Saul et al. report width of acute lesions of 5.9 ± 2.5 mm (ventricle) [SHP⁺94]. Similar sizes were found by Wood & Fuller in the ventricles (5.4 ± 0.48 mm) [WF02]. A stronger difference in size can be observed in lesion depth, which varies from 2.8 ± 0.7 mm [WF02] to 4.2 ± 2.0 mm [SHP⁺94] for the ventricles [SHP⁺94].

1.4.2 Chronic effect

Most of the studies agree that lesions grow after successful ablation of the myocardium. Lesion width in the ventricles increased to 7.2 ± 1.0 mm after 22 days [WF02] and to 7.4 ± 2.5 mm after one month [SHP⁺94]. Lesion depth in the ventricles increased as well to 3.3 ± 0.4 mm and to 4.5 ± 1.9 mm after 22 days and one month, respectively.

The growth of RFA lesions has been described by Nath et al. [NDH94] and van Brakel et al. [vBBS⁺04]. Van Brakel especially reported, that transmuralty of RFA lesion increases over time [vBBS⁺04].

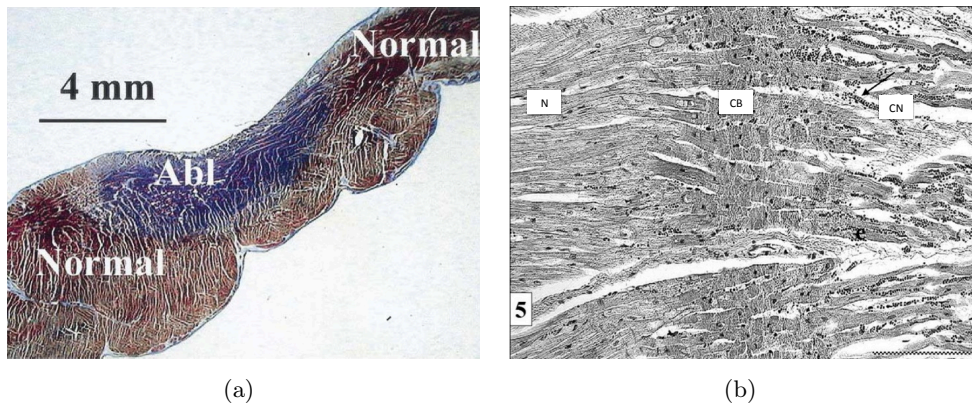


Figure 7.7: (a) Ablation lesion in myocardium, Gomorri's trichrome staining. Lesion looks blue and unaffected tissue is red. Image taken from [TGB+03]. (b) Cardiac RFA lesion, showing three zones: N = normal myocardium, CB = borderline zone of contraction band necrosis, CN = zone of coagulation necrosis. H & E staining, bar is 200 μ . Image taken from [ADW+05]

1.5 Lesion Characteristics & Modelling

RFA impacts the ventricular myocardial tissues in various ways. Fig. 7.7(a) shows a cardiac RFA lesion, post ablation. The lesion (marked "Abl"), consists of necrotic cells. Necrosis is found in roughly two zones, as can be seen in Fig. 7.7(b). The zone that was nearest to the electrode shows coagulation necrosis (marked "CN"), in which the cell structure is totally disrupted. It can be recognised by a loss of cell definition, separation of the fibres by oedema, extravascular red blood cells, and loss of nuclei and cross-striations [TGB+03]. Around this zone of coagulation necrosis, a border zone with partial necrosis exists (marked "CB"). In this zone, the cross striations and sarcolemma are partially preserved. This zone is sometimes hard to distinguish, but is important to recognise, as recovery of the cells might undo the electric isolation.

Normal (N), CB and CN are modelled as the three main compartments of the RF ablation model. In a short term, the necrotic tissue (CN) is surrounded by inflammatory tissue and oedema. These tissue types might remain conductive, but conduction slowing might occur. In a long term, it is possible to model ablation lesions as non-conducting myocardial tissue (CN), maybe surrounded by CB with diffuse fibrotic tissue.

1.5.1 Electrophysiology

Wood & Fuller [WF02] have stated the acute and chronic electrophysiological changes in and around the RF lesions. For the acute effect, they have shown significant reduction in APD50 (41% less), APD90 (19% less), APDmax (16% less), and conduction time (from 16 ± 3 msec to 13 ± 4 msec) in the border zone surrounding the necrotic

core, post ablation. For the chronic effect, these electrophysiological changes were resolved within 22 ± 13 days of lesion formation. These studies were similar to the findings of Wu et al [WFCT99]. Ge et al. found similarly that APD, AP amplitude, resting potential and dV/dt is decreased in a radius of up to 8mm around acute lesions [GSGK95].

Thus, for modelling the acute effect of RFA lesions, we chose to have a slowed conduction and shorter APD in the border zone, mainly comprising of inflammatory tissue and oedema. On the other hand, for modelling the chronic effect, we chose to have a healthy action potential morphology in the border zone, along with diffuse fibrosis.

1.5.2 Fibre Orientation

Ndrepepa and Estner state that tissue under the effect of RF current loses its normal fibre orientation [NE06]. They do not state how fibre structure changes. The necrotic tissue is considered to be non-conductive. The border zone tissue is assumed to have slowed conduction during the acute effect of RFA and normal in chronic RFA. The border zone tissue is assumed to have fibre structure changes, similar to peri-infarct regions (Fig. 6.4) but with a texture of diffuse fibrosis (Fig. 6.4E) (to have less arrhythmogenic substrate, as compared to patchy fibrosis (Fig. 6.4D) found in peri-infarct regions). On a macroscopic level, the diffuse fibrosis is assumed to have rather isotropic conduction properties.

In contrast to detailed electrophysiological modelling, the change in fibre structure might impact active and passive mechanical properties of the myocardium, thus it is probably necessary to be considered in future mechanical simulations.

2 Radiofrequency Ablation on VT patients

2.1 Simulation of Radiofrequency Ablation

In this work, we focus only on modelling the state of RFA lesions post ablation therapy, and not during the therapy. A rule-based modelling approach of RFA lesions post ablation therapy was applied, due to the lack of imaging data post RF ablations, due to an ICD implantation. As discussed in section 1.4, we used the lesion size as described in the literature, to model the acute and chronic effects of RFA therapy. Fig. 7.8 shows acute and chronic RFA lesions created on a cardiac tissue slab, along with the different compartments of the model. The loss in normal fibre orientations were also modelled synthetically by generating random fibre orientations in the necrotic core and border zones, as shown in Fig. 7.9.

2.2 Short Term Effect of RF Ablation

Fig. 7.8(top row) & Fig. 7.9(a) were used to model the acute effects of RFA lesions. The necrotic core was modelled as electrophysiologically inactive, with no conduction at all. The border zones were considered to have slower conduction and shorter

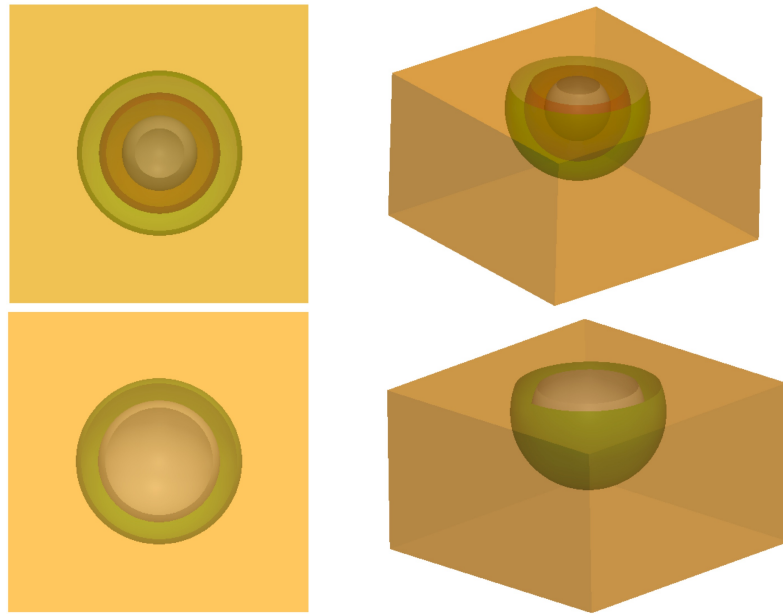


Figure 7.8: Cardiac tissue slab preparation to evaluate RF ablation simulations for acute (top row) and chronic effects (bottom row). Acute effects show a necrotic core (grey) with a borderzone (dark red) corresponding to inflammation and a borderzone (green) corresponding to the gradient of damaged tissue from necrosis to healthy tissue. Chronic effects show an increase of the necrotic core size (black) with a borderzone (green) having diffuse texture tissue, which represents the gradient between necrosis and healthy tissue.

APD morphology, due to reasons as described in section 1.5.1. The diffuse fibrosis was modelled macroscopically, with a mixture of 20% anisotropic and 80% isotropic propagation (as detailed in section 2.1.1 Eq. 6.1 with $k = 0.8$). In order to study those effects in details, we simulated such behaviour on a cardiac tissue slab and the results are shown in Fig. 7.10(a). For patient-specific RF ablation simulations after the data acquisition, only those exit points, which had high occurrence rate are chosen as ablation targets, to have a robust approach. Fig. 6.16 shows such locations for a patient data.

The VT-Stim modelling is then re-simulated on the personalised electrophysiological model, after embedding of the acute RFA lesions. This derives a new VT risk, in terms of VT inducibility maps. If VT is still induced, also after the formation of RFA lesions, new exit points are mapped and modelled with acute RFA lesions, until no VT is inducible with all protocols as described in table C.4.

Finally, all the exit points mapped during this process are marked as potential exit points for planning of RFA therapy.

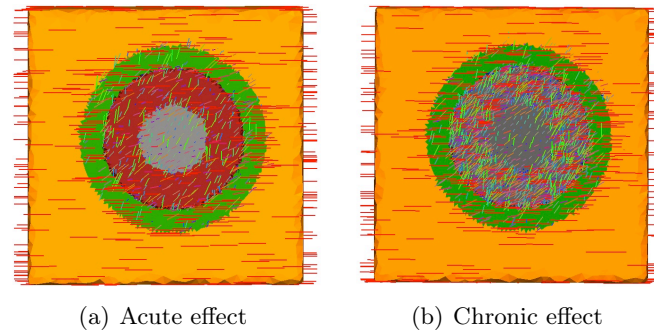


Figure 7.9: Synthetic disorganisation of myocardial fibres in border zones (dark red and green) and necrotic core (black) for electrophysiology simulations with RFA lesions. For fibre colours refer Fig. 6.4.

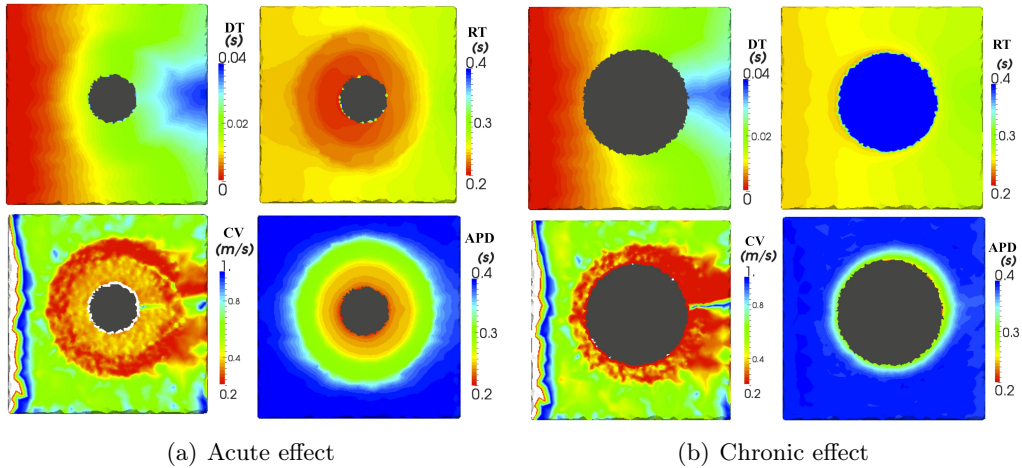


Figure 7.10: Simulation of acute & chronic effects for RFA lesions on a cardiac tissue slab.

2.3 Long Term Effect of RF Ablation

Fig. 7.8(bottom row) & Fig. 7.9(b) were used to model the chronic effects of RFA lesions. The necrotic core was again considered to be electrophysiologically inactive, but with an increase in its size due to the findings described in section 1.4. The border zones were decreased in size, with the recovery of healthy electrophysiological behaviour, in the presence of diffuse fibrosis, with reasons as explained in section 1.5. These effects were studied on the cardiac tissue slab with results shown in Fig. 7.10(b).

After data acquisition, VT-Stim modelling is performed on the personalised electrophysiological model with embedding of chronic RFA lesions, as shown in Fig. 7.11. One of its potential use is to assess the VT recurrence rate after the RFA therapy.

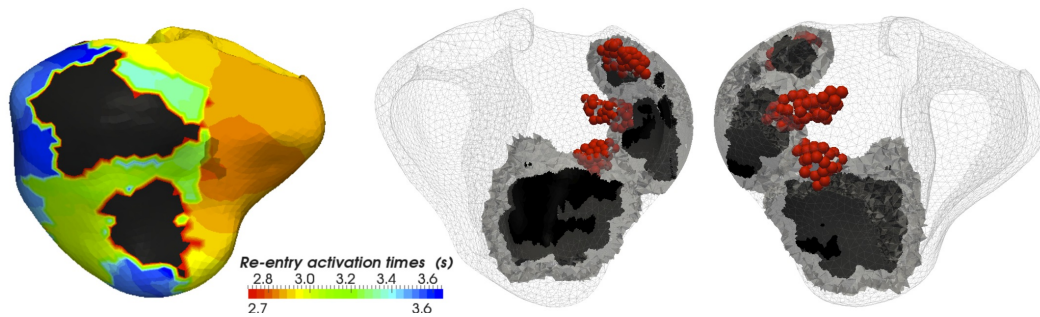


Figure 7.11: (middle & right) Placement of chronic RFA lesions (in red) planned with *in silico* VT-Stim study for the personalised clinical data. One of the re-entry map studied for RFA planning (left), others are shown in Appendix D in Table D.5.

3 Conclusion

In this work, we proposed a rule based modelling approach for RF ablation lesions based on the state of the art studies. This approach was carried out due to the lack of patient's imaging data, on RF ablation lesions. As the patients had a pacemaker implanted at the end of the ablation procedure. This rule based modelling approach also incorporated the acute and chronic effects of the RFA lesions. The chronic RFA lesions were then used in the *in silico* simulation of VT stimulation study post ablation therapy to assist in estimating the success of RFA lesions *in silico* and locating the potential RFA targets.

Part IV

CLINICAL APPLICATION &
VALIDATION

Planning of Radio Frequency Ablation using *in-vivo* Clinical Data

Contents

1	Introduction	114
2	Methods	115
2.1	Clinical Study: Patient Recruitment and Pacing Protocol	115
2.2	Data Analysis	116
2.3	VT Modelling Study: Personalisation and Pacing Protocol	117
3	Results	122
3.1	Estimation of the patient-specific spatial heterogeneities	122
3.2	Correlation of the spatial heterogeneities: Inter-patients	124
3.3	Induced VT: Clinical observations vs. Model predictions	126
3.4	VT & Exit point predictions	127
4	Discussion	128
4.1	Tissue conductivity & APD restitution slope heterogeneity	128
4.2	Data Limitations & Model personalisation	130
4.3	VT Model Predictions & Simplifications	131
5	Conclusion	131

Based on:

[RCD⁺12] J. Relan, Z. Chen, H. Delingette, R. Karim, W. Schulze, J. Bostock, C. A. Rinaldi, K. Rhode, N. Ayache, R. Razavi and M. Sermesant. Role of spatial heterogeneity of restitution and conduction in ischemic ventricular tachycardia: a combined clinical and modelling study. 2012. Article in preparation.

Background – Steep and shallow action potential duration (APD) restitution curves as well as varying conduction velocity (CV) have been shown to facilitate wave-break and ventricular arrhythmias. However the influence of the spatial heterogeneity of APD restitution and CV at the heart scale on the onset of ischemic ventricular tachycardia (VT) in patients is unknown.

Objective – Using a combined modelling and clinical approach, our objectives were to: (1) determine the patient-specific spatial heterogeneity of APD restitution and CV over the left ventricular (LV) endocardium, (2) correlate this heterogeneity with the observed VT exit points, and (3) to use a model to predict the exit points and the VT circuits based on the given spatial heterogeneities, and compare with clinical observations.

Methods – We studied 6 cardiac patients, 4 with ischemic heart disease (IHD) and 2 with dilated cardiomyopathy (DCM). An electrophysiological study was performed on each patient with a non-contact electro-anatomical mapping system. The eventual scars were segmented from a high resolution late gadolinium enhanced cardiac magnetic resonance imaging (LGE-CMR). Two of the IHD patients were mapped during a complete VT stimulation study. A simplified biophysical monodomain action potential model was personalised to the patient's anatomy (including scars and peri-infarct areas) to estimate the spatial heterogeneities, and used for VT prediction using an *in silico* VT stimulation study with Wellen's protocol.

Results – Spatial heterogeneity of the maximum APD restitution slopes was higher for IHD cases than DCM cases. Distribution of the maximum APD for the restitution curves was less heterogeneous for all cases, thus proved to be less discriminative. Exit points were observed to lie in the regions with low conductivity, steeper restitution slope and higher maximum APD islands.

Conclusions – Patient-specific spatial heterogeneity of APD restitution and CV seem to be good indicators for the locations of crucial entry/exit points of VT circuits. The personalised *in silico* VT-Stim model was sufficient to predict the macroscopic characteristics of the VT circuits and the entry/exit point locations as observed in the clinical data, along with some additional clinically unobserved entry/exit points.

1 Introduction

Radio-frequency (RF) ablation therapy are increasingly being used to treat drug resistant ventricular arrhythmia, especially those related to ischaemic cardiomyopathy to provide a curative therapy. These procedures can be very effective but still have unsatisfactory success rates widely ranging from 50–90%, with a 20–40% late recurrence rate, due to a lack of clinical consensus on the optimum RF ablation strategy [ASAG09]. There is a need for identifying those at high risk of developing

ventricular arrhythmia as well as a need for substantial guidance in designing the optimum ablation strategy [SKS⁺93].

Computational modelling of cardiac arrhythmogenesis and arrhythmia maintenance using such models has made a significant contribution to the understanding of the underlying mechanisms [CW91, WFE⁺01, PK95, JG96, CF04, CR95]. These studies have shown a host of factors involved in the onset of arrhythmia with wave fragmentation and spiral wave breakups, taking into account of real ventricular geometry [TT09], tissue heterogeneity in repolarisation [KSGH08, PCV⁺11] and APD restitution [YFRM05, ART07] and CV restitution [BG02]. A combined clinical study and synthetic modelling of APD restitution was shown in [NBS⁺06]. In this paper, we studied these properties for clinical datasets and evaluated how these properties are involved in the induction of ventricular tachycardia in ischaemic cardiomyopathy.

To introduce models directly into clinical practice, and to personalise with patients data, we used a coupled personalisation framework [RCS⁺11], which is fast and combines the benefits of an Eikonal (EK) model [SCMV⁺05] with those of a simplified biophysical model, the Mitchell-Schaeffer (MS) model [MS03], as explained in Chapter 4.

Model personalisation is performed to estimate patient-specific APD restitution and CV heterogeneity. This heterogeneity is then correlated with clinically observed exit points. The resulting personalised 3D MS model is then used to simulate a clinical VT-Stimulation (VT-Stim) study to predict the VT isochrones and exit points which are then compared with clinically observed VT. The spatial heterogeneity of the observed exit points sites during the sustained VT are characterised and correlated with the electrophysiology characteristics such as APD restitution and CV heterogeneity at the region.

2 Methods

2.1 Clinical Study: Patient Recruitment and Pacing Protocol

We studied 6 cardiac patients, n=4 with Ischemic Heart Disease (IHD) & n=2 with Dilated Cardio-Myopathy (DCM). Two cases (IHD_1 & IHD_2) had undergone an invasive programmed ventricular stimulation (chronic ischemia patients; LV ejection fraction $\leq 45\%$), while the other cases had simultaneous non-contact mapping of the LV during multi-site pacing. The study protocol was reviewed and approved by local institution's ethics committee. Written consent was obtained before the study. Pre-op, the patients were scanned with MRI for cine-MR (function), 3D SSFP (anatomy), LE MR (scar imaging) and tagged MR (motion).

Pacing was performed from the RV apex and a standard Wellen's protocol was applied during the VT stimulation study, a multi-array catheter (MEA) was positioned within the LV for electro-anatomical non-contact mapping (EnSite Velocity, St. Jude Medical, USA). Patient 1 had induced sustained monomorphic VT (SMVT) with a cycle length of 275 ms at stage 11 (500ms S1, with S2 and S3 just above

VERP) of the Wellen's protocol. While patient 2 had SMVT with a cycle length of 245 ms at stage 4 (600ms S1, with S2 at 360 ms), as shown in Fig. 8.3, Fig. 8.4 & Fig. 8.5.

Unipolar electrograms recorded from the MEA were filtered with a Band Pass filter (BPF) (High Pass filter cutoff (HPF_c): 10 Hz and Low Pass filter cutoff (LPF_c): 30 Hz) for prominent QRS detection referred as V_{dep} henceforth, and with BPF (HPF_c : 0.5 Hz and LPF_c : 30 Hz) for T-Wave detection referred as V_{rep} henceforth, from the electrophysiological recorder (EnSite Velocity, St Jude Medical, USA) and exported for offline analysis.

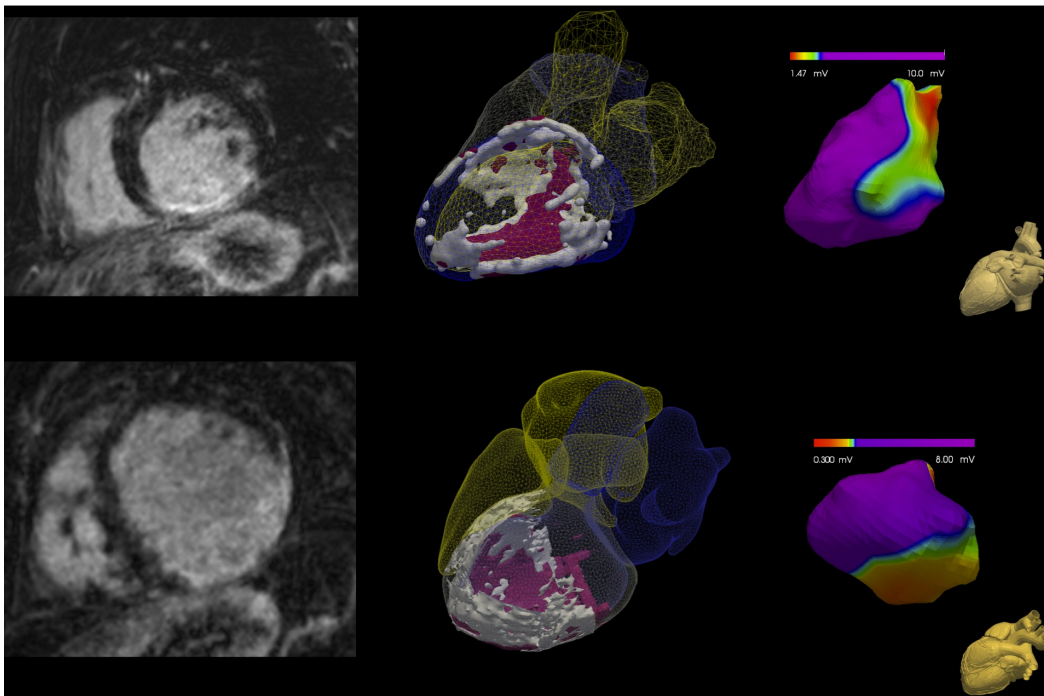


Figure 8.1: (left) High Resolution LE MRI, (middle) whole heart model segmented from 3D SSFP MRI with scars in violet and PIZ in grey, (right) EnSite study with low amplitude scars highlighted. Top row is for IHD_1 and bottom for IHD_2

2.2 Data Analysis

2.2.1 Anatomical Data

Cardiac magnetic resonance imaging (CMR) data of the cardiac structure were acquired on a 1.5T scanner (Philips Healthcare, Best, Netherland). 3-dimensional (3D) anatomical data were acquired with high-resolution late-gadolinium enhancement (LGE) CMR (1.3x1.3x2.6) for scar characterization. A 3D model of the whole heart was obtained after segmentation of the structural images. The LV myocardial scar distribution was segmented using signal intensity (SI) based analysis from

the high-resolution 3D LGE-CMR images. Using the full width at half maximum (FWHM) method [KFFK09] all pixels with SI values up to half of the maximum SI were automatically characterised as scar core. Pixels with signal intensity higher than 2 standard-deviation above the SI from the manually selected remote healthy myocardium and below that identified as scar core were automatically assigned as being the grey zone, regions where there is a mixture of scars and healthy myocardium, i.e. infarct border zone [KFFK09]. A volumetric ventricular model of the heart was then derived incorporating the information of scars and peri-infarct areas, as illustrated in Fig. 8.1.

2.2.2 Electrical Mapping Data

The depolarisation times were detected within the QRS window and were derived from the zero crossings of the Laplacian of the measured unipolar electrograms V_{dep} . The surface Laplacian of electrograms gave good results even in the case of multiple deflections and allowed detection of local activation without the interference from far-field activities [CWSdG+00]. The repolarisation times were detected within the ST window for the V_{rep} signals, and were derived using the "alternative method" as compared to the standard Wyatt method, as explained previously in [NBS+06].

The Activation Recovery Interval (ARI) is an established surrogate measure for APD and APD restitution [YFRM05]. Steady-state ARI restitution curves were estimated at steady state rate during sinus rhythm and right ventricular pacing frequencies (600, 500 & 400 ms).

2.3 VT Modelling Study: Personalisation and Pacing Protocol

A 3D simplified biophysical monodomain action potential MS model was personalised to the patient's electrophysiology mapping data, to estimate the hidden properties of the cardiac tissue and to predict VT isochrones.

Cardiac tissue conductivity is a crucial feature for the detection of conduction pathologies. The Apparent Conductivity (AC) of the tissue was estimated using a coupled personalisation framework, which combines the merits of a fast Eikonal (EK) model [SCMV+05] with those of a simplified biophysical model [MS03, FK98]. More details on this method can be found in [RCS+11] and chapter 4. The conductivity parameter estimated within the scar and peri-infarct tissue was spatially graded with the normalised spatial intensity distribution seen from the LGE-CMR. The computed gradation was inversely proportional to the normalised intensity distribution, i.e. the higher the signal intensity seen on LGE-CMR images, the lower the tissue conductivity, thus representing scar.

APD restitution is an electrophysiological property of the cardiac tissue and defines the adaptation of APD as a function of the heart rate. Its slope has a heterogeneous spatial distribution, which plays a crucial role in arrhythmogenesis [CF04, NBS+06, CBC+11]. The APD restitution curve (APD-RC) defines the relationship between the diastolic interval (DI) of one cardiac cycle and the APD

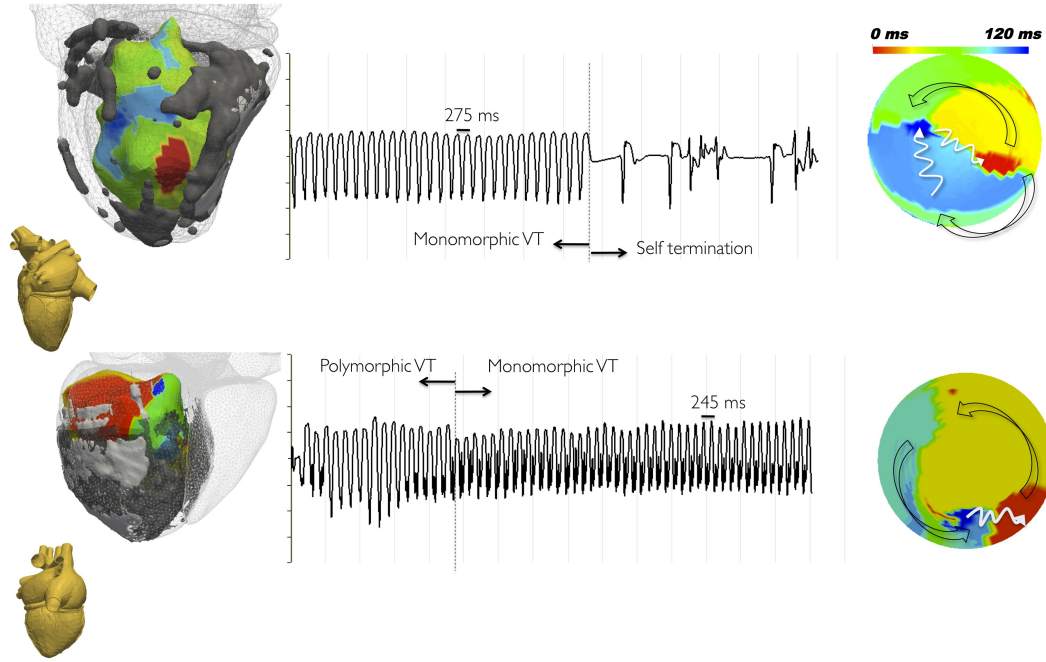


Figure 8.2: Sustained induced VT cycles observed for IHD_1 (top) (cycle length: 275 ms) and IHD_2 (bottom) (cycle length: 245 ms). (left) Induced VT isochrones with exit points (red) in correlation with scars (white) and PIZ (grey). (right) LV bullseye representation of VT isochrones.

of the subsequent cardiac cycle. The slope of these RCs is controlled by a model parameter τ_{open} of MS model and depicts the APD heterogeneity present at multiple heart rates. APD-RC for MS model is explicitly derived as previously described [MS03],

$$APD_{n+1} = f(DI_n) = \tau_{close} \ln \left\{ \frac{1 - (1 - h_{min})e^{\frac{-DI_n}{\tau_{open}}}}{h_{min}} \right\} \quad (8.1)$$

where $h_{min} = 4(\tau_{in}/\tau_{out})$ and n is the cycle number. The maximum value of APD is also explicitly derived as $APD_{max} = \tau_{close} \ln(1/h_{min})$.

APD-RC was fitted to the steady-state ARI *versus* DI points derived from the mapping data, for various pacing frequencies, using a non-linear constrained Active-Set Algorithm based optimisation of parameters τ_{open} and τ_{close} . A single APD-RC was fitted for each measured point from the MEA. Minimum DI (DI_{min}) (the minimum non-refractory DI) can also be computed explicitly from the estimated parameter values (Fig. 4.7c) using Eq. 4.9 as described in chapter 4.

For simplicity and allowing comparison of results with previous findings [YFRM05, NBS⁺06], a standard restitution curve for steady-state ARI *versus* DI was also fitted

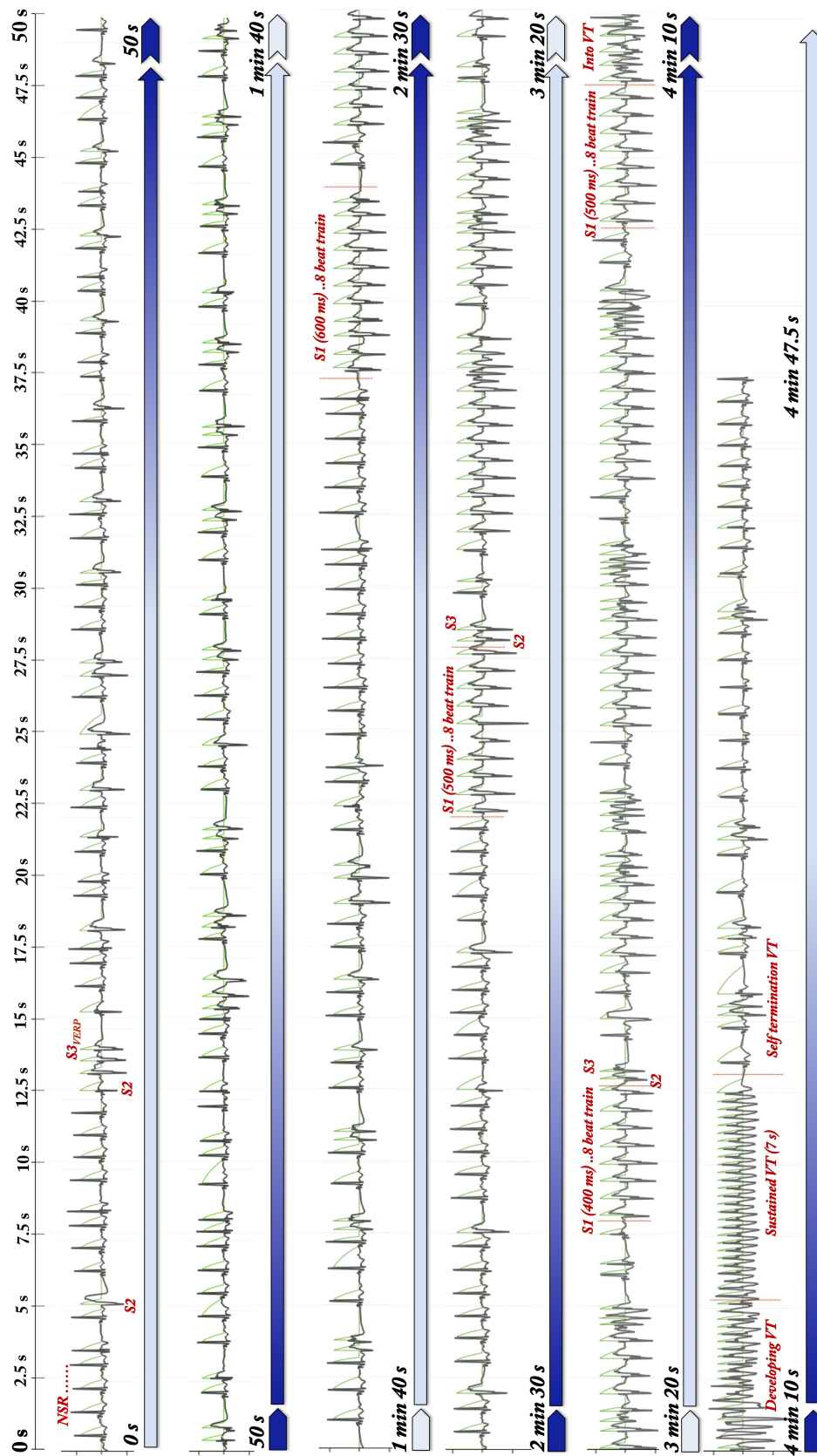


Figure 8.3: Measured electrograms (grey) on MEA and estimated pseudo action potential (green) for analysis, for the clinical VT stimulation study for patient IHD_1.

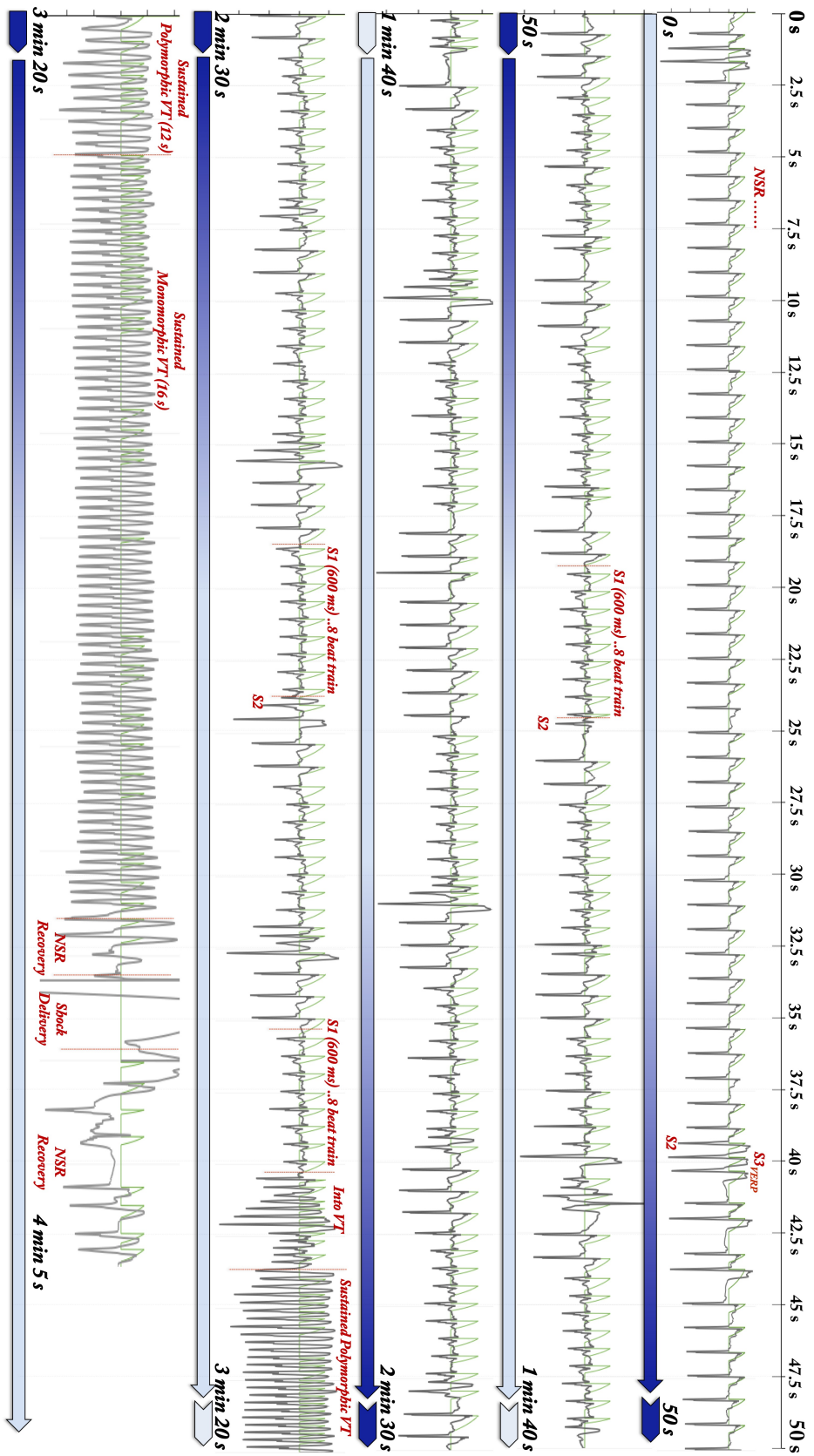


Figure 8.4: Measured electrograms (grey) on MEA and estimated pseudo action potential (green) for analysis, for the clinical VT stimulation study for patient IHD_2

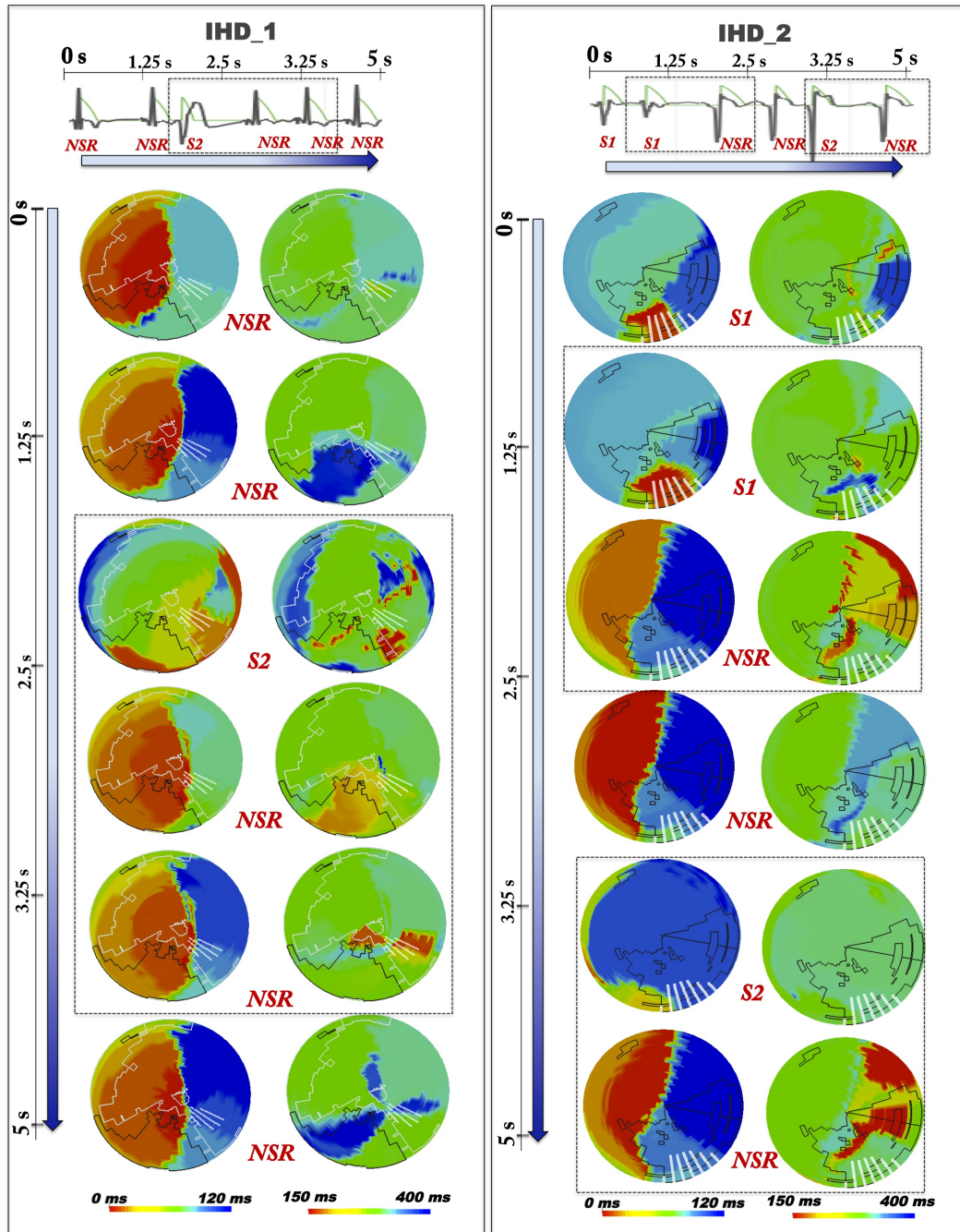


Figure 8.5: Change of depolarisation time isochrones and APD maps with dynamic pacing. Boxes highlight the regions showing an increase in APD heterogeneity for the cycles following pacing S1 & S2, thus possessing an increased vulnerability of inducing VT.

using a least-squares fit to the mono-exponential function (EXP-RC):

$$ARI = ARI_{SS} - ae^{-DI/b} \quad (8.2)$$

where the ARI_{SS} (maximum APD), a and b are the parameters of the fit. The maximum value of the slope from the fitted EXP-RC curves, is then computed explicitly from the derivative of EXP-RCs using a fixed DI_{min} (100 ms), the results of which are shown in Fig. 8.8(b). The slope is also computed analytically for comparison with [NBS⁺06] and is given by:

$$S_{max} = (a/b)e^{-DI_{min}/b} \quad (8.3)$$

where S_{max} is the maximum slope for EXP-RC curves. Previously estimated DI_{min} using Eq. 4.9 were used here. The results are shown in Fig. 8.8(d).

Next, the personalised model was used to predict VT circuits, using an *in silico* programmed ventricular stimulation (VT-Stim) study from RV apex with Wellen's protocol. Each stage of the VT-Stim was simulated in parallel on a cluster of computers, and tested for induced VT. Simulated induced VT cycle isochrones were computed to locate the earliest activation times site, which corresponded to the exit point of the re-entrant VT circuit. As these are the areas which fire abnormally at higher pacing sites, due to the local trapping of the signal.

The model was also tested for simulated VT-Stim study with pacing at different sites in RV. All the exit points identified from induced SMVT from the simulated VT-Stim study, were then correlated with the spatial heterogeneities of the CV, APD restitution and the scar and peri-infarct tissue distribution.

3 Results

3.1 Estimation of the patient-specific spatial heterogeneities

Fig. 8.6 shows the spatial heterogeneities of the tissue conductivity and APD restitution property, estimated for the ischaemic heart disease (IHD) and non-ischaemic dilated cardiomyopathy (DCM) patient groups. For study subjects, IHD_1 and IHD_2, the clinically observed exit points are also overlaid on the maps (transparent white dots).

IHD_1 shows most of the spatial heterogeneity of the maximum slopes and maximum APDs for the APD-RC present in and around the scar regions, where the tissue conductivity represented by the parameter AC had also low values (Fig. 8.6). The same observation is noted for IHD_2.

The clinically observed exit points during induced SMVT for IHD_1 & IHD_2, lied in the regions with higher maximum APD and higher maximum restitution slope compared to the surrounding tissue as seen from the Fig. 8.6. The tissue conductivity in the exit point regions were low. Low conduction velocity along with steeper restitution slope and higher maximum APD as an island amidst of

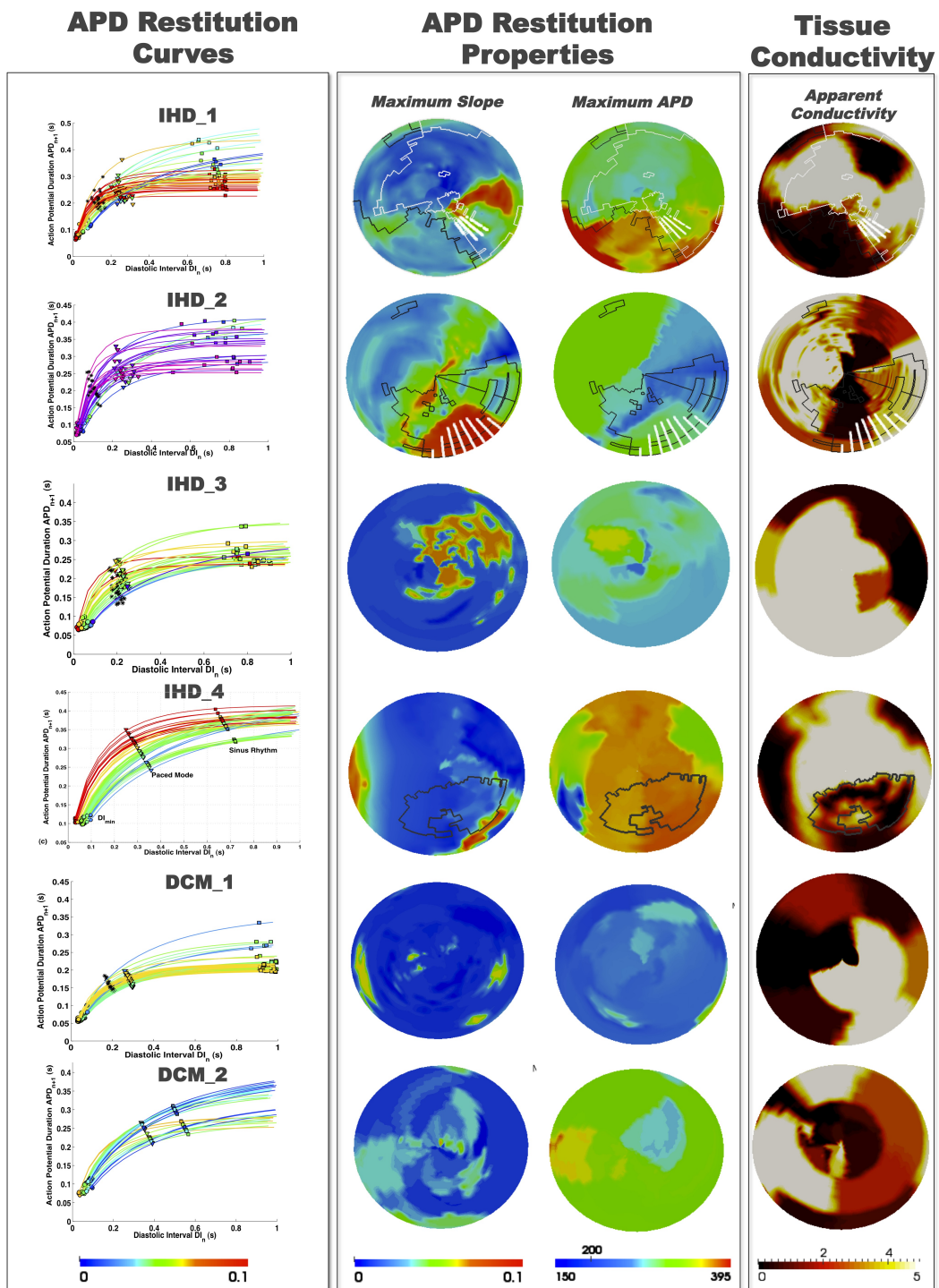


Figure 8.6: Patient-specific APD-RCs, LV bulls eye representation of the spatial distribution of the maximum restitution slope and maximum APD for APD-RCs, and parameter AC. Scars (black contours), and peri-infract areas (white contours) are also overlaid for some cases, along with clinically observed exit points (transparent white dots).

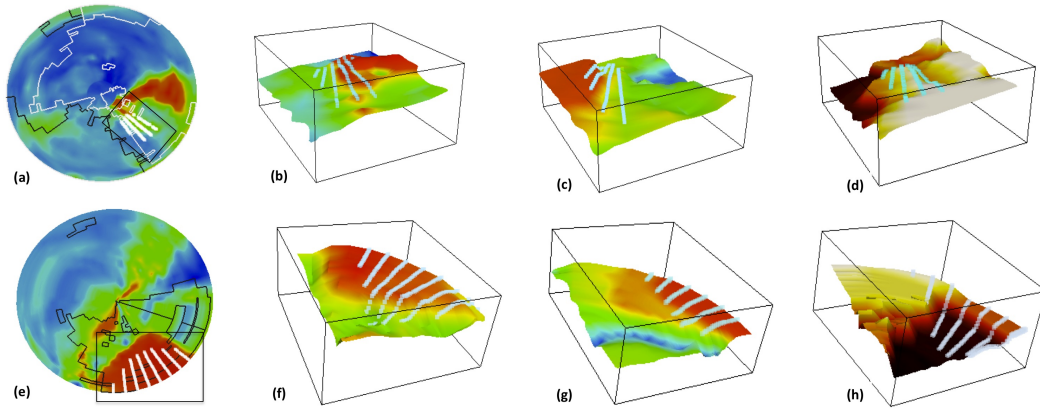


Figure 8.7: Spatial heterogeneity of maximum restitution slope (a & b, e & f), maximum APD (c & g) for APD-RCs and CV (d & h) , for exit point regions. They lie in the isolated islands of maximum restitution slope, with a larger maximum APD for APD-RCs, and on the borders of AC maps. Top row: IHD_1, Bottom row: IHD_2. For colour scale, refer Fig. 8.6.

lower maximum APDs, were some of the main properties observed for the exit point regions, as shown in Fig. 8.7.

The other ischaemic cases (IHD_3 & IHD_4) had left bundle branch block (LBBB) on resting electrocardiogram and were potential candidates for cardiac resynchronisation therapy (CRT). They showed comparatively lower heterogeneity for the maximum APD-RC slope and maximum APD as seen in Fig. 8.6. IHD_4 case had scars present on the posterior LV wall, which is also reflected in the spatial distribution of AC values. Whereas IHD_3 had scars present on the anterior LV wall. IHD_3 also showed higher heterogeneity of the maximum APD-RC slope and maximum APD on the anterior side, where the scars were present.

DCM cases showed less heterogeneity for the maximum restitution slope and maximum APD, compared to the IHD cases (Fig. 8.6). DCM cases had LBBB and did show the presence of low tissue conductivity near the septal areas.

3.2 Correlation of the spatial heterogeneities: Inter-patients

Fig. 8.8 shows the inter-patient variability of the maximum restitution slope and the maximum APD for IHD and DCM cases. The overlaid horizontal grey line in the Fig. 8.8 shows the values observed for literature values of the model parameters [MS03], representing the healthy cardiac tissue.

The spatial heterogeneity of the maximum APD-RC slope as well as EXP-RC slope (explicit slope with fixed DI_{min}) proved to be the most discriminative feature to distinguish between the IHD and DCM subjects, as shown in Fig. 8.6 & Fig. 8.8(b). The IHD subjects clearly showed a higher spatial heterogeneity of maximum APD-RC & explicit EXP-RC slope, than the DCM subjects. IHD_3 also showed the

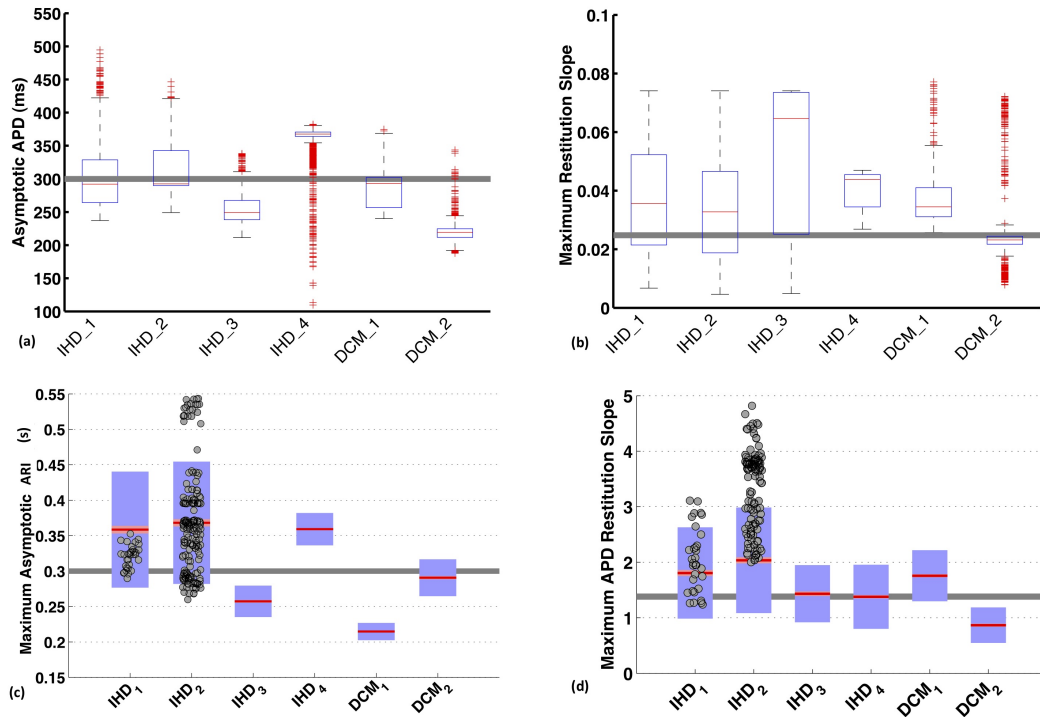


Figure 8.8: Box plots of spatial heterogeneity of the maximum APD (a & c) for APD-RCs and maximum restitution slope (b & d) for EXP-RCs (slopes calculated explicitly using fixed DI_{min}), for the different IHD and DCM cases. (c & d) show the values for the exit points in grey dots, over the box plots of the whole LV, for maximum APD (c) for APD-RCs and maximum restitution slope (d) for EXP-RCs (slopes calculated analytically using Eq. 8.3 with previously estimated DI_{min}). Exit points are seen to have steeper (higher) restitution slope (mostly > 1.2) (d) but heterogeneous APD values (c)

highest spatial heterogeneity of the explicit EXP-RC slope compared to the other IHD cases. This may be due to the patchy distribution in the scar regions on the anterior side compared with other IHD subjects in whom the scar distribution is more confluent. DCM cases had comparatively more homogeneous distribution of the maximum APD-RC slope as also seen in Fig. 8.6

IHD subjects had comparatively higher mean maximum APD than DCM subjects. The spatial distribution of the maximum APD value did not prove to be as discriminative as that of maximum APD-RC & explicit EXP-RC slope, however more spatial heterogeneity was observed for both IHD_1 and IHD_2, both of whom had positive clinical VT-Stim study.

3.3 Induced VT: Clinical observations vs. Model predictions

The clinical protocol of VT-Stim study performed on the study subjects IHD_1 and IHD_2 was simulated *in silico* on the personalised 3D monodomain action potential model, incorporating information both from patient's anatomy and scar core distribution, grey zone/peri-infarct zone distribution, along with the mapped LV electrophysiology data

The protocol was simulated with the same RV apex pacing location with Wellen's protocol. VT was induced at stage 7 of the Wellen's protocol (Paced driving-train S1 at 400 ms, sensed first extra stimulus S2 at 200 ms and sensed 2nd extra stimulus S3 at 100 ms). The model also predicted different VT circuits with different pacing conditions, which are mentioned in details in the next section.

Personalised model of IHD_1 did predict a sustained VT re-entry circuit with an activation pattern, which was macroscopically similar to the clinically observed one, initiating from the LV lateral wall, spreading anteriorly and then return to the lateral wall via the posterior wall as seen in Fig. 8.9. The cycle lengths of the re-entrant VT matched between the model predicted and the clinically observed (clinical: 275 ms model predicted: 260 ms for IHD_1 & clinical: 245 ms model predicted: 250 ms for IHD_2). The exit points observed clinically also did match well with the predicted ones.

The model enabled the prediction of a 3-dimensional VT circuit as opposed to the 2-dimensional VT activation pattern observed by the MEA by taking into account of the geometric information gathered from CMR such as scar distribution and LV myocardial thickness. This gave additional insights to the wave propagation within the myocardium, with the given spatial distribution of the scars and the peri-infarct areas. This is seen as the red geodesic path computed in the myocardium from the predicted VT isochrones. This path shows the main VT circuit/loop to be broken in order to successfully terminate VT. The points with the latest activation time around the scars were also computed, these points are clinically termed as entry-points. As a case of ischemic VT, the wave is believed to be trapped within the scars and peri-infarct zone, between the entry and exit points. This trapped wave circuit is estimated in 3D from the predicted VT isochrones, and this incorporates the scar and peri-infarct heterogeneity details from the LE-MR. The results are shown in Fig. 8.10. The estimated trapped path surrounds the scar core and lies within the PIZ and healthy tissue. This gives us insights on how transmural the isthmus representing the trapped path is? Successful VT termination through ablation is achieved when this trapped path is successfully broken with ablation lesions.

Personalised IHD_1 model also predicted a spiral point as observed on the anterior side from Fig. 8.9. The spiral tip computed within the myocardium is shown by a blue path in Fig. 8.9. The spiral tip was developed due to the slowing down of the wave at higher pacing rates in the low conductivity region observed by the LV EP mapping data on the anterior side as seen in Fig. 8.6.

Personalised model of IHD_2 VT-stim model also predicted a positive VT-stim study with re-entrant VT induced at Stage of the Wellen's protocol. This again

correlated with the clinically observed VT circuit. However the direction of the activation pattern during the predicted re-entrant VT is reversed from that observed clinically. Wave directions in ischemic VTs is highly dependent on the wave dynamics and inter-wave collisions, the most significant factors contributing in the sustainability of re-entrant VT are the electroanatomical properties at the entry and exit points. The exit points predicted for this case did match with the clinical ones. The main VT circuit in the myocardium computed from the geodesic path of the predicted VT isochrones is shown in red in Fig. 8.9.

This case also had a lower conductivity distribution compared to IHD_1, as seen in Fig 8.6. Thus this case went into fibrillation soon after the development of VT. Also the patient was given a shock during the clinical VT-Stim study to terminate VT, which was slowly developing into VF

From the model predictions of IHD_2 case, we could see that lower conductivity distribution along with heterogeneous spatial distribution of the maximum restitution slope and maximum APD of APD-RC were associated with higher risk of degeneration to VF. However more studies are needed to support this hypothesis.

3.4 VT & Exit point predictions

In silico personalised models offer much more flexibility than the clinical VT-Stim procedure, as the model can simulate any combination of paced stimuli from different locations, with varying pacing rate which may not be feasible in clinical practice. We tested this by simulating the VT-Stim studies from different points of the heart. We compared the electro-anatomical characteristics of the pacing sites in those simulated studies which induced sustained VT and those failed to induce sustained VT. This analysis gave us some insights to whether pacing from a particular site with certain electro-anatomical properties such as the surrounding heterogeneity in restitution and conductivity were more likely to induce VT.

Fig. 8.11 shows the various sustained VT isochrones predicted with the personalised model for various pacing locations in the RV. Predicted exit points locations correlate very well with the scar and PIZ distribution. Most of the exit points lied on the boundary of scars for IHD_1 case, and within the islands of the scar for IHD_2 case. IHD_1 case also had some exit points lying in the healthy tissue regions on the free wall region, due to presence of higher maximum restitution slope as seen from Fig. 8.11. These predicted exit points could be potential targets for ablation. However for more robustness, we could also grade these predictions with the occurrence probability, induced VT cycle lengths and duration of sustained VT.

For both cases these exit points also correlate well with the heterogeneity of maximum restitution slopes of APD-RC, and mostly lie in the islands of higher maximum slope. as shown in Fig. 8.11 and Fig. 8.6.

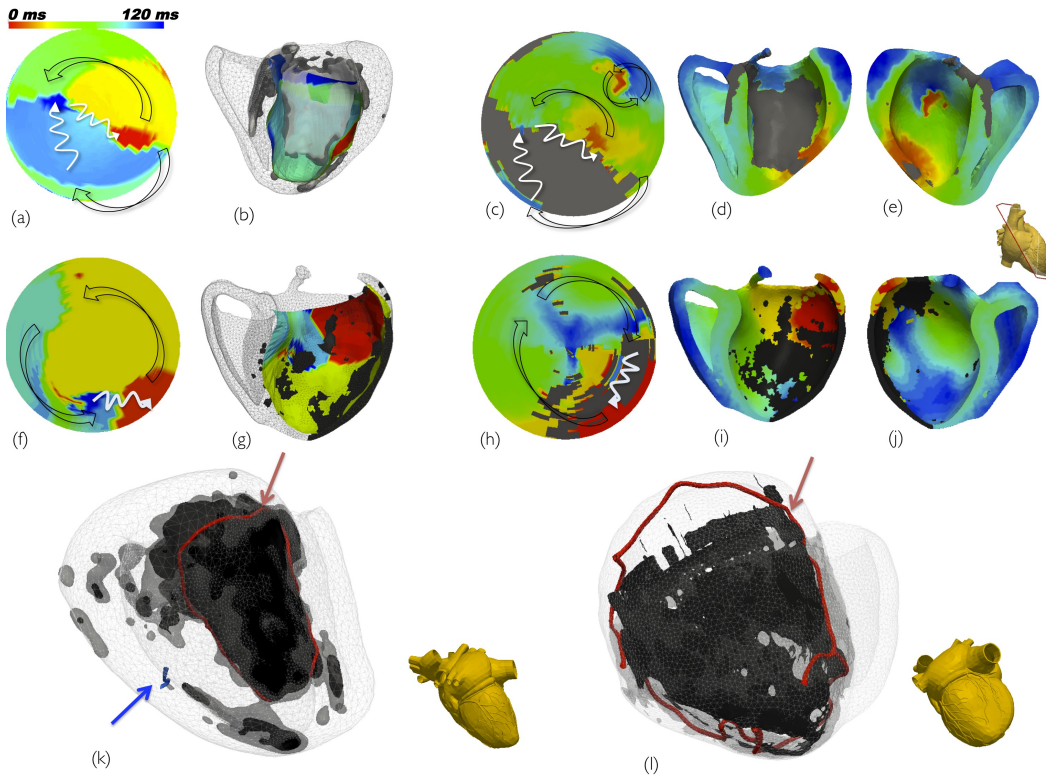


Figure 8.9: Predicted VT isochrones (c,d,e) with the personalised VT-Stim model in comparison with clinical data (a,b) for IHD_1, same for IHD_2 in the second row. (k) The geodesic path of the sustained VT circuit in the myocardium representing the VT loop in red (pointed by red arrow), and the spiral tip computed in blue (pointed by blue arrow), fr IHD_1. (l) same for IHD_2

4 Discussion

4.1 Tissue conductivity & APD restitution slope heterogeneity

Non-contact EP mapping of the left ventricle allowed characterization the global LV APD restitution and tissue conductivity properties for the IHD and DCM patients in the study. Regional scars were observed in IHD patients on LGE-CMR whereas it was not observed in DCM patients. DCM patients had lower spatial heterogeneity of APD restitution as compared to IHD cases, thus showing the presence of scars altering the cardiac restitution properties, thus making it pro-arrhythmic. Our findings did match with those found in [YFRM05, NBS+06]. Also apex to base gradients of the heterogeneity were not consistent within the findings. IHD cases had islands of steeper restitution slope present amidst of shallow slopes, which is one the factors to prove pro-arrhythmic.

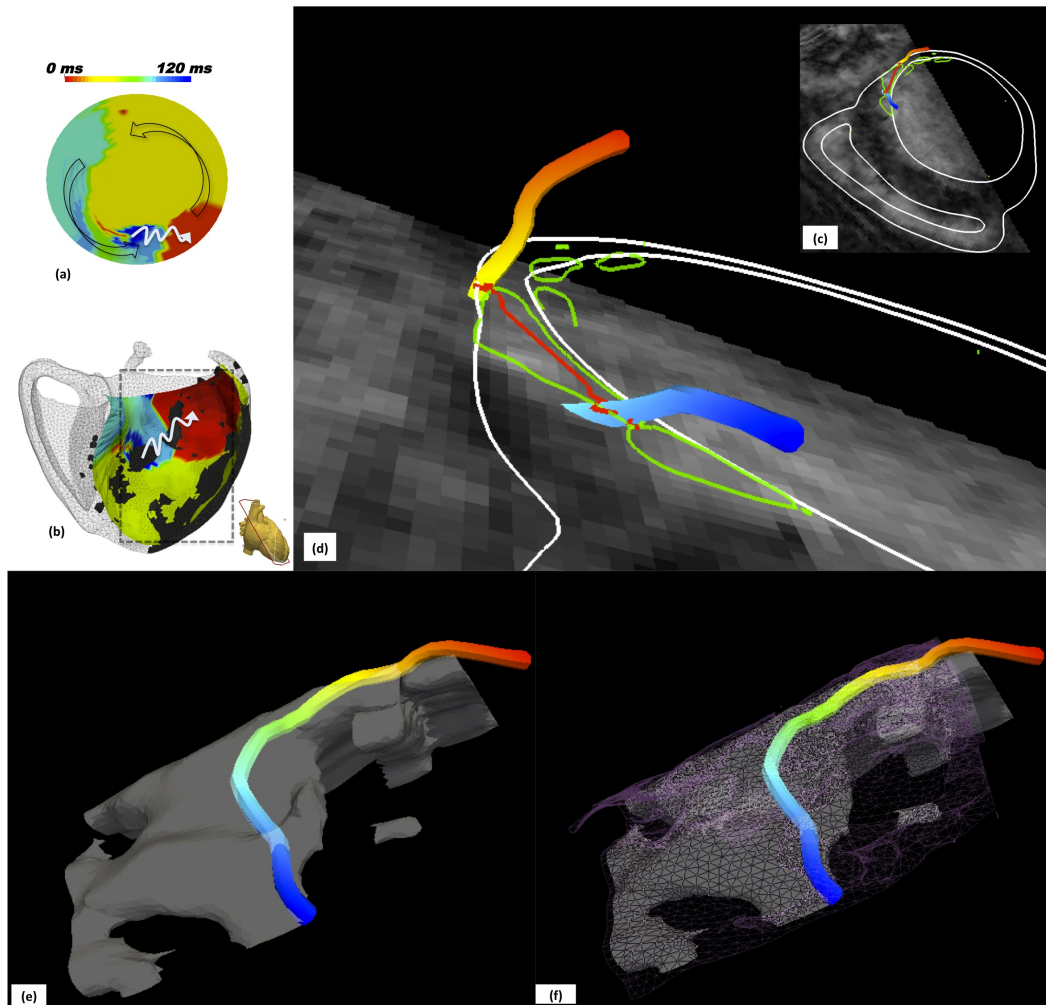


Figure 8.10: Estimation of the 3D myocardial geodesic path (white schematic path in a & b) between the entry and exit points, taking into account myocardial scar and PIZ heterogeneity. (c & d) shows the 3D estimated path from the simulations for IHD_2, along with LE CMR. White contours are for the segmented myocardium, green contours are for the scar core and PIZ. Red line represents the path in plane of LE CMR slice, which clearly shows the action potential wave path which is trapped between PIZ and scar core. Colours on the 3D path show the activation time (Blue: late activation, entry point and Red: early activation, exit point). (e) shows the 3D trapped path surrounding the scar core (solid structure) and (f) shows it to be lying within PIZ & between the scar core and PIZ (wired structure).

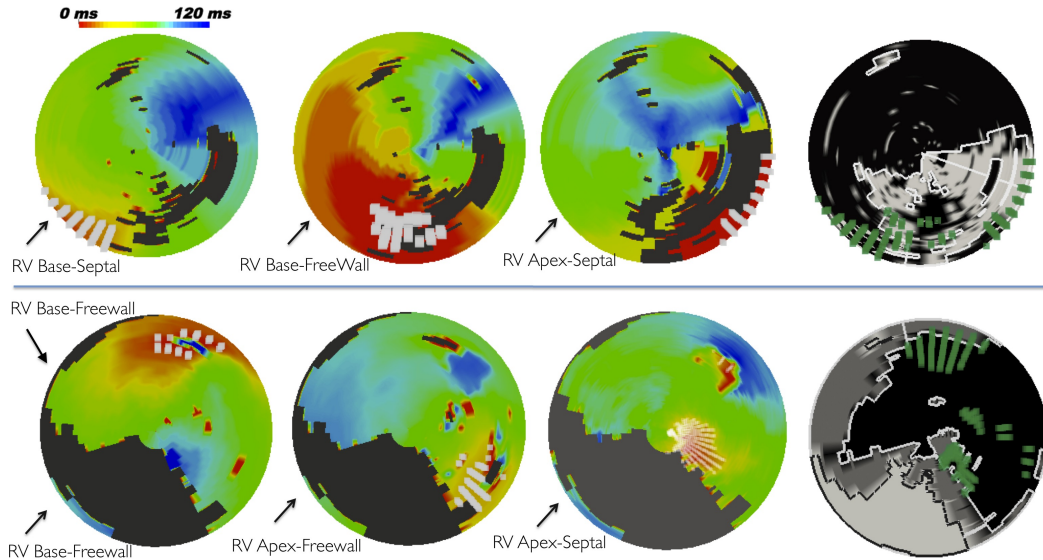


Figure 8.11: LV bulls eye representation of various model predicted sustained VT isochrones for different pacing sites, with exit points overlaid (transparent white dots). (right) Location of predicted exit points (green) in correlation with scar and PIZ heterogeneity. (top) IHD_2 & (bottom) IHD_1. For Bull's eye nomenclature please refer Fig. 3.4.

4.2 Data Limitations & Model personalisation

As only LV endocardial mapping data were used in this paper, there were several data limitations for model personalisation, few of which are: (i) Lack of estimation of local RV and transmural spatial distributions of conductivity and restitution properties. A global estimation of the tissue conductivity was done using body surface ECG waveforms as explained before. (ii) As non-contact mapping data was used, the CV estimation of the fast conducting regions, on the inverse mapped estimates of the EnSite LV surface areas was unreliable. Thus CV restitution heterogeneity could not be estimated. However this heterogeneity could also play a role in the initiation of VT. (iii) Usage of Non-Contact Mapping (NCM) data and EP and MR fusion errors. Although NCM data do have an advantage of measuring temporal EP data with more spatial acquisition (surface) than the contact mapping data (point), the NCM data can be challenging for local depolarisation and repolarisation time estimations. Also uncertainty on the data can be added due to the difficult registration between the EnSite LV surface and the MR-derived LV surface (Fig. 8.5). (iv) IHD_1 and IHD_2 cases had undergone a clinical VT-Stim study thus had sufficient number (3-4) of steady state ARI & DI measurements for each of the S1 overdrive pacing frequency, to fit APD-RCs. However for the other cases which underwent CRT, only two heart rates were used for fitting APD RCs. Thus an assumption was made by considering the sinus rhythm APD, as a constraint on the maximum

value of APD RCs controlled by the model parameter τ_{close} , while the paced mode APD was used to adjust the RC slope controlled by the parameter τ_{open} . However, more measurements for frequencies in the slope region (region between minimum DI and maximum value of APD on APD RC) could have depicted the RC slope more accurately. (v) ARI data was used as an APD surrogate to fit the APD-RCs, using unipolar extracellular potentials. This could under-estimate the underlying real APD restitution heterogeneity. (vi) Mono-exponential RCs provided an accurate fit to the vast majority of the data, however when the model APD-RC was fitted with non-linear optimisation. The model parameter range was constrained to have more physiological values. This had some misfits leading to few errors on APD-RC fitting (mean)

4.3 VT Model Predictions & Simplifications

In order to have a clinically relevant model for personalisation with patient-specific data and VT risk assessment, the MS model used had several simplifications, few of which are, (i) No actual Purkinje network modelling. Exact locations of these Purkinje network extremities are ambiguous and inextractable from the patients data, although they could play a crucial role in arrhythmogenesis [BGR⁺06, SSW⁺04]. However, a high conductivity endocardial region was obtained, which may be inferred as depicting the underlying Purkinje network with personalisation (Fig 8.6). A local estimation of endocardial restitution properties (Fig 8.6) also helped potentially depict the abnormalities in the Purkinje network around scars, leading to arrhythmia generation. (ii) Use of an atlas-based cardiac fibre model. Extraction of true *in vivo* cardiac fibre orientations is the subject of ongoing research and including them would give more accuracy to the VT-Stim predictions and inducibility maps. Finally, orthotropic anisotropy could change the model behaviour, but acquiring patient-specific data on cardiac laminar sheets seems even more challenging. (iii) Model complexity was reduced in the VT prediction, due to the absence of all ionic currents in details. However the model exhibits the main macroscopic properties of the tissue (conductivity, APD and CV restitution) all of which play a role in the initiation of VT, as shown in Fig. 8.9.

5 Conclusion

Patient-specific spatial heterogeneity of the maximum restitution slope for APD-RCs are good indicators in distinguishing IHD patients from DCM cases. Exit points are present in regions with low conductivity, steeper restitution slope and higher maximum APD islands. Simplified MS model after personalisation, was sufficient to predict macroscopic VT circuits and exit point locations. The personalised model was able to predict other potential clinically unobserved exit points. This opens up possibilities of evaluating the role of patient-specific models in the clinics to provide aid in planning and delivery of RF ablation.

Part V

CONCLUSION

Conclusions & Perspectives

Contents

1	Contributions	135
2	Perspectives	138
2.1	Methodological perspectives	138
2.2	Short-term & Mid-term clinical perspectives	140
2.3	Long-term clinical perspectives	141

In this thesis, we proposed a novel macroscopic personalisation framework for 3D cardiac electrophysiology models to the state of the art clinical electrophysiology mapping (contact and non-contact) data. The framework estimated the apparent tissue conductivity, tissue APD and the APD & CV restitution properties from the data. We then demonstrated the ability of the personalised EP model, with patient-specific tissue heterogeneities to simulate patient-specific ischemic VT, with the simulation of an *in silico* VT stimulation study. We also proposed a rule based RF ablation modelling approach to simulate acute and chronic effects of RF ablation. Last, we demonstrated and validated the predictive power of the model for ischemic VT patterns, with *in vivo* clinical data.

In this chapter, we summarise the contributions of each chapter & discuss the perspectives of the work presented in this thesis.

1 Contributions

Building personalised EP models using *ex vivo* data

This work was performed to propose a novel method for estimating *volumetric* model parameters from *surface* data with single and multiple pacing frequencies. The macroscopic features to which the 3D EP model was personalised to, were the tissue conductivity (estimated from the action potential wave CV), tissue APD and APD & CV restitution. This framework estimated all the model parameters making the model heart-specific. Also due to the high spatial and temporal resolution of the *ex vivo* optical data, we evaluated the sensitivity of the personalisation to different pacing scenarios and demonstrated it's robustness. The volumetric predictive power of the model for paced action potential waves under different epi- and endocardial pacing scenarios was also tested. This work was published in [RPD⁺11, RPD⁺10, RSP⁺09a, RSP⁺09b]

Building personalised EP models using *in vivo* non-contact mapping data

In this work, we extended the proposed personalisation framework to a coupled model personalisation framework, for a fast estimation of the hidden parameters of the tissue such as conductivity and APD restitution to enable clinical use. The personalisation algorithm coupled a simple eikonal model to a simplified biophysical MS model, thus combining the benefits of both models. Here we demonstrated a coarse-to-fine approach (multi-resolution) for personalisation, where we could use a personalised simpler model to initialise the personalisation of more complex model. The personalised MS model is then planned to predict patient-specific VT, with the estimated patient-specific tissue heterogeneities. These results are then demonstrated on a first cohort of clinical cases in chapters 6 & 8. This work was published in [RCS⁺11, RCS⁺10].

Building personalised EP models using *in vivo* contact mapping data

This work showed the application of the proposed coupled personalisation framework to the *in vivo* contact mapping data. As the study was performed on an alive infarcted porcine heart, imaging the cardiac fibre orientations with DT-MRI after sacrifice was feasible. The cardiac fibre orientations were incorporated inside the model personalisation for a more accurate tissue conductivity estimation (especially in the regions around scars). We also tested the influence of mapping details on the model personalisation algorithm. We found that personalisation using epicardial mapping gave a conductivity estimation closest to the one obtained with personalisation using both endocardial and epicardial mapping, and also showed a low prediction error. On the other hand, the personalisation with endocardial mapping had an important deviation from the estimated distribution obtained with both endocardial & epicardial mapping. It also had an important prediction error on the epicardial surface. Thus, within this experimental setting, epicardial mapping proved to be a sufficient acquisition to reproduce a tissue conductivity distribution, closer to the one estimated using both endocardial and epicardial mapping. This was also the case when the personalisation was done on similar data from a clinical case [KRC⁺11]. However such finding has to be tested on other configurations, for different healthy and pathological cases. This work was published in [RSDA11].

Personalised Ventricular Tachycardia modelling

In this work, we illustrated the main macroscopic characteristics of an ischemic VT. These include the structural and functional heterogeneity of the tissue near the scars i.e. peri-infarct zones (PIZ). PIZ are crucial in the initiation and sustainment of ischemic VT. Macroscopic structural heterogeneity was achieved as follows. The incorporation of a decrease in fibre organisations in PIZ was done, by using a mixture of anisotropic and isotropic propagation, the ratio of which was controlled

by the percentage of patchiness in the fibrotic tissue. The fibrosis was modelled for its macroscopic behaviour using multi-domain models, which included healthy myocytes and collagen network. The collagen network was modelled by an isotropic diffusion term with low conductivity, to account for the high resistivity whereas the domain of healthy myocytes is modelled with anisotropic diffusion term with normal cardiac tissue conductivity. Macroscopic functional heterogeneity was achieved from the patient-specific tissue heterogeneities estimated (CV, APD, CV & APD restitution) using the proposed coupled personalisation framework. Later, we demonstrated the simulation of an *in silico* VT stimulation study using the personalised and adapted MS model, to quantify VT risk *in silico*, in terms of VT inducibility maps, VT re-entry patterns and VT exit point maps (potential RF ablation targets). This work was published in [RCS⁺11] & euHeart project deliverable [RDS⁺11].

Modelling Radio-Frequency Ablation

This work proposed a rule based modelling approach for RF ablation lesions based on the state of the art studies. This approach was carried out due to the lack of patient's imaging data, on RF ablation lesions, as the patients had a pacemaker implanted at the end of the ablation procedure. This rule based modelling approach also incorporated the acute and chronic effects of the RFA lesions. The chronic RFA lesions were then used in the *in silico* simulation of VT stimulation study post ablation therapy to assist in estimating the success of RFA lesions *in silico* and locating the potential RFA targets. This work was reported in euHeart project deliverable [RDS⁺11]

Planning of RF Ablation lines using *in vivo* data

In this work, the aim was two-fold. Firstly, we studied the role of spatial heterogeneity of cardiac tissue properties such as conduction and APD restitution in ischemic VT patients who underwent the clinical VT Stimulation study with non-contact mapping of LV. Patient-specific spatial heterogeneity of the maximum restitution slope for APDRCs were found to be good indicators in distinguishing IHD patients from DCM cases. Exit points were present in regions with low conductivity, steeper restitution slope and higher maximum APD islands. Personalised MS model was sufficient to predict macroscopic VT circuits and exit point locations, based on the observed spatial heterogeneities. Secondly, the personalised model was used for *in silico* simulation of VT stimulation study and was able to predict other potential clinically unobserved exit points. This opens up possibilities of evaluating the role of patient-specific models in the clinics to provide aid in planning and delivery of RF ablation. This work will be published in [RCD⁺12].

2 Perspectives

2.1 Methodological perspectives

Model complexity for Ventricular Tachycardia Choosing appropriate model complexity and completeness for a given application is crucial. We chose to use the MS model [MS03] (derived from FK model [FK98]) to simulate ischemic VT electrophysiology, as it had the essential components playing a role in the genesis of ischemic VT such as CV, APD and their respective restitution. The estimated spatial heterogeneity of these parameters were the key factors in VT induction. As demonstrated in Chapter 8, we were able to reproduce the macroscopic VT circuits as observed in the clinical data, along with the same exit points as observed clinically.

However, there is a need to evaluate the model complexity required to model accurately the dynamics of VT over various cycles, as this could play a crucial role in VT sustainment and termination. This needs personalisation of more complex models from the sparse *in vivo* clinical data.

Multi-resolution personalisation of models More complex & complete models are known to have a strong impact on the tractability [GNK05] and on the parameters identifiability [FN09] from clinical data. A fast coupled personalisation framework was introduced for the first time, including the multi-resolution coarse-to-fine approach, to personalise complex & more complete models with simpler models [RCS+10, RCS+11]. The framework was used on clinical interventional datasets with non contact mapping. The results obtained were very encouraging. The estimated conductivity and APD restitution parameters were able to distinguish between the healthy areas and the pathological ones (scar and isthmus). This shows a potential impact on personalising more complete models to sparse clinical data for much better understanding of the wave dynamics. A first step towards this was achieved by personalising TNNP model using coupled personalisation framework with MS model, to *ex vivo* data [CSL+11]. The results were very encouraging and helped built more complete personalised ventricular models.

This coarse-to-fine approach can be directly applied to personalise most of the parameters of more complete models, such as [FK98] & [BOCF08]. This model coupling is corroborated with the fact, that models [BOCF08], & [FK98] & [MS03] belong to a family of Fenton-Karma models.

Computational cost reduction Complex & complete models are also computationally quite expensive, thus they are restricted to the research world for understanding complex cardiac phenomenons. In order to translate those models to the clinical world for application on patients, there is a huge need to make models as real-time as possible. With the current computational power, this can be achieved by either designing sophisticated algorithms to reduce (adaptivity in space and time, operator splitting, lookup tables) [VBLP09] or parallelise computations [PDR+06, BCF+09] or by making complex models simpler and approxi-

mate [BWZ⁺02]. The other solution is increase the computational power by using graphics processing units (GPU) [VBLP09]. However it is still lacking substantial progress to be realistic to come into clinics. Thus, there is a need to make simulations as real-time as possible to have models predict virtual *in silico* scenarios directly during the clinical interventional procedure.

In this thesis, we showed the compatibility and versatility of our model personalisation framework to various clinical mapping data and showed promising results on the prediction of macroscopic wave dynamics for pacing and arrhythmogenesis. And as MS model is a simplified biophysical model with less number of variables to compute, it is possible to achieve real-time or close to real-time simulations with this model with GPU implementations. A step towards this is being taken at our laboratory at INRIA Sophia Antipolis, to make use of *in silico* models in clinics

Uncertainty with in vivo clinical data Acquisition of *in vivo* clinical cardiac EP mapping data has many errors sources few of which are registration, interpolation, catheter sliding, catheter movement with breathing and cardiac motion. These errors are different in magnitude, for different electroanatomic mapping sources. Non-contact mapping (NCM) is believed to have additional inverse mapping errors against contact mapping, but offers an advantage of higher spatial acquisition for each cycle mapped, for e.g. whole LV is mapped during one beat and several of such cycles can be mapped during the study. A great advantage of NCM can be seen in Fig 8.3 & 8.4, where the whole VT stimulation study was mapped with NCM. On the other side, contact mapping (CM) offers the advantage of more accuracy on the mapped signal locations than NCM, but at the expense of low spatial coverage than NCM for a single beat. i.e for CM, signals are recorded just over few points of the catheter at a time instant, and the catheter is needed to be moved over the heart surface again to have the whole area mapped. CM gathers data for different heart cycles over the different spatial recording points and then synchronises the QRS waves to derive the activation maps. CM shows a great potential of reliability in the location of the signal, apart from the registration errors. Thus CM can be used for recording activities in the areas of deceased heart tissue. CM is also proved to have lower far-field effect on the recording signals, than NCM. Thus based on patients study requirements, different mapping techniques are used., as shown in Table 2.1.

However, such errors should be taken into account during model personalisation. In the proposed work, we do consider the registration errors between the catheter gathered points and the MR derived surface, as a penalty factor in the tissue conductivity estimation, as described in chapter 5, However this approach gives a more deterministic parameter map, whereas a probabilistic tissue conductivity map, as described in [KRC⁺11] with a confidence interval based on the uncertainty in mapping technique, can additionally guide the clinicians in the decision taking.

2.2 Short-term & Mid-term clinical perspectives

Potential clinical impacts from the findings Based on the various studies performed during this work, we suggest following potential clinical impacts of the immediate findings.

As volumetric predictive power of the model for paced wave dynamics under different pacing scenarios was studied extensively and demonstrated promising prediction results [RPD⁺11], this shows the efficiency of using such personalised models for planning *in vivo* clinical CRT studies, for wave predictions under various pacing protocols.

The proposed personalisation framework was applied extensively to various mapping datasets (optical [RPD⁺11], contact [RSDA11] & non-contact mapping [RCS⁺11]). This shows compatibility and versatility of the framework in clinical routines.

In [RSDA11], we revealed the sufficiency of the epicardial mapping compared to endocardial mapping (usually performed) for the model personalisation, to capture sinus rhythm wave dynamics. This was also corroborated using probabilistic model personalisation with CM clinical data in [KRC⁺11]. This suggests sufficiency of non-invasive ECGI derived on the epicardium from BSP mapping, for model personalisation and better model predictions. This directs us towards non-invasive model personalisation.

In [RCD⁺12] we demonstrated that model personalisation provides patient-specific spatial heterogeneity maps, which can already help locate the potential exit points, the main targets for RF ablation. Also the model was able to be used to predict the other potential clinically unobserved exit points, when paced from other sites in the heart.

Potential clinical application *In silico* simulation of VT stimulation study with 3D patient-specific models (incorporating the information from MR anatomy, scar & PIZ anatomy and EP mapping data), was demonstrated in [RCD⁺12]. This approach leads us to study more clear insights on the patient's VT substrates *in silico*. And also proves to be a beneficial clinical tool for VT stratification and RF ablation planning. Study on modelling chronic RFA lesions with *in silico* VT-stim study is demonstrated in this thesis. This study can provide a tool for evaluating the success of the RFA therapy in post ablation weeks. However the main bottleneck to this integration is the computational complexity of the model, which needs to be addressed first.

Another potential application of the proposed *in silico* VT-Stim tool, would be to provide patient-specific optimal placement of ICD catheter leads to avoid tachycardia inducibility and provide quick cease of arrhythmia with anti-tachycardia pacing, without needing a shock to cease it. This could be achieved by looking at patient-specific inducibility maps (Fig 6.14) and avoiding those areas for catheter placements for ICD.

2.3 Long-term clinical perspectives

Intra-operative model-based guidance in EP mapping systems As discussed in this work, estimated spatial heterogeneity maps from model personalisation can help locate potential vulnerable areas of VT. Thus it could prove to be beneficial to derive such maps during the mapping procedure simultaneously in the EP Cath lab. This would need integration of the model in the mapping system, which could be personalised with a dynamic optimisation algorithm such as Kalman filter [WB95], that increases in accuracy with more mapping cycles acquisition during the EP study. The personalised model can then be used directly in the Cath lab to predict different virtual scenarios during the interventional therapy on a simulation software and help taking decisions. Another potential use of the model could be to provide EP model based interpolation of wave isochrones, in the non-mappable areas such as the myocardium. Such interpolation would take into account the patient-specific anatomy, scars and PIZ, along with a prior information (atlas based) on cardiac fibre orientations.

Pre-operative non-invasive VT risk stratification VT risk stratification in terms of VT inducibility maps, re-entry and exit maps, can be an efficient clinical tool in planning a patient-specific RF ablation therapy. In this work we used clinical data comprising of anatomical imaging, scar imaging and electrophysiology study data. We built models incorporating all this information together, along with atlas based fibre orientations to come up with a patient-specific sinus rhythm and VT simulations, and consecutively plan the RFA therapy *in silico*. We also were able to demonstrate the VT re-entry validation against clinical datasets. All this study proves that it is possible to use models in clinics to guide the planning and decision taking before the actual RFA operation procedure being carried out on the patient. However the main drawback in this approach was using invasive EP study data for RFA planning, such data is hard to accumulate before the RFA procedure. Thus there is a need to use all non-invasive data possible for RFA planning.

Based on this work, we can categorise the main data required to personalise an EP model to predict VT into 3 sets: 1) Anatomical data, 2) Scar data and 3) Electrophysiology data. Thus for a non-invasive VT risk stratification, the way to approach prediction of VT would be in the following two ways:

1) Body surface mapping based. Recently, [Rud10, WCZ⁺11, WSD⁺07] have demonstrated the clinical use of ECGI with epicardial activation patterns. This technique is still undergoing clinical study, and doesn't generate epicardial repolarisation patterns and APD maps. In our clinical VT stimulation studies acquired at KCL, UK and presented in this work, we did acquire a simultaneous BSPM and non-contact mapping data in collaboration with IBT, Germany. The synchronisation of this data for a VT cycle is shown in Appendix D Table D.7 & Table D.8. This allowed us to estimate the correlation between the two invasive and non-invasive data. However we need to design an efficient algorithm for inverse map the non-invasive data along with APDs and their restitution heterogeneities, as they play a crucial

role in ischemic VT as discussed in Chapter 8. This data could then be used to personalise the model and perform *in silico* VT-Stim studies.

2) Image based. This approach can be again divided in two ways: Purely anatomical and scar imaging based, where we could use a high resolution LE CMR imaging to predict the potential isthmuses within the myocardium [PDARG⁺11]. The prediction can be done by looking at the intensity profiles along the scar and PIZ areas within the myocardium, this could derive maps such as Fig 6.7(a) & Fig 6.7(b). Such maps can reveal small islands of healthy tissue present amidst of scar regions, which are potential candidates of VT re-entry trapped paths based on a priori information and clinical understanding of VT schematics. Such trapped paths are also revealed with VT-Stim modelling as shown in Fig 8.10. The second approach would be to use machine learning on the relationship between EP signals (electrograms recorded by CM or NCM) and MRI intensity profiles acquired from previous invasive clinical studies and use it to predict the potential EP fractionation maps and heterogeneity maps of APD, CV and their restitution. This machine learning requires training on a lot of datasets to have more accurate predictions, and is our on going work with Bordeaux University Hospital. These heterogeneity maps can then be used for VT-Stim simulation to study the VT dynamics.

In this PhD, we explored how the close integration of mathematics, computer science and medicine into model-based approaches can leverage on the important progress made in imaging of the human body in order to provide tools for challenging cardiac interventions.

List of Publications

This thesis is largely based on the following first author publications and submitted articles:

1 First-authored Methodological Papers (Peer-Reviewed)

Journal Papers

- [RCD⁺12] J. Relan, Z. Chen, H. Delingette, R. Karim, W. Schulze, J. Bostock, C. A. Rinaldi, K. Rhode, N. Ayache, R. Razavi and M. Sermesant. Role of spatial heterogeneity of restitution and conduction in ischemic ventricular tachycardia: a combined clinical and modelling study. 2012. Article in preparation.
- [RCS⁺11] J. Relan, P. Chinchapatnam, M. Sermesant, K. Rhode, M. Ginks, H. Delingette, C. A. Rinaldi, R. Razavi, and N. Ayache. Coupled personalization of cardiac electrophysiology models for prediction of ischaemic ventricular tachycardia. *Journal of the Royal Society Interface Focus*, 1(3):396–407, 2011.
- [RPD⁺11] J. Relan, M. Pop, H. Delingette, G. Wright, N. Ayache, and M. Sermesant. Personalisation of a cardiac electrophysiology model using optical mapping and MRI for prediction of changes with pacing. *IEEE Transactions on Bio-Medical Engineering*, 58(12):3339–3349, 2011.

Conference Papers

- [RCS⁺10] J. Relan, P. Chinchapatnam, M. Sermesant, K. Rhode, H. Delingette, R. Razavi, and N. Ayache. Coupled personalisation of electrophysiology models for simulation of induced ischemic ventricular tachycardia. In *Medical Image Computing and Computer-Assisted Intervention–MICCAI 2010*, volume 6362 of LNCS, pages 420–428. Springer, 2010.
- [RSD⁺09] J. Relan, M. Sermesant, H. Delingette, M. Pop, GA Wright, and N. Ayache. Quantitative comparison of two cardiac electrophysiology models using personalisation to optical and MR data. In *Biomedical Imaging: From Nano to Macro, 2009. ISBI'09. IEEE International Symposium on*, pages 1027–1030. IEEE, 2009.

- [RSP⁺09a] J. Relan, M. Sermesant, M. Pop, H. Delingette, M. Sorine, G. Wright, and N. Ayache. Parameter estimation of a 3D cardiac electrophysiology model including the restitution curve using optical and MR data. In Olaf Dössel and Wolfgang C. Schlegel, editors, *World Congress on Medical Physics and Biomedical Engineering*, volume 25/IV of *IFMBE Proceedings*, pages 1716–1719. Springer, September 2009.

Workshop Papers

- [RSDA11] J. Relan, M. Sermesant, H. Delingette, and N. Ayache. Personalisation of a 3D ventricular electrophysiological model, using endocardial and epicardial contact mapping and MRI. In *Statistical Atlases and Computational Models of the Heart. Imaging and Modelling Challenges - Second International Workshop, STACOM 2011, Held in Conjunction with MICCAI 2011*, pages 14–22, 2011.
- [RPD⁺10] J. Relan, M. Pop, H. Delingette, G. Wright, N. Ayache, and M. Sermesant. Estimation of Reaction, Diffusion and Restitution Parameters for a 3D Myocardial Model Using Optical Mapping and MRI. In *MICCAI Workshop (STACOM) and (CESC'10)*, volume 6364 of *LNCS*, pages 270–280. Springer, 2010.
- [RSP⁺09b] J. Relan, M. Sermesant, M. Pop, H. Delingette, M. Sorine, G. Wright, and N. Ayache. Volumetric prediction of cardiac electrophysiology using a heart model personalised to surface data. In *MICCAI Workshop on Cardiovascular Interventional Imaging and Biophysical Modelling - CI2BM09*, pages 19–27, 2009.

Abstracts

- [RSC⁺10] J. Relan, M. Sermesant, P. Chinchapatnam, H. Delingette, K. Rhode, R. Razavi, and N. Ayache. Personalisation of a 3D macroscopic cardiac electrophysiology model for simulation of induced ischemic ventricular tachycardia. First VPH Conference (VPH2010), Brussels, September 2010.
- [RS⁺09] J. Relan, M. Sermesant, , H. Delingette, M. Pop, M. Sorine, G.A. Wright, and N. Ayache. Personalisation of 3D cardiac electrophysiology models for valid predictions: A step towards patient-specific ventricular tachycardia modelling. *The Cardiac Physiome: Multi-scale and Multi-physics Mathematical Modelling Applied to the Heart*, Cambridge, UK, July 2009.

2 Clinical Abstracts

- [CJS⁺11] H. Cochet, A. S. Jadidi, F. Sacher, N. Derval, M. Sermesant, J. Relan, S. J. Kim, P. Bordachar, P. Ritter, M. Hocini, M. Montaudon, F. Laurent,

N. Ayache, M. Haïssaguerre, and P. Jais. Ventricular scar at cardiac CT correlates to critical isthmuses of ventricular tachycardia circuits and sites of slow conduction during sinus rhythm - evidence for clinical use of CT integration into 3D mapping systems. In *Heart Rhythm Society '11*, May 2011.

[JCS⁺11] A. S. Jadidi, H. Cochet, F. Sacher, S. J. Kim, M. Sermesant, J. Relan, N. Derval, S. Miyazaki, A. Shah, D. Scherr, S. B. Wilton, P. Pascale, L. Roten, M. Pederson, S. Knecht, P. Bordachar, P. Ritter, M. Hocini, M. Montaudon, F. Laurent, N. Ayache, M. Haïssaguerre, and P. Jais. Ventricular scar imaging at MRI correlates to critical isthmuses of ventricular tachycardia circuits and sites of slow conduction during sinus rhythm - utility of integrating MR-data into 3D mapping systems. In *Heart Rhythm Society '11*, May 2011.

[CJC⁺11] H. Cochet, A. S. Jadidi, O. Corneloup, M. Lederlin, J. Relan, M. Montaudon, M. Sermesant, P. Jaïs, and F. Laurent. Myocardial scar modeling from delayed enhancement MRI: Usefulness for the guidance of ventricular tachycardia mapping and ablation. In *Radiological Society of North America, RSNA '11*, November 2011.

3 Co-authored Publications

Journal Papers

[KRC⁺11] E. Konukoglu, J. Relan, U. Cilingir, B. Menze, P. Chinchapatnam, A. Jadidi, H. Cochet, M. Hocini, H. Delingette, P. Jaïs, M. Haïssaguerre, N. Ayache, and M. Sermesant. Efficient probabilistic model personalization integrating uncertainty on data and parameters: Application to eikonal-diffusion models in cardiac electrophysiology. *Progress in Biophysics and Molecular Biology*, 107:134–146, 2011.

[CSL⁺11] O. Camara, M. Sermesant, P. Lamata, L. Wang, M. Pop, J. Relan, M. De Craene, H. Delingette, H. Liu, S. Niederer, A. Pashaei, G. Plank, D. Romero, R. Sebastian, K.C.L. Wong, H. Zhang, N. Ayache, A.F. Frangi, P. Shi, N.P. Smith, and G.A. Wright. Inter-model consistency and complementarity: Learning from ex-vivo imaging and electrophysiological data towards an integrated understanding of cardiac physiology. *Progress in Biophysics and Molecular Biology*, 107:122–133, 2011.

[PSL⁺12] M. Pop, M. Sermesant, G. Liu, J. Relan, T. Mansi, A. Soong, J.M. Peyrat, M.V. Truong, P. Fefer, E.R. McVeigh, et al. Construction of 3D MR image-based computer models of pathologic hearts, augmented with histology and optical fluorescence imaging to characterize action potential propagation. *Medical Image Analysis*, 16:505–523, 2012.

[PSK⁺11] E. Pernod, M. Sermesant, E. Konukoglu, J. Relan, H. Delingette, and N. Ayache. A multi-front eikonal model of cardiac electrophysiology for in-

teractive simulation of radio-frequency ablation. *Computers and Graphics*, 35:431–440, 2011.

- [[SCC⁺12](#)] M. Sermesant, R. Chabiniok, P. Chinchapatnam, T. Mansi, F. Billet, P. Moireau, J.M. Peyrat, K. Wong, J. Relan, K. Rhode, M. Ginks, P. Lambiase, H. Delingette, M. Sorine, C.A. Rinaldi, D. Chapelle, R. Razavi, and N. Ayache. Patient-specific electromechanical models of the heart for the prediction of pacing acute effects in CRT: A preliminary clinical validation. *Medical Image Analysis*, 16(1):201–215, 2012.
- [[SdVM⁺11](#)] N. Smith, A. de Vecchi, M. McCormick, D. Nordsletten, O. Camara, A.F. Frangi, H. Delingette, M. Sermesant, J. Relan, N. Ayache, M. W. Krueger, W. Schulze, R. Hose, I. Valverde, P. Beerbaum, C. Staicu, M. Siebes, J. Spaan, P. Hunter, J. Weese, H. Lehmann, D. Chapelle, and R. Razavi. euheart: Personalized and integrated cardiac care using patient-specific cardiovascular modelling. *Journal of the Royal Society Interface Focus*, 1(3):349–364, 2011.

Conference Papers

- [[PSRD10](#)] E. Pernod, M. Sermesant, J. Relan, and H. Delingette. Interactive real time simulation of cardiac radio-frequency ablation. In *Proc. of Eurographics Workshop on Visual Computing for Biology and Medicine (2010) (VCBM'2010)*, pages 91–98, Leipzig, August 2010.

Workshop Papers

- [[LMR⁺09](#)] H. Lamecker, T. Mansi, J. Relan, F. Billet, M. Sermesant, N. Ayache, and H. Delingette. Adaptive tetrahedral meshing for personalized cardiac simulations. In *MICCAI Workshop on Cardiovascular Interventional Imaging and Biophysical Modelling (CI2BM09)*, pages 149–158, London United Kingdom, 2009.

4 European project deliverables

- [[RDS⁺11](#)] J. Relan, H. Delingette, M. Sermesant, N. Ayache, M. W. Krueger, W. Schulze, G. Seemann, and O. Dössel. Planning of Radiofrequency Ablation for Patients with Ventricular Tachycardia. Deliverables D6.3.2, European project euHeart, June 2011.
- [[KSS⁺11](#)] M. W. Krueger, W. Schulze, G. Seemann, O. Dössel, J. Relan, H. Delingette, M. Sermesant, and N. Ayache. Planning of Radiofrequency Ablation for patients with Atrial Fibrillation. Deliverables D6.3.1, European project euHeart, June 2011.

- [KRD⁺11] M. W. Krueger, J. Relan, H. Delingette, W. Schulze, G. Seemann, and O. Dössel. Model personalization for AF and VT simulations. Deliverables D6.2.2, European project euHeart, January 2011.
- [KRD⁺10] M. W. Krueger, J. Relan, H. Delingette, M. Sermesant, N. Ayache, G. Seemann, and O. Dössel. Computational models for AF and VT simulation. Deliverables D6.2.1, European project euHeart, May 2010.

Part VI

APPENDIX

Quantitative Comparison of Two Cardiac Electrophysiology Models

In order to translate the important modelling work into clinical tools, the selection of the best model for a given application is crucial. In this paper, we quantitatively compare personalisation of two different cardiac electrophysiology models on the same dataset, in order to help such a selection. One is a phenomenological model, the Aliev-Panfilov model (1996), and the other one is a simplified ionic model, the Mitchell-Schaeffer model (2003). In the preliminary steps of model personalisation, we optimise the forward problem with the determination of an optimum time integration scheme for each model, which could result in stable and accurate simulations without the use of unnecessary expensive high temporal and spatial resolutions. Next, we personalise the two models by optimising their respective parameters, to match the depolarisation and repolarisation maps obtained ex-vivo from optical imaging of large porcine healthy heart. Last, we compare the personalisation results of the two different models.

Based on: [RSD⁺09] J. Relan, M. Sermesant, H. Delingette, M. Pop, GA Wright, and N. Ayache. Quantitative comparison of two cardiac electrophysiology models using personalisation to optical and MR data. In *Biomedical Imaging: From Nano to Macro, 2009. ISBI'09. IEEE International Symposium on*, pages 1027–1030. IEEE, 2009.

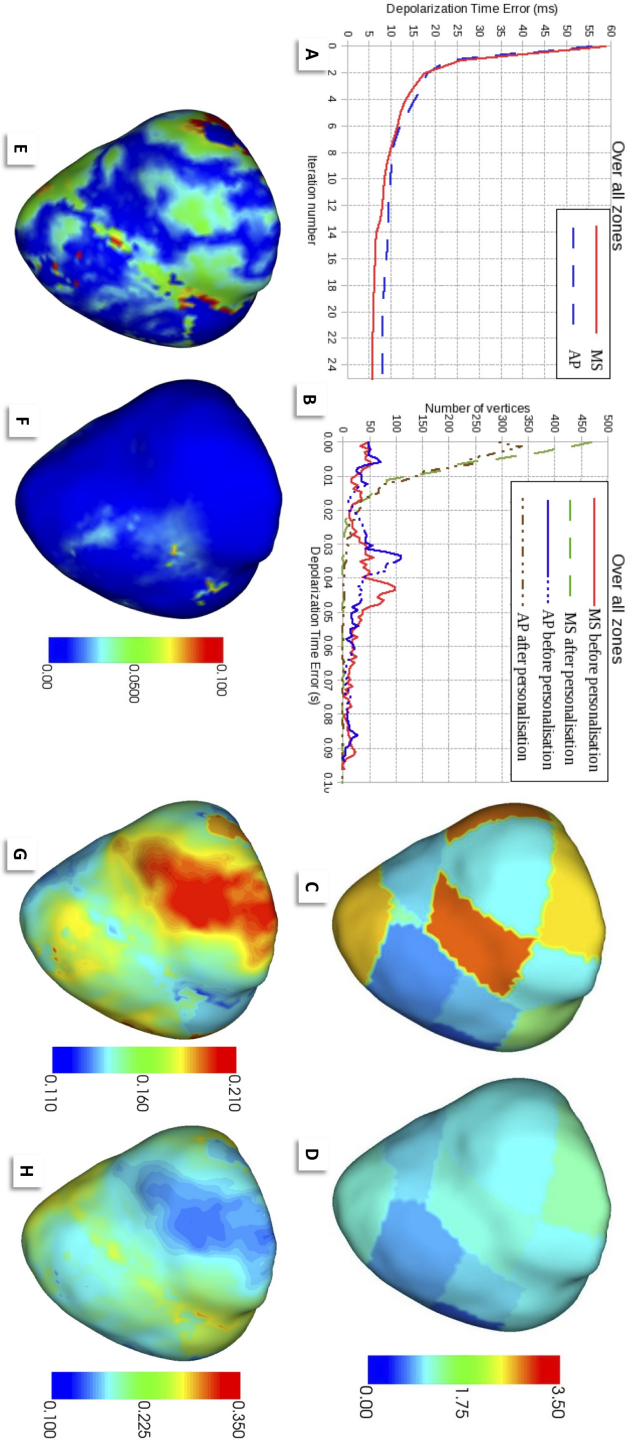


Figure A.1: (A) Depolarisation time error descent and (B) histogram for the two models. Maps of parameter d for (C) Aliev-Panfilov model and (D) Mitchell-Schaefter model. APD error maps (in s) after personalisation for (E) Aliev-Panfilov model and (F) MS model. Maps of (G) parameter α for Aliev-Panfilov model and (H) parameter τ_{close} for MS model for APD.

Time Integration schemes & Spatial and Temporal resolution

Contents

1	Time integration	153
1.1	First Order Schemes	153
1.2	Second Order Schemes	154
1.3	Third Order Schemes	155
2	Choosing optimum spatial & temporal resolutions	155

1 Time integration

A variety of explicit, semi-implicit and implicit schemes categorised as first, second and third order schemes have been evaluated for cardiac bidomain model [EB08]. Here we implemented and evaluated these schemes for monodomain MS model in terms of solution accuracy, stability, and computational time. Monodomain MS model can be written in a generic way as,

$$\begin{cases} \partial_t u = D(u) + F(u, z) \\ \partial_t z = G(u, z) \end{cases} \quad (\text{B.1})$$

where D represents the diffusion term and F, G represents the reaction term of the model and n is the current iteration number. The different schemes were implemented as follows:

1.1 First Order Schemes

Explicit Euler is given as:

$$\begin{cases} \frac{u^{n+1} - u^n}{\delta t} = D(u^n) + (F(u^n, z^n)) \\ \frac{z^{n+1} - z^n}{\delta t} = G(u^n, z^n) \end{cases} \quad (\text{B.2})$$

Crank-Nicolson (CN) is given as:

$$\begin{cases} \frac{u^{n+1} - u^n}{\delta t} = \frac{1}{2}D(u^{n+1}) + \frac{1}{2}D(u^n) + (F(u^n, z^n)) \\ \frac{z^{n+1} - z^n}{\delta t} = G(u^n, z^n) \end{cases} \quad (\text{B.3})$$

Forward-Backward Euler is given as:

$$\begin{cases} \frac{u^{n+1} - u^n}{\delta t} = D(u^{n+1}) + (F(u^n, z^n)) \\ \frac{z^{n+1} - z^n}{\delta t} = G(u^n, z^n) \end{cases} \quad (\text{B.4})$$

Implicit-Explicit (IMEX) is given as:

$$\begin{cases} \frac{\frac{3}{2}u^{n+1} - 2u^n + \frac{1}{2}u^{n-1}}{\delta t} = D(u^{n+1}) + (F(u^n, z^n)) \\ \frac{\frac{3}{2}z^{n+1} - 2z^n + \frac{1}{2}z^{n-1}}{\delta t} = G(u^{n+1}, z^{n+1}) \end{cases} \quad (\text{B.5})$$

Backward Euler (Implicit) is given as:

$$\begin{cases} \frac{u^{n+1} - u^n}{\delta t} = D(u^{n+1}) + (F(u^{n+1}, z^{n+1})) \\ \frac{z^{n+1} - z^n}{\delta t} = (G(u^{n+1}, z^{n+1})) \end{cases} \quad (\text{B.6})$$

1.2 Second Order Schemes

Second-order Backward Differentiation Formula (SBDF) is given as:

$$\begin{cases} \frac{\frac{3}{2}u^{n+1} - 2u^n + \frac{1}{2}u^{n-1}}{\delta t} = D(u^{n+1}) + (2F(u^n, z^n) - F(u^{n-1}, z^{n-1})) \\ \frac{\frac{3}{2}z^{n+1} - 2z^n + \frac{1}{2}z^{n-1}}{\delta t} = 2G(u^n, z^n) - G(u^{n-1}, z^{n-1}) \end{cases} \quad (\text{B.7})$$

Crank-Nicolson Adams-Bashforth (CNAB) is given as:

$$\begin{cases} \frac{u^{n+1} - u^n}{\delta t} = \frac{1}{2}D(u^{n+1}) + \frac{1}{2}D(u^n) \\ \quad + \left(\frac{3}{2}F(u^n, z^n) - \frac{1}{2}F(u^{n-1}, z^{n-1})\right) \\ \frac{z^{n+1} - z^n}{\delta t} = \left(\frac{3}{2}G(u^n, z^n) - \frac{1}{2}G(u^{n-1}, z^{n-1})\right) \end{cases}$$

Modified Crank-Nicolson Adams-Bashforth (MCNAB) is given as:

$$\begin{cases} \frac{u^{n+1} - u^n}{\delta t} = \frac{9}{16}D(u^{n+1}) + \frac{3}{8}D(u^n) + \frac{1}{16}D(u^{n-1}) \\ \quad + \left(\frac{3}{2}F(u^n, z^n) - \frac{1}{2}F(u^{n-1}, z^{n-1})\right) \\ \frac{z^{n+1} - z^n}{\delta t} = \left(\frac{3}{2}G(u^n, z^n) - \frac{1}{2}G(u^{n-1}, z^{n-1})\right) \end{cases} \quad (\text{B.8})$$

Implicit Gear is given as:

$$\begin{cases} \frac{\frac{3}{2}u^{n+1} - 2u^n + \frac{1}{2}u^{n-1}}{\delta t} = D(u^{n+1}) + F(u^{n+1}, z^{n+1}) \\ \frac{\frac{3}{2}z^{n+1} - 2z^n + \frac{1}{2}z^{n-1}}{\delta t} = (G(u^{n+1}, z^{n+1})) \end{cases} \quad (\text{B.9})$$

1.3 Third Order Schemes

Third order SBDF is given as:

$$\left\{ \begin{array}{l} \frac{11}{6}u^{n+1} - 3u^n + \frac{3}{2}u^{n-1} - \frac{1}{3}u^{n-2} \\ \hline \delta t \end{array} \right. = \begin{array}{l} D(u^{n+1}) + (3F(u^n, z^n) \\ - 3F(u^{n-1}, z^{n-1}) - F(u^{n-2}, z^{n-2})) \end{array}$$

$$\left\{ \begin{array}{l} \frac{11}{6}z^{n+1} - 3z^n + \frac{3}{2}z^{n-1} - \frac{1}{3}z^{n-2} \\ \hline \delta t \end{array} \right. = \begin{array}{l} 3G(u^n, z^n) \\ - 3G(u^{n-1}, z^{n-1}) + G(u^{n-2}, z^{n-2}) \end{array}$$

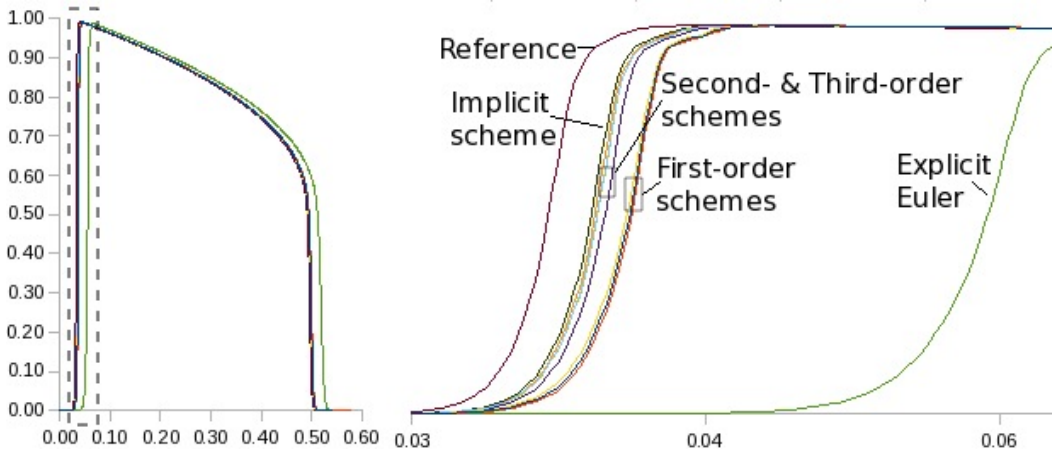


Figure B.1: Transmembrane potential u wave for MS model and zoom (dashed box), temporally integrated with different schemes, on $h = 1.5mm$, $\delta t = 1ms$ in comparison with reference (abscissa: normalised potential vs time (s)).

2 Choosing optimum spatial & temporal resolutions

A reference solution approximately representing the exact solution of the model is computed using finer 3D mesh resolution (mean edge length of tetrahedra) δx and temporal resolution δt ($\delta x = 0.13mm$ and $\delta t = 10^{-6}s$), with implicit scheme. Stability of a given time integration scheme is determined by varying the model parameter controlling the wave speed, and observing the solution for oscillations, for a range of δx and δt . Second order schemes are observed to be more stable at higher wave speed and large time steps. Whereas accuracy is determined with constant model parameters and by computing the wave speed error (as shown in Figure B.1, similar for MS model) with respect to the reference solution for a range of δx and δt . And we observe that for small δx and small δt , all time integration schemes are comparable, for small δx and large δt higher than first order schemes provide relative wave speed error $< 1\%$ and for large δx the wave speed error is

high irrespective of time integration scheme used. Computational time (2.16 GHz, dual core, 2.0 GiB) of one time step for explicit and semi-implicit schemes are comparable and is relative to the mesh size (for ≈ 247250 number of tetrahedra) $\approx 1s$ and for fully implicit schemes $\approx 1s$ for small δt to $\approx 3s$ for large δt . From all of this analysis, we determine an optimum δx , time integration scheme and δt for the model. By optimum value, we mean the largest possible value for which the relative error $< 10\%$. For MS model the optimum time integration scheme was MCNAB (second order) (see Equation B.8) with $\delta t = 0.1ms$, and optimum $\delta x \approx 1.0 - 1.5mm$ with one time step computation time $\approx 1s$.

Model specifications and performance

In this thesis, the MS model personalisations were performed on a volumetric tetrahedral mesh of a 2 valve or 4 valve bi-ventricular anatomy with a Mean Edge Length (MEL) of 1.0 *mm* and ≈ 65547 number of tetrahedrons. The model parameters, simulation, personalisation, VT induction specifications and VT-Stim protocol used are detailed in Table [C.1](#), [C.2](#), [C.3](#) & [C.4](#) respectively, unless they are specified in the chapters.

Table C.1: Electrophysiology Model Parameters

EK Model		MS Model	
Parameter	Value	Parameter	Value
DT-MRI/Atlas(<i>ex-vivo</i>)/Synthetic(-80,80)		DT-MRI/Atlas(<i>ex-vivo</i>)/Synthetic(-80,80)	
DT-MRI/Atlas(<i>ex-vivo</i>)/Synthetic(-80,80)	2.5	DT-MRI/Atlas(<i>ex-vivo</i>)/Synthetic(-80,80)	2.5
DT-MRI/Atlas(<i>ex-vivo</i>)/Synthetic(-80,80)	estimated	DT-MRI/Atlas(<i>ex-vivo</i>)/Synthetic(-80,80)	coupled
DT-MRI/Atlas(<i>ex-vivo</i>)/Synthetic(-80,80)	2.5	DT-MRI/Atlas(<i>ex-vivo</i>)/Synthetic(-80,80)	0.003 s
DT-MRI/Atlas(<i>ex-vivo</i>)/Synthetic(-80,80)	0.003 s	DT-MRI/Atlas(<i>ex-vivo</i>)/Synthetic(-80,80)	0.06 s
DT-MRI/Atlas(<i>ex-vivo</i>)/Synthetic(-80,80)		DT-MRI/Atlas(<i>ex-vivo</i>)/Synthetic(-80,80)	estimated
DT-MRI/Atlas(<i>ex-vivo</i>)/Synthetic(-80,80)		DT-MRI/Atlas(<i>ex-vivo</i>)/Synthetic(-80,80)	estimated
DT-MRI/Atlas(<i>ex-vivo</i>)/Synthetic(-80,80)		DT-MRI/Atlas(<i>ex-vivo</i>)/Synthetic(-80,80)	0.13
DT-MRI/Atlas(<i>ex-vivo</i>)/Synthetic(-80,80)		DT-MRI/Atlas(<i>ex-vivo</i>)/Synthetic(-80,80)	0.2
DT-MRI/Atlas(<i>ex-vivo</i>)/Synthetic(-80,80)		DT-MRI/Atlas(<i>ex-vivo</i>)/Synthetic(-80,80)	0.2

Table C.2: Model simulation & personalisation specifications

EK Model		MS Model	
Spatial Integration		Spatial Integration	
Spatial step size (MEL) $\delta(x)$	FMM	Spatial step size (MEL) $\delta(x)$	FEM
Spatial step size (MEL) $\delta(x)$	1.0 mm	Spatial step size (MEL) $\delta(x)$	1.0 mm
Temporal Integration		Temporal Integration	
Temporal step size $\delta(t)$	-	Temporal step size $\delta(t)$	MGNAB
Computational Time (CT) per 10 $\delta(t)$	-	Computational Time (CT) per 10 $\delta(t)$	0.03 ms
CT for 1 cycle dep phase (150 ms)	\approx 1-2 s	CT for 1 cycle dep phase (150 ms)	\approx 1 s
AC Estimation Time	\approx 30-40 min	AC Estimation Time	-
Coupled conductivity Estimation Time	-	Coupled conductivity Estimation Time	\approx 1 s
Restitution Estimation Time	-	Restitution Estimation Time	\approx 2-5 min

Table C.3: Induced VT specifications (Table D.3 & D.4)

VT-stim protocol	Over-drive pacing
VT-stim location	LV endocardium - apex
VT-stim pacing frequency	150 bpm
VT-stim pacing duration	5 s
Induced VT type	sustained monomorphic VT
Induced VT frequency	240 bpm

Table C.4: *in-silico* VT-Stim protocol specifications (Table D.5 & Fig 8.11)

	OverDrivePacing	S1-S2	S1-S2-S3
Pacing Frequency	100, 120, 150, 180bpm	100bpm - 10 ms ↓, 150bpm - 10ms ↓	100bpm - 230ms - 10ms ↓, 150bpm - 270ms - 10ms ↓
Number of Paced Stimuli	6	4	4
Number of Extra-stimuli	-	1	2
Stimulus Site	All-over	RV-Apex, RV Outflow tract, Peri-infarct area	RV-Apex, RV Outflow tract, Peri-infarct area
Stimulus type	Voltage	Voltage	Voltage
Sinus Rhythm (SR) rate	65bpm	65bpm	65bpm
			Wellens protocol [WBS85]
Pacing Sequence			SR - 1 S1, SR - 2 S1, 100bpm - 1 S1, 100bpm - 2 S1, 120bpm - 1 S1, 120bpm - 2 S1, 140bpm - 1 S1, 140bpm - 2 S1, SR - 3 S1, 100bpm - 3 S1, 120bpm - 3 S1, 140bpm - 3 S1
Number of Paced Stimuli			4
Stimulus Site			RV-Apex, RV Outflow tract, Peri-infarct area
Stimulus type			Voltage
Sinus rhythm rate			65bpm

Figure Glossary

This appendix provides a glossary of figures containing snapshots of EP personalisation, prediction, VT simulation & VT data movies. It also shows snapshots of a movie on synchronisation of the minimal invasive non-contact mapping data & non-invasive BSPM during VT, a work done in collaboration with KCL, London and IBT, Germany. It also provides figures on various VT re-entry patterns inducible with various VT-Stim simulations at different pacing sites with different pacing protocols.

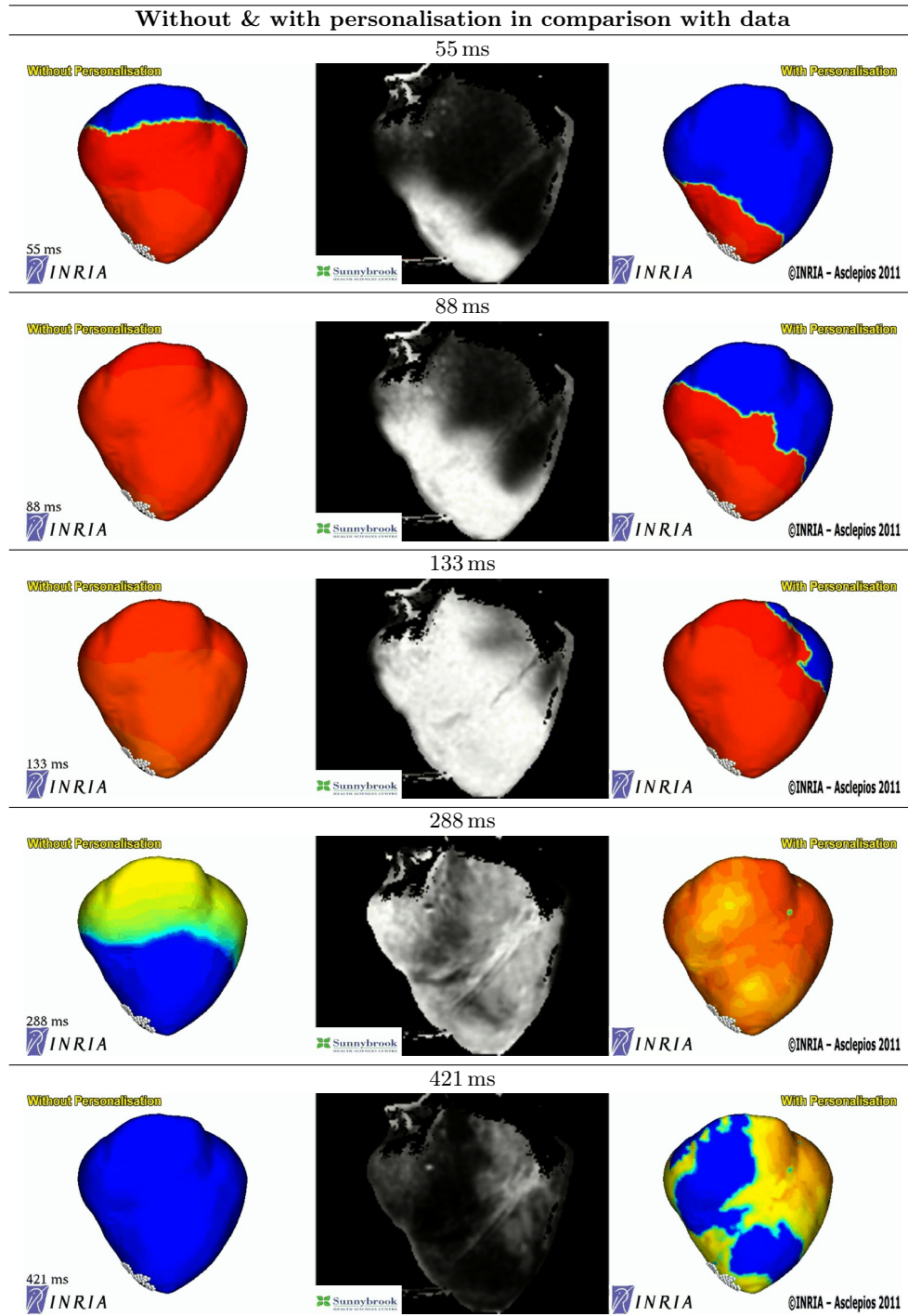
1 EP model personalisation to *ex-vivo* optical data

Table D.1: Simulation of MS model without personalisation (left) and with personalisation (right) for 1B-LV-Epi-r pacing, in comparison with optical data (middle).

2 EP model prediction to various pacing locations

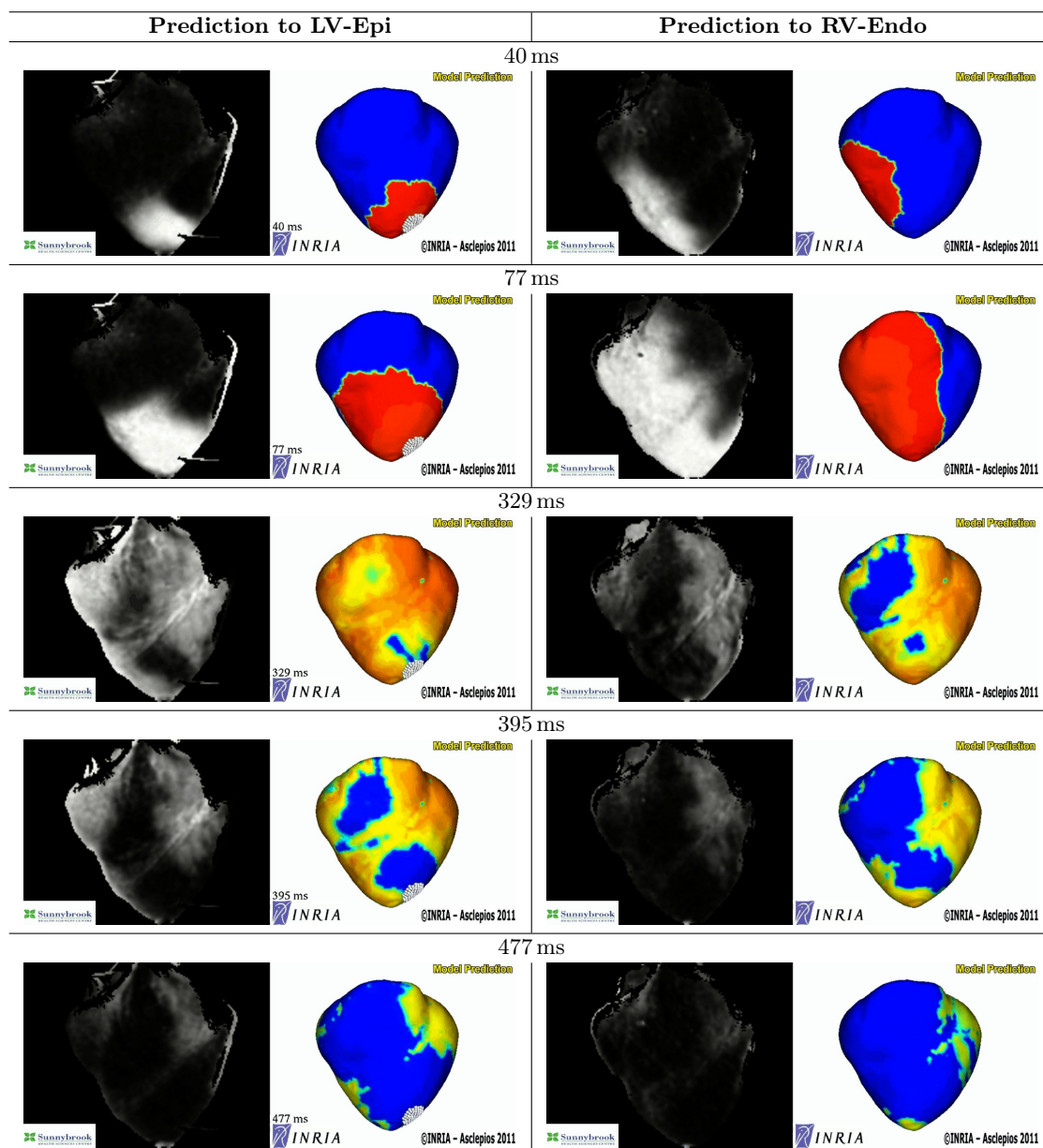


Table D.2: Prediction of MS model after personalisation, for 1A-LV-Epi-l (left) & 1D-RV-Endo pacings (right), in comparison with optical data.

3 VT induction after personalisation

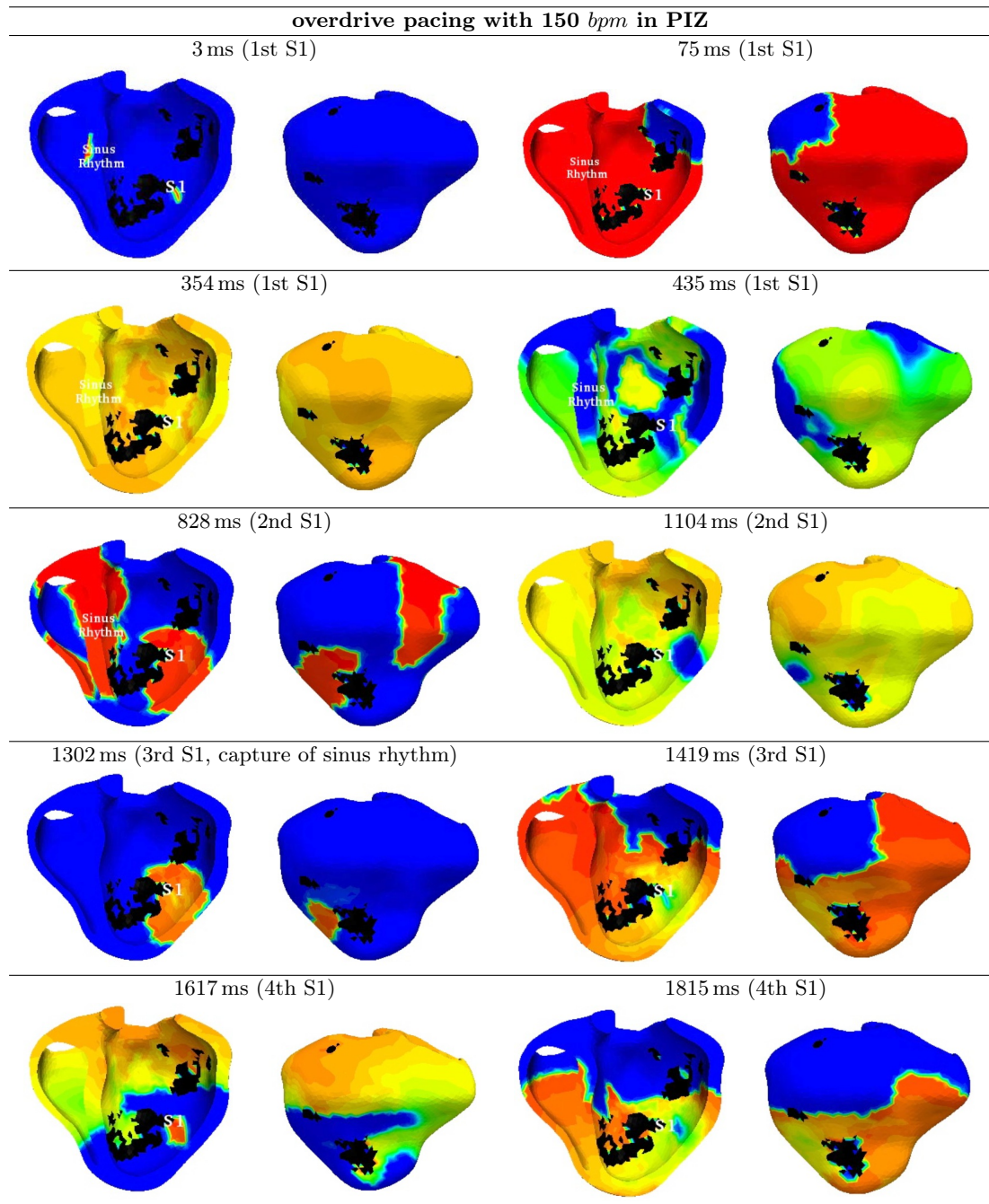


Table D.3: VT-stim modelling using personalised electrophysiological model. (red - depolarised & blue - repolarised)

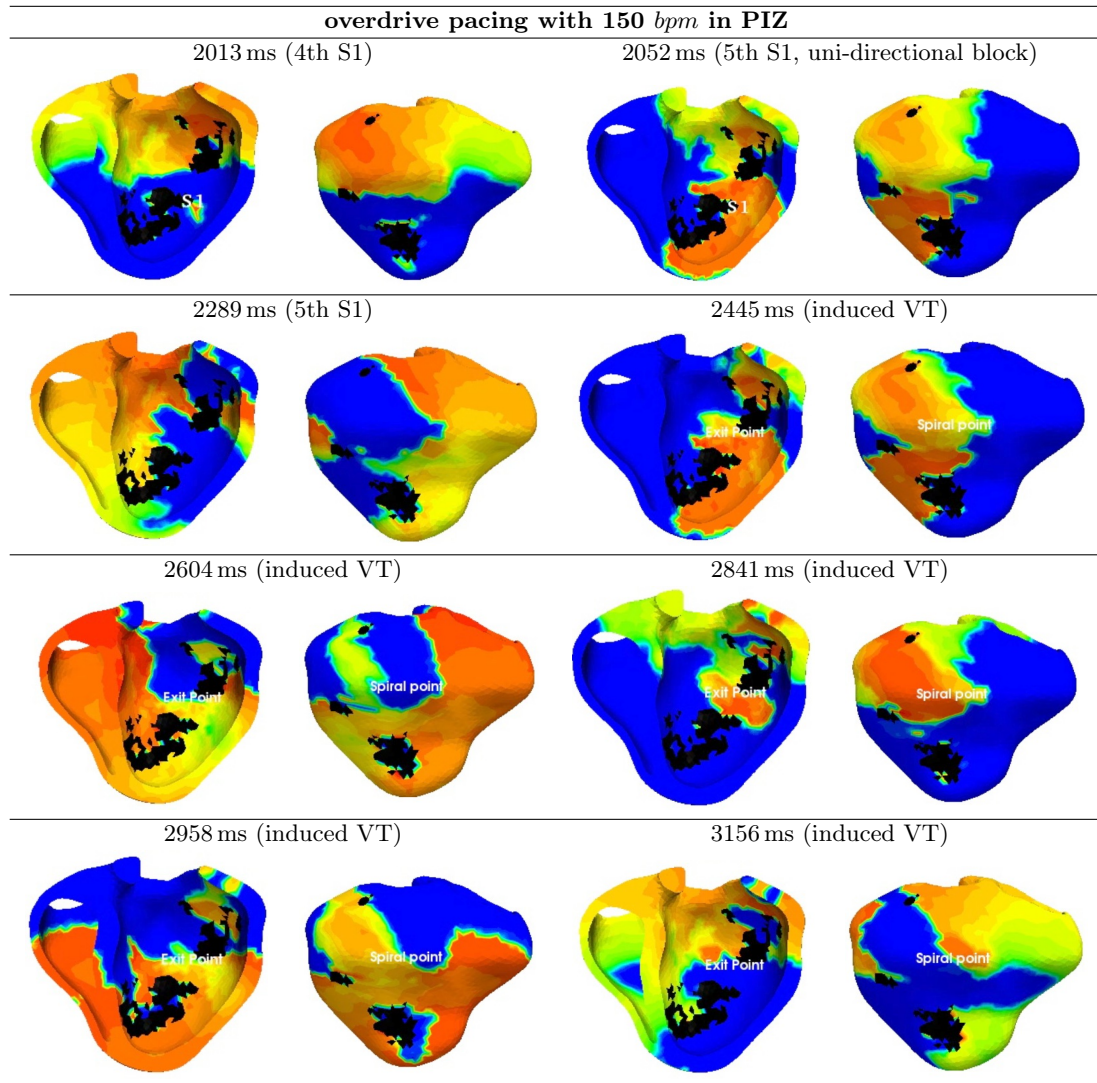


Table D.4: VT-stim modelling using personalised electrophysiological model (continued from table D.3). (red - depolarised & blue - repolarised)

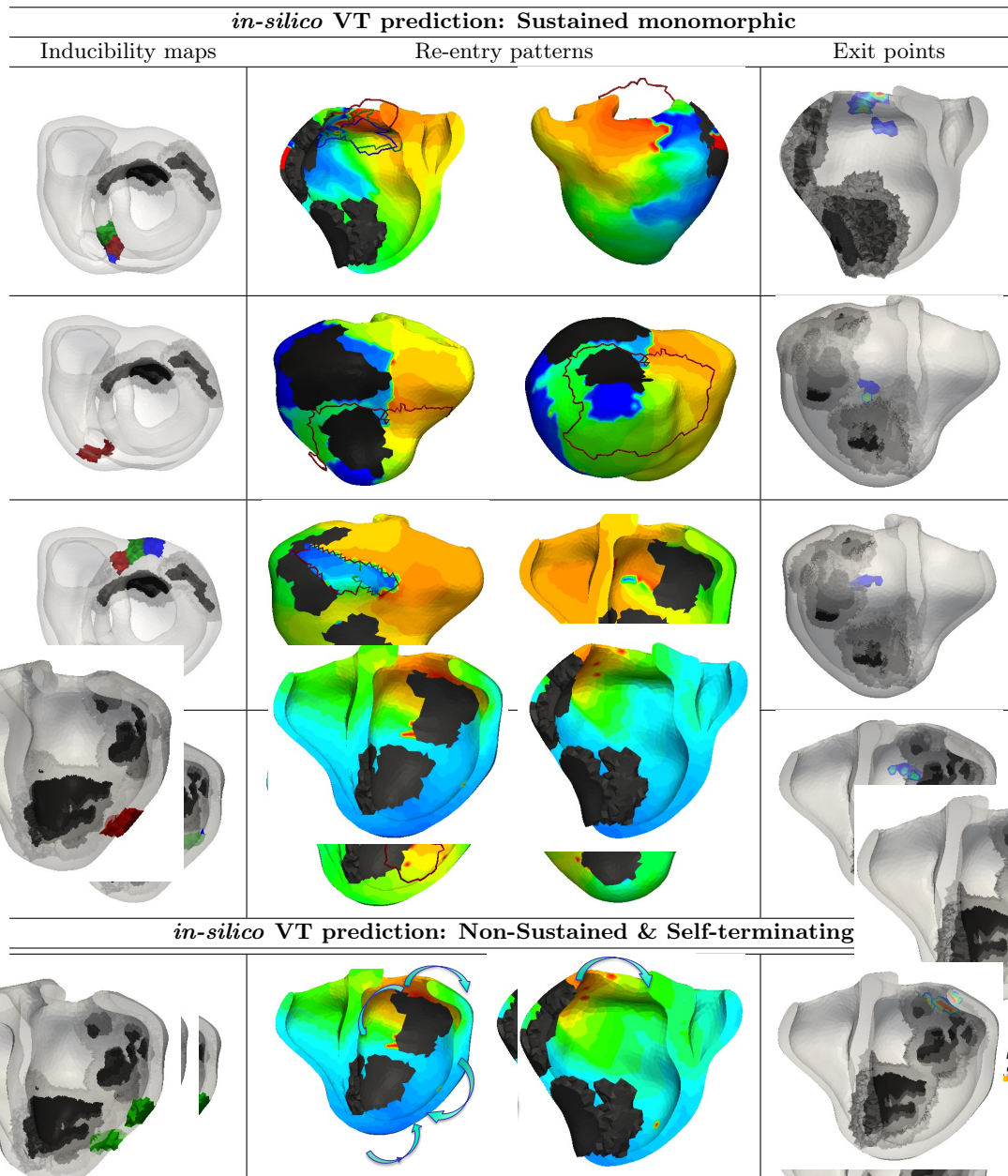
4 *in-silico* RFA planning after personalisation

Table D.5: *in-silico* VT-stim modelling predictions for various protocols (over-drive, S1-S2, S1-S2-S3-S4, etc) & various pacing locations using personalised electrophysiological model. Inducibility maps: pacing locations with successful induction of VT, Re-entry patterns: isochrones for predicted VT re-entry circuits & Exit points: points triggering the VT circuits (potential RFA targets)

5 Induced VT circuit from clinical data

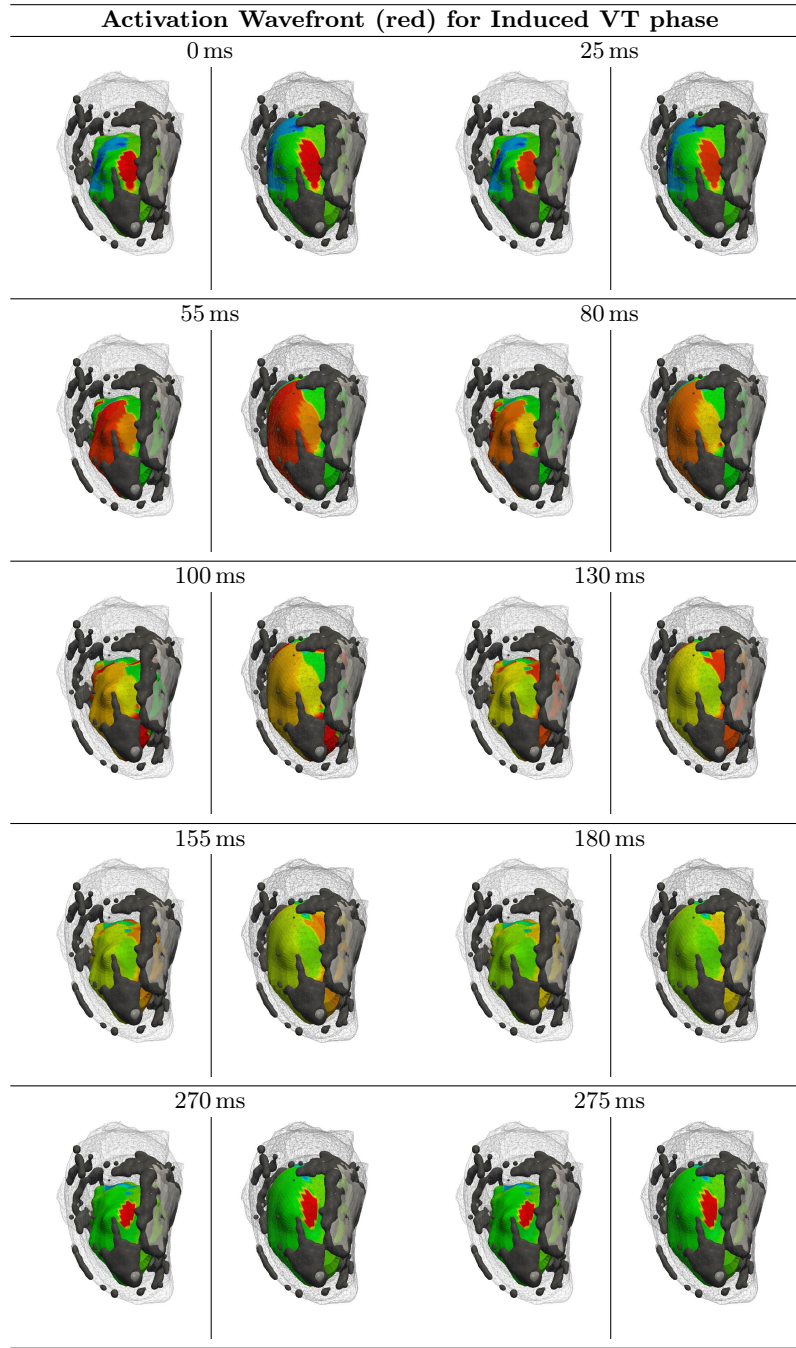


Table D.6: Propagation of the activation wavefront in red showing the VT circuit in time, for the induced VT phase observed in the clinical data (IHD_1) during a clinical VT stimulation study.

6 Integration of BSPM - Ensite Mapping

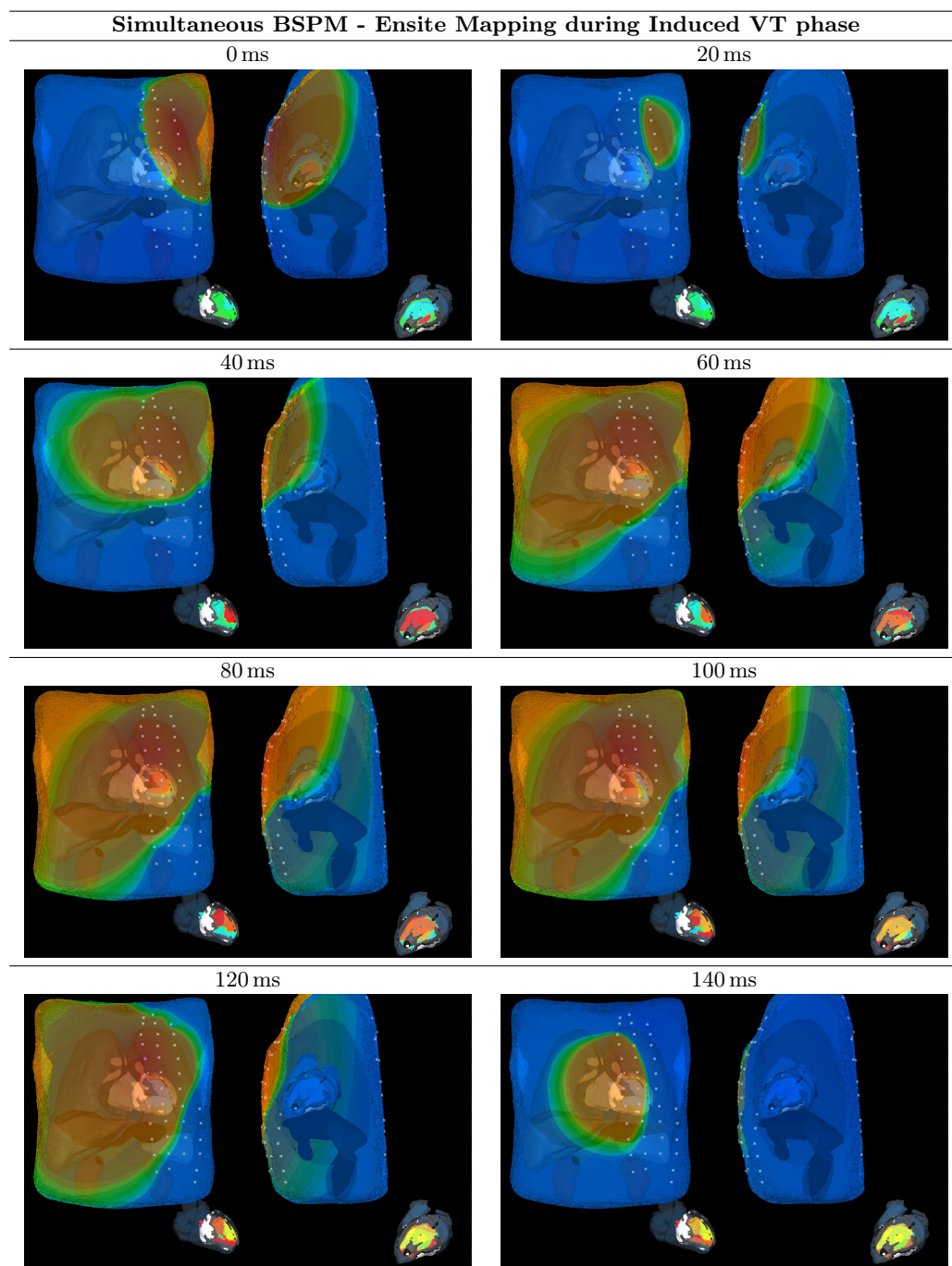


Table D.7: Integration of the simultaneous intra-cardiac electro-anatomical mapping and measured BSPM, for the induced VT phase. Work in collaboration with IBT Germany & KCL London.

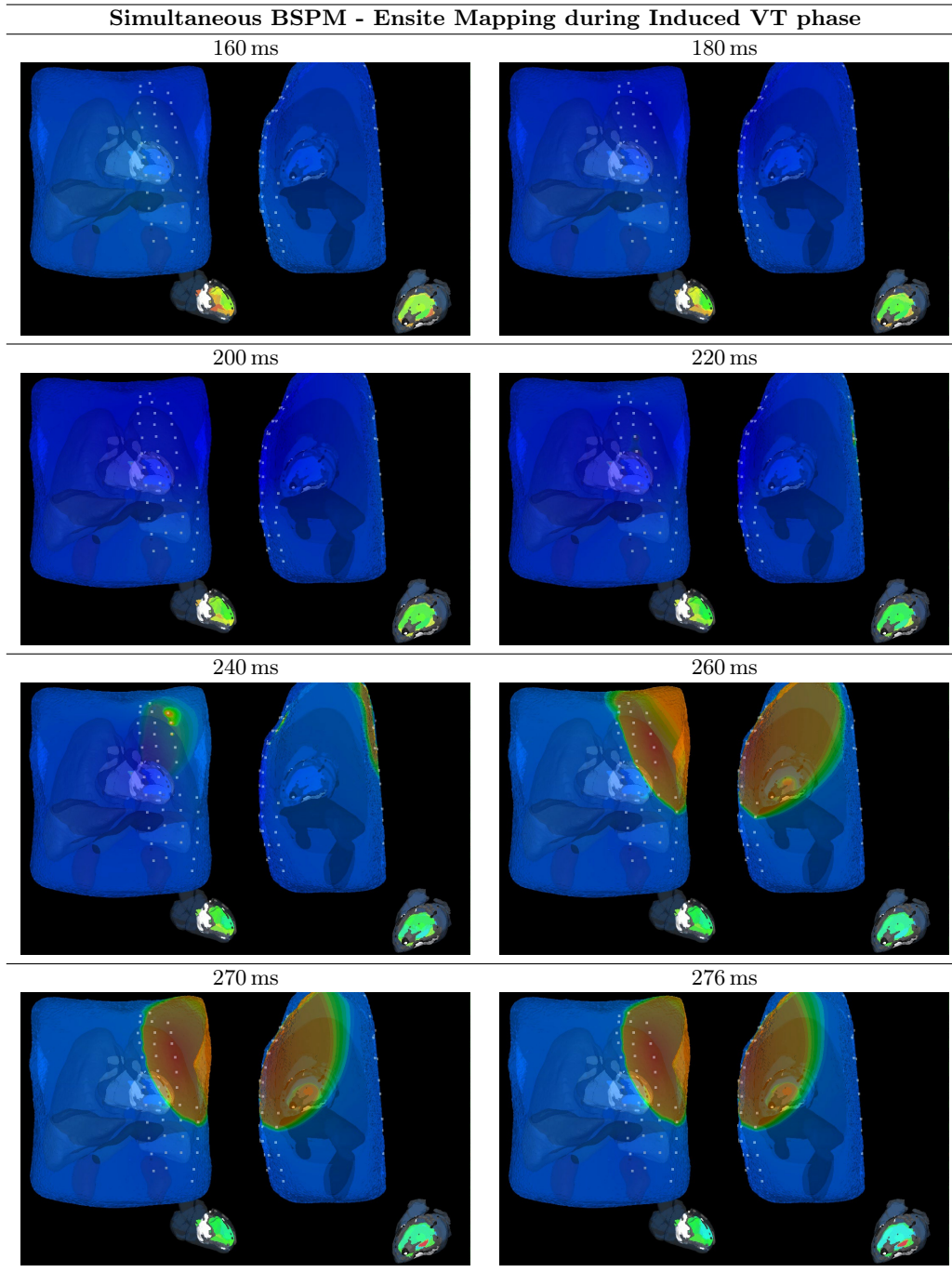


Table D.8: Integration of the simultaneous intra-cardiac electro-anatomical mapping and measured BSPM, for the induced VT phase. Work in collaboration with IBT Germany & KCL London.

7 Clinical VT-Stim protocol

Ventricular Tachycardia (VT) stimulation protocol

Equipment needed

Defibrillator attached to patient
 Resuscitation equipment
 BP monitor
 Saturations probe
 12 lead ECG
 Josephson catheter and cable

The techniques used to induce a tachyarrhythmia are known as programmed electrical stimulation. The Wellens protocol is a 12 stage procedure used to attempt to induce VT.

VT stimulation protocol - Wellens

- Stage 1 – 1x sensed extra (S2) from 360, decrement until ventricular refractory period (VERP) reached. Then increase by 10ms until consistent capture
- Stage 2 – add a second sensed beat (S3) from 360ms, decrement until VERP
- Stage 3 – 600ms 8 beat drive train (S1) with S2 from 360msec and decrement until VERP
- Stage 4 – 600ms (S1), S2 at consistent capture and introduce S3 at 360msec and decrement to VERP
- Stage 5 – 500ms (S1) introducing S2 as stage 3
- Stage 6 – 500ms (S1) and S2, introduce S3 as in stage 4
- Stage 7 – 400ms (S1) introduce S2
- Stage 8 – 400ms (S1) and S2, introduce S3
- Stage 9 – return Stage 2, sensed extras S2 and S3 at just above VERP and add S4 at 360ms and decrement to VERP
- Stage 10 – 600ms (S1) drive train with S2 and S3 just above VERP (as in stage 4 and add S4 at 360ms and decrease to VERP
- Stage 11 – 500ms(S1) drive train, with S2 and S3 just above VERP (as in stage 6, add S4 and decrement
- Stage 12 – 400ms (S1) drive, with S2 and S3 (as in stage 8) and add S4, decrement to VERP.

No VT induced

- Consider alternate site pacing ie RVOT
- Consider isoprenaline bolus or infusion

Figure D.1: Wellens protocol, the pacing protocol used for VT-Stim study at KCL, London.

Bibliography

- [ADW⁺05] H. Aupperle, N. Doll, T. Walther, C. Ullmann, H.A. Schoon, and F. Wilhelm Mohr. Histological findings induced by different energy sources in experimental atrial ablation in sheep. *Interactive Cardio-Vascular and Thoracic Surgery*, 4(5):450, 2005. (Cited on page 105.)
- [AKTM09] G.K. Andrikopoulos, K. Kappos, S. Tzeis, and A.S. Manolis. Contact and non-contact electroanatomic mapping in electrophysiology. *Hospital Chronicles*, 1(1 sup):44–48, 2009. (Cited on pages 15 and 79.)
- [ART07] H. Arevalo, B. Rodriguez, and N. Trayanova. Arrhythmogenesis in the heart: Multiscale modeling of the effects of defibrillation shocks and the role of electrophysiological heterogeneity. *Chaos: An Interdisciplinary Journal of Nonlinear Science*, 17:015103, 2007. (Cited on pages 53, 79, 88 and 115.)
- [ASAG09] E.M. Aliot, W.G. Stevenson, and J.M. Almendral-Garrote. EHRA/HRS expert consensus on catheter ablation of ventricular arrhythmias. *Europace*, 11:771–817, 2009. (Cited on pages 52, 78 and 114.)
- [AUR⁺03] B. Avitall, D. Urboniene, G. Rozmus, D. Lafontaine, R. Helms, and A. Urbonas. New cryotechnology for electrical isolation of the pulmonary veins. *Journal of Cardiovascular Electrophysiology*, 14:281–286, 2003. (Cited on page 97.)
- [BCF⁺09] R. Bordas, B. Carpentieri, G. Fotia, F. Maggio, R. Nobes, J. Pitt-Francis, and J. Southern. Simulation of cardiac electrophysiology on next-generation high-performance computers. *Philosophical Transactions of the Royal Society A: Mathematical, Physical and Engineering Sciences*, 367(1895):1951–1969, 2009. (Cited on page 138.)
- [BE93] M. Bär and M. Eiswirth. Turbulence due to spiral breakup in a continuous excitable medium. *Physical Review E*, 48(3):1635–1637, 1993. (Cited on page 26.)
- [BEL03] Y. Bourgault, M. Ethier, and V.G. LeBlanc. Simulation of electrophysiological waves with an unstructured finite element method. *ESAIM: Mathematical Modelling and Numerical Analysis*, 37(04):649–661, 2003. (Cited on page 20.)
- [Ber00] R.D. Berger. Repolarization alternans: toward a unifying theory of reentrant arrhythmia induction. *Circulation Research*, 87(12):1083–1084, 2000. (Cited on page 25.)

- [BG02] I. Banville and R.A. Gray. Effect of action potential duration and conduction velocity restitution and their spatial dispersion on alternans and the stability of arrhythmias. *Journal of cardiovascular electrophysiology*, 13(11):1141–1149, 2002. (Cited on pages 53 and 115.)
- [BGR⁺06] F. Bogun, E. Good, S. Reich, D. Elmouchi, P. Igie, D. Tschopp, S. Dey, A. Wimmer, K. Jongnarangsin, H. Oral, et al. Role of Purkinje fibers in post-infarction ventricular tachycardia. *Journal of the American College of Cardiology*, 48(12):2500, 2006. (Cited on pages 65 and 131.)
- [BHZ94] VN Biktashev, AV Holden, and H. Zhang. Tension of organizing filaments of scroll waves. *Philosophical Transactions of the Royal Society of London. Series A: Physical and Engineering Sciences*, 347(1685):611–630, 1994. (Cited on page 26.)
- [BOCF08] A. Bueno-Orovio, E.M. Cherry, and F.H. Fenton. Minimal model for human ventricular action potentials in tissue. *Journal of theoretical biology*, 253(3):544–560, 2008. (Cited on pages 53 and 138.)
- [BOPGF04] A. Bueno-Orovio, V.M. Pérez-García, and F.H. Fenton. Spectral methods for partial differential equations in irregular domains: the spectral smoothed boundary method. *Arxiv preprint math/0406327*, 2004. (Cited on page 23.)
- [BP84] R.C. Barr and R. Plonsey. Propagation of excitation in idealized anisotropic two-dimensional tissue. *Biophysical journal*, 45(6):1191–1202, 1984. (Cited on page 21.)
- [BQH⁺07] A. Baher, Z. Qu, A. Hayatdavoudi, S.T. Lamp, M.J. Yang, F. Xie, S. Turner, A. Garfinkel, and J.N. Weiss. Short-term cardiac memory and mother rotor fibrillation. *American Journal of Physiology-Heart and Circulatory Physiology*, 292(1):H180–H189, 2007. (Cited on page 80.)
- [BR77] GW Beeler and H. Reuter. Reconstruction of the action potential of ventricular myocardial fibres. *The Journal of physiology*, 268(1):177, 1977. (Cited on page 32.)
- [BRB07] S. Bauer, G. Röder, and M. Bär. Alternans and the influence of ionic channel modifications: Cardiac three-dimensional simulations and one-dimensional numerical bifurcation analysis. *Chaos: An Interdisciplinary Journal of Nonlinear Science*, 17(1):015104–015104, 2007. (Cited on page 80.)
- [BRE⁺06] M.J. Bishop, B. Rodriguez, J. Eason, J.P. Whiteley, N. Trayanova, and D.J. Gavaghan. Synthesis of voltage-sensitive optical signals:

- application to panoramic optical mapping. *Biophysical journal*, 90(8):2938–2945, 2006. (Cited on page 49.)
- [BWZ⁺02] O. Bernus, R. Wilders, C.W. Zemlin, H. Vershelde, and A.V. Panfilov. A computationally efficient electrophysiological model of human ventricular cells. *American Journal of Physiology- Heart and Circulatory Physiology*, 282(6):H2296, 2002. (Cited on pages 26, 32, 53 and 139.)
- [Cai08] J.W. Cain. A kinematic model of wave propagation. 2008. (Cited on page 43.)
- [CBC⁺11] R.H. Clayton, O. Bernus, E.M. Cherry, H. Dierckx, F.H. Fenton, L. Mirabella, A.V. Panfilov, F.B. Sachse, G. Seemann, and H. Zhang. Models of cardiac tissue electrophysiology: Progress, challenges and open questions. *Progress in Biophysics and Molecular Biology*, 104(1-3):22 – 48, 2011. Cardiac Physiome project: Mathematical and Modelling Foundations. (Cited on pages 18, 52, 60 and 117.)
- [CD99] D. Cioranescu and P. Donato. *An introduction to homogenization*. Oxford University Press New York, 1999. (Cited on page 84.)
- [CF04] E.M. Cherry and F.H. Fenton. Suppression of alternans and conduction blocks despite steep APD restitution: electrotonic, memory, and conduction velocity restitution effects. *American Journal of Physiology- Heart and Circulatory Physiology*, 286(6):H2332, 2004. (Cited on pages 23, 53, 60, 80, 87, 115 and 117.)
- [CFGR90] P. Colli Franzone, L. Guerri, and S. Rovida. Wavefront propagation in an activation model of the anisotropic cardiac tissue: asymptotic analysis and numerical simulations. *Journal of mathematical biology*, 28(2):121–176, 1990. (Cited on pages 18, 53 and 56.)
- [CFGV⁺82] P. Colli-Franzone, L. Guerri, C. Viganotti, E. Macchi, S. Baruffi, S. Spaggiari, and B. Taccardi. Potential fields generated by oblique dipole layers modeling excitation wavefronts in the anisotropic myocardium. comparison with potential fields elicited by paced dog hearts in a volume conductor. *Circulation research*, 51(3):330–346, 1982. (Cited on page 19.)
- [CFPT05] P. Colli Franzone, LF Pavarino, and B. Taccardi. Simulating patterns of excitation, repolarization and action potential duration with cardiac bidomain and monodomain models. *Mathematical biosciences*, 197(1):35–66, 2005. (Cited on page 20.)
- [CGH03] E.M. Cherry, H.S. Greenside, and C.S. Henriquez. Efficient simulation of three-dimensional anisotropic cardiac tissue using an adaptive

- mesh refinement method. *Chaos*, 13(3):853–865, 2003. (Cited on pages 20 and 21.)
- [CGPT98] P. Colli Franzone, L. Guerri, M. Pennacchio, and B. Taccardi. Spread of excitation in 3-D models of the anisotropic cardiac tissue. II. Effects of fiber architecture and ventricular geometry. *Mathematical biosciences*, 147(2):131–172, 1998. (Cited on page 32.)
- [CGT00] A.R. Conn, N.I.M. Gould, and P.L. Toint. *Trust-region methods*. Society for Industrial Mathematics, 2000. (Cited on page 41.)
- [CH04] R.H. Clayton and A.V. Holden. Filament behavior in a computational model of ventricular fibrillation in the canine heart. *Biomedical Engineering, IEEE Transactions on*, 51(1):28–34, 2004. (Cited on page 79.)
- [CJC⁺11] H. Cochet, A. S. Jadidi, O. Corneloup, M. Lederlin, J. Relan, M. Montaudon, M. Sermesant, P. Jaïs, and F. Laurent. Myocardial scar modeling from delayed enhancement MRI: Usefulness for the guidance of ventricular tachycardia mapping and ablation. In *Radiological Society of North America, RSNA '11*, November 2011. (Cited on page 145.)
- [CJS⁺11] H. Cochet, A. S. Jadidi, F. Sacher, N. Derval, M. Sermesant, J. Relan, S. J. Kim, P. Bordachar, P. Ritter, M. Hocini, M. Montaudon, F. Laurent, N. Ayache, M. Haïssaguerre, and P. Jais. Ventricular scar at cardiac CT correlates to critical isthmuses of ventricular tachycardia circuits and sites of slow conduction during sinus rhythm - evidence for clinical use of CT integration into 3D mapping systems. In *Heart Rhythm Society '11*, May 2011. (Cited on page 144.)
- [CJSB95] J. L. Cox, R. D. Jaquiss, R. B. Schuessler, and J. P. Boineau. Modification of the maze procedure for atrial flutter and atrial fibrillation. ii. surgical technique of the maze iii procedure. *The Journal of Thoracic and Cardiovascular Surgery*, 110:485–495, 1995. (Cited on page 97.)
- [Cla08] R.H. Clayton. Vortex filament dynamics in computational models of ventricular fibrillation in the heart. *Chaos: An Interdisciplinary Journal of Nonlinear Science*, 18(4):043127–043127, 2008. (Cited on page 79.)
- [CNLH04] J.C. Clements, J. Nenonen, PKJ Li, and B.M. Horáček. Activation dynamics in anisotropic cardiac tissue via decoupling. *Annals of biomedical engineering*, 32(7):984–990, 2004. (Cited on page 20.)
- [Cou96] M. Courtemanche. Complex spiral wave dynamics in a spatially distributed ionic model of cardiac electrical activity. *Chaos: An Interdisciplinary Journal of Nonlinear Science*, 6(4):579–600, 1996. (Cited on page 21.)

- [CPSW06] D. Chung, M. Pop, M. Sermesant, and G.A. Wright. Stereo reconstruction of the epicardium for optical fluorescence imaging. In *MIC-CAI Workshop on Biophotonics for diagnosis and treatment. IMM-Technical Report*, pages 33–40, 2006. (Cited on page 36.)
- [CR95] C.E. Clancy and Y. Rudy. Linking a genetic defect to its cellular phenotype in a cardiac arrhythmia. *Biol*, 9:295–305, 1995. (Cited on pages 53, 87 and 115.)
- [CRG⁺08] P. Chinchapatnam, K.S. Rhode, M. Ginks, C.A. Rinaldi, P. Lambiase, R. Razavi, S. Arridge, and M. Sermesant. Model-based imaging of cardiac apparent conductivity and local conduction velocity for diagnosis and planning of therapy. *Medical Imaging, IEEE Transactions on*, 27(11):1631–1642, 2008. (Cited on pages 23, 34, 53, 56, 59 and 68.)
- [CSL⁺11] O. Camara, M. Sermesant, P. Lamata, L. Wang, M. Pop, J. Re-lan, M. De Craene, H. Delingette, H. Liu, S. Niederer, A. Pashaei, G. Plank, D. Romero, R. Sebastian, K.C.L. Wong, H. Zhang, N. Ayache, A.F. Frangi, P. Shi, N.P. Smith, and G.A. Wright. Inter-model consistency and complementarity: Learning from ex-vivo imaging and electrophysiological data towards an integrated understanding of cardiac physiology. *Progress in Biophysics and Molecular Biology*, 107:122–133, 2011. (Cited on pages 138 and 145.)
- [CTSG04] J.W. Cain, E.G. Tolkacheva, D.G. Schaeffer, and D.J. Gauthier. Rate-dependent propagation of cardiac action potentials in a one-dimensional fiber. *Physical Review E*, 70(6):061906–1–061906–7, 2004. (Cited on pages 38, 39, 42 and 43.)
- [CVT⁺01] H. Cao, V. R. Vorperian, S. Tungjitkusolmun, J. Z. Tsai, D. Haemerich, Y. B. Choy, and J. G. Webster. Flow effect on lesion formation in rf cardiac catheter ablation. *IEEE Transactions on bio-Medical Engineering*, 48:425–433, 2001. (Cited on page 100.)
- [CW91] M. Courtemanche and Arthur T. Winfree. Re-entrant rotating waves in a beeler–reuter based model of two-dimensional cardiac electrical activity. *Int. J. Bifurcation & Chaos*, (1):431–444, 1991. (Cited on pages 25, 53, 87 and 115.)
- [CWSdG⁺00] R Coronel, F J Wilms-Schopman, J R de Groot, M J Janse, F J van Capelle, and J M de Bakker. Laplacian electrograms and the interpretation of complex ventricular activation patterns during ventricular fibrillation. *J Cardiovasc Electrophysiol*, 11(10):1119–1128, Oct 2000. (Cited on pages 55 and 117.)

- [DBVR06] J.M.T. De Bakker and H. Van Rijen. Continuous and discontinuous propagation in heart muscle. *Journal of cardiovascular electrophysiology*, 17(5):567–573, 2006. (Cited on pages [81](#), [82](#) and [87](#).)
- [DEP] I. Deisenhofer, H. Estner, and A. Pustowoit. volume Catheter Ablation of Cardiac Arrhythmias, chapter Catheter ablation of atrial fibrillation, pages 211–246. Steinkopff. (Cited on page [97](#).)
- [Dös00] O. Dössel. Inverse problem of electro-and magnetocardiography: Review and recent progress. *International Journal of Bioelectromagnetism*, 2(2), 2000. (Cited on page [17](#).)
- [DPS⁺92] J.M. Davidenko, A.V. Pertsov, R. Salomonsz, W. Baxter, and J. Jalife. Stationary and drifting spiral waves of excitation in isolated cardiac muscle. 1992. (Cited on page [79](#).)
- [EB08] M. Ethier and Y. Bourgault. Semi-implicit time discretization schemes for the bidomain model. *SIAM J. NUMER. ANAL.*, 46:2443–2468, 2008. (Cited on pages [21](#), [38](#) and [153](#).)
- [Eic03] O. J. Eick. Factors influencing lesion formation during radiofrequency catheter ablation. *Indian Pacing and Electrophysiology Journal*, 3:117–128, 2003. (Cited on page [99](#).)
- [ENS04] I.R. Efimov, V.P. Nikolski, and G. Salama. Optical imaging of the heart. *Circulation research*, 95(1):21, 2004. (Cited on pages [13](#) and [34](#).)
- [ESHP⁺99] A. El-Shalakany, T. Hadjis, P. Papageorgiou, K. Monahan, L. Epstein, and M.E. Josephson. Entrainment/mapping criteria for the prediction of termination of ventricular tachycardia by single radiofrequency lesion in patients with coronary artery disease. *Circulation*, 99(17):2283, 1999. (Cited on page [98](#).)
- [FC08] F. H Fenton and E. M. Cherry. Models of cardiac cell. *Scholarpedia*, 3(8):1868, 2008. (Cited on pages [19](#), [23](#), [24](#) and [52](#).)
- [FD09] D. Farina and O. Dössel. Non-invasive model-based localization of ventricular ectopic centers from multichannel eeg. *International Journal of Applied Electromagnetics and Mechanics*, 30(3):289–297, 2009. (Cited on page [17](#).)
- [FGDSG07] I. Ferreira-González, L. Dos-Subirá, and G.H. Guyatt. Adjunctive antiarrhythmic drug therapy in patients with implantable cardioverter defibrillators: a systematic review. *European heart journal*, 28(4):469–477, 2007. (Cited on page [4](#).)

- [Fit61] R. Fitzhugh. Impulses and physiological states in theoretical models of nerve membrane. *Biophysical Journal*, 1(6):445–466, 1961. (Cited on pages [22](#), [32](#) and [53](#).)
- [FK98] F Fenton and A Karma. Vortex dynamics in three-dimensional continuous myocardium with fiber rotation: Filament instability and fibrillation. *CHAOS*, 8:20–47, 1998. (Cited on pages [23](#), [26](#), [37](#), [57](#), [68](#), [117](#) and [138](#).)
- [Fle10] C.P. Fleming. Characterization of cardiac tissue using optical coherence tomography. 2010. (Cited on pages [82](#) and [83](#).)
- [FN09] M. Fink and D. Noble. Markov models for ion channels: versatility versus identifiability and speed. *Philosophical Transactions of the Royal Society A: Mathematical, Physical and Engineering Sciences*, 367(1896):2161, 2009. (Cited on pages [49](#) and [138](#).)
- [FNC⁺11] Martin Fink, Steven A. Niederer, Elizabeth M. Cherry, Flavio H. Fenton, Jussi T. Koivumäki, Gunnar Seemann, Rüdiger Thul, Henggui Zhang, Frank B. Sachse, Dan Beard, Edmund J. Crampin, and Nicolas P. Smith. Cardiac cell modelling: Observations from the heart of the cardiac physiome project. *Progress in Biophysics and Molecular Biology*, 104(1-3):2 – 21, 2011. Cardiac Physiome project: Mathematical and Modelling Foundations. (Cited on pages [18](#) and [52](#).)
- [FP63] R. Fletcher and M.J.D. Powell. A rapidly convergent descent method for minimization. *The Computer Journal*, 6(2):163, 1963. (Cited on page [43](#).)
- [FP04] P.C. Franzone and L.F. Pavarino. A parallel solver for reaction-diffusion systems in computational electrocardiology. *Mathematical models and methods in applied sciences*, 14:883–912, 2004. (Cited on page [20](#).)
- [GJ⁺98] RA Gray, J. Jalife, et al. Ventricular fibrillation and atrial fibrillation are two different beasts. *Chaos (Woodbury, NY)*, 8(1):65, 1998. (Cited on page [79](#).)
- [GJP⁺95] R.A. Gray, J. Jalife, A. Panfilov, W.T. Baxter, C. Cabo, J.M. Davidenko, and A.M. Pertsov. Nonstationary vortexlike reentrant activity as a mechanism of polymorphic ventricular tachycardia in the isolated rabbit heart. *Circulation*, 91(9):2454–2469, 1995. (Cited on page [27](#).)
- [GNK05] A. Garny, D. Noble, and P. Kohl. Dimensionality in cardiac modelling. *Progress in biophysics and molecular biology*, 87(1):47–66, 2005. (Cited on pages [49](#) and [138](#).)

- [GSG⁺07] D.A. Gerneke, G.B. Sands, R. Ganesalingam, P. Joshi, B.J. Caldwell, B.H. Smaill, and I.J. Legrice. Surface imaging microscopy using an ultramiller for large volume 3d reconstruction of wax-and resin-embedded tissues. *Microscopy research and technique*, 70(10):886–894, 2007. (Cited on page 21.)
- [GSGK95] Y. Z. Ge, P. Z. Shao, J. Goldberger, and A. Kadish. Cellular electrophysiological changes induced in vitro by radiofrequency current: comparison with electrical ablation. *Pacing and Clinical Electrophysiology : PACE*, 18:323–333, 1995. (Cited on page 106.)
- [H⁺93] C.S. Henriquez et al. Simulating the electrical behavior of cardiac tissue using the bidomain model. *Critical reviews in biomedical engineering*, 21(1):1, 1993. (Cited on page 18.)
- [Hae10] D. Haemmerich. Biophysics of radiofrequency ablation. *Critical Reviews in Biomedical Engineering*, 38:53–63, 2010. (Cited on page 97.)
- [Hai91] D. E. Haines. Determinants of lesion size during radiofrequency catheter ablation: The role of electrode-tissue contact pressure and duration of energy delivery. *Journal of Cardiovascular Electrophysiology*, 2:509–515, 1991. (Cited on page 100.)
- [Hai93] D. E. Haines. The biophysics of radiofrequency catheter ablation in the heart: the importance of temperature monitoring. *Pacing and Clinical Electrophysiology : PACE*, 16:586–591, 1993. (Cited on pages 99, 100 and 101.)
- [Hai08] D. E. Haines. *Catheter Ablation of Cardiac Arrhythmias: Basic Concepts and Clinical Applications*, volume Third Edition, chapter Biophysics and pathophysiology of lesion formation by transcatheter radiofrequency ablation, pages 20–34. Blackwell Futura, WILEY Online Library, 2008. (Cited on pages 99, 100, 101 and 102.)
- [Han99] P.C. Hansen. *The L-curve and its use in the numerical treatment of inverse problems*. IMM, Department of Mathematical Modelling, Technical University of Denmark, 1999. (Cited on page 41.)
- [HBP⁺07] E.M.C. Hillman, O. Bernus, E. Pease, M.B. Bouchard, and A. Pertsov. Depth-resolved optical imaging of transmural electrical propagation in perfused heart. *Optics express*, 15(26):17827, 2007. (Cited on pages 13 and 14.)
- [HCM01] H.V. Huikuri, A. Castellanos, and R.J. Myerburg. Sudden death due to cardiac arrhythmias. *New England Journal of Medicine*, 345(20):1473–1482, 2001. (Cited on page 3.)

- [HH52] A.L. Hodgkin and A.F. Huxley. A quantitative description of membrane current and its application to conduction and excitation in nerve. *The Journal of physiology*, 117(4):500, 1952. (Cited on page [32](#).)
- [HHG⁺89] G. Hindricks, W. Haverkamp, H. Gulker, U. Rissel, T. Budde, K. D. Richter, M. Borggreffe, and G. Breithardt. Radiofrequency coagulation of ventricular myocardium: improved prediction of lesion size by monitoring catheter tip temperature. *European Heart Journal*, 10:972–984, 1989. (Cited on page [102](#).)
- [HMY⁺05] C.J. Hyatt, S.F. Mironov, F.J. Vetter, C.W. Zemlin, and A.M. Pertsov. Optical action potential upstroke morphology reveals near-surface transmural propagation direction. *Circulation research*, 97(3):277, 2005. (Cited on page [49](#).)
- [HP90] CS Henriquez and R. Plonsey. Simulation of propagation along a cylindrical bundle of cardiac tissue. ii. results of simulation. *Biomedical Engineering, IEEE Transactions on*, 37(9):861–875, 1990. (Cited on page [21](#).)
- [HSE⁺09] B. Hanson, P. Sutton, N. Elameri, M. Gray, H. Critchley, J.S. Gill, and P. Taggart. Interaction of activation–repolarization coupling and restitution properties in humansclinical perspective. *Circulation: Arrhythmia and Electrophysiology*, 2(2):162–170, 2009. (Cited on page [23](#).)
- [HZS⁺08] C.J. Hyatt, C.W. Zemlin, R.M. Smith, A. Matiukas, A.M. Pertsov, O. Bernus, et al. Reconstructing subsurface electrical wave orientation from cardiac epi-fluorescence recordings: Monte carlo versus diffusion approximation. *Opt Express*, 16:13758–72, 2008. (Cited on page [13](#).)
- [JCS⁺11] A. S. Jadidi, H. Cochet, F. Sacher, S. J. Kim, M. Sermesant, J. Relan, N. Derval, S. Miyazaki, A. Shah, D. Scherr, S. B. Wilton, P. Pascale, L. Roten, M. Pederson, S. Knecht, P. Bordachar, P. Ritter, M. Hocini, M. Montaudon, F. Laurent, N. Ayache, M. Haïssaguerre, and P. Jais. Ventricular scar imaging at MRI correlates to critical isthmuses of ventricular tachycardia circuits and sites of slow conduction during sinus rhythm - utility of integrating MR-data into 3D mapping systems. In *Heart Rhythm Society '11*, May 2011. (Cited on page [145](#).)
- [JG96] J. Jalife and R. Gray. Drifting vortices of electrical waves underlie ventricular fibrillation in the rabbit heart. *Acta physiologica scandinavica*, 157(2):123–132, 1996. (Cited on pages [53](#), [79](#), [87](#) and [115](#).)

- [Jos08] M.E. Josephson. *Clinical cardiac electrophysiology: techniques and interpretations*. Lippincott Williams & Wilkins, 2008. (Cited on pages 25 and 26.)
- [KBMP06] V.D. Khait, O. Bernus, S.F. Mironov, and A.M. Pertsov. Method for the three-dimensional localization of intramyocardial excitation centers using optical imaging. *Journal of biomedical optics*, 11:034007, 2006. (Cited on page 13.)
- [KDP⁺06] P. Kovoov, M. P. J. Daly, J. Pouliopoulos, K. Byth, B. I. Dewsnap, V. E. Eipper, T. Yung, J. F. B. Uther, and D. L. Ross. Comparison of radiofrequency ablation in normal versus scarred myocardium. *Journal of Cardiovascular Electrophysiology*, 17:80–86, 2006. (Cited on page 100.)
- [KFFK09] H.W. Kim, A. Farzaneh-Far, and R.J. Kim. Cardiovascular magnetic resonance in patients with myocardial infarction: current and emerging applications. *Journal of the American College of Cardiology*, 55(1):1–16, 2009. (Cited on pages 20 and 117.)
- [KKS09] J.P. Keener, J. Keener, and J. Sneyd. *Mathematical physiology: Cellular physiology*. Springer Verlag, 2009. (Cited on pages 18, 32, 38, 53, 56 and 59.)
- [KR04] A.G. Kléber and Y. Rudy. Basic mechanisms of cardiac impulse propagation and associated arrhythmias. *Physiological reviews*, 84(2):431–488, 2004. (Cited on page 18.)
- [KRC⁺11] E. Konukoglu, J. Relan, U. Cilingir, B. Menze, P. Chinchapatnam, A. Jadidi, H. Cochet, M. Hocini, H. Delingette, P. Jaïs, M. Haïssaguerre, N. Ayache, and M. Sermesant. Efficient probabilistic model personalization integrating uncertainty on data and parameters: Application to eikonal-diffusion models in cardiac electrophysiology. *Progress in Biophysics and Molecular Biology*, 107:134–146, 2011. (Cited on pages 74, 136, 139, 140 and 145.)
- [KRD⁺10] M. W. Krueger, J. Relan, H. Delingette, M. Sermesant, N. Ayache, G. Seemann, and O. Dössel. Computational models for AF and VT simulation. Deliverables D6.2.1, European project euHeart, May 2010. (Cited on page 147.)
- [KRD⁺11] M. W. Krueger, J. Relan, H. Delingette, W. Schulze, G. Seemann, and O. Dössel. Model personalization for AF and VT simulations. Deliverables D6.2.2, European project euHeart, January 2011. (Cited on page 147.)
- [KS98] J. Keener and J. Sneyd. *Mathematical Physiology*. Springer, 1998. (Cited on page 22.)

- [KSGH08] M.J. Killeen, I.N. Sabir, A.A. Grace, and C.L.H. Huang. Dispersions of repolarization and ventricular arrhythmogenesis: Lessons from animal models. *Progress in biophysics and molecular biology*, 98(2-3):219–229, 2008. (Cited on pages 53, 88 and 115.)
- [KSS⁺11] M. W. Krueger, W. Schulze, G. Seemann, O. Dössel, J. Relan, H. Delingette, M. Sermesant, and N. Ayache. Planning of radiofrequency ablation for patients with atrial fibrillation. Deliverables D6.3.1, European project euHeart, June 2011. (Cited on pages 95 and 146.)
- [KTTN⁺08] R.H. Keldermann, K.H.W.J. Ten Tusscher, M.P. Nash, R. Hren, P. Taggart, and A.V. Panfilov. Effect of heterogeneous apd restitution on vf organization in a model of the human ventricles. *American Journal of Physiology- Heart and Circulatory Physiology*, 294(2):H764, 2008. (Cited on pages 41, 42, 62 and 80.)
- [LGL⁺03] D.S. Lee, L.D. Green, P.P. Liu, P. Dorian, D.M. Newman, F.C. Grant, J.V. Tu, and D.A. Alter. Effectiveness of implantable defibrillators for preventing arrhythmic events and death* 1: A meta-analysis. *Journal of the American College of Cardiology*, 41(9):1573–1582, 2003. (Cited on page 4.)
- [LGT03] G.T. Lines, P. Grottum, and A. Tveito. Modeling the electrical activity of the heart: a bidomain model of the ventricles embedded in a torso. *Computing and Visualization in Science*, 5(4):195–213, 2003. (Cited on page 18.)
- [LHS09] R.A. Lasher, R.W. Hitchcock, and F.B. Sachse. Towards modeling of cardiac micro-structure with catheter-based confocal microscopy: a novel approach for dye delivery and tissue characterization. *Medical Imaging, IEEE Transactions on*, 28(8):1156–1164, 2009. (Cited on page 22.)
- [LM03] D. Lin and F.E. Marchlinski. Advances in ablation therapy for complex arrhythmias: atrial fibrillation and ventricular tachycardia. *Current Cardiology Reports*, 5(5):407–414, 2003. (Cited on pages 97, 98 and 99.)
- [LMR⁺09] Hans Lamecker, Tommaso Mansi, Jatin Relan, Florence Billet, Maxime Sermesant, Nicholas Ayache, and Hervé Delingette. Adaptive tetrahedral meshing for personalized cardiac simulations. In *MICCAI Workshop on Cardiovascular Interventional Imaging and Biophysical Modelling (CI2BM09)*, pages 149–158, London United Kingdom, 2009. (Cited on page 146.)

- [LR91] C. Luo and Y. Rudy. A model of the ventricular cardiac action potential. depolarization, repolarization, and their interaction. *Circulation Research*, 68(6):1501, 1991. (Cited on pages 32 and 52.)
- [LSC⁺95] I.J. LeGrice, BH Smaill, LZ Chai, SG Edgar, JB Gavin, and P.J. Hunter. Laminar structure of the heart: ventricular myocyte arrangement and connective tissue architecture in the dog. *American Journal of Physiology-Heart and Circulatory Physiology*, 269(2):H571–H582, 1995. (Cited on page 21.)
- [LSP⁺08] D. Lepiller, M. Sermesant, M. Pop, H. Delingette, G. Wright, and N. Ayache. Cardiac electrophysiology model adjustment using the fusion of MR and optical imaging. volume 5241 of LNCS, pages 678–685. Springer, 2008. (Cited on page 34.)
- [Mar02] E. Marbán. Cardiac channelopathies. *Nature*, 415(6868):213–218, 2002. (Cited on page 11.)
- [MGBD10] R. Miri, I.M. Graf, J.V. Bayarri, and O. Dössel. Applicability of body surface potential map in computerized optimization of biventricular pacing. *Annals of biomedical engineering*, 38(3):865–875, 2010. (Cited on page 17.)
- [MH96] I. D. McRury and D. E. Haines. Ablation for the treatment of arrhythmias. In *Proc. of the IEEE*, volume 84, pages 404–416, 1996. (Cited on pages 102 and 103.)
- [MHK⁺93] F. Morady, M. Harvey, S.J. Kalbfleisch, R. El-Atassi, H. Calkins, and J.J. Langberg. Radiofrequency catheter ablation of ventricular tachycardia in patients with coronary artery disease. *Circulation*, 87(2):363, 1993. (Cited on page 98.)
- [MKDB⁺91] F. Morady, A. Kadish, M. De Buitelir, WH Kou, H. Calkins, S. Schmaltz, S. Rosenheck, and J. Sousa. Prospective comparison of a conventional and an accelerated protocol for programmed ventricular stimulation in patients with coronary artery disease. *Circulation*, 83(3):764, 1991. (Cited on page 90.)
- [MKY⁺02] F. Murgatroyd, A. D. Krahn, R. Yee, A. Skanes, and G. J. Klein. *Handbook of Cardiac Electrophysiology: A Practical Guide to Invasive EP Studies and Catheter Ablation*. Remedica Publishing, 2002. (Cited on pages 10, 25, 78 and 80.)
- [MLC⁺11] N. Mewton, C.Y. Liu, P. Croisille, D. Bluemke, and J.A.C. Lima. Assessment of myocardial fibrosis with cardiovascular magnetic resonance. *Journal of the American College of Cardiology*, 57(8):891–903, 2011. (Cited on pages 81 and 82.)

- [MS03] C.C. Mitchell and D.G. Schaeffer. A two-current model for the dynamics of cardiac membrane. *Bulletin of mathematical biology*, 65(5):767–793, 2003. (Cited on pages [23](#), [33](#), [37](#), [38](#), [39](#), [42](#), [53](#), [57](#), [58](#), [61](#), [62](#), [68](#), [69](#), [115](#), [117](#), [118](#), [124](#) and [138](#).)
- [MVDS⁺06] V. Moreau-Villéger, H. Delingette, M. Sermesant, H. Ashikaga, E. McVeigh, and N. Ayache. Building maps of local apparent conductivity of the epicardium with a 2-D electrophysiological model of the heart. *Biomedical Engineering, IEEE Transactions on*, 53(8):1457–1466, 2006. (Cited on page [34](#).)
- [MZC⁺00] F.E. Marchlinski, E.S. Zado, D.J. Callans, V.V. Patel, M.S. Ashar, H.H. Hsia, and A.M. Russo. Hybrid therapy for ventricular arrhythmia management. *Cardiology Clinics*, 18(2):391–406, 2000. (Cited on page [98](#).)
- [NAY62] J. Nagumo, S. Arimoto, and S. Yoshizawa. An active pulse transmission line simulating nerve axon. *Proceedings of the IRE*, 50(10):2061–2070, 1962. (Cited on page [79](#).)
- [NBS⁺06] M.P. Nash, C.P. Bradley, P.M. Sutton, R.H. Clayton, P. Kallis, M.P. Hayward, D.J. Paterson, and P. Taggart. Whole heart action potential duration restitution properties in cardiac patients: a combined clinical and modelling study. *Experimental physiology*, 91(2):339, 2006. (Cited on pages [53](#), [55](#), [60](#), [88](#), [115](#), [117](#), [118](#), [122](#) and [128](#).)
- [NDH94] S. Nath, J. P. DiMarco, and D. E. Haines. Basic aspects of radiofrequency catheter ablation. *Journal of Cardiovascular Electrophysiology*, 5:863–876, 1994. (Cited on pages [99](#), [100](#), [102](#) and [104](#).)
- [NE06] G. Ndrepepa and H. Estner. volume Catheter Ablation of Cardiac Arrhythmias, chapter Ablation of cardiac arrhythmias ? energy sources and mechanisms of lesion formation, pages 35–53. Steinkopff, 2006. (Cited on pages [96](#), [97](#), [99](#), [101](#), [102](#) and [106](#).)
- [NK⁺93] JC Neu, W. Krassowska, et al. Homogenization of syncytial tissues. *Critical reviews in biomedical engineering*, 21(2):137, 1993. (Cited on page [18](#).)
- [NLWH93] S. Nath, C. 3rd Lynch, J. G. Wayne, and D. E. Haines. Cellular electrophysiological effects of hyperthermia on isolated guinea pig papillary muscle. implications for catheter ablation. *Circulation*, 88:1826–1831, 1993. (Cited on pages [100](#) and [102](#).)
- [NMLBY07] S. Nattel, A. Maguy, S. Le Bouter, and Y.H. Yeh. Arrhythmogenic ion-channel remodeling in the heart: heart failure, myocardial infarction, and atrial fibrillation. *Physiological reviews*, 87(2):425, 2007. (Cited on page [88](#).)

- [Nob62] D. Noble. A modification of the hodgkin-huxley equations applicable to purkinje fibre action and pace-maker potentials. *Journal of Physiology*, 160:317–352, 1962. (Cited on page 22.)
- [NRAA⁺10] A. Natale, A. Raviele, A. Al-Ahmad, O. Alfieri, E. Aliot, J. Al-mendral, G. Breithardt, J. Brugada, H. Calkins, D. Callans, et al. Venice chart international consensus document on ventricular tachycardia/ventricular fibrillation ablation. *Journal of Cardiovascular Electrophysiology*, 21(3):339–379, 2010. (Cited on pages 90, 97 and 98.)
- [NTR⁺10] S. Nakahara, R. Tung, R. J. Ramirez, J. Gima, I. Wiener, A. Mahajan, N. G. Boyle, and K. Shivkumar. Distribution of late potentials within infarct scars assessed by ultra high-density mapping. *Heart Rhythm : the Official Journal of the Heart Rhythm Society*, 7:1817–1824, 2010. (Cited on page 103.)
- [NVKN98] D. Noble, A. Varghese, P. Kohl, and P. Noble. Improved guinea-pig ventricular cell model incorporating a diadic space, IKr and IKs, and length-and tension-dependent processes. *The Canadian journal of cardiology*, 14(1):123, 1998. (Cited on pages 32 and 52.)
- [NWK⁺94] S. Nath, J. G. Whayne, S. Kaul, N. C. Goodman, A. R. Jayaweera, and D. E. Haines. Effects of radiofrequency catheter ablation on regional myocardial blood flow. possible mechanism for late electrophysiological outcome. *Circulation*, 89:2667–2672, 1994. (Cited on pages 102 and 103.)
- [OKT⁺87] T. Osaka, I. Kodama, N. Tsuboi, J. Toyama, and K. Yamada. Effects of activation sequence and anisotropic cellular geometry on the repolarization phase of action potential of dog ventricular muscles. *Circulation*, 76(1):226–236, 1987. (Cited on page 23.)
- [Org03] World Health Organization. *World Health Report 2003: A Vision for Global Health. Shaping the Future*. World Health Organization, 2003. (Cited on page 3.)
- [Org04] World Health Organization. The global burden of coronary heart disease. the atlas of heart disease and stroke, 2004. (Cited on page 3.)
- [Org09] World Health Organization. Cardiovascular disease. fact sheet n. 317, September 2009. (Cited on page 3.)
- [Pan02] AV Panfilov. Spiral breakup in an array of coupled cells: the role of the intercellular conductance. *Physical review letters*, 88(11):118101, 2002. (Cited on page 83.)

- [PB00] R. Plonsey and R.C. Barr. *Bioelectricity: a quantitative approach*. Springer, 2000. (Cited on page 18.)
- [PCV⁺11] E. Pueyo, A. Corrias, L. Virág, N. Jost, T. Szél, A. Varró, N. Szentandrassy, P.P. Nánási, K. Burrage, and B. Rodríguez. A multiscale investigation of repolarization variability and its role in cardiac arrhythmogenesis. *Biophysical Journal*, 101(12):2892–2902, 2011. (Cited on page 115.)
- [PDARG⁺11] E. Perez-David, A. Arenal, J.L. Rubio-Guivernau, R. del Castillo, L. Atea, E. Arbelo, E. Caballero, V. Celorrio, T. Datino, E. Gonzalez-Torrecilla, et al. Noninvasive identification of ventricular tachycardia-related conducting channels using contrast-enhanced magnetic resonance imaging in patients with chronic myocardial infarction: comparison of signal intensity scar mapping and endocardial voltage mapping. *Journal of the American College of Cardiology*, 57(2):184, 2011. (Cited on page 142.)
- [PDR⁺06] M. Potse, B. Dubé, J. Richer, A. Vinet, and R.M. Gulrajani. A comparison of monodomain and bidomain reaction-diffusion models for action potential propagation in the human heart. *Biomedical Engineering, IEEE Transactions on*, 53(12):2425–2435, 2006. (Cited on pages 20 and 138.)
- [Per97] A. Pertsov. Scale of geometric structures responsible for discontinuous propagation in myocardial tissue. *Discontinuous Conduction in the Heart*. New York, NY: Futura, pages 273–293, 1997. (Cited on page 82.)
- [PK95] A. Panfilov and JP Keener. Re-entry in an anatomical model of the heart. *Chaos, Solitons & Fractals*, 5(3-4):681–689, 1995. (Cited on pages 53, 79, 87 and 115.)
- [PPR⁺05] S. Petersen, V. Peto, M. Rayner, J. Leal, R. Luengo-Fernandez, and A. Gray. European cardiovascular disease statistics. *London: British Heart Foundation*, 2005. (Cited on page 3.)
- [PRB⁺09] C. Pierre, O. Rousseau, Y. Bourgault, et al. Segmented medical images based simulations of cardiac electrical activity and electrocardiogram: a model comparison. 2009. (Cited on page 20.)
- [PSK⁺11] E. Pernod, M. Sermesant, E. Konukoglu, J. Relan, H. Delingette, and N. Ayache. A multi-front eikonal model of cardiac electrophysiology for interactive simulation of radio-frequency ablation. *Computers and Graphics*, 35:431–440, 2011. (Cited on page 145.)

- [PSL⁺09] M. Pop, M. Sermesant, D. Lepiller, M.V. Truong, E.R. McVeigh, E. Crystal, A. Dick, H. Delingette, N. Ayache, and G.A. Wright. Fusion of optical imaging and MRI for the evaluation and adjustment of macroscopic models of cardiac electrophysiology: A feasibility study. *Medical Image Analysis*, 13(2):370–380, 2009. (Cited on pages 13, 33, 34, 35 and 36.)
- [PSL⁺12] M. Pop, M. Sermesant, G. Liu, J. Relan, T. Mansi, A. Soong, J.M. Peyrat, M.V. Truong, P. Fefer, E.R. McVeigh, et al. Construction of 3D MR image-based computer models of pathologic hearts, augmented with histology and optical fluorescence imaging to characterize action potential propagation. *Medical Image Analysis*, 16:505–523, 2012. (Cited on pages 13 and 145.)
- [PSM⁺09] M. Pop, M. Sermesant, T. Mansi, E. Crystal, J. Detsky, Y. Yang, P. Fefer, E. McVeigh, A. Dick, N. Ayache, and G. Wright. Characterization of post-infarct scars in a porcine model - a combined experimental and theoretical study. *Functional Imaging and Modeling of the Heart 2009 (FIMH'09)*, 5528:1–10, 2009. (Cited on pages 82 and 83.)
- [PSP⁺07] J.M. Peyrat, M. Sermesant, X. Pennec, H. Delingette, C. Xu, E.R. McVeigh, and N. Ayache. A computational framework for the statistical analysis of cardiac diffusion tensors: Application to a small database of canine hearts. *Medical Imaging, IEEE Transactions on*, 26(11):1500–1514, 2007. (Cited on page 53.)
- [PSRD10] Erik Pernod, Maxime Sermesant, Jatin Relan, and Hervé Delingette. Interactive real time simulation of cardiac radio-frequency ablation. In *Proc. of Eurographics Workshop on Visual Computing for Biology and Medicine (2010) (VCBM'2010)*, pages 91–98, Leipzig, August 2010. Best Paper Award. (Cited on page 146.)
- [PSSL08] A.J. Pope, G.B. Sands, B.H. Smaill, and I.J. LeGrice. Three-dimensional transmural organization of perimysial collagen in the heart. *American Journal of Physiology-Heart and Circulatory Physiology*, 295(3):H1243–H1252, 2008. (Cited on page 21.)
- [PVOC09] M. Potse, A. Vinet, T. Opthof, and R. Coronel. Validation of a simple model for the morphology of the t wave in unipolar electrograms. *American Journal of Physiology- Heart and Circulatory Physiology*, 297(2):H792, 2009. (Cited on page 55.)
- [QGCW00] Z. Qu, A. Garfinkel, P.S. Chen, and J.N. Weiss. Mechanisms of discordant alternans and induction of reentry in simulated cardiac tissue. *Circulation*, 102(14):1664–1670, 2000. (Cited on page 25.)

- [QR91] W. Quan and Y. Rudy. Termination of reentrant propagation by a single stimulus: a model study. *Pacing and Clinical Electrophysiology*, 14(11):1700–1706, 1991. (Cited on page 25.)
- [RCD⁺12] J. Relan, Z. Chen, H. Delingette, R. Karim, W. Schulze, J. Bostock, C. A. Rinaldi, K. Rhode, N. Ayache, R. Razavi, and M. Sermesant. Role of spatial heterogeneity of restitution and conduction in ischemic ventricular tachycardia: a combined clinical and modelling study. *Heart Rhythm*, 2012. Article in submission. (Cited on pages 6, 113, 137, 140 and 143.)
- [RCS⁺10] J. Relan, P. Chinchapatnam, M. Sermesant, K. Rhode, H. Delingette, R. Razavi, and N. Ayache. Coupled personalisation of electrophysiology models for simulation of induced ischemic ventricular tachycardia. In *Medical Image Computing and Computer-Assisted Intervention—MICCAI 2010*, volume 6362 of LNCS, pages 420–428. Springer, 2010. (Cited on pages 49, 51, 91, 136, 138 and 143.)
- [RCS⁺11] J. Relan, P. Chinchapatnam, M. Sermesant, K. Rhode, M. Ginks, H. Delingette, C. A. Rinaldi, R. Razavi, and N. Ayache. Coupled personalization of cardiac electrophysiology models for prediction of ischaemic ventricular tachycardia. *Journal of the Royal Society Interface Focus*, 1(3):396–407, 2011. (Cited on pages 6, 51, 77, 115, 117, 136, 137, 138, 140 and 143.)
- [RDS⁺11] J. Relan, H. Delingette, M. Sermesant, N. Ayache, M. W. Krueger, W. Schulze, G. Seemann, and O. Dössel. Planning of radiofrequency ablation for patients with ventricular tachycardia. Deliverables D6.3.2, European project euHeart, June 2011. (Cited on pages 6, 77, 95, 137 and 146.)
- [RJ01] D.S. Rosenbaum and J. Jalife. *Optical mapping of cardiac excitation and arrhythmias*. Wiley-Blackwell, 2001. (Cited on page 13.)
- [Rog02] J.M. Rogers. Wave front fragmentation due to ventricular geometry in a model of the rabbit heart. *Chaos: An Interdisciplinary Journal of Nonlinear Science*, 12(3):779–787, 2002. (Cited on page 79.)
- [Rot92] B. J. Roth. How the anisotropy of the intracellular and extracellular conductivities influences stimulation of cardiac muscle. *Journal of Mathematical Biology*, 30(6):633–46, 1992. (Cited on page 18.)
- [RPD⁺10] J. Relan, M. Pop, H. Delingette, G. Wright, N. Ayache, and M. Sermesant. Estimation of reaction, diffusion and restitution parameters for a 3D myocardial model using optical mapping and MRI. In *MICCAI Workshop (STACOM) and (CESC'10)*, volume 6364 of LNCS, pages 270–280. Springer, 2010. (Cited on pages 31, 62, 135 and 144.)

- [RPD⁺11] J. Relan, M. Pop, H. Delingette, G.A. Wright, N. Ayache, and M. Sermesant. Personalisation of a cardiac electrophysiology model using optical mapping and MRI for prediction of changes with pacing. *IEEE Transactions on Bio-Medical Engineering*, 58(12):3339–3349, 2011. (Cited on pages 6, 31, 62, 135, 140 and 143.)
- [RPP⁺12] L. Roten, M. Pederson, P. Pascale, A. Shah, S. Eliautou, D. Scherr, F. Sacher, and M. Haïssaguerre. Noninvasive electrocardiographic mapping for prediction of tachycardia mechanism and origin of atrial tachycardia following bilateral pulmonary transplantation. *Journal of Cardiovascular Electrophysiology*, 2012. (Cited on page 17.)
- [RS⁺09] J. Relan, M. Sermesant, , H. Delingette, M. Pop, M. Sorine, G.A. Wright, and N. Ayache. Personalisation of 3D cardiac electrophysiology models for valid predictions: A step towards patient-specific ventricular tachycardia modelling. *The Cardiac Physiome: Multi-scale and Multi-physics Mathematical Modelling Applied to the Heart*, Cambridge, UK, July 2009. (Cited on page 144.)
- [RSB⁺05] K. Rhode, M. Sermesant, D. Brogan, S. Hegde, J. Hipwell, P. Lambiase, E. Rosenthal, C. Bucknall, S. Qureshi, J. Gill, R. Razavi, and D. Hill. A system for real-time XMR guided cardiovascular intervention. *IEEE Transactions on Medical Imaging*, 24(11):1428–1440, 2005. (Cited on pages 53 and 55.)
- [RSC⁺10] J. Relan, M. Sermesant, P. Chinchapatnam, H. Delingette, K. Rhode, R. Razavi, and N. Ayache. Personalisation of a 3D macroscopic cardiac electrophysiology model for simulation of induced ischemic ventricular tachycardia. *First VPH Conference (VPH2010)*, Brussels, September 2010. (Cited on page 144.)
- [RSD⁺09] J. Relan, M. Sermesant, H. Delingette, M. Pop, GA Wright, and N. Ayache. Quantitative comparison of two cardiac electrophysiology models using personalisation to optical and MR data. In *Biomedical Imaging: From Nano to Macro, 2009. ISBI'09. IEEE International Symposium on*, pages 1027–1030. IEEE, 2009. (Cited on pages 33, 38, 58, 143 and 151.)
- [RSDA11] J. Relan, M. Sermesant, H. Delingette, and N. Ayache. Personalisation of a 3D ventricular electrophysiological model, using endocardial and epicardial contact mapping and MRI. In *Statistical Atlases and Computational Models of the Heart. Imaging and Modelling Challenges - Second International Workshop, STACOM 2011, Held in Conjunction with MICCAI 2011*, pages 14–22, 2011. (Cited on pages 6, 67, 136, 140 and 144.)

- [RSP⁺09a] J. Relan, M. Sermesant, M. Pop, H. Delingette, M. Sorine, G. Wright, and N. Ayache. Parameter estimation of a 3D cardiac electrophysiology model including the restitution curve using optical and MR data. In Olaf Dössel and Wolfgang C. Schlegel, editors, *World Congress on Medical Physics and Biomedical Engineering*, volume 25/IV of *IFMBE Proceedings*, pages 1716–1719. Springer, September 2009. (Cited on pages [31](#), [135](#) and [144](#).)
- [RSP⁺09b] J. Relan, M. Sermesant, M. Pop, H. Delingette, M. Sorine, G. Wright, and N. Ayache. Volumetric prediction of cardiac electrophysiology using a heart model personalised to surface data. In *MICCAI Workshop on Cardiovascular Interventional Imaging and Biophysical Modelling - CI2BM09*, pages 19–27, 2009. (Cited on pages [31](#), [135](#) and [144](#).)
- [Rud10] Y. Rudy. Noninvasive imaging of cardiac electrophysiology and arrhythmia. *Annals of the New York Academy of Sciences*, 1188(1):214–221, 2010. (Cited on pages [15](#), [17](#) and [141](#).)
- [RV96] R. R. Aliev and A. V. Panfilov. A simple two-variable model of cardiac excitation. *Chaos, Solitons & Fractals*, 7(3):293–301, 1996. (Cited on pages [32](#), [33](#) and [53](#).)
- [RZ⁺05] M. Rubart, D.P. Zipes, et al. Mechanisms of sudden cardiac death. *Journal of Clinical Investigation*, 115(9):2305, 2005. (Cited on page [3](#).)
- [Sac04] F.B. Sachse. *Computational cardiology: modeling of anatomy, electrophysiology, and mechanics*. Springer-Verlag New York Inc, 2004. (Cited on page [52](#).)
- [SCC⁺12] M. Sermesant, R. Chabiniok, P. Chinchapatnam, T. Mansi, F. Billet, P. Moireau, J.M. Peyrat, K. Wong, J. Relan, K. Rhode, M. Ginks, P. Lambiase, H. Delingette, M. Sorine, C.A. Rinaldi, D. Chapelle, R. Razavi, and N. Ayache. Patient-specific electromechanical models of the heart for the prediction of pacing acute effects in CRT: A preliminary clinical validation. *Medical Image Analysis*, 16(1):201–215, 2012. (Cited on page [146](#).)
- [SCG⁺09] K.H. Schuleri, M. Centola, R.T. George, L.C. Amado, K.S. Evers, K. Kitagawa, A.L. Vavere, R. Evers, J.M. Hare, C. Cox, et al. Characterization of peri-infarct zone heterogeneity by contrast-enhanced multidetector computed tomography:: A comparison with magnetic resonance imaging. *Journal of the American College of Cardiology*, 53(18):1699–1707, 2009. (Cited on page [81](#).)
- [SCMV⁺05] M. Sermesant, Y. Coudière, V. Moreau-Villéger, K.S. Rhode, D.L.G Hill, and R. Ravazi. A fast-marching approach to cardiac electrophysiology simulation for XMR interventional imaging. In *Proceedings of*

- MICCAI'05*, volume 3750 of *LNCS*, pages 607–615. Springer, 2005. (Cited on pages 53, 56, 115 and 117.)
- [SD00] W.G. Stevenson and E. Delacretaz. Strategies for catheter ablation of scar-related ventricular tachycardia. *Current cardiology reports*, 2(6):537–544, 2000. (Cited on page 26.)
- [SDA06] M. Sermesant, H. Delingette, and N. Ayache. An electromechanical model of the heart for image analysis and simulation. *Medical Imaging, IEEE Transactions on*, 25(5):612–625, 2006. (Cited on page 38.)
- [SdVM⁺11] N. Smith, A. de Vecchi, M. McCormick, D. Nordsletten, O. Camara, A.F. Frangi, H. Delingette, M. Sermesant, J. Relan, N. Ayache, M. W. Krueger, W. Schulze, R. Hose, I. Valverde, P. Beerbaum, C. Staicu, M. Siebes, J. Spaan, P. Hunter, J. Weese, H. Lehmann, D. Chapelle, and R. Razavi. euheart: Personalized and integrated cardiac care using patient-specific cardiovascular modelling. *Journal of the Royal Society Interface Focus*, 1(3):349–364, 2011. (Cited on page 146.)
- [Ser03] M. Sermesant. *Modèle électromécanique du coeur pour l'analyse d'image et la simulation (Electromechanical Model of the Heart for Image Analysis and Simulation)*. PhD thesis, Université de Nice Sophia Antipolis, May 2003. (Cited on pages 21 and 22.)
- [SFS⁺97] W.G. Stevenson, P.L. Friedman, P.T. Sager, L.A. Saxon, D. Kocovic, T. Harada, I. Wiener, et al. Exploring postinfarction reentrant ventricular tachycardia with entrainment mapping. *Journal of the American College of Cardiology*, 29(6):1180–1189, 1997. (Cited on page 98.)
- [SGFI⁺08] E. Savio-Galimberti, J. Frank, M. Inoue, J.I. Goldhaber, M.B. Cannel, J.H.B. Bridge, and F.B. Sachse. Novel features of the rabbit transverse tubular system revealed by quantitative analysis of three-dimensional reconstructions from confocal images. *Biophysical journal*, 95(4):2053–2062, 2008. (Cited on page 22.)
- [SGH⁺05] G.B. Sands, D.A. Gerneke, D.A. Hooks, C.R. Green, B.H. Smaill, and I.J. Legrice. Automated imaging of extended tissue volumes using confocal microscopy. *Microscopy research and technique*, 67(5):227–239, 2005. (Cited on page 21.)
- [SHDB07] M.S. Spach, J.F. Heidlage, P.C. Dolber, and R.C. Barr. Mechanism of origin of conduction disturbances in aging human atrial bundles: experimental and model study. *Heart Rhythm*, 4(2):175–185, 2007. (Cited on page 83.)
- [SHP⁺94] J. P. Saul, J. E. Hulse, J. Papagiannis, R. Van Praagh, and E. P. Walsh. Late enlargement of radiofrequency lesions in infant lambs.

- implications for ablation procedures in small children. *Circulation*, 90:492–499, 1994. (Cited on page [104](#).)
- [SKD⁺07] M. Sermesant, E. Konukoglu, H. Delingette, Y. Coudiere, P. Chinchapatnam, K. Rhode, R. Razavi, and N. Ayache. An anisotropic multi-front fast marching method for real-time simulation of cardiac electrophysiology. *Functional Imaging and Modeling of the Heart*, 4466 of LNCS:160–169, 2007. (Cited on pages [23](#), [32](#) and [53](#).)
- [SKS⁺93] WG. Stevenson, H. Khan, P. Sager, Saxon LA., HR. Middlekauff, PD. Natterson, and I. Wiener. Identification of reentry circuit sites during catheter mapping and radiofrequency ablation of ventricular tachycardia late after myocardial infarction. *Circulation*, 88:1647–1670, 1993. (Cited on pages [52](#) and [115](#).)
- [SMD⁺97] S.A. Strickberger, K.C. Man, E.G. Daoud, R. Goyal, K. Brinkman, C. Hasse, F. Bogun, B.P. Knight, R. Weiss, M. Bahu, et al. A prospective evaluation of catheter ablation of ventricular tachycardia as adjuvant therapy in patients with coronary artery disease and an implantable cardioverter-defibrillator. *Circulation*, 96(5):1525, 1997. (Cited on page [98](#).)
- [SSK⁺10] G. Seemann, FB Sachse, M. Karl, DL Weiss, V. Heuveline, and O. Dössel. Framework for modular, flexible and efficient solving the cardiac bidomain equations using petsc. *Progress in Industrial Mathematics at ECMI 2008*, pages 363–369, 2010. (Cited on page [20](#).)
- [SSM⁺01] K. Soejima, M. Suzuki, W.H. Maisel, C.B. Brunckhorst, E. Delacretaz, L. Blier, S. Tung, H. Khan, and W.G. Stevenson. Catheter ablation in patients with multiple and unstable ventricular tachycardias after myocardial infarction: short ablation lines guided by reentry circuit isthmuses and sinus rhythm mapping. *Circulation*, 104(6):664, 2001. (Cited on pages [90](#) and [99](#).)
- [SSW⁺04] L. Szumowski, P. Sanders, F. Walczak, M. Hocini, P. Jais, R. Kepski, E. Szufiadowicz, P. Urbanek, P. Derejko, R. Bodalski, et al. Mapping and ablation of polymorphic ventricular tachycardia after myocardial infarction. *Journal of the American College of Cardiology*, 44(8):1700, 2004. (Cited on pages [65](#) and [131](#).)
- [TDF⁺10] A. Thiagalingam, A. D’Avila, L. Foley, J. L. Guerrero, H. Lambert, G. Leo, J. N. Ruskin, and V. Y. Reddy. Importance of catheter contact force during irrigated radiofrequency ablation: evaluation in a porcine ex vivo model using a force-sensing catheter. *Journal of Cardiovascular Electrophysiology*, 21:806–811, 2010. (Cited on page [100](#).)

- [TGB⁺03] S.P. Thomas, D.J.R. Guy, A.C. Boyd, V.E. Eipper, D.L. Ross, and R.B. Chard. Comparison of epicardial and endocardial linear ablation using handheld probes. *The Annals of thoracic surgery*, 75(2):543, 2003. (Cited on page 105.)
- [THP02] K.A. Tomlinson, P.J. Hunter, and A.J. Pullan. A finite element method for an eikonal equation model of myocardial excitation wavefront propagation. *SIAM Journal on Applied Mathematics*, 63(1):324–350, 2002. (Cited on page 56.)
- [TLHHS05] I. Turner, C. L-H Huang, and R.C. Saumarez. Numerical simulation of paced electrogram fractionation: relating clinical observations to changes in fibrosis and action potential duration. *Journal of cardiovascular electrophysiology*, 16(2):151–161, 2005. (Cited on page 83.)
- [TT09] N.A. Trayanova and B.M. Tice. Integrative computational models of cardiac arrhythmias—simulating the structurally realistic heart. *Drug Discovery Today: Disease Models*, 6(3):85–91, 2009. (Cited on pages 53, 79 and 115.)
- [TTBHP06] K.H. Ten Tusscher, O. Bernus, R. Hren, and A.V. Panfilov. Comparison of electrophysiological models for human ventricular cells and tissues. *Progress in Biophysics and Molecular Biology*, 90:326–345, 2006. (Cited on page 23.)
- [TTHP⁺07] K.H.W.J. Ten Tusscher, R. Hren, A.V. Panfilov, et al. Organization of ventricular fibrillation in the human heart. *Circulation research*, 100(12):e87–e101, 2007. (Cited on pages 24 and 80.)
- [TTNNP04] K. Ten Tusscher, D. Noble, P.J. Noble, and A.V. Panfilov. A model for human ventricular tissue. *American Journal of Physiology- Heart and Circulatory Physiology*, 286(4):H1573, 2004. (Cited on pages 24, 32 and 52.)
- [TTP03] K. Ten Tusscher and A.V. Panfilov. Influence of nonexcitable cells on spiral breakup in two-dimensional and three-dimensional excitable media. *Physical Review E*, 68(6):062902, 2003. (Cited on page 83.)
- [TTP05] K. Ten Tusscher and A.V. Panfilov. Wave propagation in excitable media with randomly distributed obstacles. *Multiscale Model Simul*, 3:265–82, 2005. (Cited on page 83.)
- [TTP07] K.H.W.J. Ten Tusscher and A.V. Panfilov. Influence of diffuse fibrosis on wave propagation in human ventricular tissue. *Europace*, 9(suppl 6):vi38–vi45, 2007. (Cited on pages 83 and 85.)

- [TWC⁺00] S. Tungjitkusolmun, E. J. Woo, H. Cao, J.-Z. Tsai, V. R. Vorperian, , and J. G.. Webster. Thermal-electrical finite element modeling for radio-frequency cardiac ablation: effects of changes in myocardial properties. *Medical Biological Engineering and Computing*, 38(11):562–568, 2000. (Cited on pages 101 and 102.)
- [VAT02] E.J. Vigmond, F. Aguel, and N.A. Trayanova. Computational techniques for solving the bidomain equations in three dimensions. *Biomedical Engineering, IEEE Transactions on*, 49(11):1260–1269, 2002. (Cited on page 20.)
- [vBBS⁺04] T. J. van Brakel, G. Bolotin, K. J. Salleng, L. W. Nifong, M. A. Alessie, W. R. J. Chitwood, and J. G. Maessen. Evaluation of epicardial microwave ablation lesions: histology versus electrophysiology. *The Annals of Thoracic Surgery*, 78:1397–402; discussion 1397, 2004. (Cited on pages 97 and 104.)
- [VBLP09] E.J. Vigmond, P.M. Boyle, L.J. Leon, and G. Plank. Near-real-time simulations of bioelectric activity in small mammalian hearts using graphical processing units. In *Engineering in Medicine and Biology Society, 2009. EMBC 2009. Annual International Conference of the IEEE*, pages 3290–3293. IEEE, 2009. (Cited on pages 138 and 139.)
- [WB95] G. Welch and G. Bishop. An introduction to the kalman filter. *University of North Carolina at Chapel Hill, Chapel Hill, NC*, 7(1), 1995. (Cited on page 141.)
- [WBS85] HJ Wellens, P. Brugada, and W.G. Stevenson. Programmed electrical stimulation of the heart in patients with life-threatening ventricular arrhythmias: what is the significance of induced arrhythmias and what is the correct stimulation protocol? *Circulation*, 72(1):1, 1985. (Cited on pages 90 and 159.)
- [WCZ⁺11] Y. Wang, P.S. Cuculich, J. Zhang, K.A. Desouza, R. Vijayakumar, J. Chen, M.N. Faddis, B.D. Lindsay, T.W. Smith, and Y. Rudy. Noninvasive electroanatomic mapping of human ventricular arrhythmias with electrocardiographic imaging (ecgi). *Science Translational Medicine*, 3(98):98ra84, 2011. (Cited on pages 15, 17 and 141.)
- [WE00] Stevenson W.G and Delacretaz E. Radiofrequency catheter ablation of ventricular tachycardia. *Heart*, 84:553–559, 2000. (Cited on page 78.)
- [WF02] M. A. Wood and I. A. Fuller. Acute and chronic electrophysiologic changes surrounding radiofrequency lesions. *Journal of Cardiovascular Electrophysiology*, 13:56–61, 2002. (Cited on pages 102, 104 and 105.)

- [WFCT99] C.C. Wu, II Fasciano, H. Calkins, and L. Tung. Sequential change in action potential of rabbit epicardium during and following radiofrequency ablation. *Journal of cardiovascular electrophysiology*, 10(9):1252–1261, 1999. (Cited on page 106.)
- [WFE⁺01] M.A. Watanabe, F.H. Fenton, S.J. Evans, H.M. Hastings, and A. Karma. Mechanisms for discordant alternans. *Journal of Cardiovascular Electrophysiology*, 12(2):196–206, 2001. (Cited on pages 25, 53, 87 and 115.)
- [WGL⁺11] M. Wood, S. Goldberg, M. Lau, A. Goel, D. Alexander, F. Han, and S. Feinstein. Direct measurement of the lethal isotherm for radiofrequency ablation of myocardial tissue. *Circulation Arrhythmia and Electrophysiology*, 2011. (Cited on page 100.)
- [WHRdM89] F. H. Wittkampf, R. N. Hauer, and E. O. Robles de Medina. Control of radiofrequency lesion size by power regulation. *Circulation*, 80:962–968, 1989. (Cited on page 100.)
- [WK07] Stevenson W.G and Soejima K. Catheter ablation for ventricular tachycardia. *Circulation*, 115:2750–60, 2007. (Cited on page 78.)
- [WSD⁺07] Y. Wang, R.B. Schuessler, R.J. Damiano, P.K. Woodard, and Y. Rudy. Noninvasive electrocardiographic imaging (ecgi) of scar-related atypical atrial flutter. *Heart rhythm: the official journal of the Heart Rhythm Society*, 4(12):1565, 2007. (Cited on pages 15 and 141.)
- [WWZ⁺11] L. Wang, K.C.L. Wong, H. Zhang, H. Liu, and P. Shi. Noninvasive computational imaging of cardiac electrophysiology for 3-d infarct. *Biomedical Engineering, IEEE Transactions on*, 58(4):1033–1043, 2011. (Cited on page 17.)
- [XQY⁺04] F. Xie, Z. Qu, J. Yang, A. Baher, J.N. Weiss, A. Garfinkel, et al. A simulation study of the effects of cardiac anatomy in ventricular fibrillation. *Journal of Clinical Investigation*, 113(5):686–693, 2004. (Cited on page 79.)
- [YFRM05] A.M. Yue, M.R. Franz, P.R. Roberts, and J.M. Morgan. Global endocardial electrical restitution in human right and left ventricles determined by noncontact mapping. *Journal of the American College of Cardiology*, 46(6):1067, 2005. (Cited on pages 53, 55, 88, 115, 117, 118 and 128.)